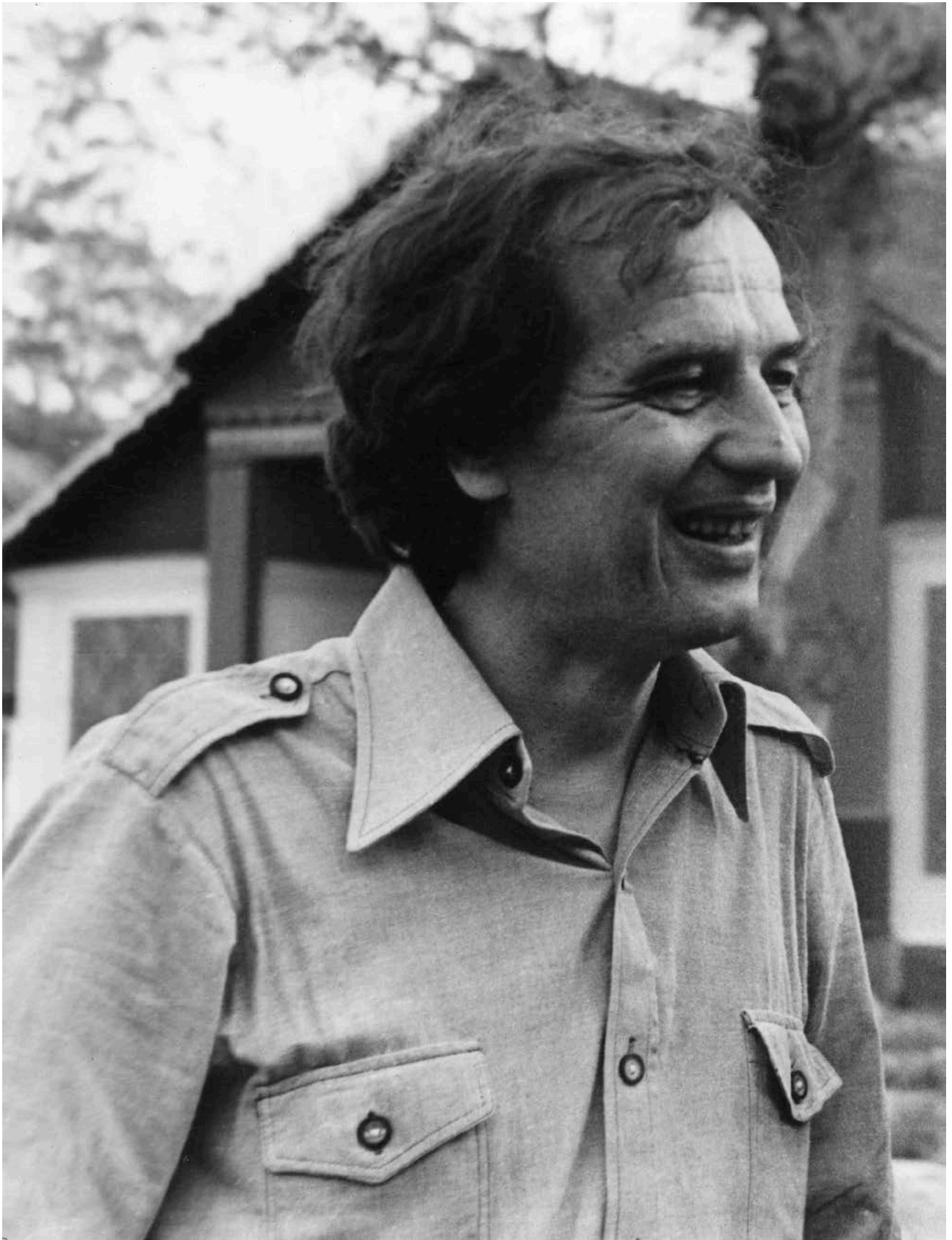


*Dedicated to Professor Boris I. Kochelaev  
on the occasion of his eightieth birthday*

**MODERN PROBLEMS  
IN CONDENSED MATTER PHYSICS**

**Vol. 2**

*From Kochelaev's scholars, colleagues and friends*



*Professor Boris Kochelaev in the late seventies*  
*Профессор Борис Иванович Кочелаев в конце семидесятых*

*Dedicated to Professor Boris I. Kochelaev  
on the occasion of his eightieth birthday*

**MODERN PROBLEMS  
IN CONDENSED MATTER PHYSICS**

**Vol. 2**



**KAZAN  
2014**

**Editors:**  
Prof. **B.Z. Malkin,**  
Prof. **Yu.N. Proshin**

**Modern Problems in Condensed Matter Physics. Vol. 2.** – Kazan: Kazan University Publishing House, 2014. – 204 p.

**ISBN 978-5-00019-258-5**

**ISBN 978-5-00019-300-6**

The present book is dedicated to Boris I. Kochelaev, professor of Theoretical Physics Department of Kazan Federal University. It contains original scientific papers by pupils and colleagues of B.I. Kochelaev devoted to his eightieth birthday. Two articles (in Russian) present reminiscences of well-known physicists, Prof. M.I. Kaganov and Prof. A.A. Kokin, about meetings with B.I. Kochelaev. Papers cover a wide range of modern problems of condensed matter physics: from physics of polymer compounds to physics of superconductors. These studies involve the ideas and methods developed by B.I. Kochelaev and refer to his scientific interests. The first collection of articles by B.I. Kochelaev's pupils (Vol. 1) has been released in 2004.

The book is intended for researchers and post-graduate students, who are interested in problems of Quantum Theory of Condensed Matter.

- © **Theoretical Physics Department of Kazan Federal University, design, 2014**
- © **Magnetic Resonance in Solids. Electronic Journal, design, 2014**
- © **Kazan University Publishing House, 2014**

*Посвящается восьмидесятилетию  
профессора Бориса Ивановича Кочелаева*

**АКТУАЛЬНЫЕ ПРОБЛЕМЫ  
ФИЗИКИ КОНДЕНСИРОВАННЫХ СРЕД**

**Том 2**



**КАЗАНЬ  
2014**

**УДК 538.9**  
**ББК 22.31**  
**А43**

**Научные редакторы:**  
профессор **Б.З. Малкин**,  
профессор **Ю.Н. Прошин**

**А43 Актуальные проблемы физики конденсированных сред. Том 2.** –  
Казань: Изд-во Казан. ун-та, 2014. – 204 с.

**ISBN 978-5-00019-258-5**

**ISBN 978-5-00019-300-6**

Настоящий сборник посвящен профессору кафедры теоретической физики Казанского федерального университета Борису Ивановичу Кочелаеву и составлен из оригинальных научных статей, написанных в основном на английском языке ко дню его восьмидесятилетия его учениками и коллегами. Также в книге помещены воспоминания известных физиков, профессора Каганова М.И. и профессора Кокина А.А., о встречах с юбиляром, написанные на русском языке. Статьи охватывают широкий круг проблем современной физики конденсированных сред: от физики полимеров до физики сверхпроводников. Объединяет представленные исследования то, что они, во всяком случае, относятся к кругу интересов Б.И. Кочелаева, в ряде работ непосредственно используются развитые им методы и идеи. Первый том был выпущен в 2004 году.

Книга предназначена для исследователей и аспирантов, интересующихся проблемами квантовой теории конденсированных сред.

**УДК 538.9**  
**ББК 22.31**

**ISBN 978-5-00019-258-5**

**ISBN 978-5-00019-300-6**

- © Кафедра теоретической физики Казанского федерального университета, оформление, 2014
- © *Magnetic Resonance in Solids. Electronic Journal*, оформление, 2014
- © Издательство Казанского университета, 2014

## Contents

Preface.....	9
<i>М.И. Каганов</i> Издаюла, часть вторая и, надеюсь, не последняя...	
<i>М.И. Каганов</i> From far away (part II) [in Russian] .....	12
<i>А.А. Кожин</i> Четыре физика в лодке на Подкаменной Тунгуске летом 1965 года	
<i>А.А. Кожин</i> Four physicists in a boat on the Podkamennaya Tunguska river in the summer of 1965 [in Russian] .....	13
<i>V.A. Atsarkin, V.V. Demidov, B.V. Sorokin</i> Resonance dc phenomena in manganite thin films .....	21
<i>S.I. Andronenko</i> Spin relaxation of Mn ions in rare earth manganites in paramagnetic region .....	29
<i>S.I. Belov, A.S. Kutuzov</i> Static magnetic susceptibility of the systems with anisotropic Kondo interaction .....	33
<i>R.G. Deminov, N.Kh. Useinov, L.R. Tagirov</i> Magnetic and superconducting heterostructures in spintronics .....	41
<i>I.M. Eremin, A.V. Chubukov</i> Antiferromagnetism in ferropnictides: selection of magnetic order and spin excitations .....	50
<i>M.V. Eremin, I.M. Shigapov, I.M. Eremin</i> Spin response in HTSC cuprates: generalized RPA approach with projection operators method .....	65
<i>N.F. Fatkullin, R. Valiullin</i> Short-time diffusion behavior of Brownian particles in porous solids .....	86
<i>I.A. Garifullin, N.N. Garif'yanov, P.V. Leksin, A.A. Kamashev, Ya.V. Fominov, J. Schumann, V. Kataev, B. Büchner</i> The peculiarities of the operation of the superconducting spin valve .....	93
<i>Y.V. Lysogorskiy, D.A. Tayurskii</i> Quantum fluids in nanoporous media - effects of the confinement and fractal geometry. Theory and simulation .....	106
<i>A. Maisuradze, A. Shengelaya, E. Pomjakushina, K. Conder, H. Keller, K.A. Müller</i> Exponential temperature dependence of the $\text{Yb}^{3+}$ relaxation in $\text{Y}_{0.98}\text{Yb}_{0.02}\text{Ba}_2\text{Cu}_3\text{O}_x$ .....	124
<i>Г.И. Миронов</i> Исследование одностенных углеродных зигзагообразных нанотрубок в модели Хаббарда в приближении статических флуктуаций	
<i>G.I. Mironov</i> Static fluctuations approach to the single-walled zigzag pattern carbon nanotubes in Hubbard model [in Russian] .....	130

<i>R.R. Nigmatullin, R.M. Rakhmatullin, S.I. Osokin</i>	
How to reduce reproducible measurements to an ideal experiment? .....	138
<i>Yu.N. Proshin, M.V. Avdeev</i>	
Proximity effect in ferromagnet/superconductor trilayers with triplet correlations in an external magnetic field .....	157
<i>E.P. Sharin</i>	
Local magnetic field distribution of the vortex lattice near surface of superconducting plate.....	172
<i>V.E. Shilov, E.V. Shilova</i>	
Influence of electron correlations on magnetic properties in transition metals in view of degeneration .....	178
<i>B. Schmidt, H.-A. Krug von Nidda, S. Riegg, S.G. Ebbinghaus, A. Reller, A. Loidl</i>	
Probing the metal-to-insulator transition in $\text{LaCu}_3\text{Ru}_x\text{Ti}_{4-x}\text{O}_{12}$ by Gd-ESR .....	182
Список научных работ Б.И. Кочелаева	
List of publications by B.I. Kochelaev .....	192
Ученики Б.И. Кочелаева	
Pupils of B.I. Kochelaev .....	203

## Preface

April, 19, 2014 is the 80th anniversary of Boris Ivanovich Kochelaev, Professor at Kazan University, the leading scientist in the field of spin dynamics in condensed matter, the brightest representative of the Kazan Physical School founded by the corresponding-member of USSR Academy of Sciences S.A. Al'tshuler.

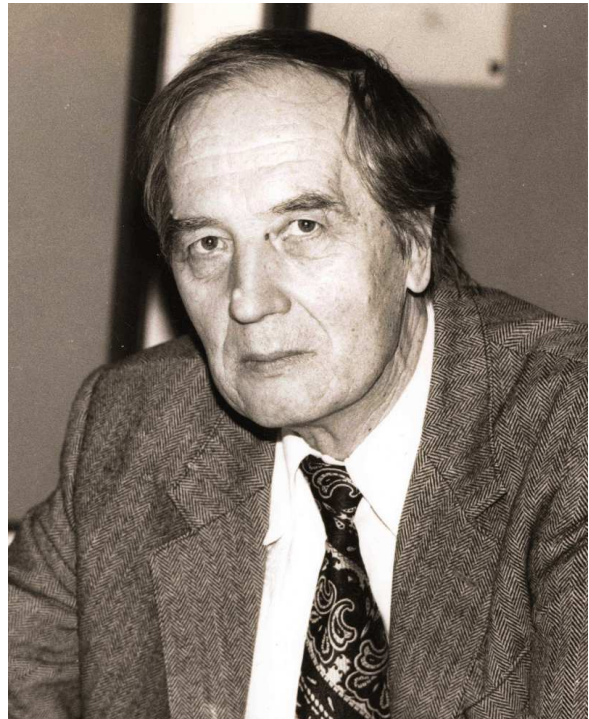
Born in 1934 in the industrial settlement DirizhablStroi (now Dolgoprudny city in the Moscow region) Boris I. Kochelaev graduated with the silver medal the secondary school in the city of Vyatskie Polyany (Kirov's region) and entered to the Physical-Mathematical Faculty at Kazan State University in 1952.

The scientific research activities of B.I. Kochelaev started during his students' years under supervision of S.A. Al'tshuler and then continued on PhD courses at the Chair of Experimental and Theoretical Physics

(1957-1960). After getting the PhD degree at Kharkov University, Boris I. Kochelaev took the positions of assistant professor, associate professor and full professor of the Chair of Theoretical Physics at Kazan State University (Now it is Kazan Federal University). He headed this Chair during 27 years (1973-2000). During more than 50 years B.I. Kochelaev is the leading lecturer at Physics Department (Now it is Institute of Physics), he has developed the lecture courses on quantum theory of solids, non-equilibrium thermodynamics and quantum statistical physics. These courses are considered as the basic education courses for the theoretical physics students.

The period for two terms in Harvard University (1963-1964) had a great impact on the scientific interests of B.I. Kochelaev. In Harvard University, under supervision of the future Nobel Prize winner professor N. Bloembergen, he solved the problem of conduction electron spin polarization and electron correlations influence on indirect exchange interactions between paramagnetic impurities in metals. In 1967 B.I. Kochelaev got the Doctoral Degree with the thesis "The theory of dynamic effects in paramagnetic crystals".

The scientific works of B.I. Kochelaev in sixties and seventies were devoted to studies of spin-phonon interactions in paramagnetic crystals. He proposed original theories of non-resonant absorption and resonant dispersion of the hypersound in a paramagnetic media, the indirect spin-spin interactions between paramagnetic ions caused by conduction electrons in semiconductors and mediated by phonons in insulators, the nuclear spin relaxation caused by electronic spin-spin interactions at ultra-low temperatures, investigated the manifestations of the dispersion of crystal vibrational spectra in the Jahn-Teller effect, derived the theory of the coupled spin-phonon excitations and determined the conditions for their appearance. Together with L.K. Aminov, B.I. Kochelaev investigated interactions between paramagnetic centers via phonons with taking into account the retardation effects. This work had the essential influence on further development of the theories of interactions between localized electrons mediated by static and dynamic crystal lattice deformations. Further investigations of non-linear phenomena in paramagnets irradiated by radio-frequency fields, light and hypersound resulted in the theory



of kinetic processes in paramagnetic crystals based on the spin temperature concept. In the framework of this theory it appeared to be possible to explain the experimentally observed phonon avalanche under saturation on the wing of the electron paramagnetic resonance (EPR) line. Also the theory of light scattering in paramagnetic insulators was developed, and the experimentally observed super-scattering of light under saturation on the wing of the EPR line was explained. B.I. Kochelaev predicted the observed later effect of non-resonant sound absorption and its giant amplification by radio-frequency fields.

Together with his PhD students, B.I. Kochelaev proposed the theory of EPR and spin relaxation in conventional superconductors with paramagnetic impurities. It has been shown that the spin dynamics and magnetic properties of impurity superconductors are determined mainly by existence of the coupled spin excitations of the conducting and localized electrons as well as by appearance of long-range correlations between paramagnetic impurities. In the framework of this theory the whole set of rather unusual experimental data on EPR in conventional superconductors obtained by the group headed by E.G. Kharakhashyan in Kazan Physical-Technical Institute was explained.

In recent years the scientific activities of B.I. Kochelaev lie in the most “hot” topics of condensed matter physics, namely, in the physics of strong-correlated electron systems. He proposed to use paramagnetic probes inside  $\text{CuO}_2$  planes to measure relaxation rates of magnetization in high- $T_c$  superconductors. The idea of Kochelaev has been successfully realized in the joint investigations with the group headed by Prof. B. Elshner in Darmstadt University. Further investigations based on the proposed method in collaboration with the group headed by the Nobel Prize winner Prof. K.A. Müller in Zürich University allowed to understand the nature of very fast electron spin relaxation and to propose the model for the observed phase separation onto nanoscale metal and insulator domains in  $\text{CuO}_2$  planes.

Low-dimensional magnets and the role of antiferromagnetic fluctuations have been investigated by B.I. Kochelaev together with his PhD student S.I. Belov. They proposed a new approach based on idea about spin waves in the media with topological excitations (skyrmions) and described in the framework of a single model static and dynamic parameters of layered magnets such as spin coherence length, magnetic susceptibility, nuclear spin relaxation rate etc.

In the last years the works of B.I. Kochelaev in collaboration with the groups headed by Prof. H.-A. Krug von Nidda and Prof. A. Loidl were devoted to the EPR investigations of the electron spin kinetics in substances with giant magnetoresistance. Together with the group headed by Dr. J. Sichelschmidt in Dresden, EPR spectra in heavy-fermion compounds below Kondo temperature were studied. These last theoretical investigations are best described by the Nobel Prize winner Prof. K.A. Müller in the paper titled “The Impact of ESR (EPR) on the Understanding of the Cuprates and Their Superconductivity” and published in the *EPR newsletter* in 2012:

*“Finally, it should be noted that this important advance was achieved by the experimental results at the universities of Darmstadt and Zürich on the one side and the deep theoretical insight of Boris Kochelaev at the Kazan State University explaining them on the other side.”*

The investigations of B.I. Kochelaev devoted to the theory of nuclear and electron spin-lattice relaxation, to the theory of magnetic resonance phenomena in insulators, metals and superconductors are well known in the world. He has been invited to the numerous international, All-Union and All-Russian conferences and scientific schools with plenary talks. The international electronic journal *Magnetic Resonance in Solids* based by B.I. Kochelaev was accepted

to index by Scopus, a world leader of the journal database. Professor Kochelaev founded his own scientific school (see also p.203). He supervised 33 PhD students, among which 9 got the Doctoral degrees, became the professors (in Russia, Germany and USA). One more Doctoral degree thesis was also consulted by him.

During many years B.I. Kochelaev is the chairperson in the Council for PhD and Doctoral degree awarding, the member of the International Committee of Scientific Society AMPERE. The Red Banner Order and the Order of the Honor, the State Award of Tatarstan Republic for science and technology awarded him. B.I. Kochelaev is the Honored Scientist of Russian Federation and Tatarstan Republic, the Honored Professor of Kazan University.

The present book is the evidence of a recognition of his scientific achievements and high-standard human nature, and the acknowledgement of deep respect from his numerous disciples and colleagues. This book can be considered as second volume and sequel of the book published ten years ago and devoted to the 70th anniversary.

We are sincerely grateful to authors of papers for fruitful cooperation. We are thankful to Dr. A.S. Kutuzov and Dr. M.V. Avdeev for their assistance during operation over manuscripts, and also to all who shared in the edition of this collection.

Kazan, April, 2014

B.Z. Malkin  
Yu.N. Proshin

## Издадека, часть вторая и, надеюсь, не последняя...

М.И. Каганов

10 лет назад в честь 70-летия Бориса Ивановича Кочелаева вышел сборник “Актуальные проблемы физики конденсированных сред”. Очень мне приятно, что первая статья после предисловия – моя заметка “Издадека”. Уже тогда мы, юбиляр и я, были далеко друг от друга. Время, прошедшее с тех пор, нас не сблизило: мы ни разу не повидались за эти годы. В статье я поделился с читателями своим тёплым, весьма уважительным отношением к Борису и Наташе.

Удивительно, но прошедшие 10 лет, не ликвидировали близости, которая была между нами. Во всяком случае, по моим ощущениям. Не хочу притворяться и утверждать, что все годы непрерывно думал о Кочелаеве. Конечно, это не так. Но, когда зашла речь о нынешнем юбилее, с которым искренне поздравляю Бориса, у меня мелькнула мысль, по советским меркам крамольная, по нынешним временам, вызывающая, наверное, улыбку. Я подумал: “У большинства, скорее всего, при упоминании Казани сразу всплывают имена Ленина, Лобачевского, у кого-то даже Ивана Грозного. А я вот прежде всего вспоминаю имена Семёна Александровича Альтшулера, Бориса Ивановича Кочелаева и Юры из Казани (Юры Прошина, который был аспирантом сразу у двух руководителей, у Б.И. и у меня).” Главное, по-прежнему “Для меня Казань – город друзей”, – это цитата из статьи. Вспоминаю свою длинную жизнь, я перебираю даты и места, где бывал. С особенным удовольствием те, где и когда мне было хорошо. Казань занимает в этих воспоминаниях весьма заметное место. А ведь начиналось всё с защиты нынешним юбиляром кандидатской диссертации в Харькове. Но и об этом есть в заметке десятилетней давности.

В конце заметки есть несколько слов, которые хочу воспроизвести сейчас: “У Бориса ощущалось спокойное понимание происходившего в стране”. Очень надеюсь, что способность спокойного понимания у Вас, Борис, сохранилась. Она нужна всегда.

Юра из Казани написал мне, что Вы в хорошей форме, работаете, читаете лекции. Обрадовался и хочу пожелать, чтобы так было и дальше. Мы оба знаем, какое место в нашей жизни занимает то, чему мы посвятили свою жизнь. И как тяжело без иногда утомительной, но необходимой занятости.

Будьте, пожалуйста, здоровы и бодры!

М.И. Каганов,  
Март 2014-го года,  
Waltham, MA, USA.

## Четыре физика в лодке на Подкаменной Тунгуске летом 1965 года

А.А. Кокин

Во время моего первого в Зеленограде очередного отпуска летом 1965 года я вместе с Б.С. Борисовым (Бобом), а также профессором Математического института АН СССР им. В.М. Стеклова С.В. Тябликовым и профессором Казанского университета Б.И. Кочелаевым совершил двухнедельное лодочное путешествие по Подкаменной Тунгуске. К сожалению, подробный дневник этого путешествия с описанием полной лодки, который вел я, не сохранился. Позже его взял у меня Б.С. Борисов, чтобы использовать в другом путешествии по Подкаменной Тунгуске без меня в 1969 г., окончившимся трагически, где он и был утерян. Я опишу это путешествие теперь по памяти.



*Организатор путешествия, профессор  
С.В. Тябликов*



*Постоянный кормчий, профессор  
Б.И. Кочелаев*



*Основные гребцы А.А. Кокин и Б.С. Борисов*

### *Четыре физика в лодке на Подкаменной Тунгуске летом 1965 года*

С.В. Тябликов был старше нас (1921 года рождения), он уже предпринял год назад попытку в одиночку побывать на Подкаменной Тунгуске. Однако заболел и вынужден был возвратиться домой. Однако свою мечту он не забросил, а стал сколачивать группу. Вначале это были Б. Кочелаев, два брата Пузея – металлурги и заядлые рыбаки и их приятель – художник (не помню их имена). Не знаю, какие узы связывали тогда Сергея Владимировича с братьями Пузеями. Потом он обратился с предложением и ко мне, я согласился и предложил взять еще Боба. Сергей Владимирович договорился с райкомом КПСС в селе Байкит на Подкаменной Тунгуске о том, что нам подготовят вместительную (на 7 человек) лодку, на которой мы поплывем вниз до Енисея. Никакой карты и лоции я не видел.

Моя жена Юля в это время с двухгодовалым Сережкой решила уехать к маме в Белоруссию на все лето.

Одновременный отлет всех членов группы не получился. Два Пузея с художником (далее эту троицу буду просто упоминать как «Пузеи») вылетели в Байкит на два дня раньше, с тем, чтобы подготовить лодку. Возможно, карты и лоции были у них. Мы же втроем вылетели до Красноярска, где встретились с Борисом Кочелаевым. Так состоялось мое знакомство с Борисом. Затем на самолете Ан-10 прилетели в Байкит, но никаких Пузеев там не нашли. Зашли в райком КПСС, где нас встретил секретарь райкома, эвенк. Он сказал, что лодку Пузеи взяли и отплыли, а другой лодки он нам дать не может. Потом, чувствуя какое-то неудобство перед московскими гостями, он сказал, что на берегу живет один человек, у него есть небольшая лодка, которую он, возможно, сможет продать. Мы нашли хозяина лодки дома. Он согласился продать нам лодку, насколько помню, за водку. Он сразу стал расхваливать свою лодку «ангарку» (не плоскодонка, а килевая). Потом, узнав, что у нас нет никакой лоции, несмотря на то, что был сильно нетрезв, начал



*Мы с Бобом отправляемся в аэропорт. Эта остановка автобуса теперь называется «Улица Юности». В Зеленограде тогда не везде был асфальт.*



подробно описывать все пороги, которые ждут нас впереди. Я все это записал в своем дневнике и, как потом оказалось, все было сказано точно. Лодка была очень ветхая, местами прогнила и разошлась, но делать было нечего.

В реке местные мальчишки ловили хариуса на «кораблик». Я присмотрелся к этой нехитрой, но очень продуктивной снасти и позже тоже соорудил такой же кораблик. Принцип ее простой: плоская доска с грузом на краю, так, чтобы она плавала вертикально, привязывалась к длинной леске, подобно тому, как привязывают воздушного змея и пускают по течению, натягивая леску. Течение воды относит кораблик на середину реки и даже к другому берегу. На длинную леску привязывают поперечные поводки с крючками, на которые насажены насекомые или искусственные «мушки». Эти поводки, когда натянута основная леска, трепещут на поверхности воды, привлекая хариуса, если он там есть. Основная пища хариуса – это насекомые, летающие низко над водой, которых он, выпрыгивая, и хватал.

Мы забрали лодку, расположились на берегу, поставили палатки и стали ее ремонтировать. Собрали на берегу куски битума, консервные банки и начали ставить заплатки, затем засмолили ее, погрузили вещи и сели сами. Лодка глубоко села, от поверхности воды до края лодки было не более 4 сантиметров.

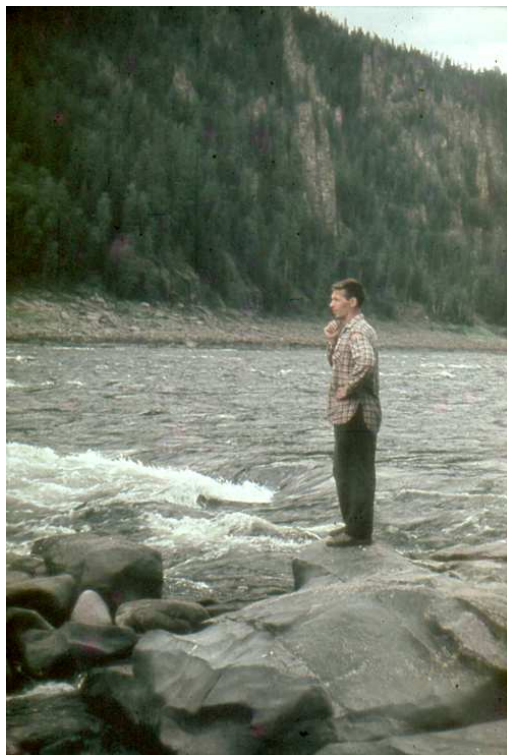
Я взял с собой свою двухстволку-тулку. У Бориса Кочелаева была серьезная двухстволка с вертикально расположенными стволами и спиннинг. У всех были высокие болотные сапоги. О спасательных жилетах тогда как-то и не думали. Боб взял с собой кинокамеру, ту которую он брал в Саяны в 1962 году. Вода в реке была теплая, комаров у воды было мало. После захода солнца комары обычно вообще исчезали. У нас были две брезентовых палатки.

Отчалили. Течение было быстрое, но спокойное. Река не широкая. На берегу чистая галечная отмель. Это след, оставляемый весенним половодьем. Я временами шел пешком с ружьем, но ничего не попадалось. Далее река широко разлилась. Лодка иногда плыла не быстрее моего шага. Иногда нужно было грести. Для этого кого-то сажали на весла.

По берегу возвышались отвесные скалы, местами в виде колонн или столбов, высотой до 40 м. Красота. Вдруг видим впереди на левом берегу какие-то люди размахивают спиннингом. Причаливаем. Это и были «Пузеи». Они встретили нас одной фразой «А, и вы приехали!» и продолжали рыбачить. Большая добротная лодка-плоскодонка стояла тут же.



*Скалы на берегу*



*Порог «Горлышко»*

Такой встречи мы не ожидали и решили не останавливаться рядом с ними, а поплыли дальше и затем встали на ночлег. Вскоре они нас обогнали и даже не пытались завязать разговор.

Первое препятствие – это резкое сужение реки названное «Горлышком» с очень быстрым течением, а за ним и шивера, названная Бабушкой, потом должен быть порог «Дедушка». Бабушку нужно было проходить слева, а Дедушку справа. Когда достигли шиверы, прошли ее спокойно и решили, что Бабушка еще впереди. В лодке остались я на веслах и Борис с кормовым веслом, остальные шли пешком. Вещи частично выгрузили. Справа скалы берегового гребня близко подходят к воде. А порог Дедушку мы приняли за Бабушку и стали проходить его слева, а не справа. Борис очень умело управлял лодкой. Где-то там, лодку захлестнула вода, промокли плохо упакованные вещи и батареи для кинокамеры Боба. Так что кино снять не удалось. Порог нам не показался грозным. Плыдем дальше. Течение спокойное, река стала шире. Навстречу попала моторная лодка с местными жителями. Они объяснили, что нами были пройдены и Бабушка, и Дедушка и с непониманием смотрели на нас: «Вы что, собираетесь утонуть на такой лодке?».

Проплыли первый населенный пункт – поселок Полигус (километров 20 от Дедушки). Это второй по величине после Байкита поселок на Подкаменной Тунгуске. Мы отплыли дальше и остановились на берегу на обед. Расслабились. Борис достал припасенную фляжку с «тутовкой» – настойкой, подаренной ему аспирантом с Кавказа, которую мы дружно и опорожнили в честь благополучного прохождения первых порогов. Сильно захмелели. Погода стала портиться. Пошел дождь. Мы с Бобом поднялись наверх, чтобы посмотреть место для палаток. Там увидели маленькую охотничью избушку, в которой и укрылись. Утром погода наладилась, и мы поплыли дальше.

Следующий порог Мучной расположен в двадцати пяти километрах ниже от Полигуса. Вот стали видны белые барашки порога. Пристаем к левому берегу, где высятся причудли-

вые утесы-столбы и идем по берегу смотреть порог. Решили полностью разгрузить лодку и перенести вещи по берегу. Снова мы с Борисом раздеваемся до трусов и кед и садимся в лодку. Борис просит меня нажимать на весла со всех сил, чтобы скорость лодки была больше скорости течения. Тогда лодка становилась управляемой, и задачей Бориса было найти нужную струю. Все прошло хорошо. Порог позади. Мы причаливаем к левому берегу и становимся на ночлег. Пока ставили палатки и разводили костер, Борис пошел со спиннингом к реке. Стало темно. Вдруг слышим его крик: «Скорее сюда с топором!». Прибегаем и видим. Борис борется с огромным, более метра, тайменем, который пытается сорваться с крючка. Отсекаем ему голову, но его могучее тело продолжает еще долго трепыхаться. Решили из части сварить уху, а другую зажарить. Мы все первый раз попробовали тайменя. Надо сказать, что для ухи он не очень годился, но жареный был



*Весной здесь круто*



*Привал на берегу. Слева направо: Б.И. Кочелаев, С.В. Тябликов, Б.С. Борисов (Боб) и А.А. Кожин (снимал с автоспуска)*



*Ночуем у костра*

великолепен. Другое дело хариус. Я уже сделал кораблик, и иногда мне удавалось наловить хариуса. Далее мы не раз останавливались на берегу. Борис забрасывал спиннинг, а я запускал кораблик. Во время плавания на реке попадались стаи плавающих уток, которых мы пытались подстрелить из лодки. Один раз попалась странная утка с длинным зубастым клювом – крохаль с белым плотным оперением на груди. Но когда мы сварили ее, есть не стали – очень сильно отдавало рыбой. По палаткам мы разделились на пары: я с Борисом в одной, а курильщики Сергей Владимирович с Бобом в другой.

В одну из дней на берегу у впадения справа небольшой речки мы с Борисом решили сходить на пару дней на охоту вверх по притоку. Палатку решили не брать, а для ночлега у костра взяли только полиэтиленовую пленку-шторку. Сергей Владимирович и Боб остались на берегу. Мы отошли от реки и попали в царство комаров. На этот случай у нас был диметилфтолат, который действовал, но недолго. Борис снова отличился. Он подстрелил сразу трех молодых глухарей, а я ничем не мог похвастать. Стало темно. Мы развели костер, натянули пленку в качестве отражателя, поели и залегли спать. Стало прохладно. Комары до утра тоже ушли спать. Обратились по азимуту, не надеясь точно выйти к нашему лагерю, но оказалось к нашему удивлению, что мы вышли к нашим палаткам всего в метрах десяти от них.

Далее мы проплыли широкий спокойный плес, после которого реку снова начинают сжимать крутые склоны. Впереди Большой или Семиверстный порог. Остановились на левом берегу. Небольшой заливчик. Пахнет гарью. Нас поразила вода, как бы кипящая от множества хариуса на поверхности. Поставили палатки, и я пошел запускать кораблик. Я только успевал его запускать и вытаскивать сразу с хариусами на всех поводках. Восторг! Один раз вытащил даже с маленьким тайменчиком на крючке. Уха получилась отличная. С берега тянуло дымом. Когда же я попытался пройти вглубь леса, то увидел под ногами тлеющий торф. Иногда из под ног вырывались искры. Тихо горела тайга. На берегу было хорошо, и я хотел бы еще здесь пожить и половить хариуса. Но Боб стал настаивать двигаться дальше, чтобы купить хлеба и еще кое-чего. С сожалением покидаем это уютное место, которое относительно мало посещается, поскольку расположено между двумя порогами.



*Боб оценивает Семиверстный порог*

Семиверстный порог состоит из двух ступеней, расположенных на расстоянии семи верст. Первая ступень самая мощная. Мы причалили к правому берегу и стали разгружать лодку и перетаскивать вещи по берегу до конца первой ступени. Снова сели налегке с Борисом в лодку и поплыли. Мое дело было налегать на весла. Прошли спокойно первую ступень, погрузили вещи, а Сергея Владимировича с Бобом отправили пешком. Далее валы были поменьше, и мы прошли вторую ступень легко, не разгружая лодку. И только, когда разворачивали лодку к берегу, чтобы пристать, черпанули левым бортом, да так, что кое-что из вещей подмокло, а один сапог Боба упал в воду и уплыл. Опять мы поступили легкомысленно, не упаковали, как следует, вещи! Стали вытаскивать все на берег и раскладывать на каменной плите для просушки. Боб, увидев, что один сапог уплыл, в сердцах выбросил и второй сапог. Развели костер, пообедали, сидим на солнышке греемся. Вдруг по реке вверх идет моторная лодка с геологами. Вообще на моторной лодке вверх по порогам идти легче, потому, что относительно камней она движется медленно и легко можно выбрать нужную струю. Увидев нас на берегу с просушкой вещей, они подплыли к нам и спросили, что произошло. Но увидев, что все в порядке, рассказали нам, что несколько ранее здесь утопили все вещи и потеряли лодку наши «Пузеи». Они не стали разгружать лодку, решили тащить ее бечевой, как бурлаки. Лодка оставалась неуправляемой и поэтому быстро перевернулась, и все вещи утонули. Теперь они сидят у геологов ниже по течению без спиннингов, ружей, палатки и прочего. Можно представить, что получилось бы в случае, если мы все были в одной лодке.

Подсохнув, мы снова погрузились в нашу «ангарку» и тронулись дальше. Наконец, на крутом берегу мы увидели несколько домиков и палатки геологов. Здесь располагалась база с названием «Фактория». Увидели и Пузеев. Они сидели у костра, над которым висел выдавший виды котелок, и рядом стояла убогая палатка. Это все, что могли дать им геологи. Мы подплыли к ним, увидели их угрюмые лица и спросили, чем мы можем помочь, не надо ли денег. Но в ответ они буркнули: «Спасибо не надо». Разговора опять не получилось. Мы не стали настаивать и поплыли дальше. Больше Пузеев мы не видели, а в Москве и Сергей Владимирович не общался с ними.

Далее по берегу попадались косари – мужики с большими бородами, где-то в стороне были деревни староверов. А впереди был еще последний порог – Вельминский.

Перед порогом снова причалили к правому берегу и пошли посмотреть русло. Порог показался серьезным, и мы решили полностью разгрузить лодку. Затем мы с Борисом заняли свои места и ринулись в порог. Борис то и дело командовал: «Сан Саныч, нажми, еще нажми!». Я нажимал изо всех сил. Борис умело направлял лодку между камней, а я, поворачивая голову вправо и влево, видел только водяные валы высотой более метра и не видел берега. Наконец мы прошли порог и причалили к берегу. Там встретили группу людей, которые не ожидали нас там увидеть. Они велели отойти подальше вниз по течению и залечь за камни. Все было готово для взрыва основных камней Вельминского порога. Прогремел взрыв. Существенных изменений в русле реки мы не заметили.

Мы погрузились в лодку и поплыли дальше. Ниже порога была небольшая Майгунская шивера. Далее река проходит последнее препятствие. Она резко сузилась и с двух сторон ее обступили скалистые утесы – Щеки.

Река становилась шире и спокойней. Путешествие приближалось к концу. Еще была не одна ночевка, но хариус больше не ловился. Наконец, впереди показалась широкая водная гладь. Это Енисей. На правом берегу у устья Подкаменной Тунгуски небольшое село Подкаменная Тунгуска – несколько старых избышек. Аэропорт и современный поселок находятся на другом берегу Енисея. Енисей широк, с сильным течением, с высокими волнами. Нечего и думать переплыть его на нашей утлой лодке. Подплываем к селу. На берегу встречаем человека, который возится с моторной лодкой. Он соглашается перевести нас на тот берег. В качестве платы берет нашу лодку. На том и решили. В аэропорту сели сразу на самолет. В Красноярске мы втроем пересели на рейс до Москвы, а Борис до Казани, и были дома в тот же день. Путешествие заняло всего около двух недель, а впечатлений мы получили на много лет.

С Борисом Кочелаевым я встречался позже в различных “Коуровках”, на Урале, общался с ним там, в частности, и во время лыжных прогулок. Крепли наши с ним человеческие и дружеские отношения. Я в это время жил в Зеленограде и работал в области полупроводниковой микроэлектроники. Мои научные интересы на тот момент практически не пересекались с научными интересами как Бориса Кочелаева, так и Сергея Владимировича Тябликова. Тесное научное общение у меня с ними, к моему глубокому сожалению, тогда так и не состоялось. В том же 1965 году была опубликована монография С.В. Тябликова “Методы квантовой теории магнетизма”, которая стала настольной книгой для всех работающих в этой области физиков. В последнее время эта книга стала настольной и для меня.

Профессор Сергей Владимирович Тябликов скончался после тяжелой болезни (рак) в расцвете творческих сил 17 марта 1968 года на 47 году жизни.

# Resonance dc phenomena in manganite thin films

V.A. Atsarkin\*, V.V. Demidov, B.V. Sorokin

V.A. Kotel'nikov Institute of Radio Engineering and Electronics of RAS 125009 Moscow

\**E-mail: atsarkin@cplire.ru*

The resonance spin rectification (RSR) and resonance magnetoresistance (RMR) have been studied on  $\text{La}_{2/3}\text{Sr}_{1/3}\text{MnO}_3$  epitaxial thin films in the temperature range of 300 – 365 K, including the Curie point ( $T_C$ ). The RSR effect is found to be caused by anisotropic magnetoresistance under conditions of the magnetic-resonance microwave pumping; it decreases upon heating and disappears at  $T_C$ . Unlike that, the RMR is maximal at  $T_C$  and shows clear correlation with the colossal magnetoresistance (CMR) of the material under study. The interpretation implies decreasing of the sample magnetization due to resonance saturation, thus leading to an increase in electric resistivity in terms of the CMR mechanism. Quantitative agreement is demonstrated between the experimental RMR data and theory accounting for Bloch-type relaxation in the vicinity of the phase transition.

**PACS:** 76.50.+g, 75.47.Gk, 76.30.-v, 75.40.-s

**Keywords:** ferromagnetic resonance, rare-earth manganites, thin films, magnetoresistance, spin rectification, magnetic relaxation

## 1. Introduction

This paper is a contribution to the book dedicated to the 80 years of Professor B.I. Kochelaev. One of the authors (V.A.A) has a pleasure to know Boris Ivanovich personally for about half a century and believes to be his friend. The main subject of B.I. Kochelaev's scientific activity is the theory of spin relaxation; in this field, his papers and lectures became classical. More specifically, his recent studies on rare-earth manganites have an impact on the work of various scientific groups worldwide. In the following paper, we present some new results obtained just on the manganite thin films, including the problems related to spin relaxation. Thus, though no references are given here to specific Kochelaev's publications, the authors acknowledge great positive influence of his scientific achievements.

Non-linear dc effects arising in conducting magnetic materials under conditions of resonance microwave pumping provide clear evidences for spin-charge interplay, thus opening a way to transfer electron spin properties to changes in electrical characteristics. Theoretical consideration of these phenomena was suggested by H.J. Juretschke as early as in 1960 [1], and soon realized experimentally [2]. More intense interest to this problem was attracted, however, after several decades, in the context of contemporary nanotechnology and prospect in spintronics [3-10]. At present, two main resonant dc phenomena in ferromagnets are known: a change in electrical resistivity (resonance magnetoresistance) and resonance spin rectification, called also microwave photovoltage, spin dynamo, magnetic-resonance electromotive force, etc. Physical mechanisms of these phenomena, as suggested in Refs. [1-10], are based on anisotropic magnetoresistance (AMR) and extraordinary Hall effect, as well as on trivial bolometric effect due to resonance microwave heating. Most of the above-cited studies were performed on conventional ferromagnetic metals such as nickel, permalloy, etc., at temperatures far below the Curie point ( $T_C$ ). Unlike that, our work is concerned with investigation of the resonant dc effects in thin films of the doped rare-earth manganites  $\text{La}_{1-x}\text{Sr}_x\text{MnO}_3$  (LSMO). This material is known to demonstrate the effect of colossal magnetoresistance (CMR) [11, 12], being prospective for the

nano-structure applications [13]. The  $T_C$  value of doped manganites is not far from the ambient temperature, providing possibility of studying the dc effects close to the critical point. This paper reports on the experimental studies and theoretical interpretation of both resonant spin rectification (RSR) and resonant magnetoresistance (RMR) in the manganite films in the temperature range including  $T_C$ . Some early data were published previously, see Refs. [14, 15].

## 2. Experimental techniques

The samples under study were thin epitaxial films of  $\text{La}_{2/3}\text{Sr}_{1/3}\text{MnO}_3$  with the thickness of 50–100 nm grown by laser ablation on single crystal  $\text{NdGaO}_3$  substrates; for details, see Ref. [16]. The Curie point of the films was, as a rule, in the range of 345–350 K, so they were ferromagnetic at room temperature.

The RSR and RMR measurements were performed with a home-made EMR<sup>†</sup> spectrometer (working at the frequency  $\omega/2\pi \sim 9.5$  GHz) which allowed access of direct electrical current and additional microwave pumping with the power  $P$  up to 1 W. The film was placed horizontally in the central maximum of the microwave magnetic field  $h$  of the  $TE_{102}$  cavity (the loaded quality factor  $Q_L = 400$ ). Platinum contacts were sputtered at the opposite ends of the film and soldered to thin wires brought out through small holes in the narrow walls of the cavity. Static magnetic field  $H$  could be rotated in the film plane, making an angle  $\alpha$  with the line connecting the contacts. The voltage  $U$  arising between the potential contacts was registered under sweeping the field  $H$  across the EMR condition either without the external direct current ( $I = 0$ , the RSR effect), or at a fixed value of  $I$  up to 30 mA. In the latter case, the 4-contact method was employed for determination of the film resistivity  $R$ . To increase sensitivity, the pumping microwave power was modulated at the frequency of 100 kHz. As a result, the voltage  $U$  to be measured was modulated as well, allowing its lock-in amplification and detection. Computer processing and accumulation were used at the final stage; as a rule, the accumulations number was about 100.

Temperature dependencies were studied in the range of 300–365 K that included the Curie point. Electrical heater was wound on the waveguide. The temperature was determined from the manganite film resistance which was preliminary calibrated with the accuracy of 0.5 K; thus, the film under study worked as a self-thermometer.

## 3. Experimental results

We start with the resonance spin rectification. Typical example of the RSR effect is shown in Fig. 1. As one can see, the signal  $U(H)$  amounts to the  $\mu\text{V}$  range; it arises just at the FMR conditions and consists of symmetric and antisymmetric contributions,  $U^s(H)$  and  $U^{as}(H)$ , which resemble the EMR absorption and dispersion lines, respectively. The sign of the voltage depends on the direction of the external field  $H$ , so the signal inverts when  $H$  is switched over, see the traces  $A$  and  $B$  in Fig. 1(a). This feature enables one to exclude extraneous contributions invariant to the sign of  $H$ , such as parasitic microwave detection etc., by using the half-difference  $U_0(H) = [U_A(H) - U_B(H)]/2$ , see Fig. 1(b). The signals showed in Fig. 1 were recorded at the microwave power  $P = 400$  mW. When  $P$  is altered, the RSR voltage  $U_0(H)$  (measured at the same temperature) varies proportionally, without change in the line shape.

In Fig. 2, the amplitude  $U_0^s$  measured at  $T = 308$  K is plotted against the angle  $\alpha$ . The angular dependence looks rather specific, showing maxima at about  $\pm 54^\circ$  and zeros at 0 and  $90^\circ$ . Note that the data can be well fitted by the function of  $\sin(\alpha)\sin(2\alpha)$ , see the dashed curve in Fig. 2.

---

<sup>†</sup>We use the term EMR (electron magnetic resonance) which implies both ferromagnetic and paramagnetic resonances, FMR and EPR.

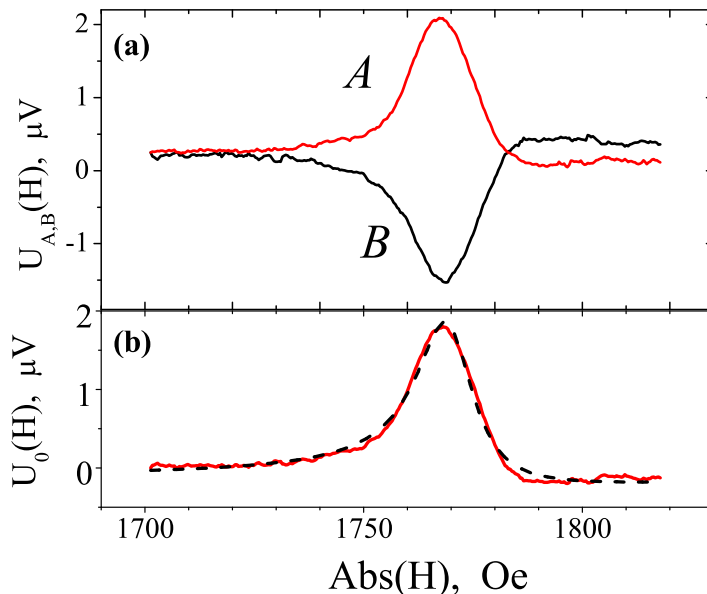


**Figure 1.** (a) The RSR voltage as recorded at opposite directions of external magnetic field  $H$ ;  $T = 308$  K,  $\alpha = 45^\circ$ ,  $P = 400$  mW. (b) The half-difference of the traces  $A$  and  $B$  (solid line) and fitting with Eq. (3) (dashed line).

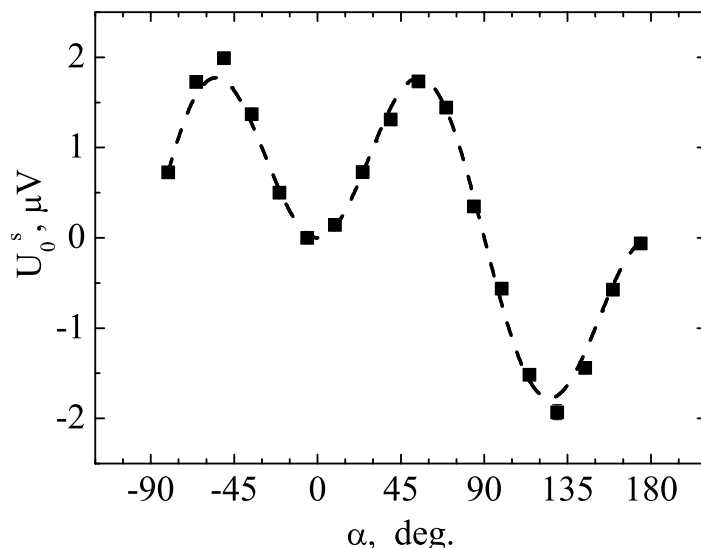


**Figure 2.** Angular dependence of the RSR voltage at  $T = 308$  K. The dashed line represents the  $\sin(\alpha) \sin(2\alpha)$  dependence.

Temperature dependence of the amplitude  $U_0$  (measured at  $\alpha = 45^\circ$ ) is presented in Fig. 3 by open circles (the right scale). The RSR voltage is maximal at room temperature and demonstrates a steep fall toward zero when approaching  $T_C$ .

Unlike the above-described RSR effect which was studied in the absence of external current, the measurements of magnetoresistance were based on the Ohm Law,  $R = U/I$ , where  $I = \text{const}$  was supplied by an external source with large enough series resistor  $r \gg R$ . The resistance  $R$  of our manganite films was in the range of 100–200 Ohm at 300 K and increased monotonically by about 3 times upon heating to 360 K, with maximum slope at  $T_C$  [14, 15]. The static field  $\mathbf{H}$  was kept perpendicular to the microwave field  $\mathbf{h}$  ( $\alpha = \pi/2$ ), providing maximum EMR absorption. The RMR effect appeared as a small increase  $\Delta U$  in the voltage when sweeping through the resonance conditions, corresponding to the resistance increment  $\Delta R$  of the order of  $10^{-4}$ – $10^{-3}$  Ohm.

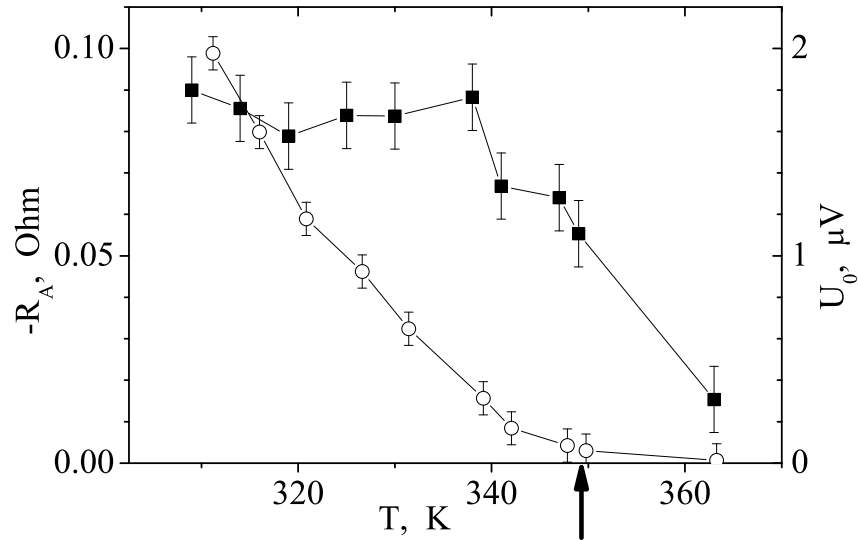


**Figure 3.** The RSR magnitude (open circles, right scale) and anisotropic part of the sample resistance (filled squares, left scale) as functions on temperature. The lines are the guides for eyes. The arrow indicates  $T_C$ .

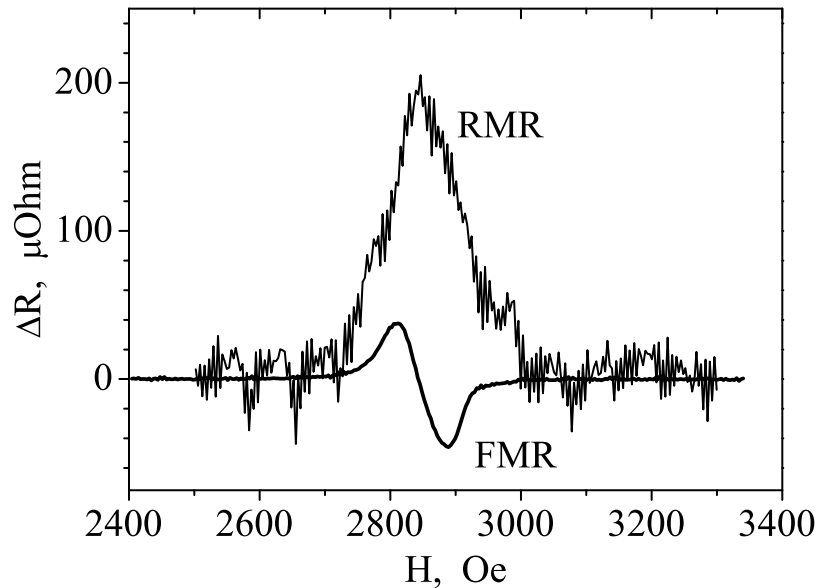


**Figure 4.** Resonance magnetoresistance recorded by sweeping through the FMR condition at  $T = 330$  K,  $P = 120$  mW. The FMR absorption derivative (in arbitrary units) is shown for comparison.

To exclude any foreign contributions, the half-difference was used of the  $U(H)$  signals recorded at opposite current directions. Typical  $\Delta R(H)$  line is shown in Fig. 4, where the derivative of the FMR absorption is given for comparison. The  $\Delta U$  magnitude was found to be proportional both to the current  $I$  and microwave power  $P$ .

Fig. 5(a) presents the temperature dependence of the resonance magnetoresistance for two manganite films. The data are normalized to the resonance absorption, with account made for the EMR line width and magnitude. It is seen that, in contrast with Fig. 3, the normalized resonance magnetoresistance increases when approaching the phase transition, attains its maximum at  $T_C$  and persists even in paramagnetic phase. This can be compared with the temperature dependence of the colossal magnetoresistance effect (CMR) as measured directly on the same films, see Fig. 5(b). The correlation of the two effects is evident.

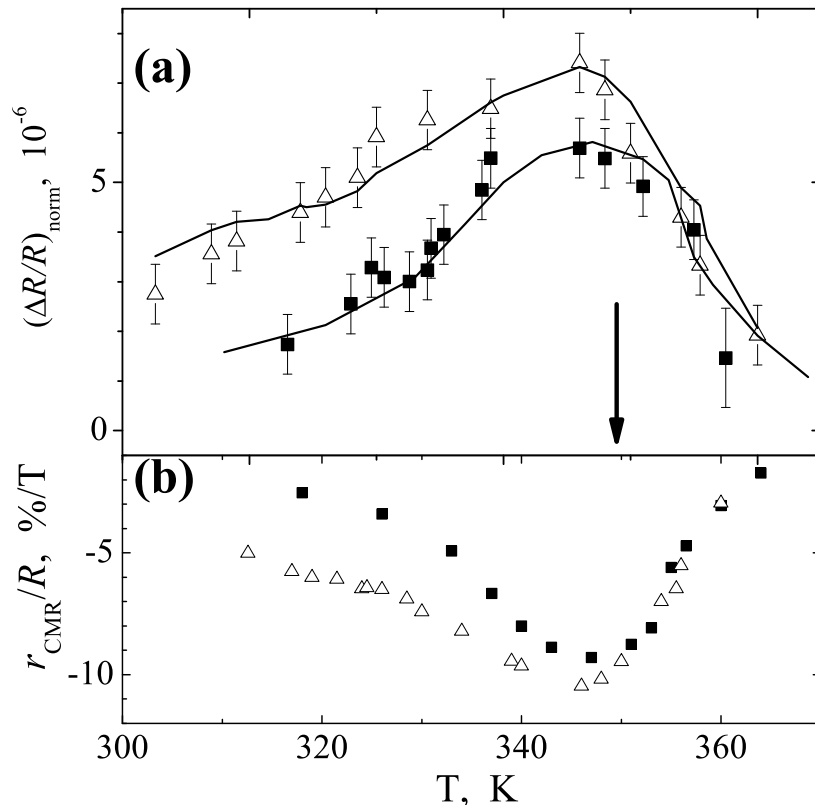


**Figure 5.** Temperature dependence of the normalized RMR magnitude (a) and differential CMR factor (b) measured on two manganite films. The curves are calculated with Eq. (5), see the text. The arrow indicates  $T_C$ .

Along with the above-described main set of experiments, the EMR spectra of the samples were recorded under the same conditions as in the RSR and RMR measurements. As it will be seen below, both the resonance field  $H_0$  and the EMR line-width  $\delta H$  are of importance for quantitative interpretation of the data obtained. In particular, the  $H_0$  values were used to calculate equilibrium magnetization  $M_0$ , according to the formula [17]

$$\omega^2 = \gamma^2 H_0 (H_0 + 4\pi M_0), \quad (1)$$

where  $\gamma$  is the gyromagnetic ratio. For the films under study, the  $M_0$  values at 300 K are about 300 Oe and decrease strongly when approaching  $T_C$ . As to the FMR line-width, it increases upon heating from 20-30 Oe at room temperature up to about 200 Oe near the phase transition, where  $\delta H$  passes through the maximum. More detailed data on EMR in the manganite films are reported in Refs. [14-16].

Further, the anisotropic part of the sample resistance  $R_A$  was determined directly as the difference between the  $R$  values measured at parallel ( $\alpha = 0$ ) and perpendicular ( $\alpha = \pi/2$ ) directions of  $H$  relative to the current  $I$ . At room temperature and  $H \sim 2$  kOe, the negative  $R_A$  values in the range from  $-0.1$  to  $-1.0$  Ohm were found in various samples. At elevated temperatures, the absolute values of  $R_A$  decreased and could not be measured with proper accuracy.

#### 4. Discussion

To interpret the data on the resonance spin rectification, we will follow the theory developed in Refs. [1, 2, 6], where two sources of the dc voltage arising under EMR conditions were considered:

the anisotropic magnetoresistance (AMR) and extraordinary Hall effect (EHE). In our case, the latter mechanism should be neglected for two reasons. First, the angular dependence of EHE differs from that shown in Fig. 2; second, the shape of the ESE signal should be nearly antisymmetric, in contrast to Fig. 2, where the  $U^s(H)$  contribution obviously predominates. Thus, only the AMR mechanism of the spin rectification will be analyzed.

Following the approach used in Ref. [6], the dc voltage  $U_0$  originates from the Ohm Law applied to the microwave current  $I_1 \cos(\omega t)$  (which determines the  $z$  axis) and anisotropic resistance  $R = R_0 + R_A \cos^2 \theta$ , where  $\theta$  is the angle between the current and magnetization  $\mathbf{M}$ . The non-linearity arises from the term

$$U_{nl}(t) = I_1 \cos \omega t \cdot R_1 \cos(\omega t + \phi), \quad (2)$$

where the oscillating resistance with the amplitude  $R_1$  is caused by the oscillations of  $\theta$  in the course of the resonant Larmor precession. The time-averaged part of Eq. (2) is just the dc voltage observed experimentally.

Thus, one should compare our data with the formulas deduced in Ref. [6] at various assumptions on the geometry of microwave currents and magnetic fields. Taking into account the  $\sin(\alpha) \sin(2\alpha)$  angular dependence (Fig. 2), the only appropriate combination is

$$U_{0z}(H) = \frac{R_A I_1}{2M_0} A_{xx} \sin \alpha \sin(2\alpha) [-h_z^i g_a(H) + h_z^r g_d(H)], \quad (3)$$

where  $A_{xx}$  is the numerical factor depending on  $H_0$ ,  $M_0$  and  $\delta H$ ;  $h_z^r$  and  $h_z^i$  are the amplitudes of the in-phase and out-of-phase components of  $h_z(t)$  as related to the microwave current;  $g_a(H)$  and  $g_d(H)$  are the form-factors corresponding to the EMR absorption and dispersion lines, respectively. Note that, according to Eq. (3), the dc voltage  $U_{0z}$  is proportional to the microwave power, in agreement with the experiment.

The dashed curve in Fig. 1(b) presents the fitting of the observed  $U_0(H)$  line with Eq. (3) (in arbitrary units, since the  $I_1$  value is unknown). The best fit was obtained at  $h_z^i/h_z^r = 3.0$ , corresponding to the phase shift of  $72^\circ$ ; this determines the ratio of the symmetric and antisymmetric components of the RSR signal.

Further, the temperature dependence  $U_0(T)$  (see Fig. 3, the right scale) together with Eq. (3) enables one to calculate the temperature dependence of the anisotropic part of the sample resistance. Making use of the directly measured value of  $R_A$  at the room temperature and the EMR data obtained at different temperatures, the  $R_A(T)$  plot was drawn (Fig. 3, the left scale). It is seen that the anisotropic magnetoresistance decreases steeply near the phase transition and practically disappears above  $T_C$ . Note that the negative sign of  $R_A$  in our samples was confirmed by both the direct measurement at the room temperature and relative polarities of  $H$  and  $U_{A,B}$ .

Passing to the results on resonance magnetoresistance, one can notice a principal difference with the above-described RSR data. In fact, the RMR effect not only does not disappear near  $T_C$ , but, on the contrary, reaches there its maximum. So, one has to look for another explanation of the observed RMR phenomenon, not reduced to the anisotropic resistance. As an alternative mechanism, the colossal magnetoresistance (CMR) may be considered, which is known to be a specific feature of the manganite materials [11, 12].

The CMR effect consists in considerable decrease of electrical resistivity due to an increase of the absolute value (the length) of the magnetization vector  $\mathbf{M}$ , caused, in its turn, by increasing

of the external magnetic field  $H$ . We suppose that partial saturation of EMR by the resonant microwave pumping leads to  $M$  decreasing and, as a result, to an increase in resistivity. This suggestion is confirmed by correlation between the RMR and CMR in the temperature range under study: as seen in Fig. 5, both effects attain their extremal values near  $T_C$  and persist in the paramagnetic phase.

It should be emphasized that the commonly used Landau-Lifshits Equation with the Gilbert relaxation term conserves the length of  $\mathbf{M}$  [17] and hence excludes applicability of the above-suggested mechanism. However, as shown by D. Garanin and his co-workers [18, 19], an additional Bloch-type relaxation term should arise due to thermal fluctuations in the vicinity of the phase transition; as a result, the so-called Landau-Lifshits-Bloch (LLB) equation was suggested. At small deviation from equilibrium and weak magnetic anisotropy, it can be represented in the form

$$\frac{\partial \mathbf{M}}{\partial t} = -\gamma [\mathbf{M} \times \mathbf{H}] - T_{1abs}^{-1} (M - M_0) \frac{\mathbf{M}}{M} - T_2^{-1} \frac{[\mathbf{M} \times [\mathbf{M} \times \mathbf{H}]]}{M \cdot H_0}, \quad (4)$$

where the second term describes the Bloch-type longitudinal relaxation along  $\mathbf{M}$  with the characteristic time  $T_{1abs}$ . Note that  $\mathbf{H}$  and  $H_0$  designate here the full and static magnetic fields, respectively.

The LLB equation (4) was solved under conditions of partial (weak) saturation of EMR by microwave power, resulting in expression for the decrement  $\Delta M$  as a function on experimental and material parameters, such as  $M_0$ ,  $H_0$ ,  $\delta H$ ,  $h$ , and  $T_{1abs}$ . Then, making use of the differential CMR value  $r_{CMR} = dR/dH$  and ‘‘absolute susceptibility’’  $\chi_{abs} = dM/dH$ , one gets for the relative increment of the resistance, normalized over the resonant microwave absorption [15]:

$$\frac{\Delta R_{res}}{R} = -\frac{\gamma h^2 T_{1abs} r_{CMR}}{2\chi_{abs}} \quad (5)$$

All parameters entering Eq. (5), with the only exception for  $T_{1abs}$ , were determined by independent measurements. Besides, the ratio  $T_{1abs}/\chi_{abs}$  should not change significantly near the Curie point [19], so the both quantities can be replaced by their values at a fixed temperature. The best fits of the temperature dependencies for two samples were attained at  $T_{1abs}(T_C) = (2.1 \pm 0.3)$  nsec; the fitting curves are shown in Fig. 5(a) by solid lines, demonstrating a good agreement. Note that the employed value of the relaxation time is consistent with the experimental data reported in Refs. [20, 21].

In conclusion, two resonant dc effects, RSR and RMR, have been observed and studied on thin epitaxial films of  $\text{La}_{2/3}\text{Sr}_{1/3}\text{MnO}_3$  in the temperature range including the Curie point. It is shown that the mechanism of the resonant spin rectification is determined by the anisotropic magnetoresistance which decreases upon heating and disappears in paramagnetic phase. Unlike this, the resonance magnetoresistance of the manganite films under study increases when approaching the critical temperature and passes through its maximum at  $T_C$ , showing strong correlation with the CMR effect. The suggested interpretation accounts for the CMR phenomenon together with partial reduction of the magnetization vector upon microwave pumping in the presence of the Bloch-type relaxation. As a result, quantitative agreement with the experiment is achieved.

## Acknowledgments

The work was partially supported by the RFBR Grants 11-02-00349 and 14-02-00165. The authors are grateful to G.A. Ovsyannikov and A.M. Petrzhik for providing with the manganite films under study.

## References

1. Juretschke H.J. *J. Appl. Phys.* **31**, 1401 (1960)
2. Egan W.G., Juretschke H.J. *J. Appl. Phys.* **34**, 1477 (1963)
3. Azevedo A., Vilela Leão L.H., Rodriguez-Suarez R.L., Oliveira A.B., Rezende S.M. *J. Appl. Phys.* **97**, 10C715 (2005)
4. Gui Y.S., Mecking N., Wirthmann A., Bai L.H., Hu C.-M. *Appl. Phys. Lett.* **91**, 082503 (2007)
5. Goennenwein S.T.B., Schink S.W., Brandlmaier A., Boger A., Opel M., Gross R., Keizer R.S., Klapwijk T.M., Gupta A., Huebl H., Bihler C., Brandt M.S. *Appl. Phys. Lett.* **90**, 162507 (2007)
6. Mecking N., Gui Y.S., Hu C.-M. *Phys. Rev. B* **76**, 224430 (2007)
7. Gui Y.S., Mecking N., Zhou X., Williams G., Hu C.-M. *Phys. Rev. Lett.* **98**, 107602 (2007)
8. Gui Y.S., Wirthmann A., Hu C.-M. *Phys. Rev. B* **80**, 184422 (2009)
9. Zhu X.F., Harder M., Wirthmann A., Zhang B., Lu W., Gui Y.S., Hu C.-M. *Phys. Rev. B* **83**, 104407 (2011)
10. Cheng X., Katine J.A., Rowlands G.E., Krivorotov I.N. *Appl. Phys. Lett.* **103**, 082402 (2013)
11. Salamon M.B., Jaime M. *Rev. Mod. Phys.* **73**, 583 (2001)
12. Nagaev E.L. *Phys. Rep.* **346**, 387 (2001)
13. Petrzhik A.M., Demidov V.V., Ovsyannikov G.A., Borisenko I.V., Shadrin A.V. *JETP* **115**, 876 (2012) [*Zh. Eksp. Teor. Fiz.* **142**, 994 (2012), in Russian]
14. Atsarkin V.A., Demidov V.V., Levkin L.V., Petrzhik A.M. *Phys. Rev. B* **82**, 144414 (2010)
15. Atsarkin V.A., Demidov V.V. *JETP* **116**, 95 (2013) [*Zh. Eksp. Teor. Fiz.* **143**, 109 (2013), in Russian]
16. Demidov V.V., Borisenko I.V., Klimov A.A., Ovsyannikov G.A., Petrzhik A.M., Nikitov S.A. *JETP* **112**, 825 (2011) [*Zh. Eksp. Teor. Fiz.* **139**, 943 (2011), in Russian]
17. Gurevich A.G., Melkov G.A. *Magnetization Oscillations and Waves*, CRC Press, Boca Raton, (1996)
18. Garanin D.A. *Phys. Rev. B* **55**, 3050 (1997)
19. Chubykalo-Fesenko O., Nowak U., Chantrell R.W., Garanin D. *Phys. Rev. B* **74**, 094436 (2006)
20. Atsarkin V.A., Demidov V.V., Vasneva G.A., Conder K. *Phys. Rev. B* **63**, 092405 (2001)
21. Atsarkin V.A., Demidov V.V., Vasneva G.A., Gotovtsev D.G. *Appl. Magn. Reson.* **21**, 147 (2001)

# Spin relaxation of Mn ions in rare earth manganites in paramagnetic region

S.I. Andronenko

Kazan Federal University, Kremlevskaya 18, 420008 Kazan, Russia

*E-mail: sergey.andronenko@gmail.com*

Role of bottlenecked spin relaxation and proportionality between small polaron hopping conductivity and electron paramagnetic resonance (EPR) linewidth (intensity) was emphasized. This idea gave a background for several experimental and theoretical investigations and it was starting point for its further generalization on variable range hopping conductivity and its influence on EPR linewidth in rare earth manganites.

**PACS:** 76.30.-v, 75.47.Lx

**Keywords:** EPR, bottlenecked spin relaxation, rare-earth manganites

## 1. Introduction

Rare earth manganites with the common formula  $A_yB_{1-y}MnO_3$  (where  $A = La, Sm, Pr$  or another rare-earth ion and  $B = Ca, Ba, Sr$ ;  $y = 1/3$ ) are members of a large series of rare-earth manganites exhibiting giant magnetoresistance. Their transport, magnetic and structural properties are very sensitive to the substitution of trivalent rare-earth ion ( $A^{3+}$ ), as well as that of divalent ions ( $B^{2+}$ ). These compounds have been the subjects of several investigations, including ferromagnetic resonance and electron paramagnetic resonance (EPR) investigations of Mn ions. Special attention was given to the spin dynamics of the Mn ions near the magnetic phase transition and explanation of pseudolinear increase in EPR linewidth in the paramagnetic state of these compounds above the Curie temperature. There are several explanations of this pseudolinear increase and one of most interesting and convincing theory was presented by group of investigators under guidance of Prof. B. Kochelaev in 2000 [1]. This outstanding paper gave new impact to understanding of the nature of the paramagnetic center responsible for the EPR signal and spin relaxation of paramagnetic centers in rare earth manganites.

In previous paper [2] a model was proposed in which a bottlenecked spin relaxation takes place from the exchange-coupled constituent  $Mn^{4+}$  ions via the  $Mn^{3+}$  Jahn-Teller ions to the lattice. The existence of magnetic polarons was proved clearly in this paper. This model provides a reasonable explanation of the observed EPR signal as well as on the observed isotope effects. Further, the idea about the proportionality of hopping conductivity of  $e_g$  electrons and EPR linewidth along with bottlenecked regime of spin relaxation in manganites was brought up in this pioneer work [1]. This idea turned out very fruitful and led to several experimental and theoretical investigations. Therefore we have to remind main important points of this work.

## 2. Spin relaxation mechanism

### 2.1. EPR linewidth

The peak-to-peak first derivative EPR linewidth for  $T > T_{min}$ , for the various manganite samples can be expressed as a sum of two terms, one of which is temperature independent, whereas the other is temperature dependent, so that  $\Delta B_{pp} = \Delta B_{pp, min} + \Delta B_{pp}(T)$ . The temperature-dependent EPR linewidth  $\Delta B_{pp}(T)$  is proportional to the magnetic susceptibility, and is given as [3, 4]:

$$\Delta B_{\text{pp}}(T) = \frac{\chi_0(T)}{\chi(T)} \Delta B_{\text{pp}}(\infty), \quad (1)$$

where  $\chi_0(T) \propto T^{-1}$  is the free spin (Curie) susceptibility;  $\chi$  is the measured susceptibility; and  $\Delta B_{\text{pp}}(\infty)$  is the temperature-independent value. Huber et al. [4] calculated the influence of exchange narrowing, using a general expression for the relaxation rate of the total spin. This approach is based on the memory function formalism developed by Mori [5], calculating  $\Delta B_{\text{pp}}(T)$  as a function of the second and fourth-order moments,  $M_2$  and  $M_4$ , and concluding, that the main reason for broadening is the variation of the orthorhombic crystal-field parameters over the various Mn ions. The influence of the antisymmetric exchange interaction (Dzialozhinsky-Moriya) on EPR linewidth was found to be important [4]. However, the calculations showed very little influence of the dipole-dipole interactions in these manganite compounds, in agreement with the calculations of Huber et al. [3, 4].

### **2.2. Bottlenecked spin relaxation**

Proportionality between the EPR linewidth and the conductivity is often observed in systems with hopping conductivity [6]. It was shown that the hopping rate of the charge carriers limits the lifetime of the spin state. This leads to a broadening of the EPR line, proportional to the hopping rate and thus to the conductivity [7]. In this case the conductivity is determined by the probability of  $e_g$  electron hopping between nearest sites  $W$ . The hopping takes place with conserving the total spin and therefore will not lead to EPR relaxation. A broadening of the EPR line arises due to the hopping of the  $e_g$  electrons via the spin-orbit coupling. The probability of hopping between the nearest sites with changing the spin can be estimated as  $W_s = W(g - 2)^2$ . The  $g$ -factor of EPR line in manganites is very close to 2. Therefore the condition for the bottleneck regime  $W_s \ll W$  is satisfied.

### **2.3. Hopping conductivity**

A linear relation between the EPR linewidth ( $\Delta B_{\text{pp}}$ ) and conductivity is often observed in systems exhibiting hopping conductivity. Rare earth manganites belong to such systems [8]. In this context, it is noted that the minimum of the EPR linewidth in manganite samples occurs at  $T_{\text{min}}$ , which is near  $T_C$ , above which it increases with increasing temperature. The temperature dependence of  $\Delta B_{\text{pp}}$  above  $T_{\text{min}}$  is very similar to that of the electrical conductivity observed in manganites [9]. Accordingly, the following expression was used to fit the EPR linewidth [3]:

$$\Delta B_{\text{pp}}(T) = \Delta B_{\text{pp}, \text{min}} + \frac{A}{T} \exp(-E_a/k_B T). \quad (2)$$

As stated above, increasing disorder in the distribution of  $\text{Mn}^{4+}$  and  $\text{Mn}^{2+}$  ions due to doping with Ba ions requires the application of variable-range-hopping (VRH) model for the charge-transfer process in manganites. Accordingly, the temperature dependence of conductivity can be expressed as [10]:

$$\sigma = \sigma_0 \exp\left(- (T_0/T)^{1/4}\right), \quad (3)$$

where  $T_0$  is the characteristic temperature; its value for manganites is around  $10^6$  K [11]. Then the EPR linewidth can be similarly expressed as [12]:

$$\Delta B_{\text{pp}}(T) = \Delta B_{\text{pp}, \text{min}} + C \exp\left(- (T_0/T)^{1/4}\right). \quad (4)$$

In Eq. 4,  $T_0 = 18/k_B \xi^3 N(E_p)$ ,  $N(E_p)$  is the density of states on the Fermi level;  $\xi$  is the localization length; it is of order of the distance between adjacent Mn ions.

### 3. The application of this theory to $(\text{La}_{0.33}\text{Sm}_{0.67})_{0.67}\text{Sr}_{0.33-x}\text{Ba}_x\text{MnO}_3$

The well-known small-polaron hopping model for the interpretation of EPR linewidth in the paramagnetic region [1] was first used to explain the linewidth behavior. In this model influence of small-polaron hopping conductivity in the paramagnetic state in highly doped manganite samples  $(\text{La}_{0.33}\text{Sm}_{0.67})_{0.67}\text{Sr}_{0.33-x}\text{Ba}_x\text{MnO}_3$  ( $x = 0.0, 0.13, 0.23, 0.33$ ) [13], accompanied by flip-flop of spins, during the transfer of electrons from  $\text{Mn}^{2+}$  to  $\text{Mn}^{3+}$ , is considered to lead to broadening of EPR linewidth, as it was explained above. The best-fit parameters in Eq. 2 are:  $\Delta B_{\text{pp},\text{min}} = 33.4, 50.5, 54.0, 64.8$  mT, and  $E_a = 0.26, 0.089, 0.090, 0.089$  eV for the samples with  $x = 0.0, 0.13, 0.23, 0.33$ , respectively. The activation energy  $E_\sigma$  was derived from temperature dependence of hopping conductivity in small polaron model. The conductivity data were fitted to temperature-dependent expression, similar to Eq. 2, obtaining the values  $E_\sigma = 0.25, 0.18, 0.18, 0.18$  eV for the samples with  $x = 0.0, 0.13, 0.23, 0.33$ , respectively. A comparison of  $E_a$  and  $E_\sigma$  values determined here reveals that these two values are equal for the sample with  $x = 0.0$  without  $\text{Ba}^{2+}$  ions, whereas the value of  $E_\sigma$  is about twice that of  $E_a$  for the samples with  $x = 0.33, 0.23$ , and  $0.13$ , in which there is a partial replacement of  $\text{Sr}^{2+}$  ions by  $\text{Ba}^{2+}$  ions. Similar effect for replacement of Ca ions by Ba ions in rare earth manganites was observed by Ulyanov et al. [14, 15]. Therefore this difference, as well abrupt change in  $E_a, E_\sigma$  depending on  $x$ , needs to be explained.

There are many evidences for variable range hopping (VRH) conductivity of manganites [16] and, in particular, for  $(\text{La}_{1/3}\text{Sm}_{2/3})_{2/3}\text{Sr}_{1/3-x}\text{Ba}_x\text{MnO}_3$  samples [17]. Assuming that the EPR linewidth is proportional to the conductivity in  $(\text{La}_{1/3}\text{Sm}_{2/3})_{2/3}\text{Sr}_{1/3-x}\text{Ba}_x\text{MnO}_3$ , whose behavior is governed by the VRH model, it is possible to describe both hopping conductivity and EPR linewidth in similar manner. Eq. (4) was used to evaluate the VRH parameter  $T_0$ . This parameter was estimated for the samples  $(\text{La}_{1/3}\text{Sm}_{2/3})_{2/3}\text{Sr}_{1/3-x}\text{Ba}_x\text{MnO}_3$  ( $x = 0.0, 0.01, 0.03, 0.06, \text{ and } 0.13, 0.23, 0.33$ ) from the dependence of EPR linewidth on temperature in the paramagnetic phase of these samples [12]. The decrease in  $T_0$  with increasing Ba content is found to be quite sharp for the Ba-content  $x = 0.0$  to  $0.1$ , but this decrease is continuous in such approach. The best-fit parameter  $T_0 = 1.64, 0.59, 0.48, 0.14, 0.07, 0.04 \times 10^6$  for  $x = 0, 0.01, 0.03, 0.06, 0.13, 0.23$ . Therefore this explanation could be considered as successful for rare earth manganites under study.

It should be noted also, that there are also alternative explanations of pseudolinear increasing EPR linewidth, for example, due phonon modulation of Dzyaloshinskii-Moriya antisymmetric interaction between exchange-coupled manganese ions [18], however, the recent experiments clearly show importance of charge transport process and static magnetization for explanation of spin relaxation of manganese ions in rare earth manganites. Here, it should mentioned also the interpretation of EPR linewidth in lightly doped manganites, such as  $\text{La}_{0.95}\text{Sr}_{0.05}\text{MnO}_3$ , which was fulfilled also with participation of Prof. B.I. Kochelaev [19, 20] and also brought new knowledge, specifically, about orbital order in manganites.

### 4. Conclusion

This outstanding work [1] gives many new ideas, becomes very significant and it was cited already more than hundred times. It enforced the investigators to many new experiments and, therefore, it brought next step in understanding of spin relaxation in rare earth manganites. In particular, it led to the generalization of this approach from small polaron hopping to variable range hopping. Finally, it was shown, that variable range hopping also could explain pseudolinear increase of EPR linewidth in paramagnetic region of rare earth manganites.

## Acknowledgments

Author would like to express sincere appreciation to Prof. B.I. Kochelaev for his encourage and support of author's work.

## References

1. Shengelaya A., Zhao Guo-meng, Keller H., Muller K.A., Kochelaev B.I. *Phys. Rev. B* **61**, 5888 (2000)
2. Shengelaya A., Zhao Guo-meng, Keller H., Muller K.A. *Phys. Rev. Lett.* **77**, 5296 (1996)
3. Huber D.L., Laura-Ccahuana D., Tovar M., Causa M.T. *J. Magn. Magn. Mater.* **310**, 604 (2007)
4. Huber D.L., Alejandro G., Caneiro A., Causa M.T., Prado F., Tovar M., Oseroff S.B. *Phys. Rev. B* **60**, 12155 (1999)
5. Mori H. *Prog. Theor. Phys.* **33**, 423 (1965)
6. Chauvet O., Stoto T., Zuppiroli L. *Phys. Rev. B* **46**, 8139 (1992)
7. Movaghar B., Schweitzer L., Overhof H. *Philos. Mag.* **37**, 683 (1978)
8. Chen X.J., Zhang C.L., Almasan C.C., Gardner J.S., Sarrao J.L. *Phys. Rev. B* **67**, 094426 (2003)
9. Zhao G.-M., Keller H., Greene R.L., Muller K.A. in *Physics of Manganites*, edited by Kaplan T.A. and Mahanti S.D., Plenum, New York, p. 221 (1999)
10. Mott N.F. *Metal-Insulator transitions*, Taylor and Francis, London, 286 p. (1990)
11. Mansuri I., Varshney D, Kaurav N., Lu C.L., Kuo Y.K. *J. Magn. Magn. Mat.* **323**, 316 (2011)
12. Andronenko S.I., Rodionov A.A., Fedorova A.V., Misra S.K. *J. Magn. Magn. Mater.* **326**, 151 (2013)
13. Misra S.K., Andronenko S.I., Asthana S., Bahadur D. *J. Magn. Magn. Mater.* **322**, 2902 (2010)
14. Ulyanov A.N., Levchenko G.G., Yu S.-C. *Sol. St. Comm.* **123**, 383 (2002)
15. Ulyanov A.N., Quang H.D., Pismenova N.E., Yu S.-C. *IEEE Trans. Magn.* **41**, 2745 (2005)
16. Vekilov Yu.Kh., Mukovskii Ya.M. *Sol. St. Comm.* **152**, 1139 (2012)
17. Guo H., Liu N., Yan G., Tong W. *J. Rare Earths* **24**, 206 (2006)
18. Rettori C., Rao D., Singley J., Kidwell D., Oseroff S.B., Causa M.T., Neumeier J.J., McClellan K.J., Cheong S.-W., Schultz S. *Phys. Rev. B* **55**, 3083 (1997)
19. Kochelaev B.I., Shilova E., Deisenhofer J., Krug von Nidda H.-A. Loidl A. Mukhin A.A. Balbashov A.M. *Mod. Phys. Lett. B* **17**, 469 (2003)
20. Deisenhofer J., Kochelaev B.I., Shilova E., Balbashov A.M., Loidl A., Krug von Nidda H.-A. *Phys. Rev. B* **68**, 214427 (2003)

# Static magnetic susceptibility of the systems with anisotropic Kondo interaction

S.I. Belov\*, A.S. Kutuzov

Kazan Federal University, Kremlevskaya 18, 420008 Kazan, Russia

\**E-mail: Sergei.Belov@kpfu.ru*

We theoretically investigated the static magnetic susceptibility in the heavy fermion compounds  $\text{YbRh}_2\text{Si}_2$  and  $\text{YbIr}_2\text{Si}_2$ . The molecular field approximation together with the renormalization of the Kondo interaction by the high energy conduction electrons excitations result in the Curie-Weiss law and Van Vleck susceptibility with temperature dependent Curie and Weiss parameters.

**PACS:** 72.15.Qm, 76.30.He, 75.30.Cr, 71.27.+a

**Keywords:** static magnetic susceptibility, Kondo lattice, Kondo effect

## 1. Introduction

Heavy fermion compounds attracted the interest of many researches in the last decades, especially since the discovery of electron spin resonance (ESR) in  $\text{YbRh}_2\text{Si}_2$  [1] at the temperatures well below the thermodynamically measured Kondo temperature  $T_K \approx 25$  K [2, 3]. A series of theoretical approaches was proposed to understand unusual behavior of these systems following both a picture of itinerant heavy electrons [4–6] and a picture of localized  $\text{Yb}^{3+}$  spins [7–17]. Peculiar properties of heavy fermion Kondo lattices are determined by the interplay of the strong repulsion of 4f-electrons on the rare earth ion sites, their hybridization with wide band conduction d-electrons and the crystal electric field (CEF) effects. Recent angle resolved photoemission measurements [18] revealed the dispersion of the CEF-split 4f states due to f-d hybridization which was interpreted within the Anderson model. At the same time the rather narrow 4f band near the Fermi energy points out the quasi-localized nature of the f-electron motion. The ESR experiments [1, 19–21] also indicate the importance of local properties: the angular dependence of the ESR  $g$ -factor, linewidth and intensity reflects the tetragonal symmetry of the CEF at the Yb-ion position. A strongly anisotropic ESR signal is observed in a broad magnetic field region 0.2–8 T with the crossover regime between Landau Fermi liquid and non-Fermi liquid states [21].

In earlier works [14–17] the spin relaxation in Kondo lattice systems was successfully studied basing on the local properties of an Yb-ion in the CEF. It was shown that the Kondo effect plays an important part in the spin kinetics of heavy fermion compounds leading to the mutual cancelation of the large relaxation rates in the collective spin mode. The strong coupling between the f- and d-electrons turned out to make a negligible contribution to the effective relaxation rate in the bottleneck regime. The ESR response is determined by the relaxation of the f- and d-electrons to the thermal bath rather than by their mutual relaxation. The peculiarities of the f-d hybridization and the 4f-states dispersion do not seem to be important for the study of the ESR phenomenon which also justifies the picture of localized f-electrons as far as it concerns the dynamical properties.

In another work [11] we investigated the static magnetic susceptibility of  $\text{YbRh}_2\text{Si}_2$  and  $\text{YbIr}_2\text{Si}_2$  at temperatures below  $T_K$ . The simplest molecular field approximation resulting in the Curie-Weiss law and Van Vleck susceptibilities gave an excellent agreement with experimental data. However, the comparison with experiment showed that the Curie constant and Weiss

temperature considerably differed for low and high temperature regions which may indicate the Kondo effect in the static susceptibility data. An importance of Kondo renormalization for spin kinetics suggests it to have an influence on the static properties as well. In this research we extend the earlier analysis of the static magnetic susceptibility taking into account its possible renormalization due to the Kondo effect.

## 2. Basic model

We start from the local properties of an Yb-ion in the tetragonal CEF. A free Yb<sup>3+</sup>-ion has a 4f<sup>13</sup> configuration with one term <sup>2</sup>F. The spin orbital interaction splits the <sup>2</sup>F term into two multiplets: <sup>2</sup>F<sub>7/2</sub> with  $J = 7/2$  and <sup>2</sup>F<sub>5/2</sub> with  $J = 5/2$ , where  $J$  denotes the value of the total momentum  $\mathbf{J} = \mathbf{L} + \mathbf{S}$  with  $\mathbf{L}$  and  $\mathbf{S}$  as the orbital and spin momentum of the ion. The excited multiplet <sup>2</sup>F<sub>5/2</sub> is separated from the ground state <sup>2</sup>F<sub>7/2</sub> by about 1 eV. Since this value is much larger than the CEF energy, we consider in the following the ground multiplet only. Within the lowest multiplet the spin and orbital momentums of the ion are expressed via its total electronic momentum and the Lande  $g$ -factor  $g_J$ :  $\mathbf{S} = (g_J - 1)\mathbf{J}$ ,  $\mathbf{L} = (2 - g_J)\mathbf{J}$ . In this way the Zeeman energy of Yb-ions can be written as follows

$$H_{ZJ} = -\mathbf{H}\mathbf{M}_J, \quad (1)$$

where  $\mathbf{H}$  denotes the external magnetic field and  $\mathbf{M}_J$  is the total magnetic moment of Yb-ions.

$$\mathbf{M}_J = -\mu_B g_J \sum_i \mathbf{J}_i. \quad (2)$$

The Kondo exchange coupling of the Yb-ion with conduction electrons and the indirect interaction between Yb-ions via the conduction electrons (RKKY interaction) are also expressed in terms of the total momentum  $J$ :

$$H_{J\sigma} = A_0(g_J - 1) \sum_i \boldsymbol{\sigma}_i \mathbf{J}_i, \quad (3)$$

$$H_{\text{RKKY}} = (g_J - 1)^2 \sum_{ij} I_{\text{RKKY}}^{ij} \mathbf{J}_i \mathbf{J}_j, \quad (4)$$

Here  $A_0$  denotes the zero order term of the Kondo exchange integral expansion in multipoles (details can be found in [22–27]),  $\boldsymbol{\sigma}_i$  is the spin density of the conduction electrons at the  $i$ -th ion site and  $I_{\text{RKKY}}^{ij}$  denotes the constant of the RKKY interaction between two Kondo ions.

The energy of the Yb-ion in the tetragonal CEF reads [28]

$$H_{\text{CEF}} = \alpha B_2^0 O_2^0 + \beta (B_4^0 O_4^0 + B_4^4 O_4^4) + \gamma (B_6^0 O_6^0 + B_6^4 O_6^4), \quad (5)$$

where  $O_k^q(\mathbf{J})$  are the equivalent operators [28],  $B_k^q$  denote the CEF parameters and  $\alpha = 2/63$ ,  $\beta = -2/1155$ ,  $\gamma = 4/27027$ . The respective eigenstates and energy splitting were found as functions of the CEF parameters in the works [11–13]. They are four Kramers doublets related to the irreducible representations  $\Gamma_7^t$  and  $\Gamma_6^t$  of the double tetragonal group [28], which are labeled in papers [12,13] by  $^1\Gamma_7^t$ ,  $^2\Gamma_7^t$ ,  $^3\Gamma_6^t$ ,  $^4\Gamma_6^t$ . Each doublet is described by the wave functions of the type

$$|n\nu\rangle = \sum_{M=-J}^J C_{n\nu M} |JM\rangle \quad (6)$$

with  $n = 0, 1, 2, 3$  and  $\nu = \uparrow, \downarrow$ . The index  $n$  numbers the energy levels of the Yb-ion in the CEF,  $\nu$  marks the states within a Kramers doublet and  $M$  is the eigenvalue of operator  $J_z$  ( $z$ -axis

coincides with tetragonal axis of CEF). In this paper we assume the Kramers doublets sequence  ${}^2\Gamma_7^t$ ,  ${}^4\Gamma_6^t$ ,  ${}^1\Gamma_7^t$ ,  ${}^3\Gamma_6^t$  as experimentally observed for YbRh<sub>2</sub>Si<sub>2</sub> by the angle resolved photoemission method [18].

The kinetic energy of conduction electrons and their Zeeman energy can be written as

$$H_c = \sum_{ij\lambda} t_{ij} c_{i\lambda}^+ c_{j\lambda} - \mu \sum_{i\lambda} c_{i\lambda}^+ c_{i\lambda}, \quad (7)$$

$$H_{Z\sigma} = -\mathbf{H}\mathbf{M}_\sigma. \quad (8)$$

Here  $\lambda = \pm 1$  labels the orientation of the conduction electron spin,  $\mu$  is the chemical potential, and  $\mathbf{M}_\sigma$  is the magnetic moment of the conduction electrons with the  $g$ -factor  $g_\sigma$ :

$$\mathbf{M}_\sigma = -\mu_B g_\sigma \sum_i \boldsymbol{\sigma}_i. \quad (9)$$

Finally, we represent the total Hamiltonian as  $H = H_0 + H_{\text{int}}$ , where

$$H_0 = H_{\text{CEF}} + H_c + H_{ZJ} + H_{Z\sigma}, \quad (10)$$

$$H_{\text{int}} = H_{J\sigma} + H_{\text{RKKY}}. \quad (11)$$

### 3. Molecular field approximation

The total magnetic susceptibility includes both the Kondo ions and conduction electrons contributions:

$$\chi_{\gamma\gamma'}^J = \left. \frac{\partial \langle M_J^\gamma \rangle}{\partial H^{\gamma'}} \right|_{\mathbf{H}=0}, \quad \chi_{\gamma\gamma'}^\sigma = \left. \frac{\partial \langle M_\sigma^\gamma \rangle}{\partial H^{\gamma'}} \right|_{\mathbf{H}=0}, \quad (12)$$

where  $\langle \dots \rangle$  means the statistical average and  $\gamma, \gamma' = x, y, z$ .

At first we consider the CEF contribution to the static susceptibility neglecting the Kondo- and RKKY interactions. The CEF symmetry implies the relation  $\chi_{\gamma\gamma'} = \delta_{\gamma\gamma'} \chi_{\gamma\gamma}$  with the non-zero diagonal components  $\chi_{xx} = \chi_{yy} = \chi_\perp$  and  $\chi_{zz} = \chi_\parallel$ . At the temperatures low compared with the CEF excited levels  $\Delta_1, \Delta_2, \Delta_3$  the Yb-ions susceptibility is divided into Curie and Van Vleck parts corresponding to the contributions of the ground and excited states, respectively:

$$\chi_{\perp,\parallel}^{0J} = \frac{C_{\perp,\parallel}^0}{T} + \chi_{\perp,\parallel}^{0,\text{VV}}, \quad (13)$$

$$C_{\perp,\parallel}^0 = N \frac{\mu_B^2 g_{\perp,\parallel}^2}{4k_B}, \quad \chi_{\perp,\parallel}^{0,\text{VV}} = N \mu_B^2 g_J^2 \sum_{n=1,2,3} \frac{1}{\Delta_n} \sum_{\nu\nu'} \langle 0\nu | J_{x,z} | n\nu' \rangle \langle n\nu' | J_{x,z} | 0\nu \rangle. \quad (14)$$

Here index “0” indicates the statistical averaging in (12) with the Hamiltonian  $H_0$  defined by the equation (10),  $N$  is the number of Yb-ions; the parameters  $g_\perp$  and  $g_\parallel$  in the Curie constants  $C_{\perp,\parallel}^0$  are actually the  $g$ -factors of the Yb-ion which become anisotropic after projection onto the ground Kramers state:

$$g_\perp = 2g_J \langle 0 \uparrow | J^x | 0 \downarrow \rangle, \quad g_\parallel = 2g_J \langle 0 \uparrow | J^z | 0 \uparrow \rangle. \quad (15)$$

As regards the conduction electrons contribution it is, in this approximation, the usual anisotropic Pauli susceptibility  $\chi_{\gamma\gamma'}^{0\sigma} = \delta_{\gamma\gamma'} \chi^{0\sigma}$  with

$$\chi^{0\sigma} = \frac{1}{2} N \mu_B^2 g_\sigma^2 \rho, \quad (16)$$

where  $\rho$  denotes the conduction electrons density of states per lattice site at the Fermi surface.

The next step is to analyze the static magnetic susceptibility as affected by the Kondo- and RKKY interactions in the simple molecular field approximation. In this case their effects are no other than renormalization of the Zeeman energy of the Yb-ions and conduction electrons, which reduces the total Hamiltonian to

$$\tilde{H} = H_{\text{CEF}} + H_c + \tilde{H}_Z \quad (17)$$

with

$$\tilde{H}_Z = -\mathbf{H}_J \mathbf{M}_J - \mathbf{H}_\sigma \mathbf{M}_\sigma. \quad (18)$$

Here

$$\mathbf{H}_J = (1 - \lambda_A \hat{\chi}^\sigma - \lambda_I \hat{\chi}^J) \mathbf{H}, \quad \mathbf{H}_\sigma = (1 - \lambda_A \hat{\chi}^J) \mathbf{H}, \quad (19)$$

where

$$\lambda_A = \frac{A_0(g_J - 1)}{N\mu_B^2 g_J g_\sigma}, \quad \lambda_I = \frac{(g_J - 1)^2}{N\mu_B^2 g_J^2} \sum_i I_{\text{RKKY}}^{ij}, \quad (20)$$

$A_0$  and  $I_{\text{RKKY}}^{ij}$  introduced in (3), (4) and  $\hat{\chi}$  denotes susceptibility tensor.

The direct calculation with the Hamiltonian (17) leads to a system of coupled equations for the conduction electrons and Yb-ions susceptibilities:

$$\begin{cases} (1 + \lambda_I \hat{\chi}^{0J}) \hat{\chi}^J + \lambda_A \hat{\chi}^{0J} \hat{\chi}^\sigma = \hat{\chi}^{0J}, \\ \hat{\chi}^\sigma + \lambda_A \hat{\chi}^{0\sigma} \hat{\chi}^J = \hat{\chi}^{0\sigma}. \end{cases} \quad (21)$$

Keeping in mind that  $\hat{\chi}^{0J}$  and  $\hat{\chi}^{0\sigma}$  are diagonal we arrive to the relations  $\chi_{\gamma\gamma'}^J = \chi_{\gamma\gamma}^J \delta_{\gamma\gamma'}$  and  $\chi_{\gamma\gamma'}^\sigma = \chi_{\gamma\gamma}^\sigma \delta_{\gamma\gamma'}$ . The non-zero components  $\chi_{xx} = \chi_{yy} = \chi_\perp$  and  $\chi_{zz} = \chi_\parallel$  are of the form

$$\chi_{\perp,\parallel}^J = \chi_{\perp,\parallel}^{0J} \frac{1 - \lambda_A \chi^{0\sigma}}{1 + (\lambda_I - \lambda_A^2 \chi^{0\sigma}) \chi_{\perp,\parallel}^{0J}}, \quad (22)$$

$$\chi_{\perp,\parallel}^\sigma = \chi_{\perp,\parallel}^{0\sigma} \frac{1 + (\lambda_I - \lambda_A) \chi_{\perp,\parallel}^{0J}}{1 + (\lambda_I - \lambda_A^2 \chi^{0\sigma}) \chi_{\perp,\parallel}^{0J}}. \quad (23)$$

Both ionic and conduction electrons' susceptibilities are seen to be renormalized by the Kondo- and RKKY interactions, moreover, the latter becomes anisotropic due to the CEF effects.

The total susceptibility  $\chi = \chi^J + \chi^\sigma$  can be represented as a sum of renormalized Curie-Weiss, Van Vleck and Pauli susceptibilities. Substituting (13) into (22), (23) we obtain

$$\chi_{\perp,\parallel} = \frac{C_{\perp,\parallel}}{T + \theta_{\perp,\parallel}} + \chi_{\perp,\parallel}^{\text{VV}} + \chi^{0\sigma} \quad (24)$$

with the temperature independent Curie constants, Weiss temperatures and Van Vleck susceptibilities:

$$C_{\perp,\parallel} = C_{\perp,\parallel}^0 \left( \frac{1 - \lambda_A \chi^{0\sigma}}{1 + (\lambda_I - \lambda_A^2 \chi^{0\sigma}) \chi_{\perp,\parallel}^{0,\text{VV}}} \right)^2, \quad (25)$$

$$\theta_{\perp,\parallel} = C_{\perp,\parallel}^0 \frac{\lambda_I - \lambda_A^2 \chi^{0\sigma}}{1 + (\lambda_I - \lambda_A^2 \chi^{0\sigma}) \chi_{\perp,\parallel}^{0,\text{VV}}}, \quad (26)$$

$$\chi_{\perp,\parallel}^{\text{VV}} = \chi_{\perp,\parallel}^{0,\text{VV}} \frac{(1 - \lambda_A \chi^{0\sigma})^2}{1 + (\lambda_I - \lambda_A^2 \chi^{0\sigma}) \chi_{\perp,\parallel}^{0,\text{VV}}}. \quad (27)$$

The Pauli susceptibility in (24) is obviously negligible compared with the other terms.

The expression (24) coincides qualitatively with the previous results [11] but in this study we consider also the contribution of the CEF excited states to the Curie-Weiss susceptibility and the conduction electrons influence on the Van Vleck part. Although the Curie-Weiss law and Van Vleck susceptibilities (24) are well fitted to experimental data the fitting parameters  $C$ ,  $\theta$  and  $\chi^{\text{VV}}$  proved to be different for low and high temperature regions. This temperature dependence may indicate the Kondo effect which leads to an additional renormalization of the static susceptibility.

## 4. Scaling corrections to the static susceptibility

### 4.1. “Poor man’s scaling”

At first glance, the standard perturbation expansion is the simplest way to develop a theory beyond the molecular field approximation. However, this is not sufficient at low temperatures: the calculations to the second order in the Kondo interaction show the logarithmic divergences of the type  $\ln(T/W)$ , where  $W$  is a conduction electron band width. The perturbation technique can be improved on the basis of the Anderson’s “poor man’s scaling” [29] method which allows one to extend the lowest order perturbation results, and effectively sum the leading order logarithmic terms.

In this research we consider the scaling procedure only within the ground Kramers doublet neglecting the renormalization effects on the CEF excited states. According to neutron scattering experiments the CEF excited levels are located at 17, 25, 43 meV (197, 290, 499 K) for YbRh<sub>2</sub>Si<sub>2</sub> [30] and 18, 25, 36 meV (209, 290, 418 K) for YbIr<sub>2</sub>Si<sub>2</sub> [31]. Therefore the low temperature physics ( $T \ll 200$  K) is well described by the lowest Kramers doublet with the total electronic momentum of the Yb-ion represented in terms of the effective spin  $S = 1/2$ :

$$J^z = \frac{g_{\parallel}}{g_J} S^z, \quad J^{x,y} = \frac{g_{\perp}}{g_J} S^{x,y}, \quad (28)$$

where  $g_{\parallel}$  and  $g_{\perp}$  are defined by (15). After projection onto the state the Kondo interaction (3) takes the form

$$H_{s\sigma} = \sum_i [J_{\perp}(S_i^x \sigma_i^x + S_i^y \sigma_i^y) + J_{\parallel} S_i^z \sigma_i^z] \quad (29)$$

with  $J_{\perp, \parallel} = A_0 \frac{g_J - 1}{g_J} g_{\perp, \parallel}$ .

The idea of “poor man’s scaling” approach is to take into account the effect of high energy excitations on low energy physics by a renormalization of coupling constants. We divide the conduction electron band into low and high energy states

$$0 < |\varepsilon_{\mathbf{k}}| < \widetilde{W}, \quad \widetilde{W} < |\varepsilon_{\mathbf{k}}| < W, \quad (30)$$

where  $W$ ,  $\widetilde{W}$  are the initial and the running bandwidth, respectively. The projection of the original Kondo interaction  $H_{s\sigma}$  (29) onto the low energy states yields a new Hamiltonian  $\widetilde{H}_{s\sigma}$  with renormalized couplings  $\widetilde{J}_{\perp}$ ,  $\widetilde{J}_{\parallel}$ . It is convenient to introduce dimensionless parameters  $U_{\perp} = (\rho \widetilde{J}_{\perp})$ ,  $U_{\parallel} = (\rho \widetilde{J}_{\parallel})$ , with  $(\dots)$  marking all new quantities. The evolution of the renormalized parameters with  $\widetilde{W}$  is described with a set of equations derived to the second order in  $U_{\perp}$ ,  $U_{\parallel}$ :

$$\frac{dU_{\perp}}{dt} = -U_{\perp} U_{\parallel}, \quad \frac{dU_{\parallel}}{dt} = -U_{\perp}^2, \quad (31)$$

where  $t = \ln(\widetilde{W}/W)$ . The initial conditions for the system (31) are the “bare” parameters of the Kondo interaction (29),

$$U_{\perp}(0) = \rho J_{\perp}, \quad U_{\parallel}(0) = \rho J_{\parallel}. \quad (32)$$

The equations (31) imply a scaling invariant

$$\bar{U}^2 = U_{\perp}^2 - U_{\parallel}^2 = U_{\perp}^2(0) - U_{\parallel}^2(0), \quad (33)$$

which does not change with renormalizing the Hamiltonian  $H_{s\sigma}$ . Although the ESR  $g$ -factor data [1] indicates  $\bar{U}^2 > 0$  ( $g_{\perp} \gg g_{\parallel}$ ), it is interesting to consider an arbitrary sign of  $\bar{U}^2$ .

At  $\bar{U}^2 > 0$  ( $g_{\parallel} < g_{\perp}$ ) the solution of equations (31) can be written in the form

$$U_{\perp} = \bar{U}/\sin \varphi, \quad U_{\parallel} = \bar{U} \cot \varphi. \quad (34)$$

Here  $\bar{U}$  means the absolute value of  $\sqrt{\bar{U}^2}$ ,  $\varphi = \bar{U} \ln(\widetilde{W}/T_{\text{GK}})$ , the abbreviation ‘‘GK’’ indicates the Kramers ground state and  $T_{\text{GK}}$  denotes a characteristic temperature given as follows

$$T_{\text{GK}} = W \exp \left[ -\frac{1}{\bar{U}} \arccos \left( \frac{g_{\parallel}}{g_{\perp}} \right) \right]. \quad (35)$$

The parameter  $T_{\text{GK}}$  is another scaling invariant representing a universal energy scale to govern all the low temperature physics.

At  $\bar{U}^2 < 0$  ( $g_{\parallel} > g_{\perp}$ ) we have

$$U_{\perp} = \bar{U}/\sinh \varphi, \quad U_{\parallel} = \bar{U} \coth \varphi, \quad (36)$$

$$T_{\text{GK}} = W \left[ \frac{g_{\parallel} + \sqrt{g_{\parallel}^2 - g_{\perp}^2}}{g_{\perp}} \right]^{-1/\bar{U}} \quad (37)$$

with  $\bar{U}$  and  $\varphi$  defined similarly to (34). In the isotropic case ( $g_{\parallel} = g_{\perp} = g$ ) both equation (35) and (37) give the standard result  $T_{\text{GK}} = W e^{-\frac{1}{\rho J}}$ .

Extending the scaling procedure down to the effective bandwidth  $\widetilde{W} = T$  we obtain the temperature dependence of renormalized Kondo couplings:

$$\varphi = \bar{U} \ln(T/T_{\text{GK}}). \quad (38)$$

One can see that the low temperature behavior of the effective Kondo couplings does not depend on the sign of the scaling invariant  $\bar{U}^2$ : at  $T \rightarrow T_{\text{GK}}$  the expressions (34) and (36) give the same result  $U_{\parallel}(T) = U_{\perp}(T) = 1/\ln(T/T_{\text{GK}})$  to the leading logarithmic order. The Kondo interaction tends to be isotropic as affected by the scaling procedure for any initial conditions. The difference between  $\bar{U}^2 > 0$  and  $\bar{U}^2 < 0$  cases is essential only at the very high temperatures compared with the conduction electrons bandwidth: for the case  $\bar{U}^2 < 0$  the renormalized Kondo couplings become almost independent of temperature in contrast with temperature behavior corresponding to the case  $\bar{U}^2 > 0$ . At  $T > T_{\text{GK}} \exp(1/\bar{U}) \sim W$  we have

$$U_{\perp} \approx 2\bar{U}(T/T_{\text{GK}})^{-\bar{U}} \approx 0, \quad U_{\parallel} \approx \bar{U} \left[ 1 + 2(T/T_{\text{GK}})^{-2\bar{U}} \right] \approx \bar{U}, \quad \bar{U}^2 < 0. \quad (39)$$

#### **4.2. Susceptibility**

The renormalized static susceptibility is formally the same as that found in the molecular field approximation (24) with the Curie constant and Weiss temperature replaced by temperature dependent parameters:

$$\tilde{\chi}_{\perp, \parallel} = \frac{\tilde{C}_{\perp, \parallel}}{T + \tilde{\theta}_{\perp, \parallel}} + \chi_{\perp, \parallel}^{\text{VV}}, \quad (40)$$

where, at  $\bar{U}^2 > 0$  ( $g_{\parallel} < g_{\perp}$ ),

$$\tilde{C}_{\perp,\parallel} = C_{\perp,\parallel} (a_{\perp,\parallel} - \bar{U} \cot \varphi), \quad \tilde{\theta}_{\perp,\parallel} = \theta_{\perp,\parallel} (a_{\perp,\parallel} - \bar{U} \cot \varphi) \quad (41)$$

with

$$a_{\perp} = \bar{U} (\varphi_0/2 + \cot \varphi_0), \quad a_{\parallel} = \bar{U} \cot \varphi_0. \quad (42)$$

Here  $\varphi_0 \equiv \varphi(T = W) = \arccos(g_{\parallel}/g_{\perp})$ ;  $\bar{U}$  and  $\varphi$  are introduced in (34). At  $\bar{U}^2 < 0$  ( $g_{\parallel} > g_{\perp}$ ) trigonometric functions should be replaced with hyperbolic ones. As we should expect the Curie constant and Weiss temperature are renormalized by the high energy conduction electrons excitations converting to functions of temperature, whereas the Van Vleck part related to the CEF excited states is not affected by the renormalization.

It is also interesting to compare our result with the one-impurity susceptibility found within the isotropic s-d model. If we drop the Weiss temperature arising from the molecular field contributions and neglect the Van Vleck contribution then, in the isotropic limit  $g_{\perp} = g_{\parallel} = g$  ( $J_{\perp} = J_{\parallel} = J$ ), we immediately obtain the well known result

$$\chi_{\perp} = \chi_{\parallel} = \frac{\mu_{\text{B}}^2 g^2}{4k_{\text{B}}T} \left[ 1 - \frac{1}{\ln(T/T_{\text{GK}})} \right], \quad (43)$$

where  $T_{\text{GK}}$  given by (35) and (37) takes the form of one-impurity Kondo temperature  $T_{\text{GK}} = W \exp(-1/\rho J)$ .

The expressions (40) – (42) describe the temperature dependence of the static magnetic susceptibility renormalized by the high energy conduction electrons excitations. At  $T \rightarrow T_{\text{GK}}$  the new Curie and Weiss parameters decrease upon lowering temperature and logarithmically diverge for any sign of  $\bar{U}^2$ :

$$\tilde{C}_{\perp,\parallel}, \tilde{\theta}_{\perp,\parallel} \sim a_{\perp,\parallel} - \frac{1}{\ln(T/T_{\text{GK}})}. \quad (44)$$

However, one must remember that the “poor man’s scaling” approach is only valid for the temperatures well above  $T_{\text{GK}}$  and the singularities indicate just a decrease of  $\tilde{C}_{\perp,\parallel}$  and  $\tilde{\theta}_{\perp,\parallel}$  with temperatures lowering to  $T_{\text{GK}}$ .

## 5. Summary

In conclusion, we carried out a theoretical analysis of the static magnetic susceptibility of  $\text{YbRh}_2\text{Si}_2$  and  $\text{YbIr}_2\text{Si}_2$ . An improved molecular field approximation approach shows that the CEF excited states give a contribution to the Curie-Weiss susceptibility and the conduction electrons influence on the Van Vleck part. Besides, an additional renormalization of the static magnetic susceptibility due to the Kondo effect converts the Curie and Weiss constants to temperature dependent functions, which agrees qualitatively with the experimental data [11]. The detailed quantitative comparison with experiment will be the subject of another paper.

## Acknowledgments

The authors are grateful to B.I. Kochelaev for the fruitful discussions and remarks.

## References

1. Sichelschmidt J., Ivanshin V. A., Ferstl J., Geibel C., Steglich F., *Phys. Rev. Lett.* **91**, 156401 (2003).
2. Trovarelli O., Geibel C., Mederle S., Langhammer C., Grosche F. M., Gegenwart P., Lang M., Sparn G., Steglich F., *Phys. Rev. Lett.* **85**, 626 (2000).

3. Köhler U., Oeschler N., Steglich F., Maquilon S., Fisk Z., *Phys. Rev. B* **77**, 104412 (2008).
4. Abrahams E., Wölfle P., *Phys. Rev. B* **78**, 104423 (2008).
5. Wölfle P., Abrahams E., *Phys. Rev. B* **80**, 235112 (2009).
6. Zvyagin A. A., Kataev V., Büchner B., *Phys. Rev. B* **80**, 024412 (2009).
7. Schlottmann P., *Phys. Rev. B* **79**, 045104 (2009).
8. Huber D. L., *J. Phys.: Condens. Matter* **21**, 322203 (2009).
9. Huber D. L., *J. Phys.: Condens. Matter* **24**, 226001 (2012).
10. Huber D. L., *Mod. Phys. Lett. B* **26**, 1230021 (2012).
11. Kutuzov A. S., Skvortsova A. M., Belov S. I., Sichelschmidt J., Wykhoff J., Eremin I., Krellner C., Geibel C., Kochelaev B. I., *J. Phys.: Condens. Matter* **20**, 455208 (2008).
12. Kutuzov A. S., Skvortsova A. M., *Magn. Reson. Solids* **11**, 7 (2009).
13. Kutuzov A. S., Skvortsova A. M., *J. Phys.: Conf. Ser.* **324**, 012039 (2011).
14. Kochelaev B. I., Belov S. I., Skvortsova A. M., Kutuzov A. S., Sichelschmidt J., Wykhoff J., Geibel C., Steglich F., *Eur. Phys. J. B* **72**, 485 (2009).
15. Belov S. I., Kutuzov A. S., Kochelaev B. I., *J. Phys.: Conf. Ser.* **324**, 012017 (2011).
16. Belov S. I., Kutuzov A. S., Kochelaev B. I., Sichelschmidt J., *J. Phys.: Condens. Matter* **24**, 365601 (2012).
17. Belov S. I., Kutuzov A. S., *Magn. Reson. Solids* **14**, 12103 (2012).
18. Vyalikh D. V., Danzenbächer S., Kucherenko Y., Kummer K., Krellner C., Geibel C., Holder M. G., Kim T. K., Laubschat C., Shi M., Patthey L., Follath R., Molodtsov S. L., *Phys. Rev. Lett.* **105**, 237601 (2010).
19. Sichelschmidt J., Wykhoff J., Krug von Nidda H.-A., Fazlishanov I. I., Hossain Z., Krellner C., Geibel C., Steglich F., *J. Phys.: Condens. Matter* **19**, 016211 (2007).
20. Gruner T., Wykhoff J., Sichelschmidt J., Krellner C., Geibel C., Steglich F., *J. Phys.: Condens. Matter* **22**, 135602 (2010).
21. Schaufuß U., Kataev V., Zvyagin A. A., Büchner B., Sichelschmidt J., Wykhoff J., Krellner C., Geibel C., Steglich F., *Phys. Rev. Lett.* **102**, 076405 (2009).
22. Taylor K. N. R., Darby M. I., *Physics of Rare Earth Solids* (Chapman and Hall, London, 1972).
23. Liu S. H., *Phys. Rev.* **121**, 451 (1961).
24. Liu S. H., *Phys. Rev.* **123**, 470 (1961).
25. Kaplan T. A., Lyons D. H., *Phys. Rev.* **129**, 2072 (1963).
26. Specht F., *Phys. Rev.* **162**, 389 (1967).
27. Druzhinin V. V., Irkhin Y. P., *JETP* **24**, 1250 (1967).
28. Abragam A., Bleaney B., *Electron Paramagnetic Resonance of Transition Ions* (Clarendon Press, Oxford, 1967).
29. Anderson P. W., *J. Phys. C* **3**, 2436 (1970).
30. Stockert O., Koza M. M., Ferstl J., Murani A. P., Geibel C., Steglich F., *Physica B* **378-380**, 157 (2006).
31. Hiess A., Stockert O., Koza M. M., Hossain Z., Geibel C., *Physica B* **378-380**, 748 (2006).

# Magnetic and superconducting heterostructures in spintronics

R.G. Deminov\*, N.Kh. Useinov, L.R. Tagirov

Institute of Physics, Kazan Federal University, Kremlevskaya 18, 420008 Kazan, Russia

\**E-mail: Raphael.Deminov@kpfu.ru*

This paper is a brief review of investigations, which were carried out during last years by team of magnetic nanostructures and spintronics laboratory, and is dedicated to the 80th anniversary of our Teacher - professor B.I. Kochelaev.

**PACS:** 74.45.+c, 74.50.+r, 74.78.Fk, 75.30.Et, 74.80.Fp

**Keywords:** magnetic, superconducting, heterostructures, spintronics

## 1. Introduction

An electron is characterized by charge ( $e$ ) and spin ( $s = 1/2$ ). Spintronics is a new approach to electronics which use control of electron transport through the spin of electron in addition to its charge for device functionality (see, for example, [1–3]).

The basic elements of spintronics are magnetic, superconducting and tunneling heterostructures. In this paper we present results of studies, which were carried out during last years by the team of Physics of Magnetic Nanostructures and Spintronics laboratory (FMNS).

## 2. Model of point contact and basics of the theory

In the present work a model of the point contact (PC) between two ferromagnetic metals (see, for example, Refs. [4, 5]) with different conduction properties of the spin sub-bands is considered. The PC is simulated by a nanosize circular hole of the radius  $a$  made in an impenetrable membrane, which divides the space on two half-spaces occupied by single-domain ferromagnetic metals (see Fig. 1). The  $z$ -axis of the coordinate system is chosen to be perpendicular to the membrane plane. A model of linear domain wall has been used to account for the finite contact length. When magnetizations on both sides of the contact is in parallel (P) alignment, there is no domain wall in the constriction, and the electric current flows through the contact independently in each of the conduction electron spin-subbands. At antiparallel (AP) alignment of the magnetizations, a domain wall is created in the constriction [6]. Simultaneously, the conduction spin-subband assignment in one of the magnetic domains reverses with respect to the previous one. In the case of a ferromagnetic PC, the band structures of the spin-subbands of the ferromagnetic metals do not coincide for either spin-up or spin-down conduction electrons. It is obvious that the potential barriers at the interface of the contact are different for the P and AP alignments. As a result, scattering of electrons associated with these potential barriers and magnetization profiles at the interface are different for the two alignments, which gives rise to magnetoresistance.

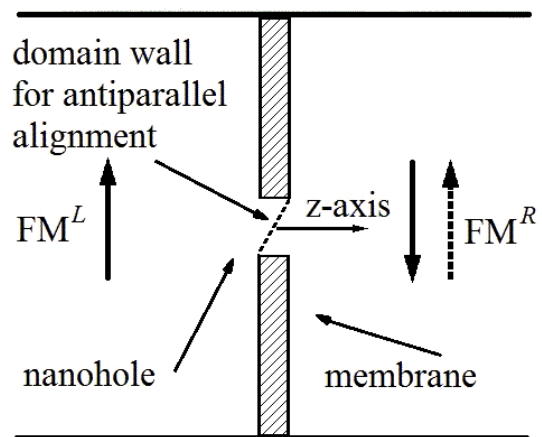


**Figure 1.** Schematic view of short channel with domain wall is shown. The arrows denote parallel and antiparallel alignments of magnetization  $FM^L$  and  $FM^R$  ferromagnetic.

The electron motion on the both sides of the contact can be described by transport equations for quasi-classical Green functions (GF's) [7]. These GF's are symmetrical and antisymmetrical with respect to  $z$  projection of the quasiparticle momentum and satisfy Boltzmann equations in the  $\tau$ -approximation. We develop a theory of electric transport through magnetic PC's taking into account gradient terms in the series expansion of GF's. The theory covers ballistic  $l > a$  and diffusive  $l < a$  regimes ( $l$  is the mean free path) to explain the variety of observed experimental data.

The case of the same ferromagnetic metal was considered in [7] in the quasi-classical approximation. Using the same approach, we give a general derivation of conductance for different ferromagnetic metals. Our aim is to calculate the spin-polarized current  $I_\alpha^z$  through the hole in response on the voltage drop  $V$  applied to the outer leads far away from the contact:

$$I_\alpha^z(z \rightarrow 0, t) = a \int_0^\infty dk J_1(ka) j_\alpha^z(0, k, t), \quad (1)$$

where  $\alpha = (\uparrow, \downarrow)$  is the spin index. Here the Bessel function  $J_1(ka)$  comes from the integration of the current density  $j_\alpha^z(z = 0, \rho)$  over the circular contact cross-section, and  $j_\alpha^z(0, k, t)$  is the Fourier transform of the current density  $j_\alpha^z(z = 0, \rho)$  over the in-plane coordinate  $\rho$ . The current density can be expressed via the antisymmetric quasi-classical GF,  $g_{a,\alpha}(0, k, t)$ , as follows ( $k_B = \hbar = 1$ ):

$$j_\alpha^z(0, k, t) = -\frac{ep_{F,\alpha,\min}^2}{2\pi} \langle \cos \theta_{L,\alpha} g_{a,\alpha}(0, \mathbf{k}, t) \rangle_L, \quad (2)$$

where  $p_{F,\alpha,\min}$  is the Fermi momentum, which is the smallest of the momentums ( $p_{F,\alpha}^L, p_{F,\alpha}^R$ ),  $\theta_{L,\alpha}$  is the angle between the  $z$  axis and the direction of movement of the electron to the hole,  $g_{a,\alpha}(0, k, t)$  is antisymmetrical with respect to  $z$  projection of the quasiparticle momentum and satisfies Boltzmann equations in the  $\tau$  approximation:

$$l_{z,\alpha} \frac{\partial g_{a,\alpha}}{\partial z} + (1 - i\mathbf{k} \cdot \mathbf{l}_{\parallel,\alpha}) g_{s,\alpha} = \langle g_{s,\alpha} \rangle, \quad (3)$$

$$l_{z,\alpha} \frac{\partial g_{s,\alpha}}{\partial z} + (1 - i\mathbf{k} \cdot \mathbf{l}_{\parallel,\alpha}) g_{a,\alpha} = 0. \quad (4)$$

Here  $g_{s,\alpha}$  is the symmetric GF,  $\mathbf{l}_{\parallel,\alpha}$  is the vector defining the electron mean free path of conduction in the contact plane whose absolute value is determined by the geometry:  $l_{\parallel,\alpha}^2 = l_\alpha^2 - l_{z,\alpha}^2$ , where  $l_{z,\alpha} = l_\alpha \cos \theta_\alpha$  is the projection on the axis  $z$ ,  $\mathbf{k}$  is the wave vector in the contact plane. The angular brackets in (2) and (3) mean averaging over the solid angle:

$$\langle g_{s,\alpha} \rangle = \frac{1}{2\pi} \int_0^{\pi/2} \int_0^{2\pi} g_{s,\alpha} \sin \theta d\theta d\varphi.$$

GF's in the Boltzmann equations (3) and (4) satisfy boundary conditions [8]:

$$g_{a,\alpha}^L(0) = g_{a,\alpha}^R(0) = \begin{cases} g_{a,\alpha}(0), & p_{\parallel,\alpha} < p_{F,\alpha}^L, p_{F,\alpha}^R, \\ 0, & p_{\parallel,\alpha} > \min[p_{F,\alpha}^L, p_{F,\alpha}^R], \end{cases} \quad (5)$$

$$2R_\alpha g_{a,\alpha}(0) = D_\alpha (g_{s,\alpha}^L(0) - g_{s,\alpha}^R(0)), \quad (6)$$

where  $p_{\parallel,\alpha}$  is the projection of the spin-dependent Fermi momentum  $p_{F,\alpha}$  on the plane of the contact,  $D_\alpha$  and  $R_\alpha = 1 - D_\alpha$  are the angular- and spin-dependent quantum-mechanical transmission and reflection coefficients, respectively. Boundary conditions (5) and (6) obey the specular reflection law:

$$p_{\parallel,\alpha} = p_{F,\alpha}^L \sin \theta_{L,\alpha} = p_{F,\alpha}^R \sin \theta_{R,\alpha}. \quad (7)$$

### 3. Spin-polarized current in ferromagnetic point contact

Solutions of equations (3) and (4) together with boundary conditions (5) and (6) lead to an expression for the spin-polarized current through PC. The basic mathematical background and calculation details can be found in articles [7,9]. We develop the theory [7,9] of electric transport through magnetic PC's using the following series expansion of the GF:

$$g_{s,\alpha}^{L(R)}(z, \varepsilon) \cong \tanh\left(\frac{\varepsilon}{2T}\right) + f_{s,\alpha}^{L(R)}(0, \varepsilon) + z \cdot \frac{\partial f_{s,\alpha}^{L(R)}(z, \varepsilon)}{\partial z}. \quad (8)$$

Here the first term corresponds to equilibrium GF  $g_s^{\text{eq}}(\varepsilon)$  far away from the contact,  $\varepsilon$  is the energy of electron,  $T$  is the temperature. The second term corresponds to the first order in the expansion of the GF and determines the current heterogeneity in the contact plane. The third term in the expansion for GF corresponds to gradients of the chemical potential. Solution of (3) and (4) taking into account all the terms in the expansion (8) leads to a rather cumbersome expression for the components to the spin current. Here we write it in the simplified form

$$I_\alpha^z = \frac{e^2 p_{F,\alpha,\text{min}}^2 a^2 V}{2\pi} \int_0^\infty dk \frac{J_1^2(ka)}{k} F_\alpha(k, \theta_{L,\alpha}), \quad (9)$$

where  $F_\alpha(k, \theta_{L,\alpha})$  represents the sum of functional dependencies and the integrals of the transmission coefficients  $D_\alpha$  of the domain wall and parameters  $l_\alpha^{L(R)}$ ,  $p_{F,\alpha}^{L(R)}$  of the metals in the contact. We write  $F_\alpha(k, \theta_{L,\alpha})$  in a form of three terms

$$F_\alpha(k, \theta_{L,\alpha}) = \langle \cos \theta_{L,\alpha} D_\alpha(\cos \theta_{L,\alpha}) \rangle_L + F_\alpha^{\text{heter}}(k, \theta_{L,\alpha}) + F_\alpha^{\text{grad}}(k, \theta_{L,\alpha}), \quad (10)$$

where the first term can be used to interpret the spin-polarized conduction in planar contacts. The second term in (10) can be used to calculate the conductivity at a nonuniform current distribution in the plane of the point contacts. The third term  $F_\alpha^{\text{grad}}(k, \theta_{L,\alpha})$  accounts for the chemical potentials bending at the borders of the heterostructure. Notice finally that the current given by equation (9) refers to a particular spin-channel of conductance. The total current through the nanocontact is the sum of currents for both spin-channels. The formal expression for the second channel is the same, but with all physical parameters referred to the second spin-channel.

### 4. Magnetoresistance of magnetic point contacts

The total current through a magnetic PC combines two spin-channels for P and AP mutual orientations of magnetizations in the magnetic domains. Then, magnetoresistance (MR) is characterized by a dimensionless ratio:

$$\text{MR} = \frac{I^{\text{P}} - I^{\text{AP}}}{I^{\text{AP}}}, \quad (11)$$

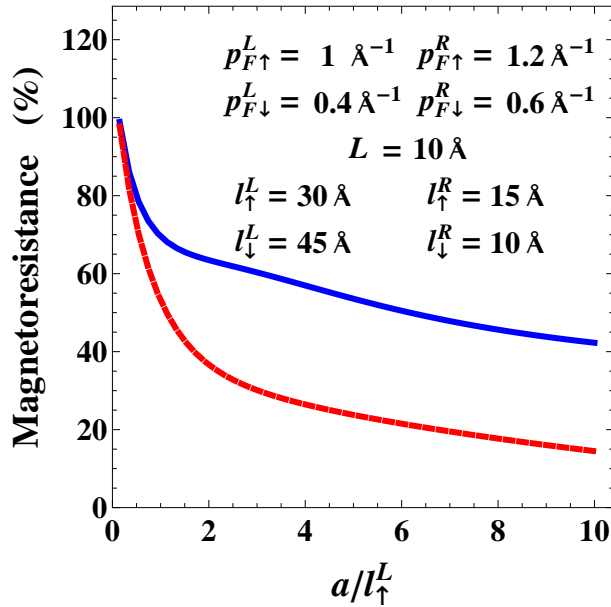


**Figure 2.** Dependence of MR on the ratio of the radius to mean free path of conduction electrons with spin up of the left magnetic domain.

in the series expansion of GF's (see Eq. (8)), and the red dashed line is calculated without gradient terms. Moreover, we investigated mean-free path effects on MR. In some cases the MR monotonously decreases as the PC cross-section increases. For some cases with a large difference in spin sub-band mean-free paths, the calculated MR shows non-monotonous behavior in the region where the radius of the contact becomes comparable with the mean-free path of electrons. We attribute this effect to the gradual change of conduction regimes from ballistic to diffusive in the vicinity of the PC upon increasing the contact cross-section size.

## 5. Superconducting heterostructures

Superconductivity (S) and ferromagnetism (F) are antagonistic long-range orders which cannot coexist in a homogeneous material. Superconductivity in contacts and superconductor-ferromagnet (SF) layered structures can be described by the quasiclassical theory of superconductivity of metals with impurities of a various origin. Prominent feature of ferromagnetic metals is nonequivalence of the Fermi impulses of spin-subbands of conduction bands of these metals. As a result of spin splitting of a ferromagnetic metal conduction band, singlet pair wave function becomes oscillating function of distance from the border with superconducting metal. If ferromagnetic metal is a film with a thickness, comparable with depth of penetration of pair wave function, the flow of pair wave function through the interface between superconducting and ferromagnetic metals becomes modulated with change of a thickness of ferromagnetic film because of changing conditions of an interference of the incident and reflected waves. As a result, a coupling between layers is modulated, and temperature of the superconducting transition  $T_c$  becomes nonmonotonic function of the ferromagnetic layer thickness. The oscillating and the reentrant behaviour of the  $T_c$  as functions of a ferromagnetic layer thickness were observed experimentally by our partners (Kishinev-Chernogolovka-Augsburg) in bilayers of niobium with an alloy copper/nickel. The unusual reentrant behaviour of superconductivity with double suppression of the critical temperature [12–15] was observed for the first time. At a thickness of the Nb layer of the order of 6.2 nanometers the temperature of superconducting transition  $T_c$  at

where  $I^{\text{P(AP)}} = I_{\uparrow}^{\text{P(AP)}} + I_{\downarrow}^{\text{P(AP)}}$ . Then, MR is positive if the physical effect itself is negative (the resistance drops when magnetic field is applied). Now, dependence of MR on the conduction band parameters of contacting ferromagnets can be analysed. To account for a finite point contact length, we place sloping-profile domain wall inside the PC for the AP alignment of magnetizations [10]. The quantum-mechanical transmission coefficient  $D_{\alpha}$  through the sloping domain wall can be calculated, see for example [11]. The details can be found in article [9]. Results of magnetoresistance (MR) calculations for different ferromagnetic metals are shown in Fig. 2. Domain wall thickness between the magnetic domains is assumed to be equal to  $L = 10 \text{ \AA}$ . The blue solid curve is calculated with gradient terms

first sharply fell down on increase in a thickness of ferromagnetic alloy before full suppression of superconductivity was achieved at a thickness of the ferromagnetic alloy  $d_{\text{CuNi}} = 2.5$  nanometers; at the further increase in a thickness  $d_{\text{CuNi}}$ , the superconductivity was restored again for  $d_{\text{CuNi}} > 24$  nanometers. Upon the further increase in a thickness of a ferromagnetic alloy the superconductivity was choked again at a thickness of an order of 38 nanometers.

The proximity effect in planar contacts between superconductors and ferromagnets was analyzed in the frame of the “dirty”-limit theory, semi-phenomenologically adapted to the case of comparable electron mean-free path and superconducting coherence length in a ferromagnet. The calculations were successfully applied to unique experiments on observation of the reentrant superconductivity in bilayers of niobium/copper-nickel alloy. The experiments on double suppression of superconductivity in the bilayers of niobium with copper-nickel alloy were correctly described. Based on material parameters, taken from the experiments, the calculations of phase diagrams for F/S/F trilayers have been done, and recommendation were formulated how to maximize the spin-valve effect in these structures.

Interference effects of the superconducting pairing wave function in thin film bilayers of Nb as a superconductor, and  $\text{Cu}_{41}\text{Ni}_{59}$  as a ferromagnetic material, lead to critical temperature oscillations and reentrant superconductivity for increasing the F-layer thickness [16–18]. The phenomenon is generated by the Fulde-Ferrell-Larkin-Ovchinnikov (FFLO) like state establishing in these geometries. So far, detailed investigations were performed on S/F bilayers. Recently, we could also realize the phenomenon in F/S bilayers where the S-metal now is grown on top of the F-material. Combining both building blocks yields an F/S/F trilayer, representing the core structure of the superconducting spin valve. Also for this geometry we observed deep critical temperature oscillations and reentrant superconductivity, which is a basis to obtain large spin-switching effect, i.e. large shift in the critical temperature, if the relative orientation of the magnetizations of the F-layers is changed from parallel to antiparallel. Ferromagnet/Superconductor/Ferromagnet (F/S/F) trilayers, in which establishing of the FFLO-like state leads to interference effects of the superconducting pairing wave function, form the core of the superconducting spin valve. The realization of strong critical temperature oscillations in such trilayers, as a function of the ferromagnetic layer thicknesses or, even more efficient, reentrant superconductivity, are the key conditions to obtain large spin valve effect, i.e. large shift in the critical temperature. Both phenomena were realized experimentally in the investigated  $\text{Cu}_{41}\text{Ni}_{59}/\text{Nb}/\text{Cu}_{41}\text{Ni}_{59}$  trilayers.

Nanolayered hybrid superconductor-ferromagnet spin-valve structure was fabricated [19,20], the resistive state of which depends on the preceding magnetic field polarity. The effect is based on a strong exchange bias (about  $-2$  kOe) on a diluted ferromagnetic copper-nickel alloy and generation of a long-range odd-in-frequency triplet pairing component. The difference of high and low resistance states at zero magnetic field is 90% of the normal state resistance for a transport current of  $250 \mu\text{A}$  and still around 42% for  $10 \mu\text{A}$ . Both logic states of the structure do not require biasing fields or currents in the idle mode. F/S/F trilayers constitute a core of the superconducting spin valve. The switching effect of the spin valve is based on interference phenomena occurring due to the proximity effect at the S/F interfaces. A remarkable effect is only expected if the core structure exhibits strong critical temperature oscillations, or most favorable, reentrant superconductivity, when the thickness of the ferromagnetic layer is increased. The core structure has to be grown on an antiferromagnetic oxide layer (or such layer to be placed on top) to pin the magnetization-orientation of one of the ferromagnetic layers by exchange bias. We demonstrated that it is possible, keeping the superconducting behavior of the core structure undisturbed.

The theory of superconductor-ferromagnet heterostructures with two ferromagnetic layers predicts generation of long-range, odd-in-frequency triplet pairing at noncollinear alignment (NCA) of the magnetizations of the F layers. This triplet pairing has been detected [21] in a Nb/Cu<sub>41</sub>Ni<sub>59</sub>/normal conducting- (nc-) Nb/Co/CoO<sub>x</sub> spin-valve-type proximity effect heterostructure, in which a very thin Nb film between the F layers serves as a spacer of normal-conducting metal. The resistance of the sample as a function of an external magnetic field shows that for not too high fields, the system is superconducting at the collinear alignment of the Cu<sub>41</sub>Ni<sub>59</sub> and Co layer magnetic moments, but switches to the normal conducting state at a NCA configuration. This indicates that the superconducting transition temperature  $T_c$  for NCA is lower than the fixed measuring temperature. The existence of the minimum  $T_c$  at the NCA regime below that one for parallel or antiparallel alignments of the F-layers magnetic moments, is consistent with the theoretical prediction of a singlet superconductivity suppression by the long-range triplet pairing generation (see below).

The upper critical magnetic field  $H_{c2}$  in thin-film ferromagnet-superconductor-ferromagnet trilayer spin-valve cores was studied experimentally and theoretically [22] in geometries perpendicular and parallel to the heterostructure surface. The series of samples with variable thicknesses  $d_{F1}$  of the bottom and  $d_{F2}$  of the top Cu<sub>41</sub>Ni<sub>59</sub> ferromagnetic (F) layers were prepared in a single run, utilizing a wedge deposition technique. The critical field  $H_{c2}$  was measured in the temperature range 0:4.8 K and for magnetic fields up to 9 T. A transition from oscillatory to reentrant behavior of the superconducting transition temperature versus F-layer thickness, induced by an external magnetic field, was observed for the first time. In order to properly interpret the experimental data, we developed a quasiclassical theory, enabling one to evaluate the temperature dependence of the critical field and the superconducting transition temperature for an arbitrary set of system parameters. A fairly good agreement between our experimental data and theoretical predictions was demonstrated for all samples, using a single set of fit parameters. This confirms the adequacy of the Fulde-Ferrell-Larkin-Ovchinnikov physics in determining the unusual superconducting properties of the studied Cu<sub>41</sub>Ni<sub>59</sub>/Nb/Cu<sub>41</sub>Ni<sub>59</sub> spin-valve core trilayers.

In cooperation with the Institute of Theoretical Physics RAS (Ya.V. Fominov) and Moscow State University (M.Yu. Kupriyanov's group) we investigated the critical temperature  $T_c$  of F2/F1/S trilayers (Fi is a ferromagnetic metal, S is a singlet superconductor), where the long-range triplet superconducting component is generated at noncollinear magnetizations of the F layers. An asymptotically exact numerical method was employed to calculate  $T_c$  as a function of the trilayer parameters, in particular, mutual orientation of magnetizations and F2/F1 interface transparencies. Earlier, we demonstrated [23,24] that  $T_c$  in such structures can be nonmonotonic function of the angle  $\alpha$  between magnetizations of the two F layers. The minimum is achieved at an intermediate  $\alpha$ , lying between the parallel (P,  $\alpha = 0$ ) and antiparallel (AP,  $\alpha = \pi$ ) cases. This implies a possibility of a triplet (TR) spin-valve effect: at temperatures above the minimum  $T_c^{\text{TR}}$  but below  $T_c^{\text{P}}$  and  $T_c^{\text{AP}}$ , the system is superconducting only in the vicinity of the collinear orientations. At certain configuration of parameters, we predicted a reentrant  $T_c$  behaviour. At the same time, considering only the P and AP orientations, we found that both the "standard" ( $T_c^{\text{P}} < T_c^{\text{AP}}$ ) and "inverse" ( $T_c^{\text{P}} > T_c^{\text{AP}}$ ) switching effects are possible depending on parameters of the system (Fig. 3).

It was shown recently the existence of the anomalous dependence of the spin-triplet correlations on the angle  $\alpha$  in F/F/S structures. We demonstrated a possibility of the spin-valve effect mode selection (standard switching effect, the triplet spin-valve effect or reentrant  $T_c(\alpha)$  dependence) by the variation of the F2/F1 interface transparency (Fig. 4).

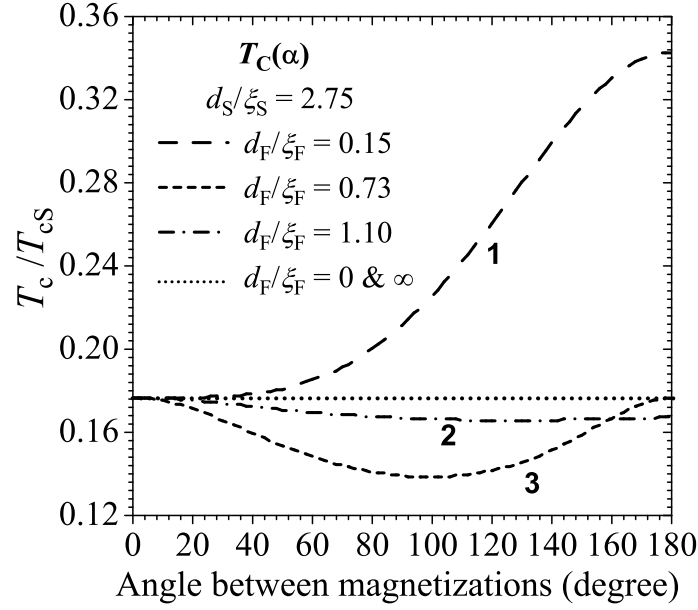


**Figure 3.** Critical temperature  $T_c$  versus the misalignment angle  $\alpha$  for the various thicknesses of the F1 layer (the F2 layer is infinitely thick) [23].

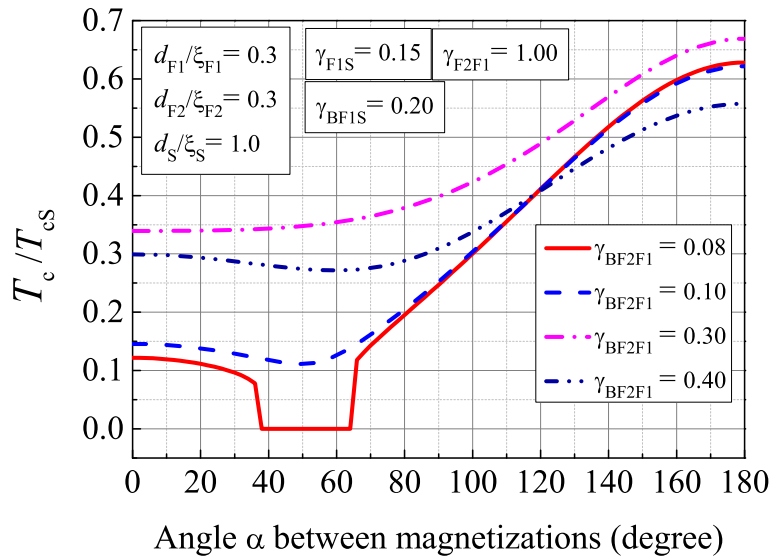


**Figure 4.** Dependence of the transition temperature  $T_c$  on the angle  $\alpha$  between magnetizations under the different F2/F1 interface transparencies [25].

## 6. Summary

The quasi-classical theory of electric transport through nanoscale contacts for the case of different ferromagnetic metals has been generalized taking into account the bending of the chemical potentials near the interface. The spin-polarized conductance and MR are calculated taking into account gradient terms and covering the ballistic ( $l > a$ ) and diffusive ( $l < a$ ) regimes. The dependences of MR on the ratio of radius contact to mean free path of conduction electrons are shown. It can be used for interpreting the experimental data and properties of PC's resistance of Fe-Co, Ni-Mumetall nanocontacts and tunnel structures of CoFeB/MgO/CoFe.

The works on superconductor-ferromagnet nano hybrids are reviewed in a view of the theoretical developments, as well as experimental realization of their unique superconducting properties projected on functional applications.

## Acknowledgments

The support by RFBR (grants No. 14-02-00348-a and No. 14-02-00793-a) is gratefully acknowledged.

## References

1. Kronmüller H., Parkin S., eds., *Handbook of Magnetism and Advanced Magnetic Materials. Volume 5: Spintronics and Magneto-electronics* (John Wiley and Sons, 2007).
2. Tsymbal E. V., Zutic I., eds., *Handbook of Spin Transport and Magnetism* (CRC Press, Taylor & Francis Group, 2012).
3. Zabel H., Farle M., eds., *Magnetic Nanostructures (Spin Dynamics and Spin Transport)* (Springer, 2013).
4. Fernández-Pacheco A., Serrano-Ramón L. E., Tyliczszak T., Chou K. W., Córdoba R., Szkudlarek A., O'Brien L., Kapusta C., Ibarra M. R., Teresa J. M. D., *Nanotechnology* **23**, 105703 (2012).
5. Doudin B., Viret M., *J. Phys.: Condens. Matter* **20**, 083201 (2008).
6. Bruno P., *Phys. Rev. Lett.* **83**, 2425 (1999).
7. Tagirov L. R., Vodopyanov B. P., Efetov K. B., *Phys. Rev. B* **63**, 104428 (2001).
8. Zaitsev A. V., *JETP* **59**, 1015 (1984).
9. Useinov A. N., Deminov R. G., Tagirov L. R., Pan G., *J. Phys.: Condens. Matter* **19**, 196215 (2007).
10. Tagirov L. R., Vodopyanov B. P., Efetov K. B., *Phys. Rev. B* **65**, 214419 (2002).
11. Landau L. D., Lifshitz E. M., *Quantum Mechanics, Third Edition: Non-Relativistic Theory (Volume 3)* (Elsevier Butterworth-Heinemann, 2005).
12. Sidorenko A. S., Zdravkov V., Kehrle J., Morari R., Obermeier G., Gsell S., Schreck M., Müller C., Ryazanov V., Horn S., Tagirov L. R., Tidecks R., *J. Phys.: Conf. Ser.* **150**, 052242 (2009).
13. Sidorenko A. S., Zdravkov V. I., Kehrle J., Morari R., Obermeier G., Gsell S., Schreck M., Müller C., Kupriyanov M. Y., Ryazanov V. V., Horn S., Tagirov L. R., Tidecks R., *JETP Letters* **90**, 139 (2009).
14. Sidorenko A. S., Zdravkov V. I., Kehrle J., Morari R., Antropov E., Obermeier G., Gsell S., Schreck M., Müller C., Ryazanov V. V., Horn S., Tidecks R., Tagirov L. R., in *"Nanoscale Phenomena, Fundamentals and Applications, NanoScience and Technology"*, edited by Hahn H., Sidorenko A., Tiginyanu I. (Springer-Verlag, Berlin, 2009) pp. 3–11.
15. Zdravkov V. I., Kehrle J., Obermeier G., Gsell S., Schreck M., Müller C., Krug H. A., Lindner J., Moosburger J., Nold E., Morari R., Ryazanov V. V., Sidorenko A. S., Horn S., Tidecks R., Tagirov L. R., *Phys. Rev. B* **82**, 054517 (2010).

16. Zdravkov V. I., Kehrle J., Obermeier G., Ulrich A., Gsell S., Schreck M., Müller C., Morari R., Sidorenko A. S., Tagirov L. R., Tidecks R., Horn S., *Supercond. Sci. Technol.* **24**, 095004 (2011).
17. Zdravkov V. I., Kehrle J., Obermeier G., Müller C., Lenk D., Morari R., Sidorenko A. S., Horn S., Tidecks R., Tagirov L. R., *J. Phys.: Conf. Ser.* **400**, 022143 (2012).
18. Kehrle J., Zdravkov V. I., Obermeier G., Garcia J., Ullrich A., Müller C., Morari R., Sidorenko A. S., Horn S., Tagirov L. R., Tidecks R., *Ann. Phys. (Berlin)* **524**, 37 (2012).
19. Zdravkov V. I., Lenk D., Morari R., Ullrich A., Obermeier G., Müller C., Krug H.-A., Sidorenko A. S., Horn S., Tidecks R., Tagirov L. R., *Appl. Phys. Lett.* **103**, 062604 (2013).
20. Zdravkov V. I., Kehrle J., Lenk D., Obermeier G., Ullrich A., Müller C., Krug H. A., Morari R., Sidorenko A. S., Tagirov L. R., Horn S., Tidecks R., *J. Appl. Phys.* **114**, 033903 (2013).
21. Zdravkov V. I., Kehrle J., Obermeier G., Lenk D., Krug H.-A., Müller C., Kupriyanov M. Y., Sidorenko A. S., Horn S., Tidecks R., Tagirov L. R., *Phys. Rev. B* **87**, 144507 (2013).
22. Antropov E., Kalenkov M. S., Kehrle J., Zdravkov V. I., Morari R., Socrovisciuc A., Lenk D., Horn S., Tagirov L. R., Zaikin A. D., Sidorenko A. S., Hahn H., Tidecks R., *Supercond. Sci. Technol.* **26**, 085003 (2013).
23. Fominov Y. V., Golubov A. A., Karminskaya T. Y., Kupriyanov M. Y., Deminov R. G., Tagirov L. R., *JETP Letters* **91**, 308 (2010).
24. Deminov R. G., Tagirov L. R., Karminskaya T. Y., Kupriyanov M. Y., Fominov Y. V., Golubov A. A., *Phys. Rev. B*, in preparation (2014).
25. Deminov R. G., Tagirov L. R., Gaifullin R. R., Karminskaya T. Y., Kupriyanov M. Y., Fominov Y. V., Golubov A. A., *J. Magn. Magn. Mater.* (2014).  
<http://dx.doi.org/10.1016/j.jmmm.2014.02.033>

# Antiferromagnetism in ferropnictides: selection of magnetic order and spin excitations

I.M. Eremin<sup>1,2,\*</sup>, A.V. Chubukov<sup>3</sup>

<sup>1</sup>Institut für Theoretische Physik III, Ruhr-Universität Bochum, D-44801 Bochum, Germany

<sup>2</sup>Kazan Federal University, Kremlevskaya 18, 420008 Kazan, Russia

<sup>3</sup>Department of Physics, University of Wisconsin-Madison, Madison, Wisconsin 53706, USA

\**E-mail: ieremin@tp3.rub.de*

Recent discovery of superconductivity in the iron-based layered pnictides with  $T_c$  ranging between 26 and 56 K generated enormous interest in the physics of these materials. Here, we review some of the peculiarities of the antiferromagnetic order in the iron pnictides, including the selection of the stripe magnetic order and the formation of the Ising-nematic state in the unfolded Brillouin zone within an itinerant description. In addition, we address the spin excitations in the magnetically ordered state and compare them critically to the experimental data. We will only focus on FeAs materials where the weak-coupling analysis seems to be applicable.

**PACS:** 76.30.-v, 68.65.-k

**Keywords:** iron-based superconductors, magnetic fluctuations, quasiparticle interference

## 1. Introduction

The comprehensive understanding of the relationship between magnetism and superconductivity in the Fe-based superconductors, discovered in 2008 by Hideo Hosono and collaborators [1], ultimately requires an analysis of the magnetic ground states in these compounds and their evolution with doping. In particular, the origin of magnetism in the FeSC parent compounds is hotly debated since it is believed that the same magnetic interactions that drive the magnetic ordering also produce the Cooper-pairing [2]. The phase diagram of ferropnictides (FPs) is similar to high- $T_c$  cuprates as it contains an antiferromagnetic (AF) phase in close proximity to the superconducting (SC) one. Most FPs exhibit an AF state at low carrier concentrations, whose suppression with doping, pressure, or disorder allows for the emergence of superconductivity. This shows strong similarities to the generic cuprate phase diagram and is evidence for the interplay between magnetism and superconductivity in the Fe-based materials. There are two important distinctions, however. First, parent compounds of FPs are antiferromagnetic *metals*, and second, the superconducting pairing symmetry in most of the materials is, most likely, an extended *s*-wave, with or without nodes [2]. The electronic structure of the parent FPs in the normal state has been measured by angle-resolved photoemission (ARPES) [3–8] and by quantum oscillations [9,10]. Both agree largely with *ab-initio* band structure calculations [11,12]. It consists of two quasi-two-dimensional near-circular hole pockets of unequal size, centered around the  $\Gamma$ -point (0,0), and two quasi-2D elliptical electron pockets centered around (0, $\pi$ ) and ( $\pi$ ,0) points in the unfolded Brillouin zone (BZ) which includes only Fe atoms. Due to the tetragonal symmetry, the two electron pockets transform into each other under rotation by 90°. In the folded BZ, which is used for experimental measurements because of the two nonequivalent As positions with respect to the Fe plane, both electron pockets are centered around ( $\pi$ , $\pi$ ). The dispersions near electron pockets and near hole pockets are reasonably close to each other apart from the sign change, i.e., there is a substantial degree of nesting between hole and electron bands. One has to mention that nesting of electron and hole bands is not always present in iron-based superconductors and we comment on these systems at the end of this chapter.

Here we analyze review theoretically the formation of antiferromagnetic order in parent FPs and its consequences for the orbital and electronic structure, as well as for the appearance of Ising-nematic order above the magnetic transition. Some of the results appeared previously in Refs. [13,14]. We will only focus on metallic FeAs materials, for which the weak-coupling analysis seems to be applicable. Neutron scattering measurements on parent FeAs pnictides have revealed the ordering momentum in the unfolded BZ to be either  $(0, \pi)$ , or  $(\pi, 0)$ , i.e., the magnetic order consists of ferromagnetic chains along one crystallographic direction and antiferromagnetic chains along the other direction. Such magnetic order emerges in the  $J_1 - J_2$  model of localized spins with exchange interactions between nearest and next-nearest neighbors  $J_1$  and  $J_2$ , respectively, for  $J_2 > 0.5J_1$  [15–19]. However, here we discuss an alternative scenario which assumes that parent FPs are good metals made of itinerant electrons, and antiferromagnetic order is of spin-density wave (SDW) type. Indeed, optical conductivity measurements observe the transfer of spectral weight from the Drude peak to a mid-infrared peak, consistent with itinerant electrons giving rise to AF order [20]. The nesting-driven mechanism is known to give rise to the incommensurate AF in Cr [21,22]. Given the electronic structure of FPs, it is natural to assume that AF order emerges, at least partly, due to near nesting between the dispersions of holes and electrons. This is confirmed by ab-initio analysis of the total energy in the antiferromagnetic state which shows that the main energy gain with respect to the paramagnetic state comes from regions of the BZ where electron and hole pockets reside [23]. Furthermore, angle-resolved photoemission spectroscopy (ARPES) find a direct relationship between nesting and the onset of AF [24]. An incommensurate AF order is also observed by neutron diffraction for some doping values [25]. Several groups have explored different aspects of this itinerant SDW model over the last years [13,26–30].

## 2. Magnetic order in ferropnictides

### 2.1. Magnetic frustration

As pointed out in the introduction the magnetic order in the FPs was originally detected by neutron scattering [31] and  $\mu$ sR experiments [32]. The magnetic transition temperature varies slightly from compound to compound and is of the order of  $T_N \sim 150$  K. In real space the magnetic ordering consists of ferromagnetic chains along one crystallographic direction in the Fe square lattice which are coupled antiferromagnetically. In momentum space the order can be characterized by the wave-vectors  $\mathbf{Q}_1 = (\pi, 0)$  or  $\mathbf{Q}_2 = (0, \pi)$ . Within the localized scenario this order emerges in the context of the  $J_1 - J_2$  model [15] for  $J_2 > 0.5J_1$  once quantum fluctuations are taken into account. In the following we review how this order appears in the itinerant picture. The schematic Fermi surface (FS) in the normal state of FPs is reproduced in Fig. 1 for the unfolded BZ (i.e. the square-lattice BZ). As we pointed out in the introduction the elliptical

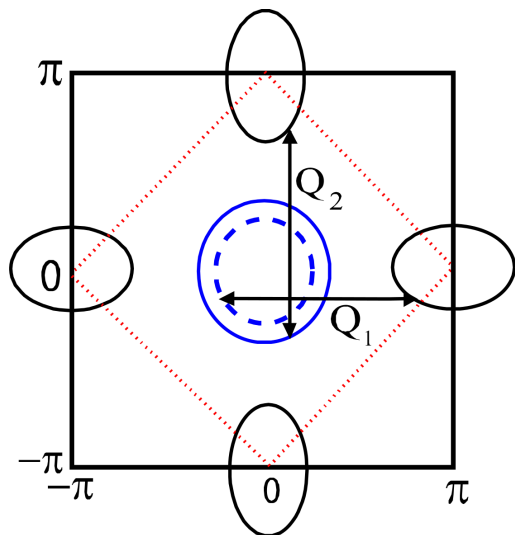


**Figure 1.** Schematic Fermi surface of ferropnictides in the unfolded Fe-based Brillouin zone with two circular hole-like pockets centered around the  $\Gamma$ -point and two elliptical electron-like pockets located around the  $(\pi, 0)$  and  $(0, \pi)$  point of the Brillouin zone, respectively.  $\mathbf{Q}_1$  and  $\mathbf{Q}_2$  represent two nesting wave vectors.

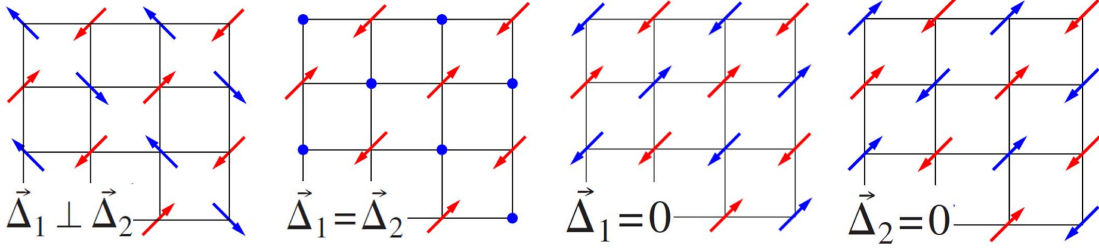


**Figure 2.** Possible real space orderings of the magnetic state. Either one of the last two corresponds to the experimentally realized one [14].

electron bands and nearly circular hole bands are nearly nested. For the Fermi surface topology of FPs it means that there are two nesting wave vectors  $\mathbf{Q}_1 = (\pi, 0)$  and  $\mathbf{Q}_2 = (0, \pi)$  between the hole- and electron-like pockets. For the idealized case of zero ellipticity of the electron pockets and equal masses for the electron and hole bands the situation is similar to the half-filled Hubbard model with nearest neighbor hopping. In particular, the susceptibility in the particle-hole channel diverges logarithmically as it usually does in the particle-particle Cooper-channel. A renormalization group analysis shows that the leading instability is magnetic [26,27]. However, here it occurs at two wave vectors  $\mathbf{Q}_1$  and  $\mathbf{Q}_2$ , leaving open the question of how only one of the two ordering vectors is selected, as it is experimentally observed.

To formulate the problem in a formal way let us start with a generic spin configuration described by two mean-field SDW order parameters  $\Delta_i$  for each of the wave vector  $\mathbf{Q}_i$  in the form

$$\mathbf{S}(\mathbf{R}) = \Delta_1 e^{i\mathbf{Q}_1 \mathbf{R}} + \Delta_2 e^{i\mathbf{Q}_2 \mathbf{R}}. \quad (1)$$

For such a configuration the Fe lattice decouples into two interpenetrating antiferromagnetically ordered sublattices with magnetizations  $\Delta_1 + \Delta_2$  and  $\Delta_1 - \Delta_2$ . However, neither the angle between the two Neel vectors is fixed nor their magnitudes. For example, in Fig. 2 we show four possible orderings for a generic  $\mathbf{S}(\mathbf{R})$  out of many possibilities. The last two configurations with one of the  $\Delta_i$  vanishing refer to the experimentally observed ones. Without loss of generality one can assume that one of the hole pockets interacts stronger with the two electron-like pockets than the other hole pocket. Therefore it is useful to consider a model consisting of a single circular hole FS centered around the  $\Gamma$ -point ( $\alpha$ -band) and two elliptical electron Fermi surface pockets centered around the  $(\pm\pi, 0)$  and  $(0, \pm\pi)$  points in the unfolded BZ ( $\beta$ -bands):

$$H_2 = \sum_{\mathbf{p}, \sigma} \left[ \varepsilon_{\mathbf{p}}^{\alpha_1} \alpha_{1\mathbf{p}\sigma}^\dagger \alpha_{1\mathbf{p}\sigma} + \varepsilon_{\mathbf{p}}^{\beta_1} \beta_{1\mathbf{p}\sigma}^\dagger \beta_{1\mathbf{p}\sigma} + \varepsilon_{\mathbf{p}}^{\beta_2} \beta_{2\mathbf{p}\sigma}^\dagger \beta_{2\mathbf{p}\sigma} \right]. \quad (2)$$

Here,  $\varepsilon_{\mathbf{p}}^{\alpha_1} = -\frac{\hbar^2 p^2}{2m_1} + \mu$  and  $\varepsilon_{\mathbf{p}}^{\beta_1} = \frac{\hbar^2 p_x^2}{2m_x} + \frac{\hbar^2 p_y^2}{2m_y} - \mu$ ,  $\varepsilon_{\mathbf{p}}^{\beta_2} = \frac{\hbar^2 p_x^2}{2m_y} + \frac{\hbar^2 p_y^2}{2m_x} - \mu$  are the dispersions of the hole and electron bands. The momenta of  $\alpha$ -fermions are counted from  $(0, 0)$ , whereas the momenta of the  $\beta_1$ - and  $\beta_2$ -fermions are counted from  $(0, \pi)$  and  $(\pi, 0)$ .

One then projects all possible electronic interactions in the SDW channel. According to the terminology of Ref. [27], the dominant contributions are the density-density interactions between  $\alpha$  and  $\beta$  fermions in the form

$$H_4 = U_1 \sum \alpha_{1\mathbf{p}_3\sigma}^\dagger \beta_{j\mathbf{p}_4\sigma'}^\dagger \beta_{j\mathbf{p}_2\sigma'} \alpha_{1\mathbf{p}_1\sigma} + \frac{U_3}{2} \sum \left[ \beta_{j\mathbf{p}_3\sigma}^\dagger \beta_{j\mathbf{p}_4\sigma'}^\dagger \alpha_{1\mathbf{p}_2\sigma'} \alpha_{1\mathbf{p}_1\sigma} + \text{h.c.} \right]. \quad (3)$$

At this level we neglect the potential angular dependencies of  $U_1$  and  $U_3$  along the FSs which arise due to orbital contents of the the Fermi pockets, which we will discuss later.

The two SDW order parameters are expressed as  $\Delta_1 \propto \sum_{\mathbf{p}} \langle \alpha_{1\mathbf{p}\delta}^\dagger \beta_{1\mathbf{p}\gamma} \sigma_{\delta\gamma} \rangle$  with momentum  $\mathbf{Q}_1$  and  $\Delta_2 \propto \sum_{\mathbf{p}} \langle \alpha_{1\mathbf{p}\delta}^\dagger \beta_{2\mathbf{p}\gamma} \sigma_{\delta\gamma} \rangle$  with momentum  $\mathbf{Q}_2$ . Without loss of generality we can set  $\Delta_1$  along the  $z$ -axis and  $\Delta_2$  in the  $xz$ -plane: in explicit form, we introduce

$$\Delta_1^z = -U_{\text{SDW}} \sum_{\mathbf{p}} \langle \alpha_{1\mathbf{p}\uparrow}^\dagger \beta_{1\mathbf{p}\uparrow} \rangle, \quad \Delta_2^{z(x)} = -U_{\text{SDW}} \sum_{\mathbf{p}} \langle \alpha_{1\mathbf{p}\uparrow}^\dagger \beta_{2\mathbf{p}\uparrow(\downarrow)} \rangle, \quad (4)$$

where  $U_{\text{SDW}} = U_1 + U_3$ .

In the simplest case all masses are equal, i.e.,  $m_x = m_y$  and  $\varepsilon_{\mathbf{p}}^{\beta_1} = \varepsilon_{\mathbf{p}}^{\beta_2} = \varepsilon_{\mathbf{p}}^\beta$ , such that all circular pockets are perfectly nested. Similarly to the single-band case we can treat the interaction term, Eq. 3, with the SDW order parameters, Eq. 4, within a mean-field approach. Performing two consecutive Bogolyubov transformations [14] the quadratic Hamiltonian can be written as

$$H_2^{\text{eff}} = \sum_{a,\mathbf{p}} \varepsilon_{\mathbf{p}}^\beta d_{a\mathbf{p}}^\dagger d_{a\mathbf{p}} + \sum_{\mathbf{p}} E_{\mathbf{p}} \left( e_{a\mathbf{p}}^\dagger e_{a\mathbf{p}} + p_{b\mathbf{p}}^\dagger p_{b\mathbf{p}} - e_{b\mathbf{p}}^\dagger e_{b\mathbf{p}} - p_{a\mathbf{p}}^\dagger p_{a\mathbf{p}} \right), \quad (5)$$

where  $E_{\mathbf{p}} = \pm \sqrt{\varepsilon_{\mathbf{p}}^2 + \Delta^2}$  and  $\Delta = \sqrt{(\Delta_1^z)^2 + \Delta_2^2}$ ,  $\Delta_2 = \sqrt{(\Delta_2^z)^2 + (\Delta_2^x)^2}$  and there is only one single self-consistent equation for the total gap magnitude

$$1 = \frac{U_{\text{SDW}}}{2N} \sum_{\mathbf{p}} \frac{1}{\sqrt{\varepsilon_{\mathbf{p}}^2 + \Delta^2}}. \quad (6)$$

It is clear that the self-consistency equation (6) only fixes the total magnitude of  $(\Delta_1^z)^2 + \Delta_2^2$  but not the magnitude and the direction of  $\Delta_1$  and  $\Delta_2$ . This implies a huge ground state degeneracy at the mean-field level, where SDW ordering corresponds to the spontaneous breaking of an  $O(6)$  symmetry. The experimentally realized states with either  $\Delta_i = 0$  are just two of infinitely many possibilities. Moreover, the degeneracy of the itinerant model is even larger than that in the localized  $J_1 - J_2$  model where the moments are fixed. In the itinerant picture the magnitude of each sublattice magnetization can vary by the cost of the other as long as their sum is kept constant.

In the following we will show that within mean-field the degeneracy can still be lifted by the ellipticity of the electron pockets or the interaction within electron or hole pockets. This explains why the particular stripe-type order is realized and then due to the magneto-elastic coupling the structural order is imposed on the lattice. However, it does not explain why the structural transition occurs sometimes at higher temperature than  $T_N$ . To cover this aspect we also briefly discuss how the wave-vector can be selected Ising-like degeneracy between  $\mathbf{Q}_1$  and  $\mathbf{Q}_2$  can be lifted prior to the onset of long-range magnetic ordering, giving rise to the so-called Ising-nematic order. We also discuss how this emergent order couples to the lattice and orbitals.

## 2.2. Lifting the magnetic ground state degeneracy at $T_N$

So far, the analysis assumed the idealized situation of fully nested circular electron and hole pockets with interactions only between holes and electrons. If one takes into account the ellipticity of the electron pockets and additional interactions the degeneracy may be lifted. One includes, in addition, the interaction between the electron pockets, i.e. four other possible  $\beta - \beta$  interactions:

$$\begin{aligned} H_4^{\text{ex}} = & U_6 \sum \beta_{1\mathbf{p}_3\sigma}^\dagger \beta_{2\mathbf{p}_4\sigma'}^\dagger \beta_{2\mathbf{p}_2\sigma'} \beta_{1\mathbf{p}_1\sigma} + U_7 \sum \beta_{2\mathbf{p}_3\sigma}^\dagger \beta_{1\mathbf{p}_4\sigma'}^\dagger \beta_{2\mathbf{p}_2\sigma'} \beta_{1\mathbf{p}_1\sigma} \\ & + \frac{U_8}{2} \sum \left[ \beta_{2\mathbf{p}_3\sigma}^\dagger \beta_{2\mathbf{p}_4\sigma'}^\dagger \beta_{1\mathbf{p}_2\sigma'} \beta_{1\mathbf{p}_1\sigma} + \text{h.c.} \right] \\ & + \frac{U_4}{2} \sum \left[ \beta_{1\mathbf{p}_3\sigma}^\dagger \beta_{1\mathbf{p}_4\sigma'}^\dagger \beta_{1\mathbf{p}_2\sigma'} \beta_{1\mathbf{p}_1\sigma} + \beta_{2\mathbf{p}_3\sigma}^\dagger \beta_{2\mathbf{p}_4\sigma'}^\dagger \beta_{2\mathbf{p}_2\sigma'} \beta_{2\mathbf{p}_1\sigma} \right]. \end{aligned} \quad (7)$$

In the AF state one again applies the sequence of Bogolyubov transformations, and takes the appropriate averages  $\langle \dots \rangle$  to obtain the contribution to the ground state energy coming from these additional interaction terms. The final correction to the ground state energy was obtained in [14] and has the form:

$$E_{\text{gr}}^{\text{ex}} = 2A^2 [(U_6 + U_8 - U_7 - U_4)] \frac{|\Delta_1|^2 |\Delta_2|^2}{\Delta^4} + 4A^2 U_7 \frac{(\Delta_1 \cdot \Delta_2)^2}{\Delta^4}. \quad (8)$$

Observe that  $E_{\text{gr}}^{\text{ex}}$  depends on  $|\Delta_1|^2 |\Delta_2|^2$  and on  $(\Delta_1 \cdot \Delta_2)^2$ , i.e., it is sensitive to both the relative values and relative directions of  $\Delta_1$  and  $\Delta_2$ . When all interactions are of equal strength, the first term vanishes, and the last term favors  $\Delta_1 \perp \Delta_2$ . In this situation, the O(6) degeneracy of the perfect-nesting model is broken, but only down to O(3)×O(3), i.e., the magnitude of the order parameter at each site is now the same because  $(\Delta_1 + \Delta_2)^2 = (\Delta_1 - \Delta_2)^2$ , but the angle between the directions of the SDW order in the two sublattices (i.e., between  $\Delta_1 + \Delta_2$  and  $\Delta_1 - \Delta_2$ ) is still arbitrary. This is exactly the same situation as in the classical  $J_1 - J_2$  model. However, once  $U_6 + U_8 - U_7 - U_4$  is nonzero, the degeneracy is broken down to a conventional O(3) already at the mean-field level. Because  $U_4$  is reduced and even changes sign under the RG flow [27], while other  $U_i$  do not flow, the most likely situation is that  $U_6 + U_8 - U_7 - U_4 > 0$ , in which case  $E_{\text{gr}}^{\text{ex}}$  is minimized when either  $\Delta_1 = 0$ , or  $\Delta_2 = 0$ , i.e., SDW order is either  $(0, \pi)$  or  $(\pi, 0)$ . This is exactly the same SDW order as observed in experiments. If  $U_6 + U_8 - U_7 - U_4$  was negative,  $E_{\text{gr}}^{\text{ex}}$  would be minimized when  $|\Delta_1| = |\Delta_2|$ , in which case the SDW OPs of the two sublattices would align orthogonal to each other. The spin configuration for such state is shown in the left panel of Fig. 2.

We also consider the impact of the elliptical distortion of the electron Fermi pockets to the enlarged O(6) symmetry of the perfect-nesting model as the electron pockets are actually ellipses rather than circles. The effective masses  $m_x$  and  $m_y$  are not equal, and  $\varepsilon_{\mathbf{k}}^{\beta_1} \neq \varepsilon_{\mathbf{k}}^{\beta_2}$ . To continue with the analytical analysis, one assumes that the ellipticity is small, and introduces  $m_x = (1 + \delta)m$  and  $m_y = (1 - \delta)m$ , where  $\delta \ll 1$ , and computes the correction to the ground state energy to second order in  $\delta$ . The contribution to the ground state energy coming from the ellipticity is

$$E_{\text{gr}}^{\text{ellipt}} = C |\Delta_1|^2 |\Delta_2|^2, \quad C = \delta^2 \frac{m\mu^2}{4\pi\Delta^4}, \quad (9)$$

where the coefficient  $C$  is positive, i.e., the correction due to the ellipticity of the electron pockets again breaks the degeneracy and selects either the  $(0, \pi)$  or  $(\pi, 0)$  state. This is again the same selection as one needs for consistency with experimentally observed magnetic order. It is remarkable that ellipticity leads to a term in the ground state energy that is similar to an effective interaction between two SDW OPs which, for  $\Delta \ll \mu$ , leads to the same selection of the ground state SDW order as the direct interaction between the two electron pockets.

### **2.3. Ising nematic order above $T_N$**

The emergence of a phase with broken rotational symmetry above or at  $T_N$  is experimentally not only manifested by a tetragonal to orthorhombic transition at  $T_s$ , but also by the onset of significant anisotropies in several quantities [33], such as dc resistivity [34, 35], optical conductivity [36, 37], and orbital occupancy [38].

Early theoretical proposals explored two alternative scenarios for the nematic order. On the one hand orbital ordering might induce the structural transition and trigger the magnetic transition at a lower temperature by renormalizing the exchange constants [39]. On the other

hand, a purely magnetic scenario based on a localized  $J_1 - J_2$  model [15], for FPs see [16, 17], is build upon the assumption that the order parameter manifold for two possible stripe magnetic orders is  $O(3) \times Z_2$  (compare to the actual degeneracy which has  $O(6)$  symmetry), with the  $Z_2$  Ising symmetry differentiating between the two possible ordering vectors  $(0, \pi)$  and  $(\pi, 0)$ . This scenario explores the possibility that the  $Z_2$  Ising variable orders before the  $O(3)$  rotational symmetry is broken, leading to an intermediate phase with a broken tetragonal symmetry but no long-range magnetic order, called Ising nematic. This magnetic scenario was later extended to itinerant systems in a phenomenological way [40, 41].

Here, we review how the Ising nematic order can be understood within a magnetic scenario for an itinerant fermionic model [13].

The onset of magnetic order with ordering vector  $(0, \pi)$  or  $(\pi, 0)$  breaks not only the  $O(3)$  spin-rotational symmetry, but also the  $C_4$  tetragonal symmetry of the lattice. Experimentally, this tetragonal symmetry breaking has however been observed at temperatures  $T_s$  larger than  $T_N$  for many compounds [33]. In the temperature regime between  $T_s$  and  $T_N$ , the system displays not only an orthorhombic distortion, but also in-plane anisotropies in several observables, such as dc [34, 35] and ac conductivities [36, 37], as well as the magnetic susceptibility [42]. Because this phase breaks the rotational symmetry of the lattice without affecting its translational symmetry, it has been called the Ising-nematic phase.

To discuss how an Ising-nematic phase appears in our model, we first note that the order parameter manifold of the ground state is  $O(3) \times Z_2$ , where the  $Z_2$  symmetry refers to selecting one of the two ordering vectors  $(0, \pi)$  or  $(\pi, 0)$ . Thus, if the  $Z_2$  symmetry is broken the system is no longer tetragonal, since the  $x$  and  $y$  directions become different inside the Fe-square unit cell. Although as discussed above both  $O(3)$  and  $Z_2$  symmetries are broken simultaneously in the mean-field level, fluctuations can split their transition temperatures. Then, the intermediate phase where the  $Z_2$  symmetry is broken but the spin-rotational  $O(3)$  symmetry is kept intact corresponds to the Ising-nematic phase [17, 40, 41, 43]. This phase is known to appear in the localized  $J_1 - J_2$  model [15, 16], and we now review its origin within our itinerant fermionic model [13]. We start from the microscopic Hamiltonian Eq. 2 and Eq. 3 and write down the partition function

$$Z \propto \int d\mathbf{\Delta}_1 d\mathbf{\Delta}_2 e^{-S_{\text{eff}}[\mathbf{\Delta}_1, \mathbf{\Delta}_2]} \quad (10)$$

in terms of the effective action for the two magnetic order parameters

$$S_{\text{eff}}[\mathbf{\Delta}_1, \mathbf{\Delta}_2] = r_0 (\mathbf{\Delta}_1^2 + \mathbf{\Delta}_2^2) + \frac{u}{2} (\mathbf{\Delta}_1^2 + \mathbf{\Delta}_2^2)^2 - \frac{g}{2} (\mathbf{\Delta}_1^2 - \mathbf{\Delta}_2^2)^2 + v (\mathbf{\Delta}_1 \cdot \mathbf{\Delta}_2)^2. \quad (11)$$

The coefficients can be computed in terms of the bare fermionic propagators and give  $u > 0$ ,  $g > 0$ , and  $v = 0$  for an expansion near perfect nesting, with  $g \propto \delta^2$ , in agreement with the results of the previous section. Indeed, mean-field minimization of this free energy yields the state  $\langle \mathbf{\Delta}_i \rangle \neq 0$  with either  $i = 1$  or  $i = 2$ .

The  $Z_2$  symmetry breaking takes place when fluctuations associated with one of the bosonic fields are larger than the fluctuations associated with the other one, e.g.,  $\langle \mathbf{\Delta}_1^2 \rangle > \langle \mathbf{\Delta}_2^2 \rangle$  while  $\langle \mathbf{\Delta}_1 \rangle = \langle \mathbf{\Delta}_2 \rangle = 0$ .

To capture this physics, we introduce the scalar fields  $\phi = \langle \mathbf{\Delta}_1^2 \rangle - \langle \mathbf{\Delta}_2^2 \rangle$  and  $\psi = \langle \mathbf{\Delta}_1^2 \rangle + \langle \mathbf{\Delta}_2^2 \rangle$  via two Hubbard-Stratonovich transformations. Note that in contrast to the previous subsection we do not treat  $\mathbf{\Delta}$  as a mean-field order but rather as a fluctuating quantity. Here the field  $\phi$  is associated with the appearance of Ising-nematic order. Focusing on the paramagnetic phase, we

integrate out the  $\Delta$  fields and obtain an effective action in terms of the new scalar fields only:

$$S_{\text{eff}}[\phi, \psi] = \int_q \left\{ \frac{\phi^2}{2g} - \frac{\psi^2}{2u} + \frac{3}{2} \log \left[ (\chi_q^{-1} + \psi)^2 - \phi^2 \right] \right\}. \quad (12)$$

The action can now be analyzed within the saddle-point approximation, which is exact in the limit where the number of components  $N$  of the  $\Delta$  field is large [13] as a function of the dimensionless *inverse* nematic coupling  $\alpha = \frac{u}{g}$ . Its magnitude can readily be computed from the microscopic Hamiltonian. Similar to the previous mean-field analysis it decreases with increasing ellipticity of the electron pockets. In terms of physical parameters the result is that, for quasi-2D systems, the splitting and the characters of the magnetic and nematic transitions depend on the dimensionless inverse nematic coupling  $\alpha = \frac{u}{g}$ , which is found to decrease with pressure but increase with electron doping (see Fig. 3).

As shown in Fig. 3, from [13], depending on the strength of the coupling  $\alpha$  different types of system behavior can be found with two distinct multi-critical points in the phase diagram namely a magnetic tri-critical point and a nematic tri-critical point. In the case of quasi-2D systems, the nematic tri-critical point precedes the magnetic one for large values of the nematic coupling (small  $\alpha$ ), magnetic order emerges simultaneously to the Ising-nematic order, via a first-order transition ( $T_N = T_s$ ). For intermediate couplings  $\alpha$ , a second-order Ising-nematic transition accompanied by a discontinuous increase of the magnetic correlation length to a larger but still finite value is found, such that the stripe magnetic order does not develop at  $T_s$  and emerges only at a smaller  $T$ . In this case, the magnetic transition is second-order and it is followed by a meta-nematic transition, in which the nematic order parameter jumps between two non-zero values. The feedback of nematic order on the magnetic spectrum causes a first-order magnetic transition simultaneously to the meta-nematic transition, but split from the second-order nematic transition. This sequence of transitions agrees with the ones observed experimentally for  $\text{BaFe}_2\text{As}_2$  [42]. For small nematic couplings (large  $\alpha$ ) a second-order Ising-nematic transition is followed by a second-order magnetic stripe transition at a smaller temperature. Within our

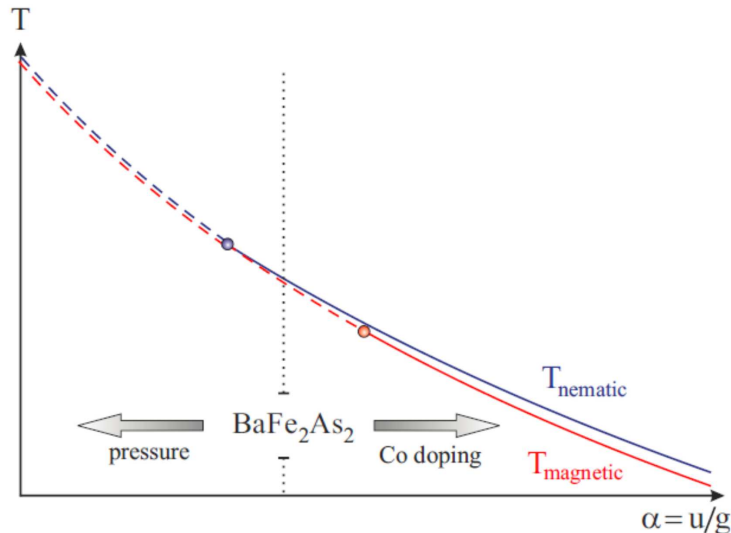


**Figure 3.** Characteristic phase diagram as function of temperature and inverse nematic coupling for strongly moderately anisotropic, quasi-two dimensional systems [13]. Red and blue curves represent magnetic and Ising-nematic transitions, respectively. We show schematically how application of pressure or electron doping (via Co substitution) changes the system behavior of  $\text{BaFe}_2\text{As}_2$ . Here a solid (dashed) line denotes a second-order (first-order) transition, and a double-dashed line indicates a simultaneous first-order transition. The two solid points mark the positions of the nematic and magnetic tri-critical points.

model, doping electrons into the system decreases the nematic coupling, driving the system to this regime of split second-order transitions. Experimentally, this sequence of transitions is observed in Co-doped BaFe<sub>2</sub>As<sub>2</sub> compounds, which display more negative carriers than the undoped parent compound.

Due to the magneto-elastic coupling and the coupling to the  $d_{xz}$  and  $d_{yz}$  Fe-orbital degrees of freedom, the onset of Ising-nematic order simultaneously triggers a non-zero orthorhombic distortion as well as ferro-orbital order [13]. Indeed, a splitting in the onsite energies of the  $d_{xz}$  and  $d_{yz}$  orbitals has been observed experimentally [38], and the sign of the splitting agrees with the one predicted by the itinerant model. We note that ferro-orbital order has also been discussed within approaches that focus on a spontaneous breaking of the  $d_{xz}$  and  $d_{yz}$  orbital symmetry (see for instance [39, 44, 45]).

In addition, one can also show that the nematic order parameter couples linearly to the orbital polarization and lattice distortion [13], and hence nematic order generates orbital and structural order. In principal all these orders break the same  $C_4$  symmetry and, therefore, appear simultaneously. From the experimental point of view this fact presents a difficulty to answer the question what is the actual driving mechanism for the structural transition. Nevertheless, so far the itinerant scenario gives a natural understanding for a variety of phenomena in the FPs phase diagrams.

### 3. Spin waves in itinerant multiorbital systems

Now, let us move to a discussion of the spin excitations below  $T_N$  in iron-based superconductors. We first generalize the self-consistent random phase approximation (RPA) formalism for the calculation of spin waves to multiorbital systems (MOS) as the FPs.

#### 3.1. Multiorbital models - spin wave theory

The main ideas are similar as for the single band model, but with additional complications due to orbital indices. In the following we follow closely [46]. We define the spin operator as

$$\mathbf{S}_s(\mathbf{q}) = \sum_{\mathbf{k}, \sigma, \sigma'} \psi_{s\sigma}^\dagger(\mathbf{k} + \mathbf{q}) \frac{\sigma_{\sigma\sigma'}}{2} \psi_{s\sigma'}(\mathbf{k}), \quad (13)$$

where  $\psi_{s\sigma}^\dagger$  is the creation operator of the orbital  $s$  with spin  $\sigma$  in the MOS. The transverse spin susceptibility in the paramagnetic state can be calculated from the spin-spin correlation function in Matsubara frequency space:

$$\chi_{st}^\pm(\mathbf{q}, i\Omega) = \int_0^\beta d\tau e^{i\Omega\tau} \langle T_\tau S_s^+(\mathbf{q}, \tau) S_t^-(\mathbf{q}, 0) \rangle. \quad (14)$$

In MOS it is convenient to introduce a dynamical spin susceptibility tensor in a more general way using four orbital indices [28, 47]

$$\begin{aligned} \chi_{spqt}^\pm(\mathbf{q}, i\Omega) &= \int_0^\beta d\tau e^{i\Omega\tau} \sum_{\mathbf{k}, \mathbf{k}', \gamma, \delta, \gamma', \delta'} \sigma_{\gamma\delta}^+ \sigma_{\gamma'\delta'}^- \\ &\times \langle T_\tau \psi_{p\gamma}^\dagger(\mathbf{k}, \tau) \psi_{q\delta}(\mathbf{k} + \mathbf{q}, \tau) \psi_{t\gamma'}^\dagger(\mathbf{k}', 0) \psi_{s\delta'}(\mathbf{k}' - \mathbf{q}, 0) \rangle. \end{aligned} \quad (15)$$

With the Green's function (GF)

$$G_{st}^\sigma(\mathbf{k}, i\omega_n) = - \int_0^\beta d\tau e^{i\omega\tau} \langle T_\tau \psi_{s\sigma}(\mathbf{k}, \tau) \psi_{t\sigma}^\dagger(\mathbf{k}, 0) \rangle \quad (16)$$

the susceptibility matrix can be written as

$$\chi_{spqt}^{\pm}(\mathbf{q}, i\Omega) = -\frac{1}{N\beta} \sum_{\mathbf{k}, i\omega_n} G_{sp}^{\uparrow}(\mathbf{k}, i\omega_n) G_{qt}^{\downarrow}(\mathbf{k} + \mathbf{q}, i\omega_n + i\Omega). \quad (17)$$

The susceptibility in the paramagnetic phase within the RPA can be written in a matrix form  $\hat{\chi}$ , see for example [47]

$$\chi_{bsta}^{\text{RPA}} = \chi_{bsta}^0 + \chi_{b'sta'}^{\text{RPA}} U_{c'b'a'd'} \chi_{bc'd'a}^0, \quad (18)$$

and the solution of the RPA in matrix form is straightforward

$$[\hat{\chi}]^{\text{RPA}} = \hat{\chi}^0 (1 - \hat{U} \hat{\chi}^0)^{-1}. \quad (19)$$

The physical susceptibility which is measured in experiment is then obtained

$$\chi_{\text{phys}}^{\text{RPA}}(\mathbf{q}, \omega) = \frac{1}{2} \sum_{st} \chi_{sstt}^{\text{RPA}}(\mathbf{q}, \omega). \quad (20)$$

However, important information is also contained in the individual components of the susceptibility tensor  $\chi_{spqt}$  which can be used to distinguish between predominantly intra- or interorbital fluctuations. The RPA in diagrammatic form is illustrated in Fig. 4

Generally, for MOS, the kinetic or tight-binding part  $H_0$  of the Hamiltonian  $H = H_0 + H_{\text{int}}$ , including the intra- and inter-orbital hoppings, can be diagonalized via a unitary transformations which gives the eigenenergies  $E_{\nu}(\mathbf{k})$  of the system. The operators in the orbital and the band basis are connected via the coefficients of the unitary transformations  $a_{\nu}^s(\mathbf{k}, \sigma)$

$$\psi_{s\sigma}(\mathbf{k}) = \sum_{\nu} a_{\nu}^s(\mathbf{k}, \sigma) \gamma_{\nu\sigma}(\mathbf{k}). \quad (21)$$

Without interactions the GFs are easily obtained as

$$G_{st}^{\sigma}(\mathbf{k}, i\omega_n) = \sum_{\nu} \frac{a_{\nu}^s(\mathbf{k}, \sigma) a_{\nu}^{t*}(\mathbf{k}, \sigma)}{i\omega - E_{\nu}(\mathbf{k})} \quad (22)$$

and the transverse spin susceptibility becomes:

$$\chi_{spqt}^{\pm}(\mathbf{q}, i\Omega) = -\frac{1}{N\beta} \sum_{\mathbf{k}, i\omega, \nu, \mu} \frac{a_{\mu}^s(\mathbf{k}, \uparrow) a_{\mu}^{p*}(\mathbf{k}, \uparrow) a_{\nu}^q(\mathbf{k} + \mathbf{q}, \downarrow) a_{\nu}^{t*}(\mathbf{k} + \mathbf{q}, \downarrow)}{[i\omega - E_{\mu}(\mathbf{k})] [i\omega + i\Omega - E_{\nu}(\mathbf{k} + \mathbf{q})]}. \quad (23)$$

The Matsubara sum can be performed via a standard contour integration and by analytic continuation  $i\Omega \rightarrow \Omega + i\Gamma$ . Observe that for large Hamiltonian matrices the coefficients  $a_{\nu}$  have to be calculated numerically by diagonalizing the Hamiltonian matrix written in  $\mathbf{k}$ -space.

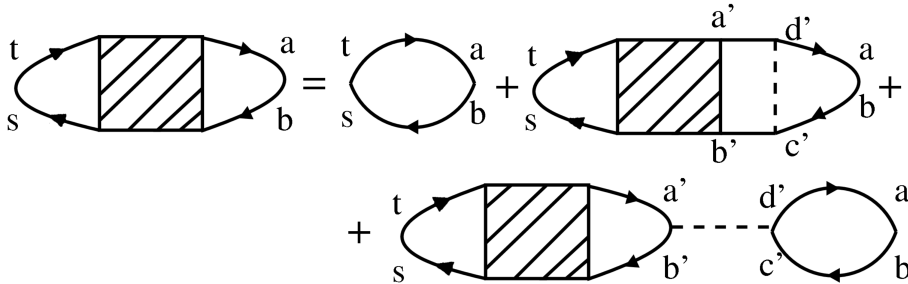


**Figure 4.** Diagrammatic form of the RPA Dyson equation for the multiorbital susceptibility. Depending on the form of the interactions ladder and bubble diagrams contribute to the longitudinal and transverse component.

In a mean-field treatment of the SDW phase, the interaction part of the hamiltonian  $H_{\text{int}}$  is decoupled with respect to a groundstate with a finite magnetization at wave vector  $\mathbf{Q}$ , e.g.  $(\pi, 0)$  or  $(0, \pi)$  for iron-based superconductors. Here, we assume that only one of them is present below  $T_N$ . The order parameters read

$$\Delta_{\nu\nu'} = \sum_{\mathbf{k}} \text{sgn}(\sigma) \left\langle \psi_{\nu\sigma}^\dagger(\mathbf{k}) \psi_{\nu'\sigma}(\mathbf{k} + \mathbf{Q}) \right\rangle. \quad (24)$$

In the magnetic state, SU(2) spin symmetry is broken which yields  $\chi^\pm \neq \frac{1}{2}\chi^{zz}$ . In addition, the AF state also breaks translational symmetry and the mean-field Hamiltonian in the reduced BZ takes the form

$$H_{\text{SDW}} = \sum_{\mathbf{k}} \hat{\psi}_\sigma^\dagger(\mathbf{k}) \begin{pmatrix} H_0(\mathbf{k}) & \sigma M \\ \sigma M & H_0(\mathbf{k} + \mathbf{Q}) \end{pmatrix} \hat{\psi}_\sigma(\mathbf{k}), \quad (25)$$

where we introduce the new spinor

$$\hat{\psi}_\sigma(\mathbf{k}) = \begin{pmatrix} \psi_\sigma(\mathbf{k}) \\ \psi_\sigma(\mathbf{k} + \mathbf{Q}) \end{pmatrix}. \quad (26)$$

Note for MOS each component of the spinor may acquire a spinor structure in orbital space as well. Then the GF acquires off-diagonal elements in momentum space and becomes a matrix. In short-hand notation, we write only the orbital index with a tilde to indicate that the momentum is shifted by the AFM wave vector. We thus obtain

$$\hat{G}_{sp} = \left\langle \begin{pmatrix} s \\ \tilde{s} \end{pmatrix} \begin{pmatrix} p^\dagger & \tilde{p}^\dagger \end{pmatrix} \right\rangle = \begin{pmatrix} G_{sp} & G_{s\tilde{p}} \\ G_{\tilde{s}p} & G_{\tilde{s}\tilde{p}} \end{pmatrix}. \quad (27)$$

Analogously, the susceptibility matrix becomes a matrix in  $\mathbf{q}$ -space [28, 46]:

$$\hat{\chi}_{spqt}^\pm = \begin{pmatrix} \chi_{spqt}^\pm(\mathbf{q}, \mathbf{q}) & \chi_{spqt}^\pm(\mathbf{q}, \mathbf{q} + \mathbf{Q}) \\ \chi_{spqt}^\pm(\mathbf{q} + \mathbf{Q}, \mathbf{q}) & \chi_{spqt}^\pm(\mathbf{q} + \mathbf{Q}, \mathbf{q} + \mathbf{Q}) \end{pmatrix}, \quad (28)$$

where the off-diagonal components, in short hand notation

$$\chi_{spqt}^\pm(\mathbf{q}, \mathbf{q} + \mathbf{Q}) = \left[ G_{sp} G_{q\tilde{t}} + G_{s\tilde{p}} G_{\tilde{q}\tilde{t}} + G_{\tilde{s}\tilde{p}} G_{\tilde{q}t} + G_{\tilde{s}p} G_{qt} \right]$$

are Umklapp susceptibilities as they connect spins with momentum shifted by the AFM wave vector, which is a reciprocal wave vector of the magnetic BZ. The detailed expressions can be found in [46].

The form of the RPA in the SDW state remains the same, see Eq. (18), with the only extension that the interaction matrix also doubles in size with  $\hat{U}$  matrices on the diagonal and zeros on the off-diagonal. To obtain the physical susceptibility we perform an RPA with Eq. (28) and trace over the orbital indices of the first entry  $\chi_{spqt}^{\text{RPA}}(\mathbf{q}, \mathbf{q})$  of the susceptibility matrix. The imaginary part is directly related to the cross section of INS measurements. We also recall that self-consistency enters via taking the same set of interaction parameters in the RPA and the Hartree-Fock mean-field equations.

### 3.2. Accidental collective modes in itinerant frustrated antiferromagnets

Before computing spin waves for realistic parameters of iron-based superconductors we again come back to the idealized model of fully nested electron and hole pockets discussed in the previous section. At a mean-field level there is a large ground state degeneracy. In a localized model this would be reflected by additional soft modes in the spin wave spectra. It is interesting to check whether signs of frustration in the magnetic excitation spectrum also show up in the itinerant description. In Fig. 5 we show the transverse (upper panel) and longitudinal (lower panel) components of the imaginary part of the spin susceptibility for zero and finite ellipticities. Observe that the magnetic order is fixed to be along  $(\pi, 0)$  wave vector. Consider first the idealized case of circular electron pockets,  $\epsilon = 0$  (left panels). In this case two out of three FS are completely gapped. In Fig. 5(a) we show the calculated imaginary part of the transverse component of the susceptibility,  $\text{Im} [\hat{\chi}_{+-}(\mathbf{q}, \Omega)]_{\text{RPA}}$ , along the direction  $(0, \pi)$  to  $(\pi, 0)$ . Because the corresponding ground state is degenerate, the excitation spectrum has a Goldstone mode at the ordering momentum  $\mathbf{Q}_1 = (\pi, 0)$  and another accidental gapless mode at  $\mathbf{Q}_2 = (0, \pi)$ . The excitations near the ordering momentum are propagating up to  $\Omega_c(\mathbf{Q}_1) = 2\Delta_1 \sim 60$  meV which is expected because both pockets separated by  $\mathbf{Q}_1$  are gapped. Excitations near  $\mathbf{Q}_2$  are also propagating, but up to smaller energies,  $\Omega_c(\mathbf{Q}_2) = \Delta_1$ , that is consistent with the fact that only one of the two pockets separated by  $\mathbf{Q}_2$  is gapped. At higher energies spin-waves enter the continuum and become overdamped Stoner-like excitations, however, still with well defined peaks. The difference between  $\Omega_c(\mathbf{Q}_1)$  and  $\Omega_c(\mathbf{Q}_2)$  is also seen in Fig. 5(c), where the longitudinal component of the susceptibility is plotted. As expected,  $\text{Im} [\hat{\chi}_{+-}(\mathbf{q}, \Omega)]_{\text{RPA}}$  vanishes below  $\Omega_c(\mathbf{Q})$ .

For finite  $\epsilon = 0.5$  the results are presented in panels (b) and (d). There are two key effects introduced by ellipticity. First, the degeneracy is now lifted [14] and the transverse excitations near  $\mathbf{Q}_2$  acquire a finite gap clearly visible in Fig. 5(b). Second, spin-wave excitations near  $\mathbf{Q}_1$  have a finite Landau damping down to  $\Omega = 0$  because the SDW order no longer completely gaps the hole and electron FSs separated by  $\mathbf{Q}_1$ . At the same time, spin-wave excitations are

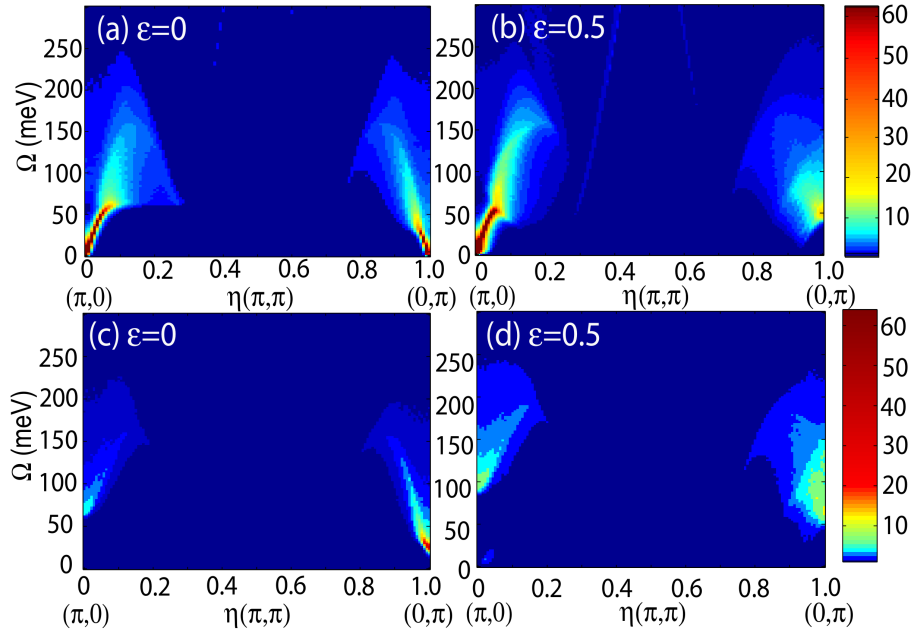


**Figure 5.** Imaginary part of the transverse (upper panel) and longitudinal (lower panel) susceptibility along  $(0, \pi) \rightarrow (\pi, 0)$  points of the Brillouin zone for two different ellipticities of the electron pockets parameterized by  $\epsilon$ . Taken from [46].

still clearly visible at low energies and do not become overdamped. The reason is that SDW coherence factors suppress the scattering between electron and hole like pockets involved in the formation of magnetic order and reduce the Landau damping around the ordering momentum  $\mathbf{Q}_1$  from  $\Omega/|\mathbf{q} - \mathbf{Q}_1|$  to  $\Omega|\mathbf{q} - \mathbf{Q}_1|$  what for linear dispersion is of the same order as  $\Omega^2$  and  $(\mathbf{q} - \mathbf{Q}_1)^2$ . Once  $\Omega$  exceeds  $\Omega_c(\mathbf{Q}_2)$ , the coherence factors no longer screen Landau damping, and spin-waves become Stoner-like, overdamped excitations. The scattering between between the pockets not involved in magnetism is not suppressed by the SDW coherence factors because  $\mathbf{Q}_2$  is not the ordering momentum, therefore, Landau damping makes the transverse excitations near  $\mathbf{Q}_2$  overdamped immediately above the gap. Note, that there is also a tendency towards incommensuration near  $\mathbf{Q}_2$ . Longitudinal excitations are still gapped up to  $\Omega_c(\mathbf{Q})$  and become Stoner-like at higher energies.

Overall, it is interesting to observe that in our itinerant description the groundstate degeneracy for the fully nested situation which arises due to frustration between the two wave vectors  $\mathbf{Q}_1$  and  $\mathbf{Q}_2$  shows up in the magnetic excitation spectrum as an additional soft mode.

### **3.3. Comparison to experiments**

After having introduced the general theory how to calculate spin waves in itinerant magnets with multiple orbitals (bands) contributing at the Fermi energy we want to compare the itinerant description of magnetism in FPs with actual experiments. As mentioned above the two orbital model can give qualitative insights especially to elucidate the role of orbital degrees of freedom. However, in addition to the wrong electronic structure in the unfolded zone it is not possible to fit the dispersion parameters of the model quantitatively to experiments such as ARPES [48]. Therefore, we will show the results for a phenomenological three band model which can be fitted to experiments [46].

Neutron scattering measurements on parent FeAs compounds revealed that magnetic order consists of ferromagnetic chains along one crystallographic direction in an Fe plane and antiferromagnetic chains along the other [31,32], i.e., the system selects  $\mathbf{Q}_{AF}$  to be either  $\mathbf{Q}_1 = (\pi, 0)$  or  $\mathbf{Q}_2 = (0, \pi)$ . Sharp propagating spin-wave like excitations have been observed near the ordering momentum (e.g.,  $\mathbf{Q}_1$ ) up to energies of around 100 meV, with different velocities along the two crystallographic directions [49,50]. At larger energies, excitations become overdamped [49].

Magnetism with  $(\pi, 0)$  stripe order arises also in the  $J_1 - J_2$  model of localized spins for  $J_2 < 0.5J_1$  [15], and it was argued that such a model can successfully describe some of the experimental data on the spin wave spectra, although, an unusually large in-plane anisotropy of the antiferromagnetic exchange between nearest neighbor spins has to be assumed [50] in order to account for the anisotropic spin wave velocities. We have seen in the first section of this review that it is possible to understand the order from an itinerant perspective, which takes into account the peculiar electronic structure of the FPs. The ellipticity of the electron pockets and interactions between them played a key role. The issue we address now is whether inelastic neutron scattering (INS) measurements of magnetic excitations can be explained within the itinerant approach, as well. This is a crucial test of the itinerant description of magnetism in FPs. In Fig. 6 we compare the calculations performed in [46] with inelastic neutron scattering experiments. Measured excitations near  $\mathbf{Q}_1$  are propagating spin-waves up to about 100 meV, with a finite but small damping. In the left panel of Fig. 6 we compare the dispersion with the experimental data [49,50]. We emphasize that both the measured and the calculated spectra have different velocities along different crystallographic directions. In the itinerant theory, it is a consequence of the non-zero ellipticity and the fact that only one electron pocket is involved

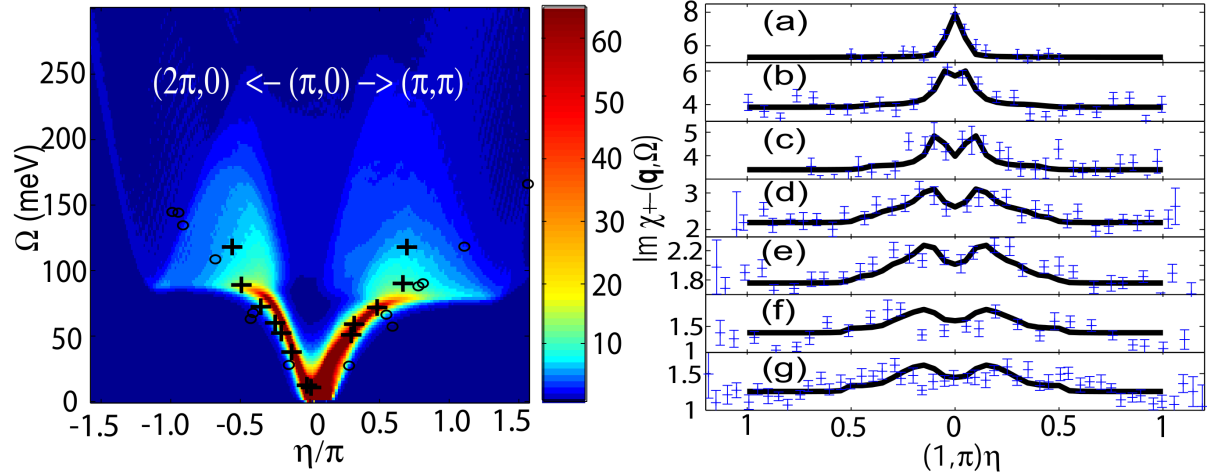


**Figure 6.** Comparison of the calculated spin excitations to experimental data of [49,50]. Taken from [46].

in the SDW formation. Remarkably, for  $\epsilon = 0.5$  ellipticity which agrees with the ARPES data the anisotropy of the spin wave velocities is the same as in the experimental INS data. Another verifiable theory prediction for this range is that the width of the spin-wave peak should scale as  $\Omega^2$ . Additionally, the excitations are still visible even when the spin-waves enter the continuum. In the right panel of Fig. 6 we compare the calculated and the measured  $\text{Im } \chi^{+-}(q, \Omega)$  along  $(0, 0) \rightarrow (\pi, 0) \rightarrow (2\pi, 0)$  direction for different  $\Omega$ . We see that the agreement is quite good even for higher frequencies.

#### 4. Discussion and conclusion

In this review we presented the itinerant description of antiferromagnetism in parent materials of the iron-based superconductors. In contrast to a purely localized scenario this theory allows for a coherent understanding of the full phase diagram of these materials as a function of doping, disorder and pressure. All the magnetic properties such as magnitude of the magnetic moment, selection of the order from the degenerate manifold of the possible ground states, appearance of the Ising nematic order above  $T_N$  and finally the anisotropic spin waves can be well understood and connected to the basic electronic structure of these materials. A particular advantage is the possibility to compute charge and spin response functions in a consistent fashion within a single formalism and for the same set of parameters.

In principle one can draw a phenomenological connection between the itinerant model and the  $J_1 - J_2$  model. First, the relationship between the real-space order parameters  $\mathbf{M}_1$  and  $\mathbf{M}_2$  and the momentum-space order parameters  $\Delta_1$  and  $\Delta_2$  is  $\Delta_1 = \mathbf{M}_1 + \mathbf{M}_2$  and  $\Delta_2 = \mathbf{M}_1 - \mathbf{M}_2$ . The scalar product  $\mathbf{M}_1 \cdot \mathbf{M}_2$  is then the same as  $\Delta_1^2 - \Delta_2^2$  and the nematic coupling is given by  $g = \zeta J_1^2 / J_2$ . Second, in the itinerant approach, the hard constraint  $\mathbf{M}_1^2 = \mathbf{M}_2^2 = 1$  is replaced by the quartic terms, which play the role of soft constraints. We see that the itinerant and the  $J_1 - J_2$  models are indeed quite similar, and in both models the Ising-nematic order results from the  $Z_2$  degeneracy of the stripe magnetic ground state. However, one has to be careful with a description of the spin waves in iron-based superconductors via  $J_1 - J_2$  like models. The original derivation of the  $J_1 - J_2$  model goes back to the single-band Hubbard model with hopping between nearest and next-nearest neighbors. Iron-based superconductors are certainly multi-orbital materials and their localized strong-coupling limit is not exactly known at present. Therefore, spin wave calculations based on the  $J_1 - J_2$  model even taking into account biquadratic couplings have limitations especially at higher energies [51].

Nevertheless, there are also limitations of the itinerant description at present. This concerns the iron chalcogenides  $\text{FeTe}_{1-x}\text{Se}_x$ . The itinerant scenario is applicable in the regime of intermediary Se doping, near the superconducting dome of the  $(x, T)$  phase diagram. In this region, the electronic structure is similar to the one considered in the itinerant model and neutron scattering [52] shows that magnetic fluctuations are peaked at the ordering vectors  $\mathbf{Q}_1 = (\pi, 0)$  and  $\mathbf{Q}_2 = (0, \pi)$ . On the other hand, the itinerant model fails for undoped sample where nesting might be absent and the magnetic order has  $(\pi/2, \pi/2)$  ordering wave vector. The same problem concerns  $\text{A}_x\text{Fe}_{2-x/2}\text{Se}_2$  [A = Cs, K, (Tl, Rb), (Tl, K)] iron-selenide compounds where the electronic structure is still discussed.

Further open issues on the theoretical side which have to be studied are the possible role of spin-orbit coupling, interaction with magnetic and non-magnetic impurities, and the doping dependence. This promises interesting perspectives for future research in the field of iron-based superconductors.

## Acknowledgments

We acknowledge helpful discussions with A. Akbari, Ph. Brydon, R. Fernandes, J. Knolle, P. Hirschfeld, S. Maiti, R. Moessner, J. Schmalian, R. Thomale, M. Vavilov, and W. Rowe.

It is a pleasure for both authors to submit this work to a collection of papers dedicated to 80th birthday of B.I. Kochelaev. The quality of his research, his dedication to physics and high moral standards are guides for many of his more junior colleagues, including us, to follow. We wish Boris Ivanovich happiness and many more productive years.

## References

1. Kamihara Y., Watanabe T., Hirano M., Hosono H. *J. Am. Chem. Soc.* **130**, 3296 (2008)
2. Hirschfeld P.J., Korshunov M.M., Mazin I.I. *Rep. Prog. Phys.* **74**, 124508 (2011)
3. Liu C., Samolyuk G.D., Lee Y., et al. *Phys. Rev. Lett.* **101**, 177005 (2008)
4. Terashima K., Sekiba Y., Bowen J.H., et al. *Proc. Natl. Acad. Sci.* **106**, 7330 (2009)
5. Zabolotnyy V.B., Inosov D.S., Evtushinsky D.V., et al. *Nature* **457**, 569 (2009)
6. Yang L.X., Zhang Y., Ou H.W., et al. *Phys. Rev. Lett.* **102**, 107002 (2009)
7. Lu D.H., Yi M., Mo S.-K., et al. *Nature* **455**, 81 (2008)
8. Ding H., Nakayama K., Richard P., et al. *J. Phys.: Condens. Matter* **23**, 135701 (2011); Richard P., Sato T., Nakayama K., et al. *Rep. Prog. Phys.* **74**, 124512 (2011)
9. Coldea A.I., Fletcher J.D., Carrington A., et al. *Phys. Rev. Lett.* **101**, 216402 (2008); Shishido H., Bangura A.F., Coldea A.I., et al. *Phys. Rev. Lett.* **104**, 057008 (2010)
10. Carrington A. *Rep. Prog. Phys.* **74**, 124507 (2011)
11. Singh D.J., Du M.-H. *Phys. Rev. Lett.* **100**, 237003 (2008)
12. Boeri L., Dolgov O.V., Golubov A.A. *Phys. Rev. Lett.* **101**, 026403 (2008)
13. Fernandes R.M., Chubukov A.V., Knolle J., et al. *Phys. Rev. B* **85**, 024534 (2011)
14. Eremin I., Chubukov A.V. *Phys. Rev. B* **81**, 024511 (2010)
15. Chandra P., Coleman P., Larkin A.I. *Phys. Rev. Lett.* **64**, 88 (1990)
16. Si Q., Abrahams E. *Phys. Rev. Lett.* **101**, 076401 (2008)
17. Xu C., Muller M., Sachdev S. *Phys. Rev. B* **78**, 020501(R) (2008)

18. Yildirim T. *Phys. Rev. Lett.* **101**, 057010 (2008)
19. Uhrig G.S., Holt M., Oitmaa J., et al. *Phys. Rev. B* **79**, 092416 (2009)
20. Nakajima M., Ishida S., Kihou K., et al. *Phys. Rev. B* **81**, 104528 (2010)
21. Rice M.T. *Phys. Rev. B* **2**, 3619 (1970)
22. Keldysh L.V., Kopaev Yu.V. *Sov. Phys. Solid State* **6**, 2219 (1965)
23. Andersen O.K., Boeri L. *Annalen der Physik* **1**, 8 (2011)
24. Liu C., Kondo T., Fernandes R.M., et al. *Nature Physics* **6**, 419 (2010)
25. Pratt D.K., Kim M.G., Kreyssig A., et al. *Phys. Rev. Lett.* **106**, 257001 (2011)
26. Cvetkovic V., Tesanovic Z. *Europhys. Lett.* **85**, 37002 (2009)
27. Chubukov A.V., Efremov D.V., Eremin I. *Phys. Rev. B* **78**, 134512 (2008)
28. Brydon P.M.R., Timm C. *Phys. Rev. B* **80**, 174401 (2009); **79**, 180504(R) (2009)
29. Wang F., Zhai H., Ran Y., et al. *Phys. Rev. Lett.* **102**, 047005 (2009)
30. Platt C., Honerkamp C., Hanke W. *New J. Phys.* **11**, 055058 (2009)
31. de la Cruz C., Huang Q., Lynn J.W., et al. *Nature* **453**, 899 (2008)
32. Klauss H.-H., Luetkens H., Klingeler R., et al. *Phys. Rev. Lett.* **101**, 077005 (2008)
33. Fisher I.R., Degiorgi L., Shen Z.X. *Rep. Prog. Phys.* **74**, 124506 (2011)
34. Chu J.-H., Analytis J.G., De Greve K., et al. *Science* **329**, 824 (2010)
35. Tanatar M.A., Blomberg E.C., Kreyssig A., et al. *Phys. Rev. B* **81**, 184508 (2010)
36. Dusza A., Lucarelli A., Pfuner F., et al. *EPL* **93**, 37002 (2011)
37. Nakajima M., Liang T., Ishida S., et al. *PNAS* **108**, 12238 (2011)
38. Yi M., Lu D., Chu J.-H., et al. *PNAS* **108**, 6878 (2011)
39. Kruger F., Kumar S., Zaanen J., van den Brink J. *Phys. Rev. B* **79**, 054504 (2009)
40. Qi Y., Xu C. *Phys. Rev. B* **80**, 094402 (2009)
41. Fernandes R.M., VanBebber L.H., Bhattacharya S., et al. *Phys. Rev. Lett.* **105**, 157003 (2010)
42. Kasahara S., Shi H.J., Hashimoto K., et al. *Nature* **486**, 382 (2012)
43. Fang C., Yao H., Tsai W.-F., et al. *Phys. Rev. B* **77**, 224509 (2008)
44. Lv W., Krüger F., Phillips P. *Phys. Rev. B* **82**, 045125 (2010)
45. Chen C.-C., Maciejko J., Sorini A.P., et al. *Phys. Rev. B* **82**, 100504 (2010)
46. Knolle J., Eremin I., Chubukov A.V., Moessner R. *Phys. Rev. B* **81**, 140506 (2010)
47. Kemper A.F., Maier T.A., Graser S., et al. *New J. Phys.* **12**, 073030 (2010);  
Maier T.A., Graser S., Scalapino D.J., Hirschfeld P.J. *Phys. Rev. B* **79**, 224510 (2009)
48. Raghu S., Qi X.-L., Liu C.-X., et al. *Phys. Rev. B* **77**, 220503 (2008)
49. Diallo S.O., Antropov V.P., Perring T.G., et al. *Phys. Rev. Lett.* **102** 187206 (2009)
50. Zhao J., Adroja D.T., Yao D.-X., et al. *Nature Physics* **5**, 555 (2009)
51. Ewings R.A., Perring T.G., Gillett J., et al. *Phys. Rev. B* **83**, 214519 (2011)
52. Liu T.J., Hu J., Qian B., et al. *Nature Materials* **9**, 718 (2010)

# Spin response in HTSC cuprates: generalized RPA approach with projection operators method

M.V. Eremin<sup>1,\*</sup>, I.M. Shigapov<sup>1</sup>, I.M. Eremin<sup>1,2</sup>

<sup>1</sup>Kazan Federal University, Kremlevskaya 18, 420008 Kazan, Russia

<sup>2</sup>Institut für Theoretische Physik III, Ruhr-Universität at Bochum, D-44801 Bochum, Germany

\**E-mail: meremin@kpfu.ru*

We derive the dynamical spin susceptibility in the  $t$ - $J$ - $G$  model combining the random phase approximation (RPA) and projection operator method, which allows describing the mutual interplay between the local and the itinerant components of susceptibility. Near the antiferromagnetic wave vector the calculated dispersion of the spin excitations reproduces well the so-called hour-glass dispersion, characteristic for several layered cuprates. It is formed as a result of competition between the original spin-gap in magnon-like excitations spectrum and the superconducting gap, which affects the itinerant component of the susceptibility. Furthermore, the calculated collective spin excitations along  $(0,0)$ - $(0,\pi)$  are in agreement with the positions of the absorption peaks in the inelastic X-ray scattering spectra. They refer to the paramagnon-like modes, characteristic to the itinerant spin system, rather than magnon-like excitations that originate from short range order effect in the system of local spins at Cu sites.

**PACS:** 71.27.+a, 74.72.-h

**Keywords:** HTSC, cuprates, dynamical spin susceptibility, collective spin excitations

## 1. Introduction

The magnetic properties of high-temperature superconductors such as  $\text{YBa}_2\text{Cu}_3\text{O}_{6+y}$  are quite unusual. These materials contain charge carriers, distributed mainly over the oxygen positions in  $\text{CuO}_2$  plane and localized spins at the copper sites. Correspondingly, two approaches are used for the description of the dynamic spin susceptibility. When one starts from overdoped regime, it is naturally to employ the conventional Fermi liquid type description with effective on-site Coulomb repulsion of the carriers at the same site. If one considers the lightly doped regime, both the tendency towards Mott physics and strong antiferromagnetic correlations have to be taken into account. Here we focus on intermediate doping level, when there are both local and itinerant spins, but the system is still uniform. Possible phase separations in underdoped part of the phase diagram and existence of the spin density waves or charge density waves are not considered.

Previously [1, 2], combining projection Mori method and Green's function technique we derived an analytical formula for the spin susceptibility in superconducting cuprates. It allowed to take self consistently into account both the itinerant and the localized components of magnetic susceptibility. However, the spectrum of collective spin excitations, which is in focus of many experimental investigations, was not investigated in details. A dispersion of the collective spin excitations is needed for the construction of the microscopic theory of high temperature superconductivity, at least, when the spin fluctuations mechanism is assumed. In the present paper we systematize our results. We also discuss the possible improvement of the general expression for the spin susceptibility and will present new numerical results for real and imaginary parts of the dynamic spin susceptibility along symmetry routes of Brillouin zone in the normal and superconducting states.

## 2. Model and general expression for susceptibility

The Hamiltonian of the model is written as [1, 2]

$$H = \sum_{i,j,\sigma} t_{ij} \psi_i^{pd,\sigma} \psi_j^{\sigma,pd} + \frac{1}{2} \sum_{i,j} J_{ij} [\mathbf{S}_i \mathbf{S}_j - \frac{n_i n_j}{4}] + \frac{1}{2} \sum_{i,j} G_{ij}^{\infty} \delta_i \delta_j = H_t + H_J + H_G. \quad (1)$$

Here,  $\psi_i^{pd,\sigma}$  ( $\psi_j^{\sigma,pd}$ ) are the creation (annihilation) operators for composite quasiparticles. Symbol pd means that there is a strong coupling between copper and oxygen holes at each Cu-site in Cu-O plane, which is resembled in the formation of the so-called Zhang Rice [3-6] (copper-oxygen) singlet band at strong enough doping level. The second term  $H_J = \frac{1}{2} \sum_{i,j} J_{ij} [\mathbf{S}_i \mathbf{S}_j - \frac{n_i n_j}{4}]$  describes the superexchange interaction between Cu-spins at site  $i$  and  $j$  [7],  $n_i = \psi_i^{\uparrow,\uparrow} + \psi_i^{\downarrow,\downarrow}$  is operator of the number of spins at site  $i$ . The last term refers to screened Coulomb repulsion between doped oxygen holes,  $\delta_i = \psi_i^{pd,pd}$  is the operator of the number of copper-oxygen singlets per one unit cell.

For derivation of the spin susceptibility we employ the Green's function method and projection formalism. It is convenient to start from the equation

$$\omega \langle \langle S_q^+ | S_{-q}^- \rangle \rangle = \sum_{k'} (t_{k'+q} - t_{k'}) \langle \langle \psi_{k'+q}^{\uparrow,pd} \psi_{k'}^{pd,\downarrow} | S_{-q}^- \rangle \rangle + \sum_{j,l} J_{jl} e^{-iqR_j} \langle \langle S_l^+ S_j^z - S_l^z S_j^+ | S_{-q}^- \rangle \rangle. \quad (2)$$

Here it is assumed that  $\langle S_i^z \rangle = 0$  i.e. the long range spin order is absent,  $t_k = \sum_j t_{ij} \exp(i\mathbf{kR}_{ij})$  is usual Fourier transform of the hopping integral. On the right-hand side we get two new Green's functions. The first can be naturally referred to itinerant spins, which accompany the motion of copper-oxygen singlet correlations over Cu-O plane, whereas the second term in Eq. (2) is related to localize spins at Cu-sites.

Linearization of the anticommutator

$$\left[ \sum_{j,l} J_{jl} e^{-iqR_j} (S_l^+ S_j^z - S_l^z S_j^+), H_J \right] \cong \Omega_q^2 S_q^+ \quad (3)$$

was discussed in many papers [8-18], where

$$\Omega_q^2 = 2J_1^2 \alpha |K_1| (2 - \gamma_q) (\Delta_{sp} + 2 + \gamma_q) \quad (4)$$

is the typical expression for collective local spin excitations in layered aniferromagnets,  $\Delta_{sp}$  is dimensionless spin-gap parameter,  $\gamma_q = \cos q_x a + \cos q_y a$ ,  $\alpha$  is decoupling parameter, which is usually calculated self-consistently via the sum rule  $\langle S_i^+ S_i^- \rangle = \frac{1}{2}(1 - \delta)$  which is discussed in Appendix C,  $\delta$  is a number of carriers per one unit cell,  $K_1 = K_{01} = 4\langle S_0^z S_1^z \rangle$  is the spin-spin correlation function of nearest neighbors.

Calculation of the anticommutator  $\left[ \sum_{i,l} J_{il} e^{-iqR_i} (S_l^+ S_i^z - S_l^z S_i^+), H_t \right]$  is given in Appendix A. It is approximated as follows

$$\begin{aligned} & \left[ \sum_{i,l} J_{il} e^{-iqR_i} (S_l^+ S_i^z - S_l^z S_i^+), \sum_{j,m} t_{j,m} \psi_j^{pd,\sigma} \psi_m^{\sigma,pd} \right] \cong \\ & \cong \bar{J}_1 t_1 [2 - \cos q_x a - \cos q_y a] S_q^+ - \frac{1}{2} \sum_k (\bar{J}_{k+q} - \bar{J}_k) (t_{k+q} - t_k) \psi_{k+q}^{\uparrow,pd} \psi_k^{pd,\downarrow}. \end{aligned} \quad (5)$$

Here  $\bar{J}_k = \sum_l \bar{J}_{il} \exp(i\mathbf{k}\mathbf{R}_{il})$  and  $\bar{J}_{il} = J_{il} \langle \psi_i^{pd,\uparrow} \psi_l^{\uparrow,pd} \rangle$ . Angular brackets denote the thermodynamic average.

Using Eqs. (3), (5) we derive the equation for Fourier transform of Green's function as

$$\begin{aligned} \omega \sum_{i,l} J_{il} e^{-iqR_i} \langle \langle [(S_l^+ S_i^z - S_l^z S_i^+), H_t + H_J] | S_{-q}^- \rangle \rangle = \\ - \frac{i}{\pi} \bar{J}_1 K_1 (2 - \gamma_q) + \{ \Omega_q^2 + \bar{J}_1 t_1 [2 - \cos q_x a - \cos q_y a] \} \langle \langle S_q^+ | S_{-q}^- \rangle \rangle \\ - \frac{1}{2} \sum_k (\bar{J}_{k+q} - \bar{J}_k) (t_{k+q} - t_k) \langle \langle \psi_{k+q}^{\uparrow,pd} \psi_k^{pd,\downarrow} | S_{-q}^- \rangle \rangle. \end{aligned} \quad (6)$$

Applying projection method as it was described in Ref. [1] we write

$$\begin{aligned} i \frac{\partial \psi_k^{\uparrow,pd}}{\partial t} = \varepsilon_k \psi_k^{\uparrow,pd} + \Delta_k^{\uparrow} \psi_{-k}^{pd,\downarrow} + \frac{1}{N} \sum_q t'_{k-q} \psi_{k-q}^{\downarrow,pd} S_q^+ \\ - \frac{1}{2N} \sum_q J_q \psi_{k-q}^{\downarrow,pd} S_q^+ + \frac{1}{2N} \sum_q G'_q (\psi_{k-q}^{\uparrow,pd} \psi_q^{pd,pd} + \psi_q^{pd,pd} \psi_{k-q}^{\uparrow,pd}). \end{aligned} \quad (7)$$

The expression for the energy of quasiparticles is written as [1, 2]

$$\varepsilon_k = \sum_l \{ t_{lj} [P + (1 + 2F_{jl}^t) \langle S_j^z S_l^z \rangle / P] - \frac{2G_{jl} F_{jl}^G + J_{jl} F_{jl}^J}{1 + \delta} \langle \psi_l^{pd,\uparrow} \psi_j^{\uparrow,pd} \rangle \} e^{ikR_{jl}}. \quad (8)$$

Here,  $P = (1 + \delta)/2$ ,  $F_{jl}^t$  is projection parameter, which will be calculated later via a number of holes per one unit cell  $\delta$  and spin-spin correlation function  $\langle S_j^z S_l^z \rangle$ . It is interesting to compare the quantity in square brackets with Gutzwiller's projection factor  $2\delta/(1 + \delta)$ , which was introduced for the phenomenological description of the doping dependent bandwidth [19]. In contrast to Hubbard 1 approximation for  $\delta \rightarrow 0$  the bandwidth shrinks to zero. The same result gives expression  $P + (1 + 2F_{jl}^t) \langle S_j^z S_l^z \rangle / P$ . For this particular case one expects that the spin-spin correlation for nearest neighbors on the square lattice will be given by  $\langle S_0^z S_1^z \rangle \cong -1/4$  and  $F_1 \rightarrow 0$ . Note that the role of the last term in the bracket (8) at  $\delta \cong 0.2$  is relatively small.

The superconducting gap equation is given by [1, 2]

$$\begin{aligned} \Delta_k = \frac{1}{PN} \sum_{k'} \left( \frac{1}{2} J_{k-k'} \langle \psi_{k'}^{\uparrow,pd} \psi_{-k'}^{\downarrow,pd} \rangle - G'_{k-k'} \langle \psi_{k'}^{\uparrow,pd} \psi_{-k'}^{\downarrow,pd} \rangle \right. \\ \left. + t_{k'} \langle \psi_{k'}^{\downarrow,pd} \psi_{-k'}^{\uparrow,pd} \rangle - t'_{k'} \langle \psi_{k'}^{\uparrow,pd} \psi_{-k'}^{\downarrow,pd} \rangle \right), \end{aligned} \quad (9)$$

where  $t'_k = \sum_l t_{jl} F_{jl}^t \exp(i\mathbf{k}\mathbf{R}_{jl})$  is Fourier transform of the reduced hopping integral and  $G_q = G_q^\infty - J_1/4$ . The analysis of this equation for  $J_{k-k'} > 2G_{k-k'}$ , which we assume hereafter, reveals  $\Delta_k = \Delta(T)(\cos k_x a - \cos k_y a)/2$ . Having expression (7) one can construct the equation for functions  $\langle \langle \psi_{k'+q}^{\uparrow,pd} \psi_{k'}^{pd,\downarrow} | S_{-q}^- \rangle \rangle$  and  $\langle \langle \psi_{k'}^{pd,\downarrow} \psi_{k'+q}^{\uparrow,pd} | S_{-q}^- \rangle \rangle$ , which enter in (2) and (5). However, one has to be careful because the rule of differentiation of product composite operators, as it was pointed in Ref. [10], is different from the usual case. Before applying expression (7) we write the following relations

$$\psi_{k+q}^{\uparrow,pd} \psi_k^{pd,\downarrow} = \frac{1}{N} \sum_{i,j} \psi_i^{\uparrow,pd} \psi_j^{pd,\downarrow} (1 - \delta_{ij}) e^{-i(k+q)R_i + ikR_j} + \frac{1}{N} S_q^+, \quad (10)$$

$$\psi_k^{pd,\downarrow} \psi_{k+q}^{\uparrow,pd} = \frac{1}{N} \sum_{i,j} \psi_i^{\uparrow,pd} \psi_j^{pd,\downarrow} (1 - \delta_{ij}) e^{-i(k+q)R_i + ikR_j}. \quad (11)$$

Then carry out the differentiation of operators with lattices index (site representation) and taking into account (10) and (11) one gets

$$\begin{aligned} \omega \langle \langle \psi_{k+q}^{\uparrow,pd} \psi_k^{pd,\downarrow} | S_{-q}^- \rangle \rangle &= \frac{i}{2\pi} \left( \langle \psi_{k+q}^{\uparrow,pd} \psi_{k+q}^{pd,\uparrow} \rangle - \langle \psi_k^{\downarrow,pd} \psi_k^{pd,\downarrow} \rangle \right) \\ &+ (\varepsilon_{k+q} - \varepsilon_k) \langle \langle \psi_{k+q}^{\uparrow,pd} \psi_k^{pd,\downarrow} | S_{-q}^- \rangle \rangle \\ &- \frac{1}{N} \left( [F_J \frac{1}{2} J_q - t_k (1 - F_t)] \langle \psi_k^{\downarrow,pd} \psi_k^{pd,\downarrow} \rangle \right. \\ &- [F_J \frac{1}{2} J_q - t_{k+q} (1 - F_t)] \langle \psi_{k+q}^{\uparrow,pd} \psi_{k+q}^{pd,\uparrow} \rangle \left. \right) \langle \langle S_q^+ | S_{-q}^- \rangle \rangle \\ &- \frac{1}{N} \sum_{k'} (\varepsilon_{k'+q} - \varepsilon_{k'}) \langle \langle \psi_{k'+q}^{\uparrow,pd} \psi_{k'}^{pd,\downarrow} | S_{-q}^- \rangle \rangle + \frac{\omega}{N} \langle \langle S_q^+ | S_{-q}^- \rangle \rangle, \end{aligned} \quad (12)$$

$$\begin{aligned} \omega \langle \langle \psi_k^{pd,\downarrow} \psi_{k+q}^{\uparrow,pd} | S_{-q}^- \rangle \rangle &= \frac{i}{2\pi} \left( \langle \psi_{k+q}^{pd,\uparrow} \psi_{k+q}^{\uparrow,pd} \rangle - \langle \psi_k^{pd,\downarrow} \psi_k^{\downarrow,pd} \rangle \right) \\ &+ (\varepsilon_{k+q} - \varepsilon_k) \langle \langle \psi_k^{pd,\downarrow} \psi_{k+q}^{\uparrow,pd} | S_{-q}^- \rangle \rangle \\ &- \frac{1}{N} \left( [F_J \frac{1}{2} J_q - t_k (1 - F_t)] \langle \psi_k^{pd,\downarrow} \psi_k^{\downarrow,pd} \rangle \right. \\ &- [F_J \frac{1}{2} J_q - t_{k+q} (1 - F_t)] \langle \psi_{k+q}^{pd,\uparrow} \psi_{k+q}^{\uparrow,pd} \rangle \left. \right) \langle \langle S_q^+ | S_{-q}^- \rangle \rangle \\ &- \frac{1}{N} \sum_{k'} (\varepsilon_{k'+q} - \varepsilon_{k'}) \langle \langle \psi_{k'}^{pd,\downarrow} \psi_{k'+q}^{\uparrow,pd} | S_{-q}^- \rangle \rangle. \end{aligned} \quad (13)$$

These equations are rewritten as follows [2]

$$\langle \langle \psi_k^{pd,\downarrow} \psi_{k+q}^{\uparrow,pd} | S_{-q}^- \rangle \rangle = \frac{i}{2\pi} \chi_{k,q} + \frac{1}{N} \eta'_{k,q} \langle \langle S_q^+ | S_{-q}^- \rangle \rangle + \frac{1}{N} \zeta_{k,q} D'(\omega, q), \quad (14)$$

$$\langle \langle \psi_{k+q}^{\uparrow,pd} \psi_k^{pd,\downarrow} | S_{-q}^- \rangle \rangle = -\frac{i}{2\pi} \chi_{k,q} - \frac{1}{N} \eta''_{k,q} \langle \langle S_q^+ | S_{-q}^- \rangle \rangle - \frac{1}{N} \zeta_{k,q} D''(\omega, q). \quad (15)$$

Here

$$\begin{aligned} \chi_{k,q} &= \frac{n_{k+q} - n_k}{\omega + \varepsilon_k - \varepsilon_{k+q}}, \quad \eta'_{k,q} = \frac{1}{2} J_q \chi_{k,q} - \frac{t'_{k+q} n_{k+q} - t'_k n_k}{\omega + \varepsilon_k - \varepsilon_{k+q}}, \\ \zeta_{k,q} &= \frac{1}{\omega + \varepsilon_k - \varepsilon_{k+q}}, \quad \eta''_{k,q} = \eta'_{k,q} + \frac{P(t'_{k+q} - t'_k) - \omega}{\omega + \varepsilon_k - \varepsilon_{k+q}}, \end{aligned} \quad (16)$$

$n_k = Pf(\varepsilon_k)$  are occupation numbers,  $f(\varepsilon_k)$  is Fermi function. New Green's functions, which are appeared on right-hand side (14) and (15) are:

$$D'(\omega, q) = - \sum_k (\varepsilon_{k+q} - \varepsilon_k) \langle \langle \psi_k^{pd,\downarrow} \psi_{k+q}^{\uparrow,pd} | S_{-q}^- \rangle \rangle, \quad (17)$$

$$D''(\omega, q) = \sum_k (\varepsilon_{k+q} - \varepsilon_k) \langle \langle \psi_{k+q}^{\uparrow,pd} \psi_k^{pd,\downarrow} | S_{-q}^- \rangle \rangle. \quad (18)$$

To compute these functions the following exact relations are used [1, 2]

$$\sum_k \psi_k^{pd,\downarrow} \psi_{k+q}^{\uparrow,pd} = 0, \quad (19)$$

$$\sum_k \psi_{k+q}^{\uparrow,pd} \psi_k^{pd,\downarrow} = \sum_i S_i^+ e^{-iqR_i} = S_q^+. \quad (20)$$

Combining Eqs. (14), (15) and (19), (20) one finds

$$D'(\omega, q) = - \left\{ \frac{iN}{2\pi} \chi(\omega, q) + \eta'(\omega, q) \langle\langle S_q^+ | S_{-q}^- \rangle\rangle \right\} / \zeta(\omega, q) \quad (21)$$

and

$$D''(\omega, q) = - \left\{ \frac{iN}{2\pi} \chi(\omega, q) + [1 + \eta''(\omega, q)] \langle\langle S_q^+ | S_{-q}^- \rangle\rangle \right\} / \zeta(\omega, q). \quad (22)$$

Here,

$$\begin{aligned} \chi(\omega, q) &= \frac{1}{N} \sum_k \chi_{k,q}, & \eta'(\omega, q) &= \frac{1}{N} \sum_k \eta'_{k,q}, \\ \zeta(\omega, q) &= \frac{1}{N} \sum_k \zeta_{k,q}, & \eta''(\omega, q) &= \frac{1}{N} \sum_k \eta''_{k,q}. \end{aligned} \quad (23)$$

Taking into account that  $\sum_k (\varepsilon_{k+q} - \varepsilon_k) = 0$ , it is easy to prove that  $D'(\omega, q) = D''(\omega, q)$  and derive the relation [2]

$$F_{ij}^t = \frac{|K_{ij}|}{(1 + \delta)^2 - 2|K_{ij}|}. \quad (24)$$

Substituting  $D''(\omega, q)$  functions in (15) we get

$$\begin{aligned} \langle\langle \psi_{k+q}^{\uparrow,pd} \psi_k^{pd,\downarrow} | S_{-q}^- \rangle\rangle &= -\frac{i}{2\pi} \left[ \chi_{k,q} - \frac{\zeta_{k,q}}{\zeta(\omega, q)} \chi(\omega, q) \right] \\ &+ \frac{1}{N} \left( [1 + \eta''(\omega, q)] \frac{\zeta_{k,q}}{\zeta(\omega, q)} - \eta''_{k,q} \right) \langle\langle S_q^+ | S_{-q}^- \rangle\rangle. \end{aligned} \quad (25)$$

Then multiplying (2) by frequency and using Eq. (5) we find

$$\begin{aligned} \{ \omega^2 - \Omega_q^2 - \bar{J}_1 t_1 [2 - \cos q_x a - \cos q_y a] \} \langle\langle S_q^+ | S_{-q}^- \rangle\rangle &= -\frac{i}{2\pi} 2J_1 K_1 (2 - \gamma_q) \\ &- \frac{1}{2} \sum_k (\bar{J}_{k+q} - \bar{J}_k) (t_{k+q} - t_k) \langle\langle \psi_{k+q}^{\uparrow,pd} \psi_k^{pd,\downarrow} | S_{-q}^- \rangle\rangle \\ &+ \omega \sum_{k'} (t_{k'+q} - t_{k'}) \langle\langle \psi_{k'+q}^{\uparrow,pd} \psi_{k'}^{pd,\downarrow} | S_{-q}^- \rangle\rangle \\ &= -\frac{i}{\pi} J_1 K_1 (2 - \gamma_q) - \frac{1}{2} \sum_k (\bar{J}_{k+q} - \bar{J}_k - 2\omega) (t_{k+q} - t_k) \langle\langle \psi_{k+q}^{\uparrow,pd} \psi_k^{pd,\downarrow} | S_{-q}^- \rangle\rangle. \end{aligned} \quad (26)$$

Substituting here the expression for  $\langle\langle \psi_{k+q}^{\uparrow,pd} \psi_k^{pd,\downarrow} | S_{-q}^- \rangle\rangle$  function as given by (25), we get the equation

$$\begin{aligned} (\omega^2 - \Omega_q^2 - \bar{t}_1 J_1 [2 - \cos q_x a - \cos q_y a]) \langle\langle S_q^+ | S_{-q}^- \rangle\rangle &= \\ = -\frac{iN}{2\pi} \left[ 2J_1 K_1 (2 - \gamma_q) + \frac{\chi}{\zeta} \zeta_{tJ} - \chi_{tJ} \right] - \left[ (1 + \eta'') \frac{\zeta_{tJ}}{\zeta} - \eta''_{tJ} \right] \langle\langle S_q^+ | S_{-q}^- \rangle\rangle. \end{aligned} \quad (27)$$

Since  $N\chi_{total}^{+,-}(\omega, q) = 2\pi i \langle\langle S_q^+ | S_{-q}^- \rangle\rangle$  for the dynamical spin susceptibility per one unit cell we get

$$\chi_{total}^{+,-} = \frac{\chi\zeta_{tJ} + [2J_1K_1(2 - \gamma_q) - \chi_{tJ}]\zeta}{[1 + \eta'']\zeta_{tJ} + [\omega^2 - \Omega_q^2 - \bar{J}_1t_1(2 - \gamma_q) - \eta''_{tJ}]\zeta}. \quad (28)$$

Here the symbol  $(\omega, q)$ , which accompanies the functions  $\chi, \zeta, \eta$ , is dropped for short. The new functions with index  $tJ$  are:

$$\chi_{tJ}(\omega, q) = \frac{1}{2N} \sum_k (t_{k+q} - t_k) [\bar{J}_{k+q} - \bar{J}_k - 2\omega] \chi_{kq}, \quad (29)$$

$$\eta''_{tJ}(\omega, q) = \frac{1}{2N} \sum_k (t_{k+q} - t_k) [\bar{J}_{k+q} - \bar{J}_k - 2\omega] \eta''_{kq}, \quad (30)$$

$$\zeta_{tJ}(\omega, q) = \frac{1}{2N} \sum_k (t_{k+q} - t_k) [\bar{J}_{k+q} - \bar{J}_k - 2\omega] \zeta_{kq}. \quad (31)$$

The expression (28) can be rewritten also as follows

$$\chi_{total}^{+,-} = \frac{\chi\zeta_{tJ} + [2J_1K_1(2 - \gamma_q) - \chi_{tJ}]\zeta}{[1 + \lambda]\zeta_{tJ} + [\omega^2 - \Omega_q^2 - \bar{J}_1t_1(2 - \gamma_q) - \lambda_{tJ}]\zeta}, \quad (32)$$

where  $\lambda = \eta'' - \omega\zeta$  (this is a function like defined in [20]):

$$\begin{aligned} \lambda_{k,q} &= \eta'_{k,q} + \frac{P(t'_{k+q} - t'_k)}{\omega + \varepsilon_k - \varepsilon_{k+q}}, \\ \lambda &= \lambda(\omega, q) = \frac{1}{N} \sum_k \lambda_{k,q}, \\ \lambda_{tJ}(\omega, q) &= \frac{1}{2N} \sum_k (t_{k+q} - t_k) [\bar{J}_{k+q} - \bar{J}_k - 2\omega] \lambda_{kq}. \end{aligned}$$

It seems this form is more convenient for numerical calculations. Another form for susceptibility, which has more clear properties under electron-hole transformation, is discussed in Appendix B. Note that in numerical calculations the substitution  $\omega \rightarrow \omega + i\Gamma$  is assumed in all entering functions.  $\Gamma$  is dumping factor, which can be anisotropic along the Fermi contour. Factor  $[1 + \lambda]$  in denominator (32) reminds the corresponding Stoner's factor in random phase approximation schema (RPA) for itinerant electron system. On the other hand, the quantity  $[\Omega_q^2 - \omega^2 + \bar{J}_1t_1(2 - \gamma_q) + \lambda_{tJ}]$  is typical for localized spin-subsystem. Collective spin excitations are determined by equation

$$[1 + \lambda] \frac{\zeta_{tJ}}{\zeta} \zeta_{tJ} + [\omega^2 - \Omega_q^2 - \bar{J}_1t_1(2 - \gamma_q) - \lambda_{tJ}] = 0. \quad (33)$$

Therefore, local spin excitations (magnon-like) and itinerant holes (paramagnon-like) are coupled to each other self-consistently. In other words the total susceptibility (32) can be considered as a possible variant of description magnetic susceptibility compounds with interplay between local and itinerant spin subsystems.

### 3. Superconducting state

The expression for spin response function (32) retains its form in superconducting state as well. The entering functions, of course, modify due to Bogolyubov transformations in the superconducting state. The method of calculation can be found in Ref. [1]. The  $\chi(\omega, q)$  function at  $T < T_c$  is written like in BSC theory, except additional factor by  $P = (1 + \delta)/2$ :

$$\begin{aligned} \chi(\omega, q) = & \frac{P}{N} \sum S_{xx} \frac{f_{k+q} - f_k}{\omega + i\Gamma + E_k - E_{k+q}} + \frac{P}{N} \sum S_{yy} \frac{f_k - f_{k+q}}{\omega + i\Gamma - E_k + E_{k+q}} \\ & + \frac{P}{N} \sum S_{yx}^{(-)} \frac{f_k + f_{k+q} - 1}{\omega + i\Gamma - E_k - E_{k+q}} + \frac{P}{N} \sum S_{xy}^{(+)} \frac{1 - f_k - f_{k+q}}{\omega + i\Gamma + E_k + E_{k+q}}, \end{aligned} \quad (34)$$

$f_k = \{1 + \exp[E_k/k_B T]\}^{-1}$  is the usual Fermi function. For the sake of simplicity, we are using the following abbreviation for the coherence factors:

$$\begin{aligned} S_{xx} &= x_k x_{k+q} + z_k z_{k+q}, & S_{yy} &= y_k y_{k+q} + z_k z_{k+q}, \\ S_{yx}^{(+)} &= x_k y_{k+q} - z_k z_{k+q}, & S_{xy}^{(-)} &= y_k x_{k+q} - z_k z_{k+q}, \end{aligned} \quad (35)$$

where

$$\begin{aligned} x_k &= \frac{1}{2} \left[ 1 + \frac{\varepsilon_k - \mu}{E_k} \right], & y_k &= \frac{1}{2} \left[ 1 - \frac{\varepsilon_k - \mu}{E_k} \right], \\ z_k &= \frac{\Delta_k}{2E_k}, & E_k &= \sqrt{(\varepsilon_k - \mu)^2 + |\Delta_k|^2}. \end{aligned} \quad (36)$$

The function  $\lambda(\omega, q)$  is written as [20]

$$\begin{aligned} \lambda(\omega, q) = & \frac{1}{2} J_q F_J \chi(\omega, q) \\ & - \frac{P}{N} \left( \sum S_{xx} \frac{t'_{k+q}(f_{k+q} - 1) - t'_k(f_k - 1)}{\omega + i\Gamma + E_k - E_{k+q}} + \sum S_{yy} \frac{t'_k f_k - t'_{k+q} f_{k+q}}{\omega + i\Gamma - E_k + E_{k+q}} \right. \\ & \left. + \sum S_{yx}^{(-)} \frac{t'_k f_k - t'_{k+q}(1 - f_{k+q})}{\omega + i\Gamma - E_k - E_{k+q}} + \sum S_{xy}^{(+)} \frac{t'_k(1 - f_k) - t'_{k+q} f_{k+q}}{\omega + i\Gamma + E_k + E_{k+q}} \right). \end{aligned} \quad (37)$$

Physically last term in Eq. (37) corresponds to an effective molecular field of kinematic origin. It is strong correlation effect, because in our case the anticommutate relations are different from conventional Fermi liquid.

The function  $\zeta(\omega, q)$  is written as follows:

$$\begin{aligned} \zeta(\omega, q) = & \frac{1}{N} \sum \frac{S_{xx}}{\omega + i\Gamma + E_k - E_{k+q}} + \frac{1}{N} \sum \frac{S_{yy}}{\omega + i\Gamma - E_k + E_{k+q}} \\ & + \frac{1}{N} \sum \frac{S_{yx}^{(-)}}{\omega + i\Gamma - E_k - E_{k+q}} + \frac{1}{N} \sum \frac{S_{xy}^{(+)}}{\omega + i\Gamma + E_k + E_{k+q}}. \end{aligned} \quad (38)$$

Let us now for the moment assume that we do not have any conduction electrons (holes). Substituting zero instead Fermi functions, from expression (26) one gets

$$\chi_{local}^{+,-}(\omega, q) = \frac{-2J_1 K_1 (2 - c_q)}{\Omega_q^2 - \omega^2}. \quad (39)$$

This expression is identical to those found by many authors for lightly doped cuprates [8-17]. It is remarkable that magnetism of localized spins at  $T < T_c$  is strongly suppressed “or in other words frozen out” due to the superconducting gap, which naturally incorporated in function  $\zeta(\omega, q)$ . In opposite limit, when spin-spin correlation functions are small, and conducting bandwidth is

large enough and correspondently function  $\zeta(\omega, q)$  is small the expression (32) corresponds to generalized random phase approximation (GRPA) schema [21-23]. Moreover, in limit  $q \rightarrow 0$ ,  $\omega \rightarrow 0$  the expression (32) converts to static susceptibility expression, which corresponds to those one, which was derived in Ref. [24], beyond Green's function method.

#### 4. Numerical results

Calculated imaginary and real parts of susceptibility along triangle contour in Brillouin zone are displayed in Figs. 1-10. The chosen parameters are:  $\Gamma = 4meV$ ,  $\delta = 0.33$ . We have neglected  $J_2$  and  $K_2$  as they are small numerically. The energy dispersion was chosen according to photoemission data [25]

$$\varepsilon_k = 2t_1(\cos k_x a + \cos k_y a) + 4t_2 \cos k_x a \cos k_y a - \mu, \quad (40)$$

where (in meV):  $t_1 = 139$ ,  $t_2 = -33$ ,  $\mu = 88$ . The superconducting gap function was set in agreement with analyzes of the temperature dependencies of nuclear relaxation rate, Knight shift and superfluid density, which were discussed in Ref. [23] and [26];

$$\Delta_k = \frac{\Delta_0}{2}(\cos k_x a - \cos k_y a) \tanh \left( 1.76 \sqrt{T_c/T - 1} \right). \quad (41)$$

The decoupling parameters  $\alpha$ ,  $\beta$  and  $F_J$  below (except of specific cases in Fig. 9 ) were set by 1.

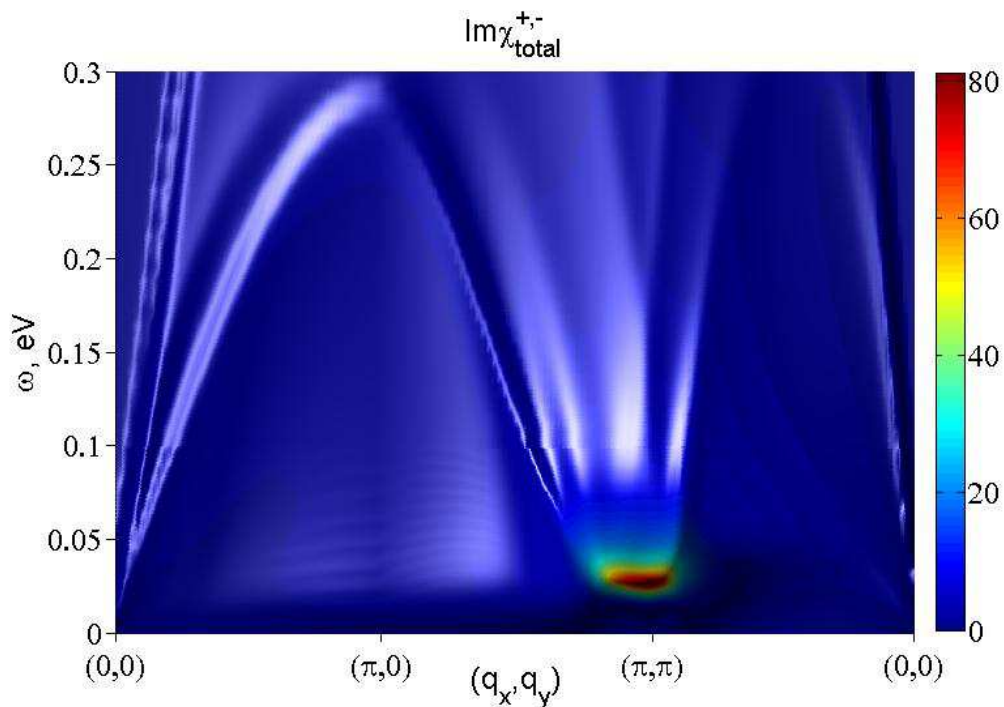


**Figure 1.** Imaginary part of the dynamical susceptibility for the normal state. Input values are:  $T = 100$  K,  $J_1 = 66$  meV,  $K_1 = -0.2$ ,  $\Delta_{sp} = 0.1$ ,  $F_t = 0.1$ . Upward dispersion can be interpreted as a damped magnon-like collective spin excitations. Vertical scale is in  $1/eV$ .

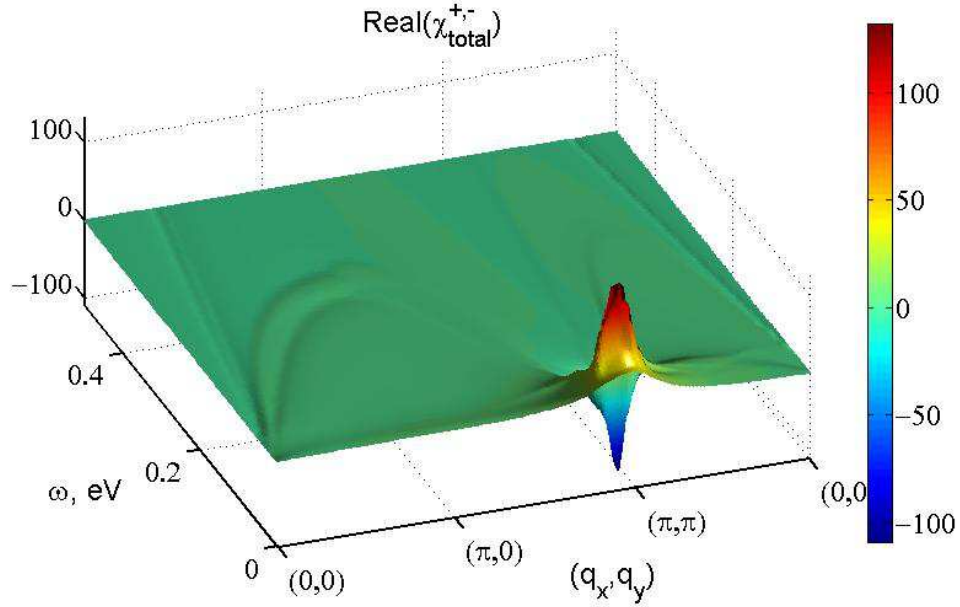


**Figure 2.** The real part of the dynamical spin susceptibility for the superconducting state. Input values are:  $T = 10$  K,  $\Delta_0 = 25$  meV,  $J_1 = 66$  meV,  $K_1 = -0.2$ ,  $\Delta_{sp} = 0.14$ ,  $F_t = 0.1$ . Vertical scale is in  $1/\text{eV}$ .

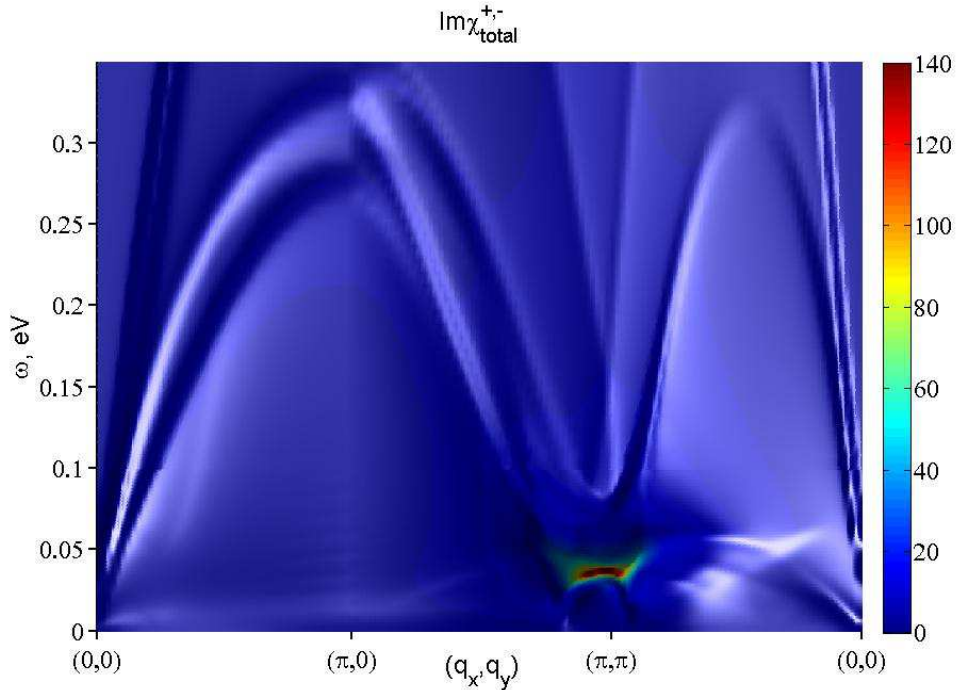


**Figure 3.** The imaginary part of the dynamical spin susceptibility for the superconducting state. Input values are:  $T = 10$  K,  $\Delta_0 = 25$  meV,  $J_1 = 66$  meV,  $K_1 = -0.2$ ,  $\Delta_{sp} = 0.14$ ,  $F_t = 0.1$ . Vertical scale is in  $1/\text{eV}$ .

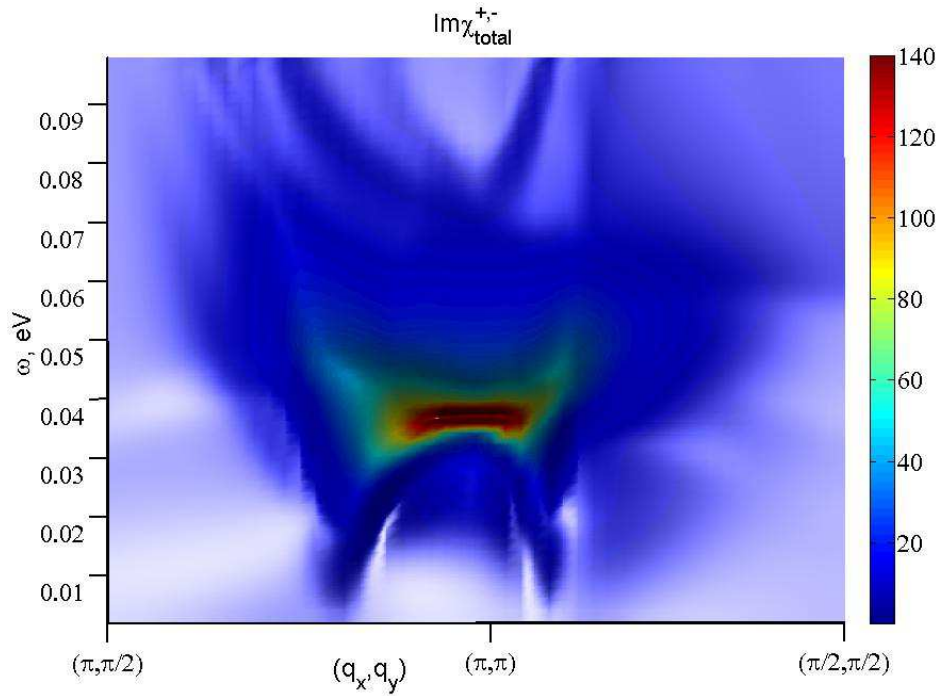


**Figure 4.** Zoomed in region of point the imaginary part of the spin susceptibility for the superconducting state. This area is usually probed by inelastic neutron scattering [27-33]. Input values are:  $T = 10$  K,  $\Delta_0 = 25$  meV,  $J_1 = 66$  meV,  $K_1 = -0.2$ ,  $\Delta_{sp} = 0.14$ ,  $F_t = 0.1$ . Vertical scale is in  $1/eV$ .

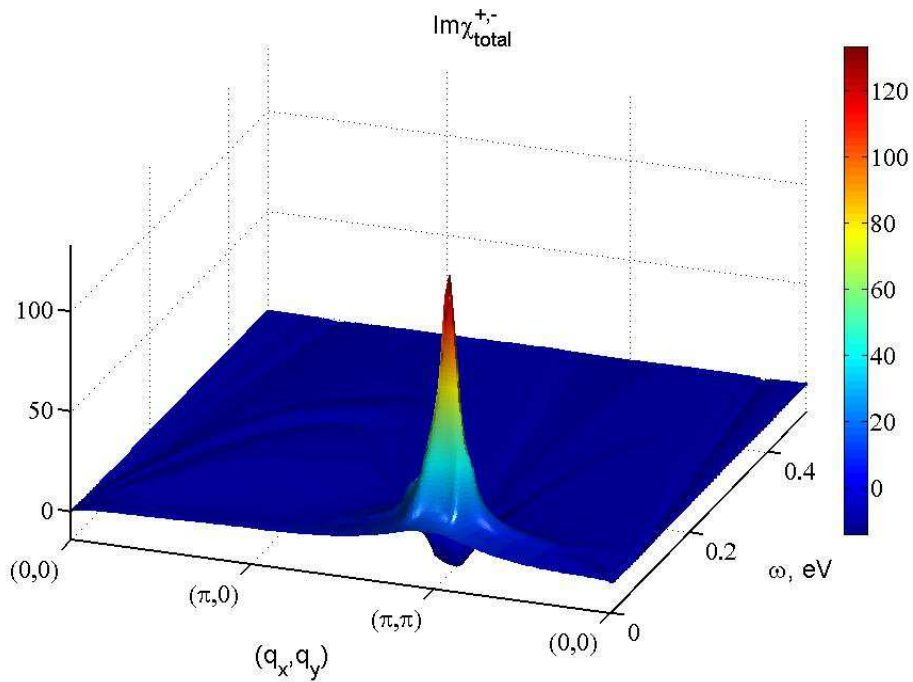


**Figure 5.** Real part of the spin susceptibility for the superconducting state. Input values are:  $T = 10$  K,  $\Delta_0 = 30$  meV,  $J_1 = 66$  meV,  $K_1 = -0.2$ ,  $\Delta_{sp} = 0.14$ ,  $F_t = 0.1$ . Vertical scale is in  $1/eV$ .

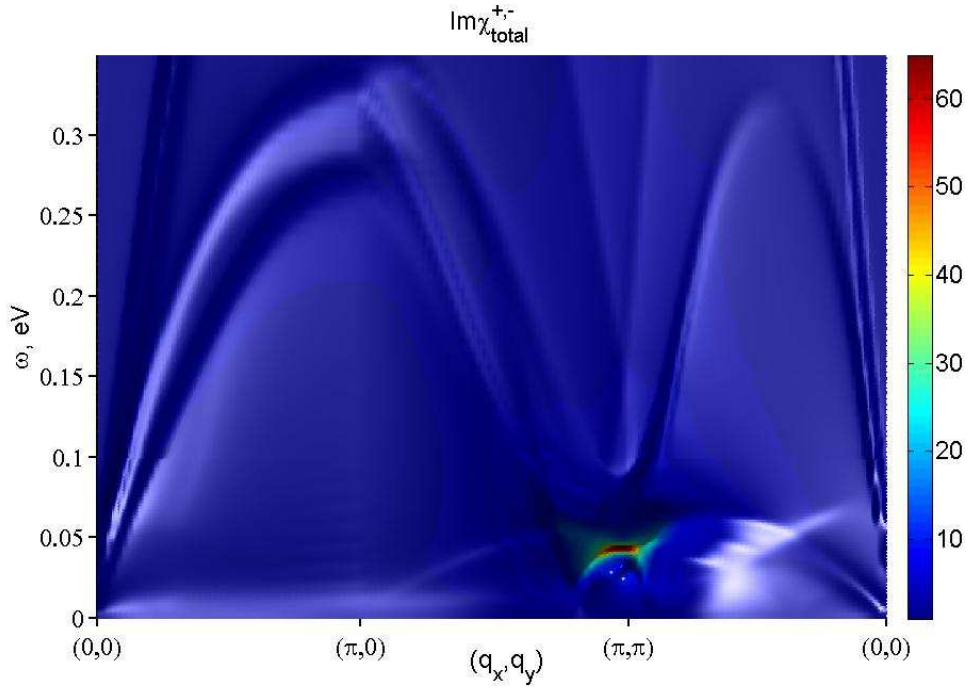


**Figure 6.** Imaginary part of the spin susceptibility for the superconducting state. Input values are:  $T = 10$  K,  $\Delta_0 = 30$  meV,  $J_1 = 66$  meV,  $K_1 = -0.2$ ,  $\Delta_{sp} = 0.14$ ,  $F_t = 0.1$ . Vertical scale is in  $1/\text{eV}$ .

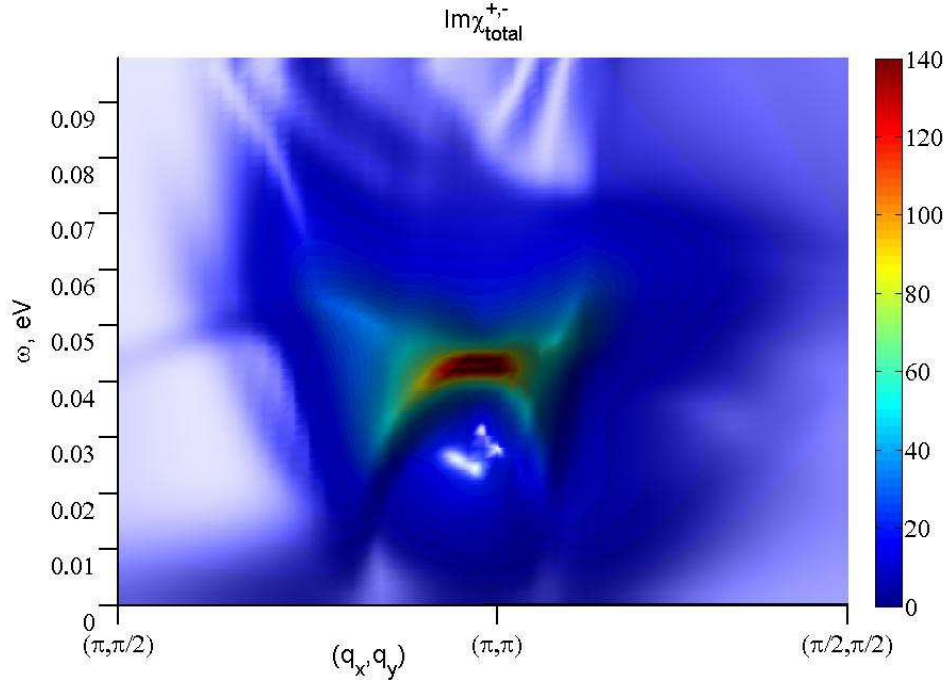


**Figure 7.** The imaginary part of the spin susceptibility for the superconducting state in region of  $(\pi, \pi)$  point. This region is usually probed by inelastic neutron scattering [27-33]. Input values are:  $T = 10$  K,  $\Delta_0 = 30$  meV,  $J_1 = 66$  meV,  $K_1 = -0.2$ ,  $\Delta_{sp} = 0.14$ ,  $F_t = 0.1$ . Vertical scale is in  $1/\text{eV}$ .

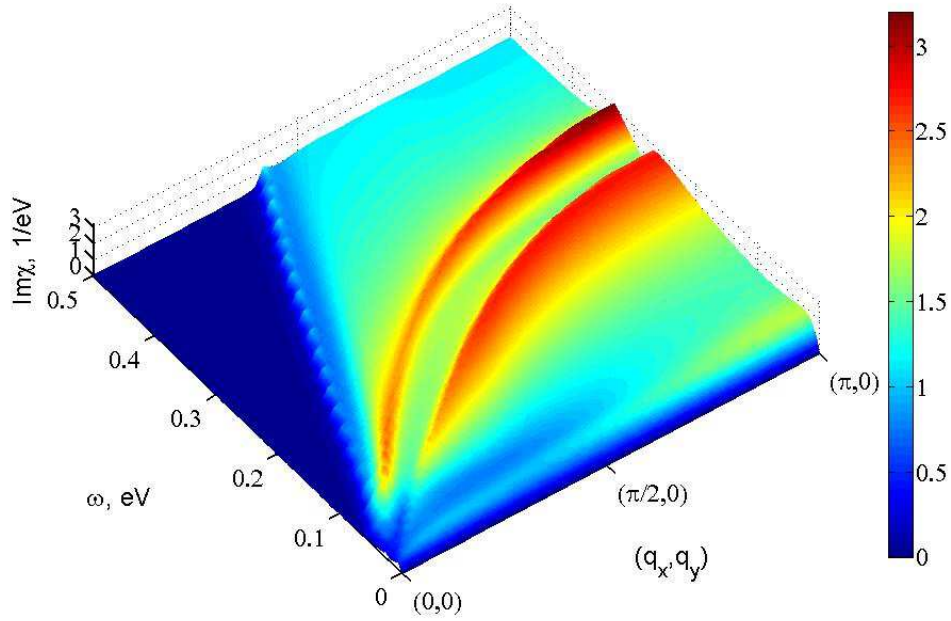


**Figure 8.** Fragment of imaginary part susceptibility in superconducting state along the line in Brillouin zone. This region is studied by resonance inelastic X-ray scattering (RIXS) [34-38]. Input values are:  $T = 10\text{ K}$ ,  $\Delta_0 = 30\text{ meV}$ ,  $J_1 = 66\text{ meV}$ ,  $K_1 = -0.2$ ,  $\Delta_{sp} = 0.14$ ,  $F_t = 0.1$ . Vertical scale is in  $1/\text{eV}$ .

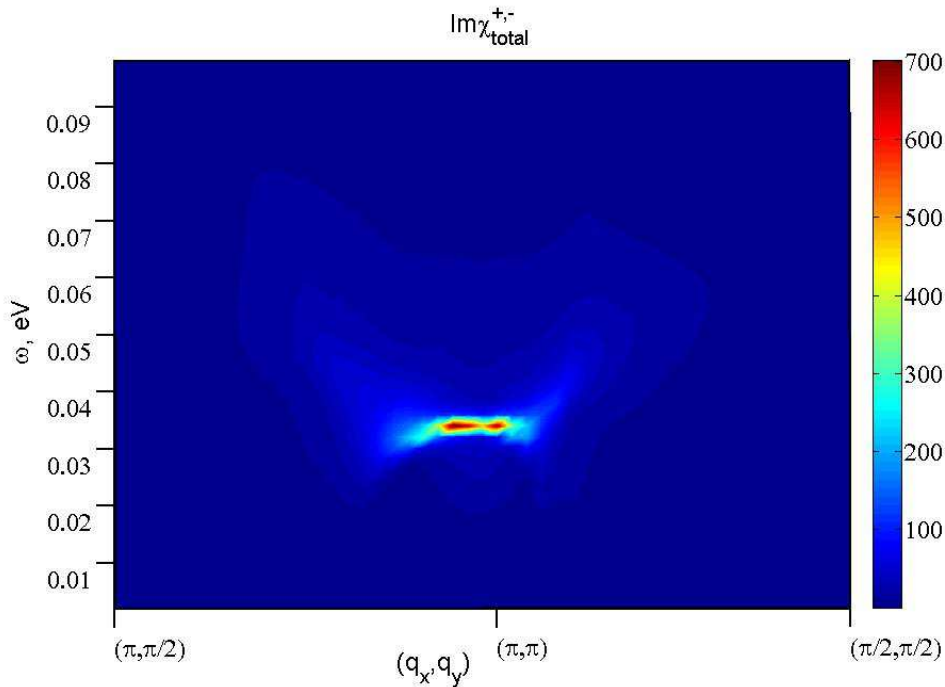


**Figure 9.** Fragment of the imaginary part of the spin susceptibility for the superconducting state near  $(\pi, \pi)$  point. Input values are:  $T = 10\text{ K}$ ,  $\Delta_0 = 25\text{ meV}$ ,  $J_1 = 70\text{ meV}$ ,  $K_1 = -0.2$ ,  $\Delta_{sp} = 0.147$ ,  $F_t = 0.1$ ,  $\beta = 0.6$ . Vertical scale is in  $1/\text{eV}$ .

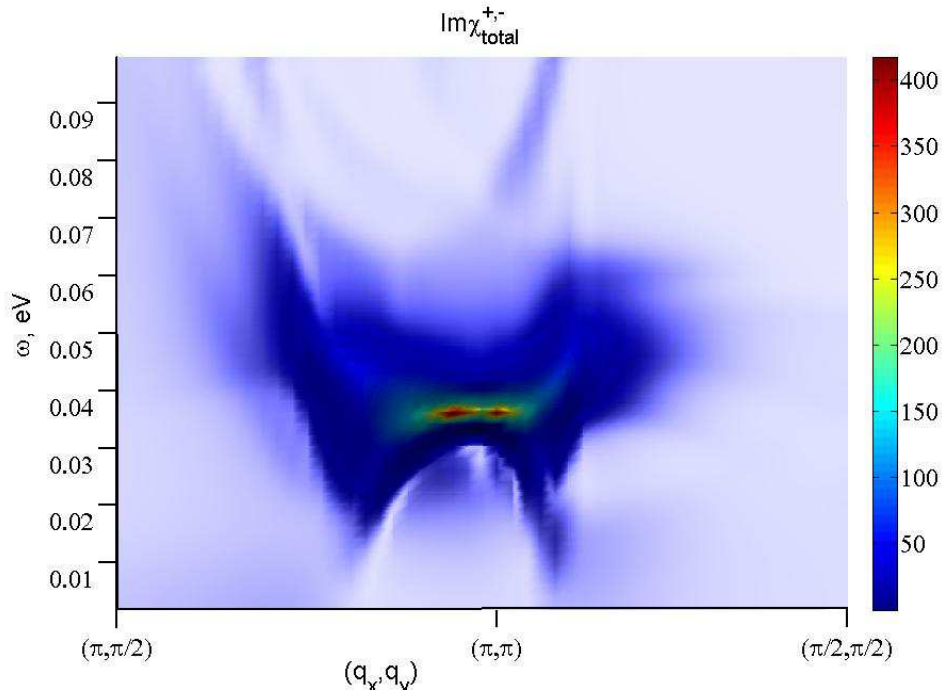


**Figure 10.** Fragment of the imaginary part of the spin susceptibility for the superconducting state near  $(\pi, \pi)$  point. Input values are:  $T = 10$  K,  $\Delta_0 = 25$  meV,  $J_1 = 76$  meV,  $K_1 = -0.152$ ,  $\Delta_{sp} = 0.17$ ,  $F_t = 0.1$ ,  $F_J = 0.89$ . Vertical scale is in  $1/\text{eV}$ .

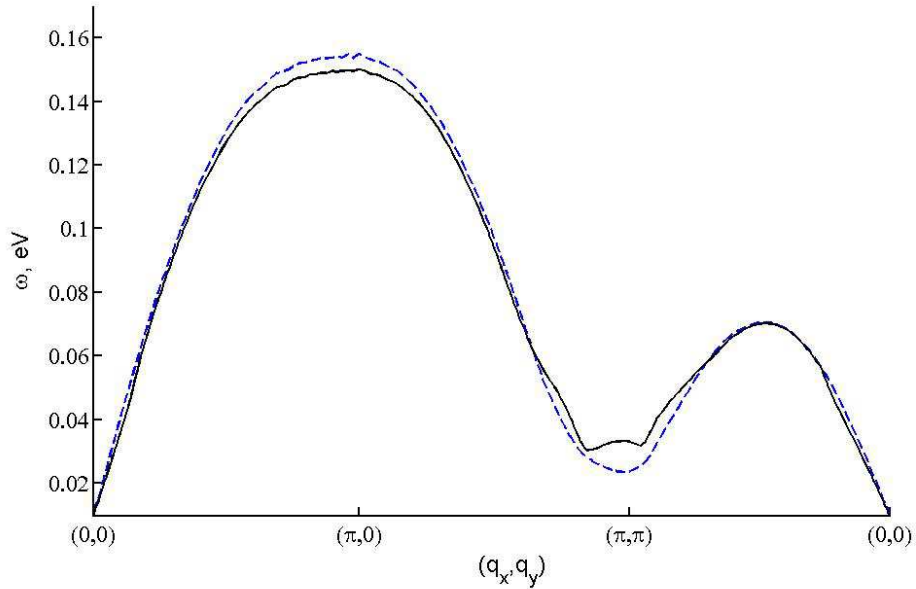


**Figure 11.** Dispersion of the collective spin excitations calculated as a solution to the equation (32) along the route  $(0, 0) - (0, \pi) - (\pi, \pi) - (0, 0)$  in the Brillouin zone for the normal state (dashed line) and superconducting one (solid line). Parameters are the same as in Fig. 3.

## 5. Conclusions and final remarks

The calculated results, shown in the previous section for the spin response near  $(\pi, \pi)$  point of the BZ resemble very strongly the experimental results reported by inelastic neutron scattering for hole doped cuprates [27-33]. Both the upward and the downward dispersions are successfully reproduced by our calculations. We have found that the fine features of the dynamical spin susceptibility near  $(\pi, \pi)$  point around the frequency 40 meV are very sensitive to the possible variation of the spin-gap ( $\Delta_{sp} \cong 0.14$  or  $\Delta_{sp} \cong 0.16$ ) and superconducting gap ( $\Delta_0 = 25$  meV or  $\Delta_0 = 30$  meV) parameters. Relatively small changes of these values lead to quite essential modification in the calculated picture. Under small changes of the input parameters the picture with the intersection of upward and downward dispersions (or in other words X-shape) in Fig. 4 and in Fig. 7 transforms to the so-called hour-glasses picture (Fig. 9).

As for the shape of the imaginary part of the spin susceptibility along the route  $(0, 0) - (\pi, 0)$  is very similar to those which was observed by inelastic resonance X-ray scattering (RIXS) [34-38]. Generally, its dispersion is not so sensitive to the possible variation of the input parameters. Double shape form calculated by us here and in Ref. [20] was not observed experimentally, probably because of the error bars in the current RIXS technique, which is about 300 meV [34-38]. It is interesting to note that the splitting between two mountain chain-like features, found in Fig. 8, is sensitive to the superconducting gap values. This fact clearly demonstrates that these mountain chain-like features are more related to the itinerant part of spin subsystem rather than to the collective spin excitation of the localized spins. Another interesting observation is that the calculated frequency plot of the collective spin excitations (Fig. 11) does not exactly corresponds to the maximum positions of imaginary part, shown in Fig. 3. Especially this can be easily seen for dispersions along the route  $(0, 0) - (\pi, 0)$ . This observation strongly supports the idea that peaks in RIXS spectra correspond to the spin excitations, which originate from paramagnon-like features of the itinerant origin rather than magnon-like excitations, which would originate from the short range order of the local spins at Cu sites. The latter explains better the nature of the high-energy spin excitations near  $(\pi, \pi)$  point with frequencies which are above  $2\Delta_0/\hbar$ .

## Acknowledgments

This work is supported by RFBR Grant 13-02-00492\_a

## Appendix A

Let us consider the commutator:

$$\left[ \sum_{i,l} J_{il} e^{-iqR_i} (S_l^+ S_i^z - S_l^z S_i^+), \sum_{j,m} t_{j,m} \psi_j^{pd,\sigma} \psi_m^{\sigma,pd} \right]. \quad (1a)$$

Using relation  $[AB, CD] = A[B, C]D + AC[B, D] + [A, C]DB + C[A, D]B$  one has

$$\begin{aligned} & \left[ \sum_{i,l} J_{il} e^{-iqR_i} (S_l^+ S_i^z - S_l^z S_i^+), \sum_{j,m} t_{j,m} \psi_j^{pd,\sigma} \psi_m^{\sigma,pd} \right] = \\ & = -\frac{1}{2} \sum J_{il} e^{-iqR_i} t_{i,m} S_l^+ (\psi_i^{pd,\uparrow} \psi_m^{\uparrow,pd} - \psi_i^{pd,\downarrow} \psi_m^{\downarrow,pd}) \\ & + \frac{1}{2} \sum J_{il} e^{-iqR_i} t_{j,i} S_l^+ (\psi_j^{pd,\uparrow} \psi_i^{\uparrow,pd} - \psi_j^{pd,\downarrow} \psi_i^{\downarrow,pd}) \\ & - \sum J_{il} e^{-iqR_i} t_{l,m} \psi_l^{pd,\downarrow} \psi_m^{\uparrow,pd} S_i^z + \sum J_{il} e^{-iqR_i} t_{j,l} \psi_j^{pd,\downarrow} \psi_l^{\uparrow,pd} S_i^z \\ & + \sum J_{il} e^{-iqR_i} t_{i,m} S_l^z \psi_i^{pd,\downarrow} \psi_m^{\uparrow,pd} - \sum J_{il} e^{-iqR_i} t_{j,i} S_l^z \psi_j^{pd,\downarrow} \psi_i^{\uparrow,pd} \\ & + \frac{1}{2} \sum J_{il} e^{-iqR_i} t_{l,m} (\psi_l^{pd,\uparrow} \psi_m^{\uparrow,pd} - \psi_l^{pd,\downarrow} \psi_m^{\downarrow,pd}) S_i^+ \\ & - \frac{1}{2} \sum J_{il} e^{-iqR_i} t_{j,l} (\psi_j^{pd,\uparrow} \psi_l^{\uparrow,pd} - \psi_j^{pd,\downarrow} \psi_l^{\downarrow,pd}) S_i^+. \end{aligned} \quad (2a)$$

Doing averaging we focus on the quantities  $J_{il} \langle \psi_i^{pd,\sigma} \psi_l^{\sigma,pd} \rangle$  and  $t_{il} \langle \psi_i^{pd,\sigma} \psi_l^{\sigma,pd} \rangle$  as suggested by Kuz'min [16]. However, assuming that  $t_{i,m} \langle \psi_i^{pd,\uparrow} \psi_m^{\uparrow,pd} \rangle = t_{i,m} \langle \psi_i^{pd,\downarrow} \psi_m^{\downarrow,pd} \rangle$ , we can see that the first two and the last two amounts in (1a) can be discarded. Further following Kuz'min suggestion for third, fourth, fifth and sixth terms we get following expressions:

$$\begin{aligned} & - \sum J_{il} e^{-iqR_i} t_{l,m} \psi_l^{pd,\downarrow} \psi_m^{\uparrow,pd} S_i^z \\ & = \frac{1}{2} \sum J_{il} e^{-iqR_i} t_{l,m} \psi_m^{\uparrow,pd} \psi_l^{pd,\downarrow} \left[ \psi_i^{\uparrow,pd} \psi_i^{pd,\uparrow} - \psi_i^{\downarrow,pd} \psi_i^{pd,\downarrow} \right] \\ & \cong \frac{1}{2} \sum J_{il} e^{-iqR_i} t_{l,m} \psi_m^{\uparrow,pd} \left[ \psi_l^{pd,\downarrow} \psi_i^{\uparrow,pd} \psi_i^{pd,\uparrow} - \langle \psi_l^{pd,\downarrow} \psi_i^{\downarrow,pd} \rangle \psi_i^{pd,\downarrow} \right] \\ & \cong -\frac{1}{2} \sum J_{il} e^{-iqR_i} t_{l,m} \psi_m^{\uparrow,pd} \psi_i^{pd,\downarrow} \langle \psi_l^{pd,\downarrow} \psi_i^{\downarrow,pd} \rangle \\ & + \frac{1}{2} \sum J_{il} e^{-iqR_i} t_{l,m} \psi_m^{\uparrow,pd} \psi_l^{pd,\downarrow} \psi_i^{\uparrow,\uparrow}, \end{aligned} \quad (3a)$$

$$\begin{aligned} \sum J_{il} e^{-iqR_i} t_{j,l} \psi_j^{pd,\downarrow} \psi_l^{\uparrow,pd} S_i^z & = \frac{1}{2} \sum J_{il} e^{-iqR_i} t_{j,l} \psi_j^{pd,\downarrow} \psi_l^{\uparrow,pd} \left[ \psi_i^{\uparrow,pd} \psi_i^{pd,\uparrow} - \psi_i^{\downarrow,pd} \psi_i^{pd,\downarrow} \right] \\ & = \frac{1}{2} \sum J_{il} e^{-iqR_i} t_{j,l} \psi_j^{pd,\downarrow} \psi_i^{\uparrow,pd} \langle \psi_i^{pd,\uparrow} \psi_l^{\uparrow,pd} \rangle - \frac{1}{2} \sum J_{il} e^{-iqR_i} t_{j,l} \psi_j^{pd,\downarrow} \psi_l^{\uparrow,pd} \psi_i^{\downarrow,\downarrow}, \end{aligned} \quad (4a)$$

$$\begin{aligned} \sum J_{il} e^{-iqR_i} t_{i,m} S_l^z \psi_i^{pd,\downarrow} \psi_m^{\uparrow,pd} & = \frac{1}{2} \sum J_{il} e^{-iqR_i} t_{i,m} \psi_i^{pd,\downarrow} \left[ \psi_l^{\uparrow,pd} \psi_l^{pd,\uparrow} - \psi_l^{\downarrow,pd} \psi_l^{pd,\downarrow} \right] \psi_m^{\uparrow,pd} \\ & = -\frac{1}{2} \sum J_{il} e^{-iqR_i} t_{i,m} \langle \psi_i^{pd,\downarrow} \psi_l^{\downarrow,pd} \rangle \psi_l^{pd,\downarrow} \psi_m^{\uparrow,pd} + \frac{1}{2} \sum J_{il} e^{-iqR_i} t_{i,m} \psi_l^{\uparrow,\uparrow} \psi_i^{pd,\downarrow} \psi_m^{\uparrow,pd}, \end{aligned} \quad (5a)$$

$$\begin{aligned}
 & - \sum J_{il} e^{-iqR_i} t_{j,i} S_l^z \psi_j^{pd,\downarrow} \psi_i^{\uparrow,pd} = \sum J_{il} e^{-iqR_i} t_{j,i} S_l^z \psi_i^{\uparrow,pd} \psi_j^{pd,\downarrow} \\
 & \cong \frac{1}{2} \sum J_{il} e^{-iqR_i} t_{j,i} \langle \psi_l^{pd,\uparrow} \psi_i^{\uparrow,pd} \rangle \psi_l^{\uparrow,pd} \psi_j^{pd,\downarrow} - \frac{1}{2} \sum J_{il} e^{-iqR_i} t_{j,i} \psi_l^{\downarrow,\downarrow} \psi_i^{\uparrow,pd} \psi_j^{pd,\downarrow}.
 \end{aligned} \tag{6a}$$

Keeping terms containing  $J_{il} \langle \psi_i^{pd,\uparrow} \psi_l^{\uparrow,pd} \rangle = \overline{J_{il}}$  we have

$$\begin{aligned}
 & -\frac{1}{2} \sum \overline{J_{il}} e^{-iqR_i} t_{l,m} \psi_m^{\uparrow,pd} \psi_i^{pd,\downarrow} + \frac{1}{2} \sum \overline{J_{il}} e^{-iqR_i} t_{j,l} \psi_j^{pd,\downarrow} \psi_i^{\uparrow,pd} \\
 & -\frac{1}{2} \sum \overline{J_{il}} e^{-iqR_i} t_{i,m} \psi_l^{pd,\downarrow} \psi_m^{\uparrow,pd} + \frac{1}{2} \sum \overline{J_{il}} e^{-iqR_i} t_{j,i} \psi_l^{\uparrow,pd} \psi_j^{pd,\downarrow} \\
 & = -\frac{1}{2} \sum \overline{J_{il}} e^{-iqR_i} t_{l,m} \psi_m^{\uparrow,pd} \psi_i^{pd,\downarrow} - \frac{1}{2} \sum \overline{J_{il}} e^{-iqR_i} t_{j,l} \psi_i^{\uparrow,pd} \psi_j^{pd,\downarrow} \\
 & + \frac{1}{2} \sum \overline{J_{il}} e^{-iqR_i} t_{i,m} \psi_m^{\uparrow,pd} \psi_l^{pd,\downarrow} + \frac{1}{2} \sum \overline{J_{il}} e^{-iqR_i} t_{j,i} \psi_l^{\uparrow,pd} \psi_j^{pd,\downarrow} \\
 & + \frac{1}{2} \sum \overline{J_{il}} e^{-iqR_i} t_{i,l} S_i^+ - \frac{1}{2} \sum \overline{J_{il}} e^{-iqR_i} t_{l,i} S_l^+.
 \end{aligned} \tag{7a}$$

Next we turn to the Fourier components:

$$S_j^+ = \frac{1}{N} \sum S_q^+ e^{iqR_j}, \tag{8a}$$

$$\psi_j^{pd,\uparrow} = \frac{1}{\sqrt{N}} \sum_k \psi_k^{pd,\uparrow} e^{-ikR_j}. \tag{9a}$$

After straightforward calculation the expression (7a) can be rewritten as

$$-\frac{1}{2} (\overline{J_{k+q}} - \overline{J_k}) (t_{k+q} - t_k) \psi_{k+q}^{\uparrow,pd} \psi_k^{pd,\downarrow} + (\overline{J_1} t_1) [2 - \cos q_x - \cos q_x] S_q^+. \tag{10a}$$

Now, consider the remaining in Eqs. (3a)-(6a) four terms:

$$\begin{aligned}
 & \frac{1}{2} \sum J_{il} e^{-iqR_i} t_{l,m} \psi_m^{\uparrow,pd} \psi_l^{pd,\downarrow} \psi_i^{\uparrow,\uparrow} - \frac{1}{2} \sum J_{il} e^{-iqR_i} t_{j,l} \psi_j^{pd,\downarrow} \psi_l^{\uparrow,pd} \psi_i^{\downarrow,\downarrow} \\
 & + \frac{1}{2} \sum J_{il} e^{-iqR_i} t_{i,m} \psi_l^{\uparrow,\uparrow} \psi_m^{pd,\downarrow} \psi_i^{\uparrow,pd} - \frac{1}{2} \sum J_{il} e^{-iqR_i} t_{j,i} \psi_l^{\downarrow,\downarrow} \psi_i^{\uparrow,pd} \psi_j^{pd,\downarrow} \\
 & \cong \frac{1}{2} \sum J_{il} e^{-iqR_i} t_{l,m} \langle \psi_m^{\uparrow,pd} \psi_i^{\uparrow,pd} \rangle \psi_l^{\uparrow,pd} \psi_i^{pd,\downarrow} - \frac{1}{2} \sum J_{il} e^{-iqR_i} t_{j,l} \langle \psi_j^{pd,\downarrow} \psi_i^{\downarrow,pd} \rangle \psi_i^{pd,\downarrow} \psi_l^{\uparrow,pd} \\
 & + \frac{1}{2} \sum J_{il} e^{-iqR_i} t_{i,m} \psi_i^{pd,\downarrow} \psi_l^{\uparrow,pd} \langle \psi_l^{pd,\uparrow} \psi_m^{\uparrow,pd} \rangle - \frac{1}{2} \sum J_{il} e^{-iqR_i} t_{j,i} \psi_i^{\uparrow,pd} \psi_l^{\downarrow,pd} \langle \psi_l^{pd,\downarrow} \psi_j^{pd,\downarrow} \rangle.
 \end{aligned} \tag{11a}$$

Let us start with the following:

$$\begin{aligned}
 & \frac{1}{2} \sum J_{il} e^{-iqR_i} t_{l,m} \langle \psi_i^{pd,\uparrow} \psi_m^{\uparrow,pd} \rangle \psi_l^{\uparrow,pd} \psi_i^{pd,\downarrow} + \frac{1}{2} \sum J_{il} e^{-iqR_i} t_{j,l} \langle \psi_j^{pd,\downarrow} \psi_i^{\downarrow,pd} \rangle \psi_l^{\uparrow,pd} \psi_i^{pd,\downarrow} \\
 & - \frac{1}{2} \sum J_{il} e^{-iqR_i} t_{i,m} \langle \psi_l^{pd,\uparrow} \psi_m^{\uparrow,pd} \rangle \psi_l^{\uparrow,pd} \psi_i^{pd,\downarrow} - \frac{1}{2} \sum J_{il} e^{-iqR_i} t_{j,i} \langle \psi_j^{pd,\downarrow} \psi_l^{\downarrow,pd} \rangle \psi_i^{\uparrow,pd} \psi_l^{pd,\downarrow}.
 \end{aligned} \tag{12a}$$

The largest terms are:

$$\begin{aligned}
 & \frac{1}{2} \sum J_{il} e^{-iqR_i} t_{l,i} \langle \psi_i^{pd,pd} \rangle \psi_i^{\uparrow,pd} \psi_l^{pd,\downarrow} + \frac{1}{2} \sum J_{il} e^{-iqR_i} t_{i,l} \langle \psi_i^{pd,pd} \rangle \psi_l^{\uparrow,pd} \psi_i^{pd,\downarrow} \\
 & - \frac{1}{2} \sum J_{il} e^{-iqR_i} t_{i,l} \langle \psi_l^{pd,pd} \rangle \psi_l^{\uparrow,pd} \psi_i^{pd,\downarrow} - \frac{1}{2} \sum J_{il} e^{-iqR_i} t_{l,i} \langle \psi_l^{pd,pd} \rangle \psi_i^{\uparrow,pd} \psi_l^{pd,\downarrow}.
 \end{aligned} \tag{13a}$$

In the uniform lattice  $\langle \psi_i^{pd,pd} \rangle = \langle \psi_l^{pd,pd} \rangle$ . Therefore, the first and fourth (second and third) do cancel each other.

Now let us discuss the role of the three-site correlations. After Fourier transform these terms are written as

$$\begin{aligned} & \frac{1}{2} \sum_{i,m} J_{il} e^{ikR_{il}} t_{lm} \langle \psi_i^{pd,\uparrow} \psi_m^{\uparrow,pd} \rangle \psi_{k+q}^{\uparrow,pd} \psi_k^{pd,\downarrow} + \frac{1}{2} \sum_{i,j} J_{il} e^{-i(k+q)R_{il}} t_{lj} \langle \psi_j^{pd,\downarrow} \psi_i^{\downarrow,pd} \rangle \psi_{k+q}^{\uparrow,pd} \psi_k^{pd,\downarrow} \\ & - \frac{1}{2} \sum_{l,m} J_{il} e^{i(k+q)R_{li}} t_{i,m} \langle \psi_l^{pd,\uparrow} \psi_m^{\uparrow,pd} \rangle \psi_{k+q}^{\uparrow,pd} \psi_k^{pd,\downarrow} - \frac{1}{2} \sum_{l,j} J_{il} e^{-ikR_{li}} t_{j,i} \langle \psi_j^{pd,\downarrow} \psi_l^{\downarrow,pd} \rangle \psi_{k+q}^{\uparrow,pd} \psi_k^{pd,\downarrow}. \end{aligned} \quad (14a)$$

Performing summation over the square lattice we find

$$\begin{aligned} & \frac{1}{2} \sum_{i,m} J_{il} e^{ikR_{il}} t_{lm} \langle \psi_i^{pd,\uparrow} \psi_m^{\uparrow,pd} \rangle - \frac{1}{2} \sum_{l,j} J_{il} e^{-ikR_{li}} t_{j,i} \langle \psi_j^{pd,\downarrow} \psi_l^{\downarrow,pd} \rangle \\ & \cong J_1 t_1 \left( 2 \langle \psi_0^{pd,\uparrow} \psi_2^{\uparrow,pd} \rangle + \langle \psi_0^{pd,\uparrow} \psi_3^{\uparrow,pd} \rangle \right) (\cos q_x + \cos q_y) \\ & - J_1 t_1 \left( 2 \langle \psi_0^{pd,\downarrow} \psi_2^{\downarrow,pd} \rangle + \langle \psi_0^{pd,\downarrow} \psi_3^{\downarrow,pd} \rangle \right) (\cos q_x + \cos q_y) = 0. \end{aligned} \quad (15a)$$

Here  $\langle \psi_0^{pd,\downarrow} \psi_2^{\downarrow,pd} \rangle$  refers to the next nearest neighbor correlation. The hopping parameters  $t_2=t_{02}$  and  $t_3=t_{03}$  are not included into consideration.

Finally the anticommutator (1a) is written as follows:

$$\begin{aligned} & \left[ \sum_{i,l} J_{il} e^{-iqR_i} (S_l^+ S_i^z - S_l^z S_i^+) , \sum_{j,m} t_{j,m} \psi_j^{pd,\sigma} \psi_m^{\sigma,pd} \right] \\ & \cong \bar{J}_1 t_1 [2 - \cos q_x a - \cos q_y a] S_q^+ - \frac{1}{2} \sum_k (\bar{J}_{k+q} - \bar{J}_k) (t_{k+q} - t_k) \psi_{k+q}^{\uparrow,pd} \psi_k^{pd,\downarrow}. \end{aligned} \quad (16a)$$

Here is, of course, an addition decoupling factor  $\beta \cong 1$  is occurred, like factor  $\alpha$  in Eq. (4). Therefore here it is logical to change the definition  $\bar{J}_1$  as follows

$$\bar{J}_1 = J_1 \beta \langle \psi_0^{pd,\uparrow} \psi_1^{\uparrow,pd} \rangle. \quad (17a)$$

It should be noted that our result (16a) is different from those which presented in the original paper [16] by factor 2. Furthermore, we do not approximate additionally the last term in Eq. (16a). The system of self-consistent equations for Green's functions can be obtained (see the main text), using expression for aticommutator, as it is given by (16a). Entering correlation functions in the normal state are calculated as follows

$$\begin{aligned} \langle \psi_j^{pd,\downarrow} \psi_l^{\downarrow,pd} \rangle &= \frac{1}{N} \sum_{k,k'} \langle \psi_k^{pd,\downarrow} \psi_{k'}^{\downarrow,pd} \rangle e^{-ikR_j + ik'R_l} \\ &= P \left( \frac{a}{2\pi} \right)^2 \int_{-\pi/a}^{\pi/a} \int_{-\pi/a}^{\pi/a} \frac{\cos(k_x R_{jl}^x + k_y R_{jl}^y)}{1 + \exp\left(\frac{\varepsilon_k - \mu}{k_B T}\right)} dk_x dk_y. \end{aligned} \quad (18a)$$

For nearest neighbors it is written as:

$$\langle \psi_0^{pd,\downarrow} \psi_1^{\downarrow,pd} \rangle = 4P \left( \frac{1}{2\pi} \right)^2 \int_0^\pi \int_0^\pi \frac{\cos q_x}{1 + \exp\left(\frac{\varepsilon_q - \mu}{k_B T}\right)} dq_x dq_y. \quad (19a)$$

Here tetragonal symmetry in Cu-O plane is assumed.

## Appendix B

The Green's function of itinerant part in Eq. (2) can be rewritten as follows [2]

$$\begin{aligned} & \sum_k (t_{k+q} - t_k) \langle \langle \psi_{k+q}^{\uparrow, pd} \psi_k^{pd, \downarrow} | S_{-q}^- \rangle \rangle \\ &= \frac{1}{2} \sum_k (t_{k+q} - t_k) \langle \langle [\psi_{k+q}^{\uparrow, pd} \psi_k^{pd, \downarrow} - \psi_{k+q}^{\downarrow, pd} \psi_k^{pd, \uparrow}] \psi_{k+q}^{\uparrow, pd} \psi_k^{pd, \downarrow} | S_{-q}^- \rangle \rangle. \end{aligned} \quad (1b)$$

In equation (16a) the last term can be rewritten as

$$\begin{aligned} -\frac{1}{2} \sum_k (\bar{J}_{k+q} - \bar{J}_k) (t_{k+q} - t_k) \psi_{k+q}^{\uparrow, pd} \psi_k^{pd, \downarrow} &= \frac{1}{2} \sum_k (\bar{J}_{k+q} - \bar{J}_k) (t_{k+q} - t_k) \psi_k^{pd, \downarrow} \psi_{k+q}^{\uparrow, pd} \\ &- \frac{1}{2N} \sum_k (\bar{J}_{k+q} - \bar{J}_k) (t_{k+q} - t_k) S_q^+. \end{aligned} \quad (2b)$$

In case of square lattice

$$-\frac{1}{2N} \sum_k (\bar{J}_{k+q} - \bar{J}_k) (t_{k+q} - t_k) \cong -2t_1 \bar{J}_1 (2 - \cos q_x a - \cos q_y a). \quad (3b)$$

Therefore the equation (16a) becomes

$$\begin{aligned} & \left[ \sum_{i,l} J_{il} e^{-iqR_i} (S_l^+ S_i^z - S_l^z S_i^+), \sum_{j,m} t_{j,m} \psi_j^{pd, \sigma} \psi_m^{\sigma, pd} \right] \\ & \cong -\bar{J}_1 t_1 [2 - \cos q_x a - \cos q_y a] S_q^+ \\ & - \frac{1}{4} \sum_k (\bar{J}_{k+q} - \bar{J}_k) (t_{k+q} - t_k) [\psi_{k+q}^{\uparrow, pd} \psi_k^{pd, \downarrow} - \psi_k^{pd, \downarrow} \psi_{k+q}^{\uparrow, pd}]. \end{aligned} \quad (4b)$$

Using (1b) and (4b) we get the following expression for spin response function

$$\chi_{total}^{+,-} = \frac{\chi \zeta_{tJ} + [2J_1 K_1 (2 - \gamma_q) - \chi_{tJ}] \zeta}{[\frac{1}{2} + \eta] \zeta_{tJ} + [\omega^2 - \Omega_q^2 - \bar{J}_1 t_1 (2 - \gamma_q) - \eta_{tJ}] \zeta}, \quad (5b)$$

where

$$\begin{aligned} \eta &= \frac{1}{N} \sum_k \eta_{k,q} = \frac{1}{2} J_q F_J \chi(\omega, q) \\ &- \frac{P}{N} \left( \sum S_{xx} \frac{t'_{k+q}(f_{k+q} - 1/2) - t'_k(f_k - 1/2)}{\omega + i\Gamma + E_k - E_{k+q}} \right. \\ &+ \sum S_{yy} \frac{t'_{k+q}(1/2 - f_{k+q}) - t'_k(1/2 - f_k)}{\omega + i\Gamma - E_k + E_{k+q}} \\ &+ \sum S_{yx}^{(-)} \frac{t'_{k+q}(f_{k+q} - 1/2) - t'_k(1/2 - f_k)}{\omega + i\Gamma - E_k - E_{k+q}} \\ &\left. + \sum S_{xy}^{(+)} \frac{t'_{k+q}(1/2 - f_{k+q}) - t'_k(f_k - 1/2)}{\omega + i\Gamma + E_k + E_{k+q}} \right), \end{aligned} \quad (6b)$$

as it was introduced in [2] and

$$\eta_{tJ}(\omega, q) = \frac{1}{2N} \sum_k (t_{k+q} - t_k) [\bar{J}_{k+q} - \bar{J}_k - 2\omega] \eta_{kq}. \quad (7b)$$

Note the denominator of the dynamical spin susceptibility can be written also via  $\eta'(w, q)$  function. Corresponding expression for  $\eta'(w, q)$  in superconducting state can be found in Ref. [1]

## Appendix C

### Spin-spin correlation functions

The spin-spin correlation functions are calculated self-consistently via expression for the dynamical spin susceptibility. It is useful to start discussion from the Fourier transform:

$$\langle S_i^- S_j^+ \rangle = \frac{1}{N^2} \sum_q \langle S_{-q}^- S_q^+ \rangle e^{iqR_{ij}}. \quad (1c)$$

Then to use Green's function technique

$$\begin{aligned} \langle S_{-q}^- S_q^+ \rangle &= \int \frac{d\omega}{e^{\beta\omega} - 1} [\langle \langle S_q^+ | S_{-q}^- \rangle \rangle_{\omega+i\varepsilon} - \langle \langle S_q^+ | S_{-q}^- \rangle \rangle_{\omega-i\varepsilon}] \\ &= \frac{N}{2\pi i} \int \frac{d\omega}{e^{\beta\omega} - 1} [\chi^{+,-}(q, \omega + i\varepsilon) - \chi^{+,-}(q, \omega - i\varepsilon)] \\ &= \frac{N}{\pi} \int \frac{d\omega}{e^{\beta\omega} - 1} \text{Im} \chi^{+,-}(q, \omega). \end{aligned} \quad (2c)$$

Since

$$\text{Im} \chi^{+,-}(q, \omega) = -\text{Im} \chi^{+,-}(q, -\omega), \quad (3c)$$

integration can be carried out only by positive values  $\omega$ . Thus, one finds

$$\begin{aligned} \langle S_i^- S_j^+ \rangle &= \frac{1}{N\pi} \sum_q \int \frac{d\omega}{e^{\beta\omega} - 1} \text{Im} \chi^{+,-}(q, \omega) e^{ikR_{ij}} \\ &= \frac{1}{\pi} \left(\frac{a}{2\pi}\right)^2 \iiint \left[ \frac{d\omega}{e^{\beta\omega} - 1} \text{Im} \chi^{+,-}(q, \omega) - \frac{d\omega}{e^{-\beta\omega} - 1} \text{Im} \chi^{+,-}(q, -\omega) \right] e^{ikR_{ij}} dk_x dk_y \\ &= \frac{1}{\pi} \left(\frac{a}{2\pi}\right)^2 \iiint \text{cth} \left( \frac{\beta\omega}{2} \right) \text{Im} \chi^{+,-}(q, \omega) e^{ikR_{ij}} d\omega dk_x dk_y. \end{aligned} \quad (4c)$$

### Sum rule

The case  $i = j$  is used for self-consistent control. Since

$$\begin{aligned} \psi_l^{\downarrow, \downarrow} + \psi_l^{\uparrow, \uparrow} + 2\psi_l^{pd, pd} &= 1 + \delta, \\ \psi_l^{\uparrow, \uparrow} - \psi_l^{\downarrow, \downarrow} &= 2S_l^z, \end{aligned} \quad (5c)$$

at  $\langle S_i^z \rangle = 0$ , and  $\langle \psi_l^{pd, pd} \rangle = \delta$  one gets

$$\frac{1 - \delta}{2} = \left(\frac{1}{\pi}\right)^3 \int_0^\pi \int_0^\pi \int_0^\infty \text{cth} \left( \frac{\beta\omega}{2} \right) \text{Im} \chi^{+,-}(q, \omega) e^{iqR_{ij}} d\omega dq_x dq_y. \quad (6c)$$

## References

1. Eremin M.V., Aleev A.A., Eremin I.M. *JETP* **106**, 752 (2008) [*Zh. Eksp. Teor. Fiz.* **133**, 862 (2008), in Russian]
2. Eremin M.V., Shigapov I.M., Eremin I.M. *Eur. Phys. J. B* **85**, 131 (2012)
3. Zhang F.C. Rice T.M. *Phys. Rev. B* **37**, R3759 (1988)
4. Eremin M.V., Solov'yanov S.G., Varlamov S.V., Brinkman D., Mali M., Markendorf R., Roos J. *JETP Lett.* **60**, 125 (1994) [*Pis'ma Zh. Eksp. Teor. Fiz.* **60**, 118 (1994), in Russian]
5. Eremin M.V., Solovjanov S.G., Varlamov S.V. *J. Phys. Chem. Solids* **56**, 1713 (1995)
6. Plakida N.M., Hayn R., Richard J.-L. *Phys. Rev. B* **51**, 16599 (1995)
7. Anderson P.W. *Science* **235**, 1196 (1987)
8. Shimahara H., Takada S. *J. Phys. Soc. Jpn.* **61**, 989 (1992)
9. Kondo J., Yamaji K. *Prog. Theor. Phys.* **47**, 807 (1972)
10. Zavidonov A.Yu., Brinkmann D. *Phys. Rev. B* **58**, 12486 (1998)
11. Jackeli G., Plakida N.M. *Theor. Math. Phys.* **114**, 335 (1998) [*TMF* **114**, 426 (1998), in Russian]
12. Winterfeldt S., Ihle D. *Phys. Rev. B* **58**, 9402 (1998)
13. Winterfeldt S., Ihle D. *Phys. Rev. B* **59**, 6010 (1999)
14. Sherman A., Schreiber M. *Phys. Rev. B* **68**, 094519 (2003)
15. Sherman A., Schreiber M. *Eur. Phys. J. B* **32**, 203 (2003)
16. Kuz'min E.V. *Low Temp. Phys.* **31**, 143 (2005)
17. Vladimirov A., Ihle D., Plakida N. *Theor. Mat. Phys.* **152**, 1331 (2007) [*TMF* **152**, 538 (2007), in Russian]
18. Mikheenkov A.V., Barabanov A.F. *JETP* **105**, 347 (2007) [*Zh. Eksp. Teor. Fiz.* **132**, 392 (2007), in Russian]
19. Anderson P.W., Lee P.A., Randeria M., Rice T.M., Trivedi N., Zhang F.C. *J. Phys.: Condens. Matter* **16**, R755 (2004)
20. Eremin M.V., Shigapov I.M., Thuy H.T.D. *J. Phys.: Condens. Matter*, **25**, 345701 (2013)
21. Field J.J. *J. Phys. C: Solid State Phys.* **5**, 664 (1972)
22. Auslender M.I., Irkhin V.Yu., Katsnelson M.I. *J. Phys. C: Solid State Phys.* **21**, 5521 (1988)
23. Mayer T., Eremin M., Eremin I., Meier P.F. *J. Phys.: Condens. Matter* **19**, 116209 (2007)
24. Eremin M.V., Solov'yanov S.G., Varlamov S.V. *JETP* **85**, 963 (1997) [*Zh. Eksp. Teor. Fiz.* **112**, 1763 (1997), in Russian]

25. Norman M.R. *Phys. Rev. B* **63**, 092509 (2000)
26. Eremin M.V., Larionov I.A., Lyubin I.E. *J. Phys.: Condens. Matter* **22**, 165704 (2007)
27. Bourges P., in *The Gap Symmetry and Fluctuations in High Temperature Superconductors*, ed. by J. Bok, G. Deutscher, D. Pavuna, and S. A. Wolf, Plenum, New York, pp. 349-371 (1998)
28. Reznik D., Bourges P., Pintschovius L., Endoh Y., Sidis Y., Masui T., Tajima S. *Phys. Rev. Lett.* **93**, 207003 (2004)
29. Reznik D., Ismer J.-P., Eremin I., Pintschovius L., Wolf T., Arai M., Endoh Y., Masui T., Tajima S. *Phys. Rev. Lett.* **78**, 132503 (2008)
30. Pailhès S., Sidis Y., Bourges P., Hinkov V., Ivanov A., Ulrich C., Regnault L.P., Keimer B. *Phys. Rev. Lett.* **93**, 167001 (2004)
31. Arai M., Nishijima T., Endoh Y., Egami T., Tajima S., Tomimoto K., Shiohara Y., Takahashi M., Garrett A., Bennington S.M. *Phys. Rev. Lett.* **83**, 608 (1999)
32. Dai P., Mook H.A., Hunt R.D., Doğan F. *Phys. Rev. B* **63**, 054525 (2001)
33. Bourges P., Sidis Y., Fong H.F., Regnault L.P., Bossy J., Ivanov A., Keimer B. *Science* **288**, 1234 (2000)
34. Le Tacon M., Ghiringhelli G., Chaloupka J., Moretti Sala M., Hinkov V., Haverkort M.W., Minola M., Bakr M., Zhou K.J., Blanco-Canosa S., Monney C., Song Y.T., Sun G.L., Lin C.T., De Luca G.M., Salluzzo M., Khaliullin G., Schmitt T., Braicovich L., Keimer B. *Nat. Phys.* **7**, 725 (2011)
35. Le Tacon M., Minola M., Peets D.C., Moretti Sala M., Blanco-Canosa S., Hinkov V., Liang R., Bonn D.A., Hardy W.N., Lin C.T., Schmitt T., Braicovich L., Ghiringhelli G., Keimer B. *Phys. Rev. B* **88**, 020501(R) (2013)
36. Braicovich L., van den Brink J., Bisogni V., Moretti Sala M., Ament L.J.P., Brookes N.B., De Luca G.M., Salluzzo M., Schmitt T., Strocov V.N., Ghiringhelli G. *Phys. Rev. Lett.* **104**, 077002 (2010)
37. Dean M.P.M., James A.J.A., Springell R.S., Liu X., Monney C., Zhou K.J., Konik R.M., Wen J.S., Xu Z.J., Gu G.D., Strocov V.N., Schmitt T., Hill J.P. *Phys. Rev. Lett.* **110**, 147001 (2013)
38. Dean M.P.M., Dellea G., Springell R.S., Yakhov-Harris F., Kummer K., Brookes N.B., Liu X., Sun Y.-J., Strle J., Schmitt T., Braicovich L., Ghiringhelli G., Božović I., Hill J.P. *Nat. Mater.* **12**, 1019 (2013)

# Short-time diffusion behavior of Brownian particles in porous solids

N.F. Fatkullin<sup>1,\*</sup>, R. Valiullin<sup>2</sup>

<sup>1</sup>Kazan Federal University, Kremlevskaya 18, 420008 Kazan, Russia

<sup>2</sup>University of Leipzig, Linnestraße 5, D-04103 Leipzig, Germany

\**E-mail: Nail.Fatkullin@kpfu.ru*

The process of self-diffusion of particles confined to porous solids is studied for time intervals corresponding to particle displacements shorter than the characteristic pore size. The solid matrix is modeled as a (random) potential field with an infinitely large potential within the solid which decays to zero at distances of the order of a few particle sizes from the pore walls. Diffusion of particles in the thus created potential field is described by the Smoluchowski diffusion equation. It is shown that, for short diffusion times, the resulting equation for the time-dependent diffusivity reproduces that earlier obtained in the literature [Mitra *et al.*, Phys. Rev. Lett. **68**, 3555 (1992)], but with the numerical constant differing by factor 2. The conditions under which this discrepancy arises are highlighted and discussed.

**PACS:** 76.30.-v, 68.65.-k

**Keywords:** diffusion, porous solids, short-time expansion, Smoluchowski equation

## 1. Introduction

Diffusion, or erratic thermal motion of molecules, is an ubiquitous phenomenon in nature, which often plays a key role in variety of bio- or physico-chemical processes. Under equilibrium conditions and in spatially homogeneous and isotropic systems, the Green's function, i.e. the probability density to find a particle at a distance  $r$  from its origin at a time instance  $t$ , is a Gaussian function. For long enough times, this leads to the fact that the mean squared displacements  $\langle r^2(t) \rangle$  grow linearly with time [1]. This regime is often referred to as normal diffusion. In many cases, however, diffusion occurs in inhomogeneous environments, with the most prominent examples being fluid transport in biological cells or porous solids. Under these conditions, some part of space becomes inaccessible for the diffusing particles, rendering the process of diffusion to deviate from the normal behavior on the length scales comparable to characteristic sizes  $\xi$  of the structural inhomogeneities. In porous media, which are in the focus of this work,  $\xi$  can be associated with typical pore sizes. In this anomalous regime of diffusion,  $\langle r^r(t) \rangle \propto t^k$  with  $0 < k < 1$ , hence referred to as sub-diffusion (notably,  $k$  may also be a function of time). For permeable media, the normal diffusion behavior can further be recovered at length scales notably exceeding  $\xi$ . Understanding the relationships between diffusion processes and structural properties of porous materials is of particular importance for predicting molecular transport in practical applications, such as oil recovery, water infiltration, etc., and for structural characterization [2].

In a most direct way, the mean squared molecular displacements can be measured using the pulsed field gradient technique of nuclear magnetic resonance (PFG NMR) [3–5]. This method is based on the positional encoding of the spin-bearing molecules and their subsequent decoding using short pulses of magnetic field gradients. Between these two pulses, a well-controlled in the experiment time  $t$  (also referred to as diffusion time) is given for system to evolve. If the molecules during the time interval  $t$  perform purely stochastic, translational motion, the measured signal intensity  $S$  is found to be attenuated by the factor

$$S(q, t)/S(0, t) = \exp \left\{ -\frac{1}{2} q^2 \langle r^2(t) \rangle \right\}, \quad (1)$$

where  $q$  is the wave number, which is controlled in the experiment. Alternatively, (1) may also be considered as a first term in the expansion in case if the Green's function cannot be approached by a Gaussian function [5]. Typically, the experimentally measured quantity  $\langle r^2(t) \rangle$  is expressed in terms of the effective diffusion coefficient  $D_e$ , which is defined via the Einstein equation

$$D_e(t) = \langle r^2(t) \rangle / 6t. \quad (2)$$

In PFG NMR, one typically explores diffusion processes in the time scale  $10^{-3} \lesssim t \lesssim 10$  s. Hence, for low molecular liquids and on the time scale of the PFG NMR measurements,  $D_e$ , as measured using this technique and as defined by (2), turns out to be, to good accuracy, constant and to coincide with the bulk self-diffusivity  $D_0$ . In porous materials, however,  $D_e$  is found to decrease with increasing time for diffusion times  $t \lesssim R^2/D_0$ , where  $R$  is the characteristic pore size [6]. This behavior can easily be revealed by combining the equations (1) and (2). The time dependence of the diffusivity results from the fact that the solid matrix is impermeable for the diffusing particles, giving rise to the reflecting boundary conditions at the pore walls. One may expect, therefore, that the effective diffusivity can be a function of the surface area, at which the reflection of the particle fluxes occurs. In the context of the PFG NMR diffusion measurements of fluids in porous solids, the understanding of the relationships between the structural parameters of porous media and the time-dependent diffusivity was put forward in Refs. [7–9]. In particular, by considering the classical Fick's diffusion equation with the boundary condition posing zero gradient of the Green's function at the pore walls it was shown that, for sufficiently short diffusion times,  $D_e$  is indeed determined by the surface-to-volume ratio  $S/V_p$  of the pore space [7]:

$$D_e(t) = D_0 \left( 1 - \frac{4S}{9V} \sqrt{\frac{D_0 t}{\pi}} + O(D_0 t) \right). \quad (3)$$

This result has further been reproduced in a number of analogous studies (see, e.g., [6, 10]). The approach based on (3) has become a robust and widely used tool for the determination of the  $S/V_p$  ratio for different porous materials by measuring the time-dependent diffusivity using PFG NMR [11–18]. It may be noted, however, that in several works an overestimation of the surface-to-volume ratio by a factor of about 2 using (3) was reported [19, 20].

The effect of the solid matrix upon diffusing particles can alternatively be described on the basis of the Smoluchowski diffusion equation [21]. In this case, the pore space and the solid are modeled as the sub-spaces with low and infinitely large potentials  $U(\mathbf{r})$ , respectively, with a smooth transition between them. Thus, close to the pore walls, the moving particles experience a change of the potential, which can effectively be treated as the action of a force  $-\partial U(\mathbf{r})/\partial \mathbf{r}$ . Diffusion of particles in the presence of a force field generated by the solid matrix, which is generally described by the Smoluchowski diffusion equation, was already considered in the literature in connection with PFG NMR experiments [22, 23]. In this work, we use this approach to study the short-time diffusion behavior of low-molecular liquids in porous materials. Because in this way the interaction of molecules with the solid can be described on a more realistic level, the main goal of this work was to establish how it may render the results obtained earlier using classical Fick's diffusion equations.

## 2. Results

In this work, the influence of the solid matrix on the confined molecules was described by means of an effective random potential  $U(\mathbf{r})$  induced by the heterogeneous medium. Within the solid, which effectively plays a role of obstacles for the Brownian particles,  $U(\mathbf{r}) \rightarrow \infty$ , while in the pore space  $U(\mathbf{r}) \rightarrow 0$ . At the pore walls, the potential falls to zero within the surface layer of the order of a few particle sizes. This length scale we denote by  $a_0$  and it may be associated with the thickness of a surface layer having different physical properties as compared to the bulk phase. In all physically relevant cases, this transition is considered to be smooth. We consider only the quenched fields  $U(\mathbf{r})$ , which do not vary in time, i.e., the molecular or particle mass is considered to be negligibly small as compared to the mass of the solid, thus the motion of the latter can be ignored.

The probability density  $W(\mathbf{r}; t)$  for the molecular displacements, namely the Green's function, satisfies the Smoluchowski equation

$$\frac{\partial}{\partial t} W(\mathbf{r}; t) = D_0 \frac{\partial}{\partial \mathbf{r}} \left[ \frac{\partial}{\partial \mathbf{r}} - \frac{1}{kT} \mathbf{f}(\mathbf{r}) \right] W(\mathbf{r}; t), \quad (4)$$

where  $D_0$  is the diffusivity in the bulk liquid,  $\mathbf{f} = -\partial U(\mathbf{r})/\partial \mathbf{r}$  is the force induced by the random potential,  $k$  is the Boltzmann constant, and  $T$  is temperature. Note that the differential operator on the right hand side of (4) is not a self-adjoint one. This makes the problem rather complex from the mathematical point of view. To simplify the problem, we introduce a new function  $\Psi(\mathbf{r}, t)$  which is related to  $W(\mathbf{r}, t)$  via

$$\Psi(\mathbf{r}, t) = W(\mathbf{r}, t) \exp \left\{ \frac{U(\mathbf{r})}{2kT} \right\}. \quad (5)$$

With (5), the Smoluchowski equation (4) becomes

$$\frac{\partial}{\partial \tau} \Psi(\mathbf{r}; t) = \Delta \Psi(\mathbf{r}; t) + \frac{1}{2} \left[ \Delta \tilde{U}(\mathbf{r}) - \frac{1}{2} (\nabla \tilde{U}(\mathbf{r}))^2 \right] \Psi(\mathbf{r}; t), \quad (6)$$

where  $\tau = D_0 t$  and  $\tilde{U}(\mathbf{r}) = U(\mathbf{r})/kT$ .

With the Green's function known, the molecular mean squared displacements (MSD) can readily be obtained:

$$\langle \mathbf{r}^2(t) \rangle = \frac{1}{Z} \int \int d^3 \mathbf{r}_1 d^3 \mathbf{r}_0 (\mathbf{r}_1 - \mathbf{r}_0)^2 W(\mathbf{r}_1, \mathbf{r}_0; t) \exp \left\{ -\frac{U(\mathbf{r}_0)}{kT} \right\}, \quad (7)$$

where the statistical integral

$$Z = \int d^3 \mathbf{r} \exp \{ -U(\mathbf{r})/kT \} = V_p \quad (8)$$

is simply equal to the total volume of the pore space. Notably, the Green's function in (7) is the density probability to find a particle at  $\mathbf{r}_1$  at the time instance  $t$  if at zero time it was located at  $\mathbf{r}_0$ . The Boltzmann factor in the integral on the right hand side of (7) accounts for the equilibrium distribution of the particles at  $t = 0$ . The effective diffusivity  $D_e$ , which is measured by PFG NMR, is related to the MSDs via (2).

It has earlier been shown [23] that (4) can be solved to yield  $D_e$ :

$$D_e(t) = D_0 \left[ 1 - \frac{D_0}{3t} \left( \frac{1}{kT} \right)^2 \int_0^t dt_1 \int_0^{t_1} dt_2 \langle \mathbf{f}(t_2) \mathbf{f}(0) \rangle \right], \quad (9)$$

where the force-force autocorrelation function  $\langle \mathbf{f}(t)\mathbf{f}(0) \rangle$  is defined as

$$\langle \mathbf{f}(t)\mathbf{f}(0) \rangle = \frac{1}{Z} \int \int d^3\mathbf{r}_1 d^3\mathbf{r}_0 W(\mathbf{r}_1, \mathbf{r}_0; t) \exp \left\{ -\frac{U(\mathbf{r}_0)}{kT} \right\} \frac{\partial}{\partial \mathbf{r}_1} U(\mathbf{r}_1) \frac{\partial}{\partial \mathbf{r}_0} U(\mathbf{r}_0). \quad (10)$$

By substituting  $W(\mathbf{r}_1, \mathbf{r}_0; t)$ , in analogue with (5), with

$$W(\mathbf{r}_1, \mathbf{r}_0; t) = \exp \left\{ -\frac{U(\mathbf{r}_1)}{2kT} \right\} \Psi(\mathbf{r}_1, \mathbf{r}_0; t), \quad (11)$$

(10) becomes

$$\langle \mathbf{f}(t)\mathbf{f}(0) \rangle = \frac{(2kT)^2}{Z} \int \int d^3\mathbf{r}_1 d^3\mathbf{r}_0 \frac{\partial}{\partial \mathbf{r}_1} \exp \left\{ -\frac{U(\mathbf{r}_1)}{2kT} \right\} \Psi(\mathbf{r}_1, \mathbf{r}_0; t) \frac{\partial}{\partial \mathbf{r}_0} \exp \left\{ -\frac{U(\mathbf{r}_0)}{2kT} \right\}. \quad (12)$$

Notably,  $\Psi(\mathbf{r}_1, \mathbf{r}_0; t)$  satisfies (6). The formal solution of the latter equation can be given as

$$\Psi(\mathbf{r}_1, \mathbf{r}_0; t) = \exp \left\{ \tau \hat{L}_1 \right\} \Psi(\mathbf{r}_1, \mathbf{r}_0; 0), \quad (13)$$

where the Liouville operator  $\hat{L}_1$  is

$$\hat{L}_1 = \Delta_1 + \frac{1}{2} \left[ \Delta_1 \tilde{U}(\mathbf{r}_1) - \frac{1}{2} (\nabla_1 \tilde{U}(\mathbf{r}_1))^2 \right]. \quad (14)$$

The subscript 1 in (14) implies that the differentiation is performed over the position coordinates  $\mathbf{r}_1$ . By noting that  $W(\mathbf{r}_1, \mathbf{r}_0; 0) = \delta(\mathbf{r}_1 - \mathbf{r}_0)$ , where  $\delta(x)$  is the Dirac delta function, and by using (11), the autocorrelation function  $\langle \mathbf{f}(t)\mathbf{f}(0) \rangle$ , as given by (12), can finally be given as

$$\langle \mathbf{f}(t)\mathbf{f}(0) \rangle = \frac{(2kT)^2}{Z} \int \int d^3\mathbf{r}_1 d^3\mathbf{r}_0 \left( \frac{\partial}{\partial \mathbf{r}_1} e^{-\frac{U(\mathbf{r}_1)}{2kT}} \frac{\partial}{\partial \mathbf{r}_0} e^{-\frac{U(\mathbf{r}_0)}{2kT}} \right) \exp \left\{ \tau \hat{L}_1 \right\} \delta(\mathbf{r}_1 - \mathbf{r}_0). \quad (15)$$

The major difficulty in evaluating (15) is imposed by the necessity to calculate the function

$$\tilde{W}(\mathbf{r}_1, \mathbf{r}_0; t) \equiv \exp \left\{ \tau \hat{L}_1 \right\} = \exp \left\{ D_0 t \left( \Delta_1 + \frac{1}{2kT} \left[ \Delta_1 U(\mathbf{r}_1) - \frac{1}{2kT} (\nabla_1 U(\mathbf{r}_1))^2 \right] \right) \right\}, \quad (16)$$

which cannot be done in the general case.

Let us therefore to consider an approximation, in which we neglect the terms containing the potential energy in the operator  $\hat{L}_1$  (14), i.e. assuming that  $\hat{L}_1 = \Delta_1$ . Under this condition,  $\tilde{W}(\mathbf{r}_1, \mathbf{r}_0; t)$  is nothing else than the Green's function for free, unrestricted diffusion, i.e.

$$\tilde{W}(\mathbf{r}_1, \mathbf{r}_0; t) = \exp \left\{ \tau \Delta_1 \right\} = \left( \frac{1}{4\pi D_0 t} \right)^{3/2} \exp \left\{ -\frac{(\mathbf{r}_1 - \mathbf{r}_0)^2}{4D_0 t} \right\}. \quad (17)$$

The approximation considered turns out to be a reasonable one for the relatively large pore sizes ( $R \gg a_0$ ) and for the observation times  $t$  satisfying the following condition

$$\tau_R = \frac{R^2}{D_0} \gg t \gg \frac{a_0^2}{D_0} = \tau_0. \quad (18)$$

In (18),  $\tau_0$  is a typical time during which the particles diffuse through the surface layer in which they experience a repulsive interaction with pore walls and  $\tau_R$  is the time to diffuse over distances of the order of the pore sizes. Note that the overall behavior of  $\langle \mathbf{f}(t)\mathbf{f}(0) \rangle$  is mainly determined by the ensemble of particles which, at initial times, were residing near the pore walls or within the surface layer  $a_0$ . In this respect, the condition 18 ensures that (i) statistics of the particle

trajectories between two successive encountering events of the surface layers is described by (17) and (ii) surface orientation between these two points does not change appreciably. With (17), the autocorrelation function simplifies to

$$\begin{aligned} \langle \mathbf{f}(t)\mathbf{f}(0) \rangle &= \\ &= \frac{(2kT)^2}{Z} \left( \frac{1}{4\pi D_0 t} \right)^{3/2} \int d^3\mathbf{r}_1 d^3\mathbf{r}_0 \left( \frac{\partial}{\partial \mathbf{r}_1} e^{-\frac{U(\mathbf{r}_1)}{2kT}} \frac{\partial}{\partial \mathbf{r}_0} e^{-\frac{U(\mathbf{r}_0)}{2kT}} \right) \exp \left\{ -\frac{(\mathbf{r}_1 - \mathbf{r}_0)^2}{4D_0 t} \right\}. \end{aligned} \quad (19)$$

Let us now to fix  $\mathbf{r}_0$  and to introduce a local coordinate system with  $Z(\mathbf{r}_0)$  axis being perpendicular and  $X(\mathbf{r}_0)$  and  $Y(\mathbf{r}_0)$  axes being parallel to the nearest pore walls, respectively. We may further assume that the potential  $U(\mathbf{r})$  varies only along  $Z(\mathbf{r}_0)$  direction, but not along  $X(\mathbf{r}_0)$  and  $Y(\mathbf{r}_0)$ . With the condition (18), (19) can be integrated over the coordinates of the position vector  $\mathbf{r}_1$  which are parallel to  $X(\mathbf{r}_0)$  and  $Y(\mathbf{r}_0)$ :

$$\begin{aligned} \langle \mathbf{f}(t)\mathbf{f}(0) \rangle &= \\ &= \frac{(2kT)^2}{Z} \left( \frac{1}{4\pi D_0 t} \right)^{1/2} \int d\tilde{z}_1 d\tilde{z}_0 d\tilde{x}_0 d\tilde{y}_0 \left( \frac{\partial e^{-\frac{U(\tilde{z}_1)}{2kT}}}{\partial \tilde{z}_1} \frac{\partial e^{-\frac{U(\tilde{z}_0)}{2kT}}}{\partial \tilde{z}_0} \right) \exp \left\{ -\frac{(\tilde{z}_1 - \tilde{z}_0)^2}{4D_0 t} \right\}. \end{aligned} \quad (20)$$

Note that have introduced a curvilinear coordinate system  $\tilde{x}_i(\mathbf{r}_0)$ ,  $\tilde{y}_i(\mathbf{r}_0)$ , and  $\tilde{z}_i(\mathbf{r}_0)$ , which is a function of only the initial position vector  $\mathbf{r}_0$ , but not  $\mathbf{r}_1$  due to (18). Indeed, as it has been discussed in the preceding paragraphs, for the time intervals considered the global surface curvature can be neglected.

The scalar product in the brackets in the integral on the right side hand of (20) is non-zero only within the surface layer close to the pore walls, i.e. when  $|\tilde{z}_i(\mathbf{r}_0)| < a_0$ , where the gradient of the potential  $U(\mathbf{r})$  has a non-zero value. Because  $D_0 t \gg a_0^2$ , we may further use an approximation

$$\exp \left\{ -\frac{(\tilde{z}_1 - \tilde{z}_0)^2}{4D_0 t} \right\} \approx 1. \quad (21)$$

This allows to integrate (20) over the  $\tilde{z}_i$  variables:

$$\int d\tilde{z}_i \frac{\partial}{\partial \tilde{z}_i} e^{-\frac{U(\tilde{z}_i)}{2kT}} = 1. \quad (22)$$

Integration over  $\tilde{x}_i(\mathbf{r}_0)$  and  $\tilde{y}_i(\mathbf{r}_0)$  yields the total surface area  $S$  of the pore walls,

$$\int d\tilde{x}_0(\mathbf{r}_0) d\tilde{y}_0(\mathbf{r}_0) = S. \quad (23)$$

With (8), (22), and (23),  $\langle \mathbf{f}(t)\mathbf{f}(0) \rangle$  is obtained as

$$\langle \mathbf{f}(t)\mathbf{f}(0) \rangle = (kT)^2 \frac{S}{V_p} \frac{2}{\sqrt{\pi D_0 t}}. \quad (24)$$

Finally, substituting (24) into (9), results in the short-time effective diffusivity

$$D_e(t) = D_0 \left( 1 - \frac{8}{9} \frac{S}{V_p} \sqrt{\frac{D_0 t}{\pi}} \right), \quad (25)$$

which is compliant with the previously derived results and differs only by the numerical constant 8/9, as compared to 4/9 in (25).

### 3. Discussion and conclusions

The diffusivity behavior at short times, as given by (3), was derived in [7] using the Fick's diffusion equation. In this approach, the existence of the impermeable pore walls is accounted for by introducing specific boundary conditions, namely by letting no flux through the pore walls or by equating the gradient of the Green's function in the normal direction to the pore walls to zero,  $\partial W(\mathbf{r}; t)/\partial r_n=0$ . In contrast, in this work the existence of the pore walls is considered on a more fundamental level by considering Brownian particles diffusing in a force field generated by the solid matrix, i.e. by applying the Smoluchowski diffusion equation. The penalty is, however, the complexity of the equations arisen, which cannot be solved for arbitrary potential fields. It is therefore certain approximations, e.g. as given by (17), have been considered. Their rigorous justification remains however under discussion.

Irrespective of the approximations used, the result obtained in this study can be considered as a rigorous upper-bound solution for the numerical constant in (25). This can be shown by taking into account the terms in the operator  $\hat{L}_1$  (14), which were neglected upon the derivation of (25). Indeed, it turns out that the integral

$$\int_{-\sqrt{D_0 t}}^{\sqrt{D_0 t}} d\tilde{z}_1 \left( \frac{\partial^2 U(z_1)}{\partial z_1^2} - \frac{1}{2kT} \left( \frac{\partial U(z_1)}{\partial z_1} \right)^2 \right) \approx -\frac{1}{2kT} \int_{-\sqrt{D_0 t}}^{\sqrt{D_0 t}} d\tilde{z}_1 \left( \frac{\partial U(z_1)}{\partial z_1} \right)^2 \leq 0 \quad (26)$$

appears to be negative. This means that the Green's function (16) will decay faster as compared to that given by (17). The faster Green's function decay, the higher is the effective diffusivity, implying a lower numerical constant in (25).

In the light of the discrepancy established between the results obtained with the two approaches, (3) and (25), it is instructive to show under which conditions (3) can be obtained using the Smoluchowski equation. Because we are concerned with the time intervals satisfying (18), the Brownian particles can displace by the distances  $\sqrt{D_0 t}$  much smaller than the typical curvature  $R$  of the pore walls. Hence diffusion parallel to the pore walls can be considered unaltered by the presence of the solid matrix and described by the Green's function for free diffusion. This justifies that the integration over the  $\tilde{x}_1(\mathbf{r}_0)$  and  $\tilde{y}_1(\mathbf{r}_0)$  variables in (19), i.e. the validity of (20). On the other hand, the times considered are much longer than the typical times  $\tau_0 \approx a_0^2/D_0$  the particles spend within the surface layers where they interact with the pore walls. It is therefore the functional form of the Green's function in the direction collinear with  $\tilde{z}_1(\mathbf{r}_0)$  can be approached by the Green's function for a half-space convoluted with the equilibrium Boltzmann distribution, i.e.

$$W_z(z_1; t) = \frac{2}{\sqrt{4\pi D_0 t}} \exp \left\{ -\frac{z_1^2}{4D_0 t} \right\} \exp \left\{ -\frac{U(z_1)}{kT} \right\}. \quad (27)$$

With (27) and (10) one can readily obtain (3). In a similar way, (3) has earlier been obtained [24].

The derivation presented in the preceding paragraph poses an important question about which of the approximations used, (17) or (27), can better describe the dynamics of the Brownian particles confined to porous solids. This question can be addressed by either performing diffusion experiments using well-characterized porous materials or by computer simulation studies. In the former case, special care has to be taken to obtain accurately the surface-to-volume ratio of the porous material and to properly account for the surface relaxation effects [8, 25, 26], which can be challenging problems. These difficulties can readily be excluded in computer simulations, e.g. in molecular dynamics studies, in which all relevant parameters can be controlled and the applicability of (17) and (27) can be verified. This work is under progress.

## References

1. Einstein A., *Ann. Phys.-Berlin* **17**, 549 (1905).
2. Cussler E. L., *Diffusion: Mass Transfer in Fluid Systems*, 3rd ed. (Cambridge University Press, Cambridge, 2009).
3. Kimmich R., *NMR: Tomography, Diffusometry, Relaxometry* (Springer-Verlag, Berlin Heidelberg, 1997).
4. Price W. S., *NMR Studies of Translational Motion* (University Press, Cambridge, 2009).
5. Callaghan P. T., *Translational Dynamics and Magnetic Resonance* (Oxford University Press, New York, 2011).
6. Grebenkov D. S., *Rev. Mod. Phys.* **79**, 1077 (2007).
7. Mitra P. P., Sen P. N., Schwartz L. M., Ledoussal P., *Phys. Rev. Lett.* **68**, 3555 (1992).
8. Mitra P. P., Sen P. N., Schwartz L. M., *Phys. Rev. B* **47**, 8565 (1993).
9. Latour L. L., Mitra P. P., Kleinberg R. L., Sotak C. H., *J. Magn. Reson. A* **101**, 342 (1993).
10. Novikov D. S., Fieremans E., Jensen J. H., Helpert J. A., *Nat. Phys.* **7**, 508 (2011).
11. Hurlimann M. D., Helmer K. G., Latour L. L., Sotak C. H., *J. Magn. Reson. A* **111**, 169 (1994).
12. Sorland G. H., *J. Magn. Reson.* **126**, 146 (1997).
13. Gjerdaker L., Sorland G. H., Aksnes D. W., *Microporous Mesoporous Mat.* **32**, 305 (1999).
14. Johns M. L., Gladden L. F., *J. Colloid Interface Sci.* **238**, 96 (2001).
15. Butler J. P., Mair R. W., Hoffmann D., Hrovat M. I., Rogers R. A., Topulos G. P., Walsworth R. L., Patz S., *J. Phys.: Condens. Matter* **14**, L297 (2002).
16. Szutkowski K., Klinowski J., Jurga S., *Solid State Nucl. Magn. Reson.* **22**, 394 (2002).
17. Miller G. W., Carl M., Mata J. F., Cates G. D., Mugler J. P., *IEEE Trans. Med. Imaging* **26**, 1456 (2007).
18. Bogdan M., Parnau A., Badea C., Ardelean I., *Appl. Magn. Reson.* **34**, 63 (2008).
19. Tyurin V. A., Maklakov A. I., *Colloid J.* **64**, 190 (2002).
20. Muncaci S., Ardelean I., *Appl. Magn. Reson.* **44**, 837 (2013).
21. Doi M., Edwards S., *The Theory of Polymer Dynamics* (Oxford University Press, Oxford, 1986).
22. Chang D. B., Cooper R. L., Young A. C., Martin C. J., Ancker-Johnson B., *J. Theor. Biol.* **50**, 285 (1975).
23. Fatkullin N. F., *J. Exp. Theor. Phys.* **98**, 2030 (1990).
24. Valiullin R., Skirda V., *J. Chem. Phys.* **114**, 452 (2001).
25. Sen P. N., *Concepts Magn. Reson. Part A* **23A**, 1 (2004).
26. Zielinski L. J., *J. Chem. Phys.* **121**, 352 (2004).

# The peculiarities of the operation of the superconducting spin valve

I.A. Garifullin<sup>1,\*</sup>, N.N. Garif'yanov<sup>1</sup>, P.V. Leksin<sup>1</sup>, A.A. Kamashev<sup>1</sup>, Ya.V. Fominov<sup>2,3</sup>,  
J. Schumann<sup>4</sup>, V. Kataev<sup>4</sup>, B. Büchner<sup>4,5</sup>

<sup>1</sup>Zavoisky Physical-Technical Institute, Kazan Scientific Center of Russian Academy of Sciences, 420029 Kazan, Russia

<sup>2</sup>L. D. Landau Institute for Theoretical Physics RAS, 119334 Moscow, Russia

<sup>3</sup>Moscow Institute of Physics and Technology, 141700 Dolgoprudny, Russia

<sup>4</sup>Leibniz Institute for Solid State and Materials Research IFW Dresden, D-01171 Dresden, Germany

<sup>5</sup>Institut für Festkörperphysik, Technische Universität Dresden, D-01062 Dresden, Germany

\**E-mail: ilgiz0garifullin@gmail.com*

Review of our recent results concerning the spin valve effect are presented. Using the spin switch design F1/F2/S proposed theoretically that comprises a ferromagnetic bilayer (F1/F2) as a ferromagnetic component, and an ordinary superconductor (S) as the second interface component, we have realized for the first time a full spin switch effect for the superconducting current. For  $\text{CoO}_x/\text{Fe1}/\text{Cu}/\text{Fe2}/\text{In}$  multilayered systems with varying Fe2-layer thickness we observed the sign-changing oscillating behavior of the spin valve effect  $\Delta T_c = T_c^{\text{AP}} - T_c^{\text{P}}$  (here  $T_c^{\text{AP}}$  and  $T_c^{\text{P}}$  are the superconducting transition temperatures for antiparallel and parallel orientations of magnetizations of the F1 and F2 layers, respectively). We have also studied the angular dependence of  $T_c$  for the spin valve system  $\text{CoO}_x/\text{Fe1}/\text{Cu}/\text{Fe2}/\text{Pb}$ . We found that this dependence is nonmonotonic when passing from the parallel to the antiparallel case of mutual orientation of magnetizations of the Fe1 and Fe2 layers and reveals a distinct minimum near the orthogonal configuration. The analysis of the data in the framework of the superconducting triplet spin valve theory gives direct evidence for the long-range triplet superconductivity arising due to noncollinearity of the two magnetizations.

**PACS:** 74.45+c, 74.25.Nf, 74.78.Fk

**Keywords:** superconductor, ferromagnet, proximity effect

## 1. Introduction

During the last decades the growing attention to the ideas and experiments concerning the development of elements of superconducting spintronics is clearly seen (see, e.g. [1,2]). In these works, in particular, the interest in the superconductor/ferromagnet/superconductor (S/F/S) heterostructures as possible elements of quantum logics was emphasized [3]. An element of a qubit [4,5] is based on the Josephson  $\pi$ -contact [6,7]. Under certain conditions such contact can be implemented in the S/F/S thin-film heterostructure. The S/F contact itself is of long-standing fundamental interest (see, e.g., [8]).

The antagonism of superconductivity and ferromagnetism consists of strong suppression of superconductivity by ferromagnetism because ferromagnetism requires parallel (P) and superconductivity requires antiparallel (AP) orientation of spins. The exchange splitting of the conduction band in strong ferromagnets which tends to align electron spins parallel is larger by orders of magnitude than the coupling energy for the AP alignment of the electron spins in the Cooper pairs in conventional superconductors. Therefore the singlet pairs with AP spins of electrons will be destroyed by the exchange field. For this reason the Cooper pairs can penetrate

into an F-layer only over a small distance  $\xi_F$ . For pure Fe the value of  $\xi_F$  is less than 1 nm (see, e.g., [9]). All details of the S/F proximity effect are well described in reviews [10–13]. One can see from these reviews that many questions concerning physics of the S/F proximity are already clarified. Nevertheless, some theoretical predictions still need to be confirmed. First, that is the implementation of the full spin valve effect based on the S/F proximity effect. The results we present in this paper may be considered as the first positive example in this field. Second, this is the long-range triplet component in the superconducting condensate which should be generated in the S/F systems and exist in the presence of the singlet superconductivity only. All experiments indicate the existence of the triplet superconductivity in the S/F/S systems. Nevertheless, the origin of the generation of the triplet superconductivity is not always confirmed by experiments.

The physical origin of the spin switching based on the S/F proximity effect relies on the idea to control the pair-breaking, and hence the superconducting (SC) transition temperature  $T_c$ , by manipulating the mutual orientation of the magnetizations of the F-layers in a heterostructure comprising, e.g., two F- and one S-layer in a certain combination. This is because the mean exchange field from two F-layers acting on Cooper pairs in the S-layer is smaller for the AP orientation of the magnetizations of these F-layers compared to the P case. The possibility to develop a real switch based on the S/F proximity effect has been theoretically substantiated in 1997 by Sanjiun Oh *et al.* [14]. They proposed the F1/F2/S layer scheme where an S-film is deposited on top of two F-layers. The thickness of F2 should be smaller than  $\xi_F$  to allow the superconducting pair wave function to penetrate into the space between F1- and F2-layers. Two years later a different construction based on an F/S/F trilayer was proposed theoretically by Tagirov [15] and Buzdin *et al.* [16, 17]. Several experimental works confirmed the predicted influence of the mutual orientation of the magnetizations in the F/S/F structure on  $T_c$  (see, e.g., [18–21]). However, the difference in  $T_c$  between the AP and P orientations  $\Delta T_c = T_c^{\text{AP}} - T_c^{\text{P}}$  (here  $T_c^{\text{AP}}$  and  $T_c^{\text{P}}$  are the superconducting transition temperatures for antiparallel and parallel orientations of magnetizations of the F1 and F2 layers, respectively) turns out to be smaller than the width of the superconducting transition  $\delta T_c$  itself. Hence a full switching between the normal and the superconducting state was not achieved. Implementation of a design similar to the F1/N/F2/S layer scheme by Oh *et al.* [14] with a  $[\text{Fe/V}]_n$  antiferromagnetically coupled superlattice instead of a single F1/N/F2 trilayer [22, 23] is not actually the spin switch device because the system can not be switched from the AP to P orientations of the magnetizations instantaneously. At the same time the analysis of the temperature dependence of the critical field has shown that implicitly  $\Delta T_c$  can reach up to 200 mK at the superconducting transition width  $\delta T_c \sim 100$  mK. Comparison of the results obtained for both proposed constructions of the spin switches gives grounds to suppose that the scheme by Oh *et al.* may be more promising for the realization of the full spin switch effect. Later on a set of asymmetric construction was proposed [24–26]. It is necessary to note that they are not still experimentally tested.

Recently [27] it was shown that precise analysis of the processes taking place in the course of the penetration of the Cooper pair from the S- into the F-layer predicts the generation of the triplet component in the superconducting condensate in the F-layer. Within the homogeneous ferromagnet such a component has zero spin of the Cooper pair ( $S_z = 0$ ). It is certainly can not be experimentally detected. At the same time the magnetic inhomogeneity leads to  $S_z = \pm 1$  [27]. In this case the triplet component can be indicated through the anomalously deep penetration of the superconducting condensate into the ferromagnet. This component should manifest itself in the systems with noncollinear orientation of magnetizations in the F-layer [28]

as well as in the systems with spatial or momentum dependence of the exchange field [29]. The series of the experiments was performed (see, e.g., reviews [12, 13, 30]) which shows the anomalous deep penetration of the superconducting condensate into the F-layer typical for the triplet superconductivity.

In the following we review the results of our recent studies of the spin valve effect [31–35].

## 2. Results and discussion

### 2.1. Full spin valve for the superconducting current in a superconductor/ferromagnet thin film heterostructure

We have fabricated a set of samples MgO(001)/CoO<sub>x</sub>/Fe1/Cu/Fe2/In which show a full switching between the SC and normal states when changing the mutual orientation of the magnetizations of F1 and F2 layers. In this construction MgO(001) is a high quality single crystalline substrate, cobalt oxide antiferromagnetic (AFM) layer plays a role of the bias layer which pins the magnetization of the F1 layer; Fe stands for the ferromagnetic F1- and F2-layers; Cu as a normal metallic N-layer which decouples the magnetizations of F1- and F2-layers; finally In is an S-layer.

The sample preparation was done by electron beam evaporation on room temperature substrates at the base pressure  $2 \cdot 10^{-8}$  mbar. The thickness of the growing films was measured by a quartz crystal monitor system. The Co oxide films were prepared by a two-step process consisting of the evaporation of a metallic Co film followed by the plasma oxidation converting Co into CoO<sub>x</sub> layer.

Before starting the measurements of the superconducting transition temperature at different mutual orientation of magnetizations of the F-layers the in-plane magnetic hysteresis loops of sample #3 in the direction of the magnetic field along the easy axis was measured by a SQUID magnetometer and is shown in Fig. 1a. This step is necessary to obtain the Fe-layers' magnetization behavior and to determine the magnetic field range where AP and P states can be achieved. The sample was cooled down in a magnetic field of +4 kOe and measured at  $T = 4$  K. Bearing in mind that the Néel temperature of the cobalt oxide is of the order of 250 K, after such cooling procedure the magnetization of the Fe1-layer turns out to be pinned by the exchange field of the AFM-layer. The magnetic field was varied from +4 kOe to -6 kOe and back again to the value of +4 kOe. Both limits correspond to the ori-

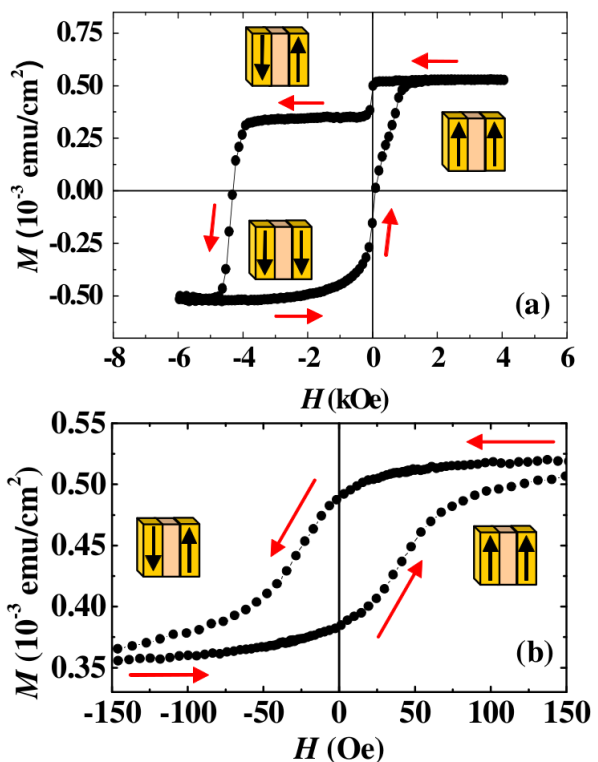


**Figure 1.** (a) Magnetic hysteresis loop for sample #3 CoO<sub>x</sub>(4 nm)/Fe1(2.4 nm)/Cu(4 nm)/Fe2(0.5 nm)/In(230 nm). Panel (b) shows part of the minor hysteresis loop for sample #3, obtained when decreasing the magnetic field from +4 kOe down to -1 kOe and increasing it up to +1 kOe. The amplitude of the minor hysteresis loops is proportional to the thickness of the free F2 layer. Coercive and saturation fields are the largest for the sample #3 and sharply decrease with increasing  $d_{\text{Fe2}}$ . [31, 33]

entation of the magnetizations of the F1- and F2-layers parallel to the applied field. For the studied sample by decreasing the field from +4kOe to the field value of the order of +50 Oe the magnetization of the free F2 layer starts to decrease. At the same time the magnetization of the F1-layer is kept by the bias  $\text{CoO}_x$  layer until the magnetic field of  $-4\text{kOe}$  is reached. Thus, in the field range between  $-0.3$  and  $-3.5\text{kOe}$  the mutual orientation of two F-layers is antiparallel. The minor hysteresis loops on the low field scale were obtained with decreasing the field from +4kOe down to  $-1\text{kOe}$  and increasing it again up to  $+1\text{kOe}$ . An exemplary loop for sample #3 is shown in Fig. 1b. In order to study the influence of the mutual orientation of the magnetizations on  $T_c$  we have cooled the samples down from room to a low temperature at the magnetic field of 4kOe applied along the easy axis of the sample just as we did it when performing the SQUID magnetization measurements. For this field both F-layers' magnetizations are aligned (see the magnetic hysteresis loops shown in Fig. 1).

Then at the in-plane magnetic field value of  $H_0 = \pm 110\text{ Oe}$  the temperature dependence of the resistivity  $R$  was recorded. In the following we focus on the spin valve sample #3  $\text{CoO}_x(4\text{ nm})/\text{Fe1}(2.4\text{ nm})/\text{Cu}(4\text{ nm})/\text{Fe2}(0.5\text{ nm})/\text{In}(230\text{ nm})$  (see Fig. 2).

For this sample  $\Delta T_c = T_c^{\text{AP}} - T_c^{\text{P}} = 19\text{ mK}$  (see Fig. 2b with an enlarged temperature scale). We also performed similar resistivity measurements of the reference sample #2R with only one Fe layer. For this sample we found  $T_c = 1.60\text{ K}$ , which does not depend on the magnetic field direction (see Fig. 2c). This  $T_c$  value is lower than that for the In single layer film (sample #1) and higher than for sample #3 (Fig. 2). This means that  $T_c$  is suppressed by the F2 layer and in turn is sensitive to the influence of the F1 layer separated from the SC In layer by a 0.5 nm thick F2 Fe layer and 4 nm thick Cu layer. As can be expected from the the S/F proximity theory, with increasing the thickness of the free F2 layer  $\Delta T_c$  decreases and becomes practically zero at 2.6 nm thick F2 layer.

The observed shift  $\Delta T_c = 19\text{ mK}$  is not the largest one among the data published before (cf., e.g., Ref. [20], where  $\Delta T_c \simeq 41\text{ mK}$  at  $\delta T_c \sim 100\text{ mK}$ ). However, very importantly it is substantially larger than  $\delta T_c$  which is of the order of 7 mK for sample #3 at  $H_0 = 110\text{ Oe}$ . This opens a possibility to switch off and on the superconducting current flowing through our samples *completely* within the temperature range corresponding to the  $T_c$ -shift by changing the mutual orientation of magnetization of F1 and F2 layers. To demonstrate this we have performed the measurements of the resistivity of sample #3 by sweeping slowly the temperature within the  $\Delta T_c$  and switching the magnetic field between +110 and  $-110\text{ Oe}$ . This central result of this part of our review is shown in Fig. 3. It gives straightforward evidence for a complete on/off switching of the SC current flowing through the sample. To the best of our knowledge this result is the first example of the realization of the full spin valve effect for the superconducting current for the layered system with the ideal contact between the layers.

## **2.2. Interference effects**

We studied the dependence of  $\Delta T_c$  on the thickness of the intermediate layer Fe2 for the series of the samples  $\text{CoO}_x(4\text{ nm})/\text{Fe1}(3\text{ nm})/\text{Cu}(4\text{ nm})/\text{Fe2}(d_{\text{Fe2}})/\text{In}(230\text{ nm})$  with the value of  $d_{\text{Fe2}}$  lying between 0.4 and 5.2 nm. The values of the switching field  $H_0$  around  $\pm 100\text{ Oe}$  turn out to be optimal for the operation of our spin valve samples. Higher values of  $H_0$  bring the system too close to the critical field  $H_c$  thus reducing strongly the  $T_c$ . On the other hand, a reduction of  $H_0$  substantially below  $\sim 100\text{ Oe}$  has also a negative twofold impact. The final width of the minor hysteresis loop is related to the formation of magnetic domains in the F2 layer, whereas the width of the loop decreases with increasing the thickness of the layer  $d_{\text{F2}}$  (Fig. 4a and b).

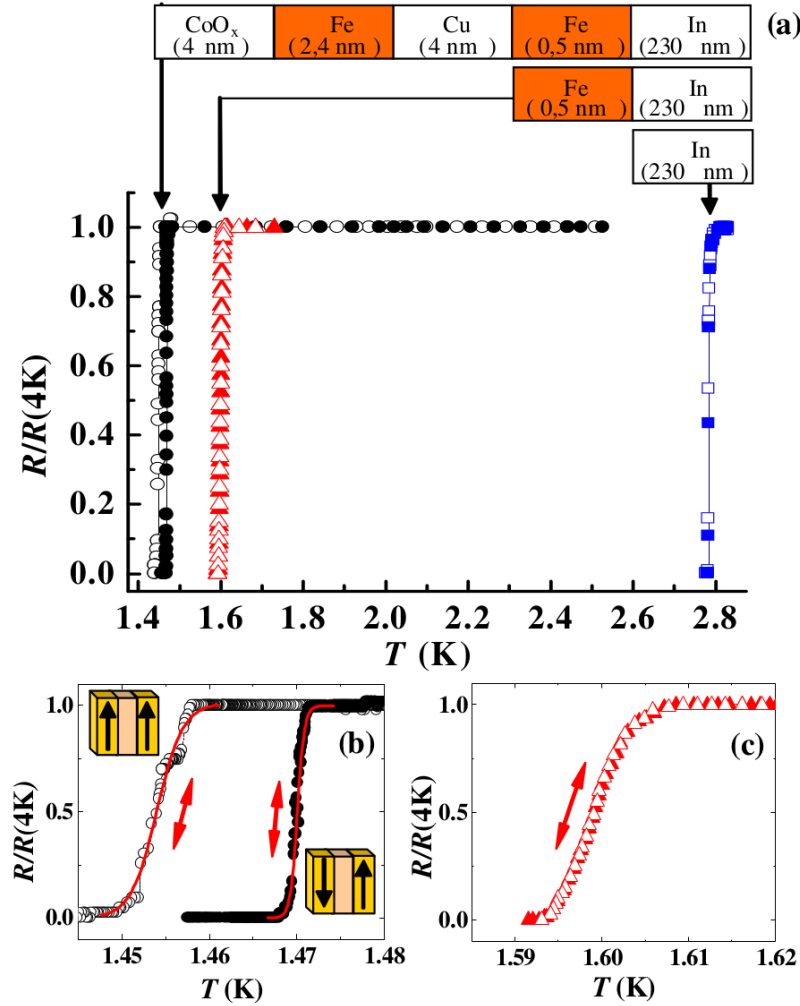


**Figure 2.** (a) Overview of the resistivity transition curves. The spin valve sample #3  $\text{CoO}_x(4 \text{ nm})/\text{Fe}1(2.4 \text{ nm})/\text{Cu}(4 \text{ nm})/\text{Fe}2(0.5 \text{ nm})/\text{In}(230 \text{ nm})$  is shown by black open ( $H_0 = +110 \text{ Oe}$ ) and closed ( $H_0 = -110 \text{ Oe}$ ) circles (see also panel (b) for detailed view). For the reference sample #2R  $\text{Fe}2(0.5 \text{ nm})/\text{In}(230 \text{ nm})$  the data are depicted by red open ( $H_0 = +110 \text{ Oe}$ ) and closed ( $H_0 = -110 \text{ Oe}$ ) triangles (see also panel (c) for detailed view). For the pure In sample #1  $\text{In}(230 \text{ nm})$  the data are presented by blue open ( $H_0 = +110 \text{ Oe}$ ) and closed ( $H_0 = -110 \text{ Oe}$ ) squares [31].

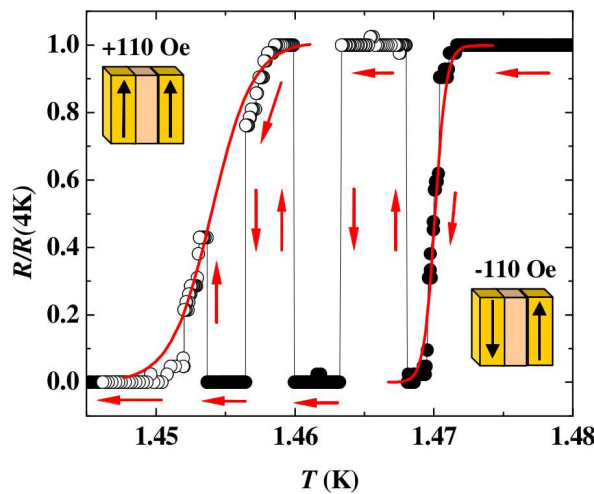


**Figure 3.** Switching between normal and superconducting states in the spin valve sample #3 during a slow temperature sweep by applying the magnetic field  $H_0 = -110 \text{ Oe}$  (closed circles) and  $H_0 = +110 \text{ Oe}$  (opened circles) in the sample plane [32, 33].

As soon as  $H_0$  gets smaller than the field strength necessary to fully polarize the magnetization of the F2 layer in the P or AP configuration, the F2 layer enters the domain state. This yields a strong broadening of the width of the superconducting transition  $\delta T_c$  (Fig. 4c and d) which clearly correlates with the width of the hysteresis loop. The increase of  $\delta T_c$  is obviously related to the occurrence of the inhomogeneous stray field perpendicular to the In film which is induced by the domains. Just in this geometry superconductivity in the In layer is extremely sensitive to magnetic fields. The second negative effect is the reduction of the difference in the  $T_c$  for the two opposite directions of the applied field  $T_c(-H_0) - T_c(H_0)$  (Fig. 4e and f), since due to the domains neither the AP nor P configuration can be fully reached at small  $H_0$ . Therefore the most optimal regime for the operation of the spin valve can be achieved in our samples by a *full suppression* of the domain state by application of a strong enough switching field  $H_0$  which yet should not be too close to  $H_c$ .

By studying our spin valve samples in this optimal regime we have observed a remarkable change of the *sign* of the spin valve effect with increasing the thickness of the free F2 layer  $d_{\text{Fe2}}$  (Fig. 4f and Fig. 5). It is positive, as expected, in the thickness range  $0.4 \text{ nm} \leq d_{\text{Fe2}} \leq 0.8 \text{ nm}$ . Surprisingly, for a rather broad range of thicknesses  $1 \text{ nm} \leq d_{\text{Fe2}} \leq 2.6 \text{ nm}$  the spin valve effect has a negative sign, i.e. the  $T_c$  for the parallel mutual orientation of the magnetizations of the F1 and F2 layers is larger than for the antiparallel orientation. Moreover, the magnitude  $\Delta T_c$  of this inverse effect is even larger than that of the positive direct effect (Fig. 5).

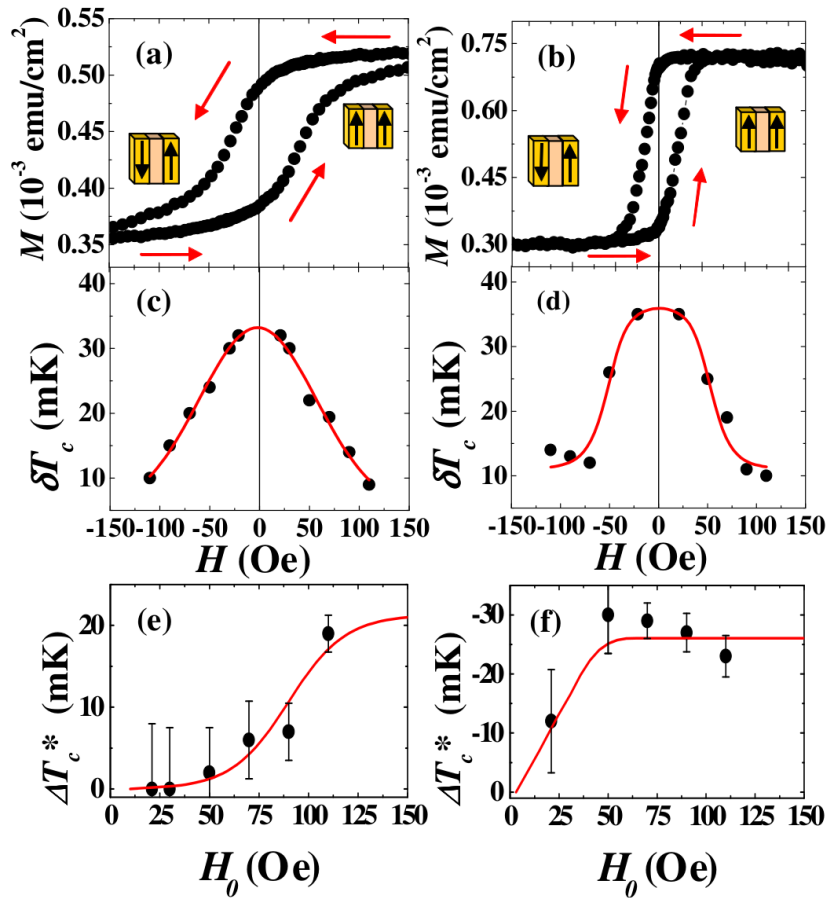


**Figure 4.** The minor hysteresis loops for the spin valve samples with  $d_{\text{Fe2}} = 0.5 \text{ nm}$  (a) and  $d_{\text{Fe2}} = 1.3 \text{ nm}$  (b) and the dependencies of  $\delta T_c$  and  $\Delta T_c^*$  on the magnetic field value: the panels (c) and (e) correspond to the sample with  $d_{\text{Fe2}} = 0.5 \text{ nm}$  and the panels (d) and (f) correspond to the sample with  $d_{\text{Fe2}} = 1.3 \text{ nm}$  [32, 33].

In the following we will discuss this striking observation with regard to three scenarios: (i) occurrence of magnetic domains in the F-layers; (ii) spin accumulation in the S-layer; (iii) quantum interference of the Cooper pair wave function in the S/F multilayer. “Old” theory of the spin valve effect based on the S/F proximity effect [14] predicts only the direct effect, i. e.  $\Delta T_c > 0$ . The inverse effect with  $T_c^{\text{AP}} < T_c^{\text{P}}$  has been reported earlier for various systems. Its origin was discussed in terms of two, in fact conflicting, scenarios (i) and (ii). In model (i) magnetic domains may influence superconductivity in two different ways. Rusanov *et al.* [36] who studied Nb/Permalloy bilayers showed that the F-layer forms a domain state near its coercive field and the S-layer experiences a lowered average exchange field seen by the Cooper pairs. This yields a direct effect which may be called a Néel’s domain wall induced enhancement of  $T_c$ .

Model (ii) is based on the giant magnetoresistance effect and predicts that the spin-polarized charge carriers should experience an enhanced spin-dependent reflection at the S/F interface in the AP state. Hence, they can accumulate in the S-layer which gives rise to a reduction of the superconducting energy gap, provided that the thickness of the S-layer is smaller than the spin diffusion length [37].

The first two scenario can be surely excluded in our case bearing in mind the field dependences of different parameters (Fig. 4). As to the third scenario indeed in a ferromagnetic layer the Cooper pair acquires a nonzero momentum due to the Zeeman splitting of electron levels and thus its wave function should oscillate in space (see, e.g., [10–13]). If the F-layer is sufficiently thin, the wave function reflected from the surface of the F-layer opposite to the S/F interface can interfere with the incoming one. Depending on the layer’s thickness the interference at the S/F interface may be constructive or destructive. This should apparently lead to the enhancement of  $T_c$  or its decrease, respectively, thus naturally explaining our main result (Fig. 5).

Interestingly, there is a recent theory [38] where the same spin switch scheme F1/F2/S is considered. The starting points there do not strictly comply with the properties of our samples: F-layers were assumed to be weak ferromagnets, simplified boundary conditions were taken implying a 100 % transparency of the F2/S and F1/F2 interfaces for the electrons and superconductivity in the “dirty” limit in the F-layer ( $l_F < \xi_F$ ) were assumed. Here  $l_F$  is the mean free path of conduction electrons. In our samples the F-layer made of iron is a strong ferromagnet with the penetration depth of the Cooper pairs into the F-layer  $\xi_F \sim 1$  nm. In this case the transparency of the S/F interface should be reduced due to the exchange splitting of the conduction band in the F-layer [9]. Also the “dirty” limit is not realized owing to a small value of  $\xi_F$ . Finally the considered model does not involve the presence of the N-layer and assumes the F1-layer to be a half infinite ferromagnetic layer.

However, it is known that in practice the S/F proximity theories developed for the “dirty” limit deliver reliable results even beyond the domain of their applicability. Indeed, despite these differences we were able to obtain a reasonably good qualitative agreement between this theory and our experimental results as demonstrated by the fit curve to the experimental  $\Delta T_c(d_{\text{Fe2}})$ -

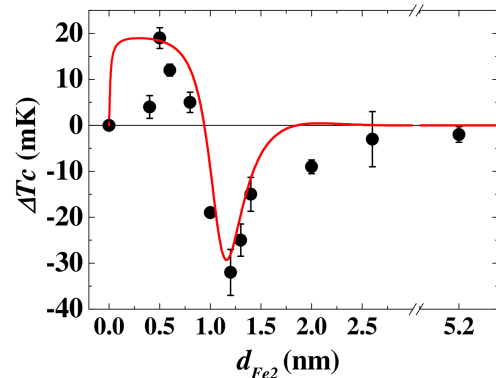


**Figure 5.** The dependence of the  $T_c$  shift  $\Delta T_c = T_c^{\text{AP}} - T_c^{\text{P}}$  on the Fe2-layer thickness  $d_{\text{Fe2}}$ . The applied switching field  $H = \pm 110$  Oe. Theoretical curve (solid line) corresponds to the calculated function  $[W(0)-W(\pi)]/W(0)$  (see [38]) normalized to our experimental data [32,33].

dependence in Fig. 5. An appreciable discrepancy with the experimental data point  $d_{\text{Fe2}} = 0.4$  nm occurs most probably because at this thickness a transition from a continuous to an island like Fe film at even smaller thicknesses  $d_{\text{Fe2}}$  does take place. The fit parameters turned out to be quite realistic. Nevertheless, it is rather desirable to get independent parameters obtained from another source. As such source the  $T_c(d_{\text{Fe2}})$  dependence should give access to the parameters of the S-layer and enable an independent estimate of the parameters of the F-layers and of the S/F interface. This is due to the fact that the value of the spin valve effect is less than 30 mK and the influence of the Fe1-layer is negligible within the scale of variation of the  $T_c(d_{\text{Fe2}})$ -dependence. A successful fitting of the  $\Delta T_c(d_{\text{Fe2}})$  dependence with this independent parameter set would provide an additional strong proof that interference of Cooper pair wave functions in the S/F proximity regime is responsible for the observed effects in the studied spin valve heterostructures.

The  $T_c(d_{\text{In}})$  dependence measured on a set of the samples with a fixed thickness of the Fe layer of 3 nm and varying In thickness  $d_{\text{In}}$  is shown in the inset of Fig. 6. It reveals a remarkably strong reduction of  $T_c$  with decreasing the  $d_{\text{In}}$  with a critical thickness for the vanishing of superconductivity  $d_{\text{In}}^{\text{crit}} \simeq 140$  nm.

A detailed dependence of the superconducting transition temperature  $T_c$  on the thickness of the Fe2 layer  $d_{\text{Fe2}}$  with the thickness of the In layer fixed at 230 nm is plotted in the main panel of Fig. 6. Comparing with the In stand alone film, the  $T_c$  drops sharply when introducing the Fe1 and Fe2 layers in the sample structure. A careful look on the data points for samples with  $d_{\text{Fe2}} \geq 0.5$  nm reveals damped oscillations of the superconducting transition temperature as a function of  $d_{\text{Fe2}}$ . With increasing  $d_{\text{Fe2}}$  the  $T_c$  first increases up to a local maximum at 2.2 K, then slightly decreases, passing through a local minimum of 2.0 K at  $d_{\text{Fe2}} \simeq 1$  nm, after that slightly increases again to a second local maximum at  $d_{\text{Fe2}} \simeq 1.3$  nm and finally saturates. Though these features are small, they cannot be ascribed to some sample artefacts or measurement uncertainties, but rather demonstrate a real physical property of the studied set of samples. The width of the superconducting transition for this series of samples does not exceed 30 mK. This

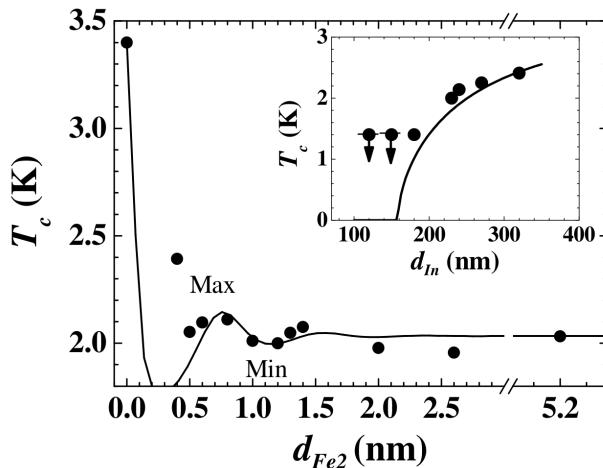


**Figure 6.** Superconducting transition temperature  $T_c$  versus the Fe2-layer thickness  $d_{\text{Fe2}}$  for the spin valve system  $\text{CoO}_x/\text{Fe1}/\text{Cu}/\text{Fe2}/\text{In}$  with a fixed thickness of the In layer  $d_{\text{In}} = 230$  nm. Inset shows the dependence of  $T_c$  on  $d_{\text{In}}$  for the set of the samples with a fixed thickness of the Fe layer  $d_{\text{Fe2}} = 3$  nm. Solid lines are theoretical fits (see the text) [33].

means that the error bars are smaller than the size of the data points in Fig. 6. Since we do not observe any broadening of the superconducting transition curve, the lateral length scale of the thickness fluctuations should be smaller than the superconducting coherence length. In this case the roughness parameter is irrelevant for the  $T_c(d_{\text{Fe2}})$  curve in Fig. 6. In addition our magnetization and ferromagnetic resonance results showing well defined sharp hysteresis loops and narrow resonance lines suggest that the Fe2 layer in our samples is continuous and uniform within the whole area of the film, at least down to 0.5 nm (the exceptional behavior of the sample with  $d_{\text{Fe2}} = 0.4$  nm is likely due to the island type of growth of the Fe2 layer at such small thickness). The easy axis of the Fe layers always lies in the plane of the film.

The proximity effect in bilayer S/F systems is usually described by the Usadel equations [39] valid in the “dirty” limit of the superconducting layer ( $l \ll \xi_0$ ). For the interpretation of our results we can use a theory for the S/F proximity effect by Tagirov [40]. It takes the finite transparency of the interface explicitly into account and is applicable for the case of a magnetic layer made of a strong ferromagnet. Such approach has been used successfully before, e.g., for the description of the oscillating behavior of the  $T_c$  in Pb/Fe bilayers by Lazar *et al.* [9]. Following the procedure described in [9] we can produce a theoretical curve drawn by a solid line in Fig. 6 which models reasonably well the experimental  $T_c(d_{\text{Fe2}})$  dependence. In particular, the small oscillations of  $T_c$  in the range  $0.5 \text{ nm} < d_{\text{Fe2}} < 2 \text{ nm}$  are well reproduced. Having established the set of parameters of the S/F proximity theory by Tagirov [40] for the  $T_c(d_{\text{Fe2}})$  dependence, we can revisit the analysis of the oscillating sign-changing dependence of the spin valve effect  $\Delta T_c(d_{\text{Fe2}})$  with the aid of the theory [38] (Fig. 5). Since the setups of these two theories are very different one should take care on the unification of the parameters. We have used these values as initial values in the modelling of the experimental dependence of the spin valve effect  $\Delta T_c(d_{\text{Fe2}})$  in the framework of the theory. Indeed, the best possible and quite satisfactory result of the modelling (Fig. 5) has been obtained by a minor variation of these initial values.

We have also performed the preliminary experimental study of the dependence of the spin valve effect on the thickness of the Fe1-layer [35]. In the theory [38] this layer was considered as half-infinite. We observed the monothonic increase of  $\Delta T_c$  when decreasing the Fe1-layer thickness from 5 down to 1 nm at two fixed values of  $d_{\text{Fe2}}$ . We extended the oprevious theory [38] for arbitrary thickness of the outer F-layer (Fe1 in notation of the present paper). The theoretical curve for  $\Delta T_c(d_{\text{Fe1}})$  and experimental data seem to be consistent. Note that the theory also predicts peculiarities of the spin valve effect at very small  $d_{\text{Fe1}}$  (due to interference features of the oscillatory proximity effect in the F-part), however we do not focus on them since we do not have experimental data for such small thicknesses due to island growth of films.

### **2.3. Triplet superconductivity**

Theory [38] predicts inevitable arising of the long range superconducting triplet component in the studied scheme of the spin valve.

In this part of our review the experimental evidence for generation of this component in the superconducting condensate in the multilayer spin valve heterostructure  $\text{CoO}_x/\text{Fe1}/\text{Cu}/\text{Fe2}/\text{Pb}$  where Lead stands instead of Indium is presented [34]. The basis of the present work has been formed by our earlier studies of the superconducting spin valve effect in the multilayer system  $\text{CoO}_x/\text{Fe1}/\text{Cu}/\text{Fe2}/\text{In}$  [31]. According to the theory [38] the activation of the triplet channel should be visible in an additional suppression of  $T_c$  for noncollinear arrangements of  $\mathbf{M}_{\text{Fe1}}$  and  $\mathbf{M}_{\text{Fe2}}$ . Unfortunately, such experiment on the  $\text{CoO}_x/\text{Fe1}/\text{Cu}/\text{Fe2}/\text{In}$  system turned out to be unrealizable under well-controlled conditions owing to a low value of  $T_c$  for indium and its extreme sensitivity to small out-of-plane tilting of the external magnetic field. In this respect Lead has much better superconducting critical parameters, which has determined its choice as an S-layer in the present work. The triplet contribution manifests itself as an observation in all spin valve samples of a very special dependence of the superconducting critical temperature  $T_c$  on the angle  $\alpha$  which the magnetization of the Fe2 layer  $\mathbf{M}_{\text{Fe2}}$  controlled by an external field makes with the magnetization of the pinned Fe1 layer. Examples of such dependences for selected spin-valve samples of different thickness  $d_{\text{Fe2}}$  are shown in Fig. 7. One can see that when changing the mutual orientation of magnetizations by a gradual in-plane rotation of the magnetic field from the P ( $\alpha = 0^\circ$ ) to the AP ( $\alpha = 180^\circ$ ) state  $T_c$  value does not change monotonically but

passes through a minimum. Importantly, for the reference sample consisting of just one Fe layer the angular variation of  $T_c$  lies within the error bars (not shown). In the following we argue that a characteristic minimum in the  $T_c(\alpha)$  close to  $\alpha = 90^\circ$  is a fingerprint of a long-range triplet superconducting component. The curve shown in Fig. 7 (left side panels) by dashed line displays imaginary monotonous angular dependence of  $T_c$  without taking into account for the triplet superconductivity. This is reference curve. Deviations  $\delta T_c$  of the actual  $T_c$  from the reference curves are, as the figures demonstrate, beyond the experimental error bars. The angular dependences of this deviation are shown on the right side panels (a), (b), and (c) of Fig. 7.

The dependence of the maximal deviation of  $T_c$  demonstrates monothonic decrease with increasing  $d_{\text{Fe}2}$ . Theory demonstrates good agreement with theoretical results.

Bearing in mind that the effect is not observed for the reference sample  $\text{CoO}_x/\text{Cu}/\text{Fe}/\text{Pb}$  with a single iron layer we interpret our finding as evidence for long-range triplet superconductivity that arises in the spin-valve samples with a noncollinear geometry of magnetizations of the Fe1 and Fe2 layers.

The suppression of  $T_c$  in the S layer of an S/F1/F2 proximity system studied in our work takes place due to “leakage” of Cooper pairs into the F-part. In this language, the generation of the long-range triplet superconductivity at noncollinear magnetizations opens up an additional channel for this leakage, hence  $T_c$  should be suppressed stronger. Note that the triplet superconducting correlations are generated from the singlet ones (conversion due to the exchange field),

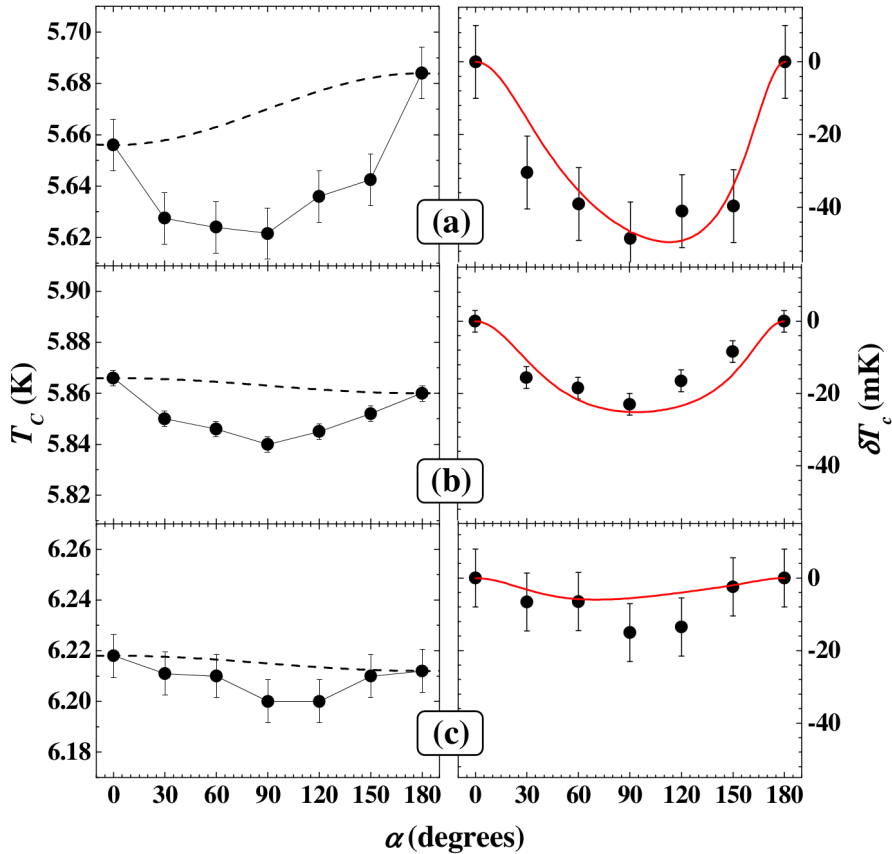


**Figure 7.** Left: dependence of the  $T_c$  on the angle between magnetizations of the Fe1 and Fe2 layers measured in a field  $H = 1$  kOe for the samples with  $d_{\text{Fe}2} = 0.6$  nm (a), 1.0 nm (b) and 1.5 nm (c). Dashed lines are the reference curves calculated without taking into account for triplet superconductivity. Right: deviations  $\delta T_c$  of the actual  $T_c$  values from the respective reference curves. Solid lines are theoretical results for  $\delta W$  (see the text) [34].

reducing the amplitude of the singlet component in the S layer and thus “draining the source” of superconductivity in the whole system. This effect is substantial since the magnitudes of the proximity-induced singlet and long-range triplet superconductivity can be of the same order near the interface of the S-layer (if the thickness of the adjacent F-layer is smaller than its coherence length).

Finally we mention, that earlier indications for long-range superconductivity in an F layer have been detected through the proximity-induced conductance [41, 42] even before the theoretical works have appeared. Recently the occurrence of the odd in the Matsubara frequency triplet superconductivity in the S/F/S systems, predicted in Ref. [28] was inferred from the experiments on Josephson junctions through observation of the anomalously deep penetration of the Cooper condensate into the F layer (see e.g. [43–49]). We note that our experiments are advantageous in that they address the primary SC parameter of the spin valve, the behavior of  $T_c$ , which is directly affected by the spin-triplet component. And, finally, recently [50] for the construction of the spin valve similar to the studied by us an evidence for generation of long range triplet pairing was also obtained.

### 3. Conclusions

In the present works we were able to realize experimentally the idea by Sanjiun Oh *et al.* [14] for the first time. We have also presented experimental evidence for the oscillating behavior of the spin valve effect in a ferromagnetic/superconductor multilayer F1/N/F2/S with a varied thickness of the ferromagnetic F2-layer. We have observed the direct spin valve effect for F2-layer thicknesses smaller than the decay length  $\xi_F$  of the Cooper pair wave function in the F2-layer and the inverse spin valve effect for larger thickness up to  $2.5 \cdot \xi_F$ . The analysis of the data suggests that the inverse spin valve effect is likely caused by the interference effects for the superconducting pairing function reflected from both surfaces of the F2-layer. And, finally, we have observed a remarkable nonmonotonic dependence of  $T_c$  on the angle between the directions of the magnetization  $\mathbf{M}$  in the Fe1 and Fe2 layers. The  $T_c$  passes through a clear minimum near the orthogonal orientation of  $\mathbf{M}_{\text{Fe1}}$  and  $\mathbf{M}_{\text{Fe2}}$  which is not expected in the case of singlet superconductivity. We argue that this particularly strong suppression of  $T_c$  in the orthogonal geometry is due to an enhanced “leakage” of the SC Cooper pairs into the F layer occurring via the long-range spin-triplet channel.

### Acknowledgments

This work was partially supported by RFBR (Grants No. 13-02-01389-a, 13-02-97037-r-Povolzhje-a and 14-02-00350-a), by Programs of the RAS, by the Ministry of Education and Science of the Russian Federation, and the program “5top100”.

### References

1. Ioffe L.B., Geshkenbein V.B., Feigel'man M.V., Fauchère A.L., Blatter G. *Nature* **398**, 679 (1999)
2. Feigel'man M.V. *Physics-Uspekhi* **42**, 823 (1999) [*Uspehi Fiz. Nauk* **169**, 917 (1999), in Russian]
3. Ryazanov V.V. *Physics-Uspekhi* **42**, 825 (1999) [*Uspehi Fiz. Nauk* **169**, 920 (1999), in Russian]
4. Ryazanov V.V., Oboznov V.A., Veretennikov A.V., Rusanov A.Yu. *Phys. Rev. B* **65**, 020501 (2001)

5. Veretennikov A.V., Ryazanov V.V., Oboznov V.A., Rusanov A.Yu., Larkin V.A., Aarts J. *Physica B* **284-288**, 495 (2000)
6. Ryazanov V.V., Oboznov V.A., Rusanov A.Yu., Veretennikov A.V., Golubov A.A., Aarts J. *Phys. Rev. Lett.* **86**, 2427 (2001)
7. Kontos T., Aprili M., Lesueur J., Grison X. *Phys. Rev. Lett.* **89**, 137007 (2002)
8. Ryazanov V.V., Oboznov V.A., Bol'ginov V.V., Prokof'ev A.S., Feofanov A.K. *Physics-Uspekhi* **47**, 732 (2004) [*Uspehi Fiz. Nauk* **174**, 795 (2004), in Russian]
9. Lazar L., Westerholt K., Zabel H., Tagirov L.R., Goryunov Yu.V., Garif'yanov N.N. Garifullin I.A. *Phys. Rev. B* **61**, 3711 (2000)
10. Izjumov Yu.A., Proshin Yu.N., Khusainov M.G. *Physics-Uspekhi* **45**, 109 (2002) [*Uspehi Fiz. Nauk* **172**, 113 (2002), in Russian]
11. Buzdin A.I. *Rev. Mod. Phys.* **77**, 935 (2005)
12. Bergeret F.S., Volkov A.F., Efetov K.B. *Rev. Mod. Phys.* **77**, 1321 (2005)
13. Efetov K.B., Garifullin I.A., Volkov A.F., Westerholt K. *Magnetic Heterostructures. Advances and Perspectives in Spinstructures and Spintransport*. Series Springer Tracts in Modern Physics, V. 227, Berlin, Springer (2007), P. 252 [arxiv: cond-mat/0610708v2]
14. Oh S., Youm D., Beasley M.R. *Appl. Phys. Lett.* **71**, 2376 (1997)
15. Tagirov L.R. *Phys. Rev. Lett.* **83**, 2058 (1999)
16. Buzdin A.I., Vedyayev A.V., Ryzhanova N.N. *Europhys. Lett.* **48**, 686 (1999)
17. Baladié I., Buzdin A., Ryzhanova N., Vedyayev A. *Phys. Rev. B* **64**, 054518 (2001)
18. Gu J.Y., You C.Y., Jiang J.S., Pearson J., Bazaliy Ya.B., Bader S.D. *Phys. Rev. Lett.* **89**, 267001 (2002)
19. Potenza A., Marrows C.H. *Phys. Rev. B* **71**, 180503(R) (2005)
20. Moraru I.C., Pratt Jr.W.P., Birge N.O. *Phys. Rev. Lett.* **96**, 037004 (2006)
21. Miao G.-X., Ramos A.V., Moodera J. *Phys. Rev. Lett.* **101**, 137001 (2008)
22. Westerholt K., Sprungmann D., Zabel H., Brucas R., Hjörvarsson B., Tikhonov D.A., Garifullin I.A. *Phys. Rev. Lett.* **95**, 097003 (2005)
23. Nowak G., Zabel H., Westerholt K., Garifullin I., Marcellini M., Liebig A., Hjörvarsson B. *Phys. Rev. B* **78**, 134520 (2008)
24. Proshin Yu.N., Zimin A., Fazleev N.G., Khusainov M.G. *Phys. Rev. B* **73**, 184514 (2006)
25. Avdeev M.V., Proshin Yu.N. *JETP* **117**, 1101 (2013) [*Zh. Eksp. Teor. Fiz.* **144**, 1251 (2013), in Russian]
26. Avdeev M.V., Tsarevskii S.L., Proshin Yu.N. *Journ. Korean Phys. Soc.* **63**, 466 (2013)
27. Bergeret F.S., Volkov A.F., Efetov K.B. *Phys. Rev. Lett.* **86**, 4096 (2001)
28. Volkov A.F., Bergeret F.S., Efetov K.B. *Phys. Rev. Lett.* **90**, 117006 (2003)
29. Mel'nikov A.S., Samokhvalov A.V., Kuznetsova S.M., Buzdin A.I. *Phys. Rev. Lett.* **109**, 237006 (2012)
30. Efetov K.B., Garifullin I.A., Volkov A.F., Westerholt K. *Magnetic Nanostructures. Spin Dynamic and Spin Transport*. Series Springer Tracts in Modern Physics, Vol. 246, Hartmut Zabel, Michael Farle (Eds.), Springer-Verlag, Berlin Heidelberg (2013), P. 85–118

31. Leksin P.V., Garif'yanov N.N., Garifullin I.A., Schumann J., Vinzelberg H., Kataev V., Klingeler R., Schmidt O.G., Büchner B. *Appl. Phys. Lett.* **97**, 102505 (2010)
32. Leksin P.V., Garif'yanov N.N., Garifullin I.A., Schumann J., Vinzelberg H., Kataev V., Klingeler R., Schmidt O.G., Büchner B. *Phys. Rev. Lett.* **106**, 067005 (2011)
33. Leksin P.V., Garif'yanov N.N., Garifullin I.A., Schumann J., Vinzelberg H., Kataev V., Klingeler R., Schmidt O.G., Büchner B. *Phys. Rev. B* **85**, 024502 (2012)
34. Leksin P.V., Garif'yanov N.N., Garifullin I.A., Fominov Ya.V., Schumann J., Krupskaya Y., Kataev V., Schmidt O.G., Büchner B. *Phys. Rev. Lett.* **109**, 057005 (2012)
35. Leksin P.V., Kamashev A.A., Garif'yanov N.N., Garifullin I.A., Fominov Ya.V., Schumann J., Hess C., Kataev V., Büchner B. *JETP Lett.* **97**, 549 (2013) [*Pis'ma Zh. Eksp. Teor. Fiz.* **97**, 478 (2013), in Russian]
36. Rusanov A.Yu., Hesselberth M., Aarts J., Buzdin A.I. *Phys. Rev. Lett.* **93**, 057002 (2004)
37. Rusanov A.Yu., Habraken S., Aarts J. *Phys. Rev. B* **73**, 06050 (2006)
38. Fominov Ya.V., Golubov A.A., Karminskaya T.Yu., Kupriyanov M.Yu., Deminov R.G., Tagirov L.R. *JETP Lett.* **91**, 308 (2010) [*Pis'ma Zh. Eksp. Teor. Fiz.* **91**, 329 (2010), in Russian]
39. Usadel K.D. *Phys. Rev. Lett* **25**, 507 (1970)
40. Tagirov L.R. *Physica C* **307**, 145 (1988)
41. Giroud M., Courtois H., Hasselbach K., Maily D., Pannetier B. *Phys. Rev. B* **58**, R11872 (1998)
42. Petrashov V.T., Sosnin I.A., Cox I., Parsons A., Troadec C. *Phys. Rev. Lett.* **83**, 3281 (1999)
43. Sosnin I., Cho H., Petrashov V.T., Volkov A.F. *Phys. Rev. Lett.* **96**, 157002 (2006)
44. Keizer R.S., Goennenwein S.T.B., Klapwijk T.M., Miao G., Xiao G., Gupta A. *Nature* **439**, 825 (2006)
45. Wang J., Singh M., Tian M., Kumar N., Liu B., Shi C., Jain J.K., Samarth N., Mallouk T.E., Chan M.H.W. *Nature Physics* **6**, 389 (2010)
46. Robinson J.W.A., Witt J.D.S., Blamire M.G. *Science* **329**, 59 (2010)
47. Anwar M.S., Czeschka F., Hesselberth M., Porcu M., Aarts J. *Phys. Rev. B* **82**, 100501 (2010)
48. Khaire T.S., Khasawneh M.A., Pratt, Jr W.P., Birge N.O. *Phys. Rev. Lett.* **104**, 137002 (2010)
49. Sprungmann D., Westerholt K., Zabel H., Weides M., Kohlstedt H. *Phys. Rev. B* **82**, 060505 (2010)
50. Zdravkov V.I., Kehrle J., Obermeier G., Lenk D., Krug von Nidda H.-A., Müller C., Kupriyanov M.Yu., Sidorenko A.S., Horn S., Tidecks R. Tagirov L.R. *Phys. Rev. B* **87**, 144507 (2013)

# Quantum fluids in nanoporous media - effects of the confinement and fractal geometry. Theory and simulation

Y.V. Lysogorskiy\*, D.A. Tayurskii

Kazan Federal University, Kremlevskaya 18, 420008 Kazan, Russia

\**E-mail: yura.lysogorskii@gmail.com*

The complex behavior of such quantum fluids like liquid  $^4\text{He}$  and liquid  $^3\text{He}$  in nanoporous media is determined by spatial quantization because of geometrical confinement as well as by significant contribution from the surface atoms. In the present report we review the procedure, results and discuss the issues for fractionalized nonextensive hydrodynamical approach to describe the properties of quantum fluids inside nanopores as well as propose the consideration of strong correlated quantum liquid by means of fractionalized Schrödinger equation and present the results of ab initio simulation of superfluid helium in nanopores of aerogel.

**PACS:** 67.25.dg, 71.15.Mb

**Keywords:** superfluid, aerogel, nanoscale physics, fractional derivative, ab initio simulations

## 1. Introduction

The zero-point energy of atoms of two stable isotopes of helium -  $^4\text{He}$  and  $^3\text{He}$  - is high enough to prevent their solidification even at extremely low temperatures without application of external pressure. So they belong to the class of quantum fluids with strong correlations between atoms but their behavior is quite different at low temperatures. The first one represents a Bose-system and shows superfluid transition at 2.17 K while atoms of  $^3\text{He}$  are governed by Fermi-statistics and superfluid transition can be observed only at much lower temperatures (about 1 mK) when the pairing of two atoms occurs. But even at liquid helium temperatures (1.5–4.2 K) the effects of quantum statistics for  $^3\text{He}$  atoms become pronounceable especially in nanoscale confinement (nanoporous media, thin adsorbed layers on solid substrates) [1–3] and in the presence of nanoscale disorder induced for example by silica aerogel strands [4]. In recent years the problem of correct description of quantum fluids in the confined geometry at nanoscale length has emerged [5–8]. It has been recognized that the quantum fluids at these circumstances can be considered as a new state of quantum matter due to close values between characteristic lengths for these quantum liquids and the size of geometrical confinement and significant contribution from the surface atoms. So one has to apply new physics to describe such systems with taking into account their complex nature. For example, last two years the attempts to develop the fractionalized two-fluid hydrodynamics for nanoporous media with fractal dimensions have been made [9, 10]. The actuality of such new hydrodynamics becomes very clear because of numerous studies of quantum liquids inside nanoporous media [11, 12] as well as because of last developments in chemical synthesis of aerogels with different network of strands (from fibrous to globular one [13]). One of the interesting obtained results is that density waves (the first sound) and temperature waves (the second sound) become strong coupled even in the absence of viscosity, so it is purely geometric effect of fractal space of nanopores [9, 10].

In the present report we will review the procedure, results and discuss the issues for this approach. The rest of this paper is organized as follows: In Section 2 a short review of the existing theoretical models for superfluid bulk helium-4 will be given. In the next Section 3 properties and

peculiarities of high-porosity aerogels filled in by superfluid helium are discussed. In Section 4 possible fractionalization of hydrodynamical model is proposed. In Section 5 another approach to consider the complex fractal structure of aerogel and its influence on superfluid helium behavior is discussed. The further extension of this approach used to formulate an fractional two fluid hydrodynamic model is presented in Section 6. The methods and results of ab initio simulation of superfluid helium inside aerogel nanopores are given in Section 7. Section 8 provides the summary.

## 2. Theoretical models for bulk superfluid helium-4

There are several approaches to describe the behavior of bulk superfluid helium-4. For example, two-fluid model [14, 15], the microscopic description based on the Gross-Pitaevskii equation [16, 17] and others.

### 2.1. Two-fluid model

The most known model is a two-fluid model (TFM) in the framework of which superfluid helium with density  $\rho$  is considered as a two component system: an uncondensed, normal component with density  $\rho_n$  with velocity  $\mathbf{v}_n$  and a condensed, superfluid component characterized by density  $\rho_s = \rho - \rho_n$  with velocity  $\mathbf{v}_s$ . Without dissipative terms one finds the following system of hydrodynamical equations (so-called Landau-Khalatnikov equations [14, 15])

$$\frac{d\rho}{dt} + \text{div}(\rho_n \mathbf{v}_n + \rho_s \mathbf{v}_s) = 0, \quad (1)$$

$$\frac{\partial}{\partial t}(\rho_n \mathbf{v}_n + \rho_s \mathbf{v}_s)_i + \frac{\partial}{\partial x_k} \Pi_{ik} = 0, \quad (2)$$

$$\frac{dS}{dt} + \text{div} S \mathbf{v}_n = 0, \quad (3)$$

$$m \frac{\partial \mathbf{v}_s}{\partial t} + m(\mathbf{v}_s \nabla) \mathbf{v}_s + \nabla \mu = 0. \quad (4)$$

The entropy is denoted by  $S$ , the mass of an atom by  $m$ , the pressure by  $p$  and the chemical potential by  $\mu$ . In (2) the stress tensor  $\Pi_{ik}$  is given by

$$\Pi_{ik} = \rho_n v_{ni} v_{nk} + \rho_s v_{si} v_{sk} + p \delta_{ik}, \quad (5)$$

and the sum over the index  $k$  is assumed.

One can obtain from these equations that there are two type of collective motion: motion of the fluid where both components move in phase is called first (ordinary) sound, while second sound is associated with out of phase motion of the two components (see Fig. 1). The above TFM equations describe the flow properties of superfluid  $^4\text{He}$  in the bulk of the liquid. They are not valid in the immediate proximity of walls and free surfaces, where the effects of so-called ‘‘healing’’ are encountered. Moreover, Landau-Khalatnikov equations cannot be used in the vicinity of  $\lambda$  point, where large variations of superfluid density in space as well as in time may occur. To resolve this problem Ginzburg and Pitaevskii have proposed to use their phenomenological theory with a complex order parameter [18]. Later this approach has been extended and modified by Khalatnikov [19]. The hydrodynamic theory of He-II incorporating the effects of quantum healing and relaxation has been developed by Hills and Roberts [17, 20]. Later Guerst [21] has proposed the general phenomenological theory of superfluid  $^4\text{He}$  unifying and extending Landau-Khalatnikov, Hills-Roberts and Ginzburg-Pitaevskii theories.

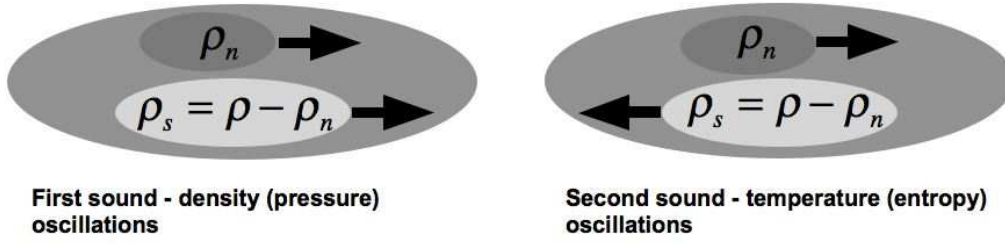


**Figure 1.** Schematic view of sound modes in superfluid helium-4 in the framework of two-fluid hydrodynamic model.

## 2.2. Nonlinear Schrödinger equation

If the short range pair interaction between particles can be written as  $U(x - x') = U_0\delta(x - x')$ , where  $N_0 = \int |\Psi|^2 d^3x$  denotes the number of particles in condensate and  $V_0$  stands for total condensate volume, than one can obtain *nonlinear Schrödinger equation* [16] in the following form

$$i\frac{\partial\Psi}{\partial t} = -\frac{1}{2}\nabla^2\Psi + |\Psi|^2 - \Psi. \quad (6)$$

Here average density  $\rho_0 = N_0/V_0$  is supposed to be equal to unit, the units of length and time are defined as  $\hbar/\sqrt{\rho_0 U_0}$  and  $\hbar/(\rho_0 U_0)$  respectively. Strictly speaking this equation is valid only for absolute zero temperature, when all atoms of He-II are in the condensate state and depletion of this state is negligible so one can write for the condensate wave function  $\Psi(x, t) = \sqrt{\rho(x, t)}e^{i\theta(x, t)}$ . Substituting last equation for  $\Psi(x, t)$  and separating real and imaginary parts in (6) one can obtain

$$\frac{\partial\rho}{\partial t} + \nabla \cdot \rho v = 0, \quad (7)$$

$$\frac{\partial v}{\partial t} + \nabla \frac{v^2}{2} + \frac{1}{\rho}\nabla \frac{\rho^2}{2} = -\nabla \left( \frac{(\nabla\rho)^2}{8\rho^2} - \frac{\nabla^2\rho}{4\rho} \right), \quad (8)$$

where  $v \equiv \nabla\theta$ . Except for high-order derivatives in right hand side of equation (8), which can be omitted in hydrodynamical limit, the system of equations (7)-(8) is equivalent to Euler equations for nonrotating ideal fluid with a pressure defined as  $p(\rho) \equiv \rho^2/2$ . The pressure depends only on density  $\rho$  because the fluid is considered at absolute zero temperature.

To consider dynamics of He-II at nonzero temperature, Hills and Roberts have improved TFM [17] by introducing additional terms which were proportional to the gradient of superfluid component. In this case equation (4) can be rewritten as

$$\frac{\partial\mathbf{v}_s}{\partial t} + \nabla \left( \frac{\mathbf{v}_s^2}{2} + \mu \right) = \nabla \left( \eta(\rho_s)\nabla^2\rho_s + \frac{1}{2}\frac{d\eta}{d\rho_s}(\nabla\rho_s)^2 \right), \quad (9)$$

where  $\eta(\rho_s)$  denotes some function to be defined; stress tensor has to be modified and rewritten as

$$\Pi_{ij} \equiv \rho_n v_{ni} v_{nj} + \rho_s v_{si} v_{sj} + \eta \nabla_i \rho_s \nabla_j \rho_s + \left( p - \eta \rho_s \nabla^2 \rho_s - \frac{1}{2} \frac{\rho_s \eta}{\rho_s} (\nabla \rho_s)^2 \right) \delta_{ij}. \quad (10)$$

New terms including spatial derivatives of  $\rho_s$  are responsible for macroscopic quantum effects, like healing length [17].

### 2.3. Correlated density matrix theory

Another way to describe a such quantum strongly correlated system like superfluid helium is *correlated density matrix* [22] theory that provides the method of choice to analyze the microscopic structure of strongly correlated quantum fluids in thermal equilibrium. This theory allows to study the combined effects of dynamic correlations and quantum-statistical effects in correlated Bose and Fermi liquids. The final outcome of the correlated density matrix theory is that the properties of strongly correlated quantum fluids at finite temperatures can be studied with reference to the background gas of renormalized free particles (bosons or fermions). The mass of such a renormalized boson or fermion depends in a specific form on temperature, bulk particle number density of the many-body system, and eventually on momentum.

### 2.4. Extended irreversible thermodynamics

Recently it was shown [23,24] that the main properties of superfluid helium, both in the absence and in the presence of dissipation, can be explained using a monofluid model based on the *extended irreversible thermodynamics* where four fields, namely density, temperature, velocity, and heat flux are involved as independent fields. This model is able to explain the propagation of the two sounds that are typical of helium II, and the attenuation calculated for such sounds is in agreement with the experiment results. The model is more general than the standard TFM because it allows that a small amount of entropy is associated with helium when it flows through a porous medium (see next section).

## 3. Aerogel

Silica aerogels are synthesized via a sol-gel process and hypercritical drying which enable production of tenuous solids with porosity  $\phi$  as large as 99.8% and unique acoustic properties. Silica aerogel are known to be good examples of fractal materials. As revealed by small-angle x-ray-scattering (SAXS) experiments or small-angle neutron-scattering (SANS) experiments, they are made of a disorder, but homogeneous, array of connected fractal clusters resulting from the aggregation of primary particles. The analysis of the wave-vector dependence of the scattering intensity  $I(q)$  has permitted the determination of two characteristic length scales which are the average size  $a \approx 10 \text{ \AA}$  of the particles and the average size of the clusters  $\xi \approx 100 \text{ \AA}$ . At length scales from  $a$  to  $\xi$  silica aerogels show a fractal behavior [25].

The computational confirmation for cluster structure of aerogel has been obtained by modeling as well as by the geometrical analysis of the diffusion limited cluster-cluster aggregation [26,27].

Also it has been demonstrated [7] that it is long-correlated structure of aerogel that makes an essential influence on liquid  $^4\text{He}$  behavior near  $\lambda$ -point.

### 3.1. Behavior of $^4\text{He}$ inside aerogel

There has been considerable interest in the behavior of superfluid  $^4\text{He}$  in the presence of a random disorder induced by highly open porous media, like aerogel. Understanding the results of acoustic experiments is important when dealing with porous media. Use of liquid  $^4\text{He}$  offers unique advantages due to the existence of the superfluid phase with more than one sound mode. In a porous media where the normal component is clamped by its viscosity and only the superfluid component can move, fourth sound (relative motion of the superfluid and normal fluids) propagates and can be used to determine the superfluid fraction.

The high-porosity aerogels are so soft that the aerogel matrix clamped with normal fluid is caused to move as by the pressure and temperature gradients, unlike other porous media. This results in sound mode intermediate between first and fourth sound [28] and a second-sound-like mode [29]. In this case, proposed by Biot the theory of acoustic propagation in porous, fluid filled, macroscopically homogeneous and isotropic media [30], is not applicable.

It is very interesting to study the possible influence of geometrical confinement with fractal dimensionality on the flow properties of superfluid  $^4\text{He}$  in the framework of TFM. In order to shed a light on geometrical factor itself one can neglect here by quantum healing and any dissipative processes.

### 3.2. Nonextensivity

So hereafter we suppose that effectively aerogel can be considered as a cluster with a fractal mass dimension [31] the nanopores of which are filled in by liquid helium.

Note that thermodynamic limit conditions are violated for helium atoms inside nanopores because of a huge inner pore surface of aerogel (up to  $3000 \text{ m}^2/\text{g}$  for an aerogel with density  $2 \text{ mg}/\text{cm}^3$ ). Namely the ratio of total number of helium atoms  $N$  to the total cluster volume  $V$  is not constant at  $N, V \rightarrow \infty$  and nonextensivity of physical properties takes place for helium atoms in two nanopores. In this case the methods of non-extensive thermodynamics [32] should be applied to construct the two-fluid hydrodynamic model and non-extensive entropy like Tsallis entropy should be introduced. We have to note here that beyond thermodynamic limit even the usual Boltzmann-Gibbs entropy becomes non-additive, but the additivity is restored when thermodynamic limit conditions are taken [33].

## 4. Fractionalized and nonextensive hydrodynamical model

In general case a macroscopic quantity  $Q(A, B)$  associated with the total system may be expressed in terms of the same quantity associated with the subsystems,  $Q(A)$  and  $Q(B)$  [34]

$$Q(A, B) = f_{\lambda_Q}[Q(A), Q(B)], \quad (11)$$

where  $f_{\lambda_Q}$  is a symmetric bivariate function depending on a constant  $\lambda_Q$ . Of course, for given quantity  $Q$  there exist many functions which satisfy the composability property (11). However, additional assumptions drastically reduce their number. For example, the thermodynamic equilibrium may be used as a constraint on the form of  $f_{\lambda_Q}$  in Eq. (11). For energy  $E_\lambda$  [35] and entropy  $S_q$  [36] of helium inside nanopores it leads to

$$E_\lambda(A + B) = E_\lambda(A) + E_\lambda(B) + \lambda E_\lambda(A)E_\lambda(B), \quad (12)$$

$$S_q(A + B) = S_q(A) + S_q(B) + qS_q(A)S_q(B), \quad (13)$$

where  $\lambda$  and  $q$  are parameters of nonextensivity and are determined by the properties of system. Suppose that a local equilibrium between liquid  $^4\text{He}$  in different nanopores takes place. So we can re-define such thermodynamics quantities as temperature and pressure in the following manner [37]

$$T_{\text{phys}} = \frac{1 + qS_q}{1 + \lambda E_\lambda} \left( \frac{\partial E_\lambda}{\partial S_q} \right)_V, \quad (14)$$

$$p_{\text{phys}} = \frac{T_{\text{phys}}}{1 + qS_q} \left( \frac{\partial S_q}{\partial V} \right)_E. \quad (15)$$

Further, it is possible to introduce the spatial pressure and density distributions in fractal cluster as it has been made in our previous work [9]

$$p_{\text{phys}}(r) = p_f(r)\chi_p(r), \quad (16)$$

$$\rho_{\text{phys}}(r) = \rho_f(r)\chi_p(r), \quad (17)$$

where  $r$  is distance from center of fractal cluster,  $p_f(r)$  is distribution of pressure in pore,  $\chi_p(r)$  is a fractal factor-function. In the case of Euclidean space with  $D = 3$  this factor-function should be equal to unit:  $\chi_p(r) \equiv 1$ . Such kind of fractionalization procedure can be applied to any thermodynamic quantity  $A$  i.e.

$$A = A_f(X, Y, Z, \dots)\chi_A(r), \quad (18)$$

$$\lim_{D \rightarrow 3} \chi_A = 1. \quad (19)$$

From the defined thermodynamic quantities (14, 15) and eqn. (16) the fractal factor-functions for energy, entropy and temperature are derived

$$\chi_E = \chi_S = \frac{\chi_p}{1 + \lambda E_f(1 - \chi_p)}, \quad (20)$$

$$\chi_T = \frac{1 + qS_f\chi_S}{1 + qS_f} \frac{1 + \lambda E_f}{1 + \lambda E_f\chi_E}. \quad (21)$$

Because all thermodynamic quantities should be expressed in terms of physical (observable) variables, one can propose the following definition of the generalized free energy

$$F = E - T_{\text{phys}}S_{\text{phys}} = E - \left( \frac{\partial E}{\partial S_{\text{phys}}} \right) S_{\text{phys}}. \quad (22)$$

which represents no more than the Legendre transformation. So the entropy differential equals to

$$dS_{\text{phys}} = \frac{1 + \lambda E_\lambda}{1 + qS_q} dS_q, \quad (23)$$

In the first order with respect to  $\lambda E_f$  and  $qS_q$  the entropy can be written as:

$$S_{\text{phys}} = \frac{1}{q} \ln(1 + qS_q) + \lambda \int \frac{E_\lambda(S_q) dS_q}{1 + qS_q} \approx S_q - qS_q \frac{S_q}{2} + \lambda \int E_\lambda dS_q. \quad (24)$$

Finally the fractal factor-function for  $S_{\text{phys}}$  is

$$\chi_{S_p} = \chi_S + \chi_p(\chi_p - 1) \left( \frac{\lambda E_f - qS_f}{2} + \lambda H \right), \quad (25)$$

where  $H = 1/S_f \int E_f dS_f$ . After substitution the fractionalized thermodynamical quantities into TFM one can derive the main system of equations for the *fractionalized two-fluid hydrodynamic model*

$$\frac{\partial \rho_f}{\partial t} \chi_p + \text{div}(\rho_{sf} \chi_p \mathbf{v}_s + \rho_{nf} \chi_p \mathbf{v}_n) = 0, \quad (26)$$

$$\frac{\partial \rho_f \sigma_f}{\partial t} \chi_{S_p} + \text{div}(\rho_f \sigma_f \chi_{S_p} \mathbf{v}_n) = 0, \quad (27)$$

$$\rho_{sf} \chi_p \frac{\partial \mathbf{v}_s}{\partial t} = -\frac{\rho_{sf}}{\rho_f} \nabla(p_f \chi_p) + \rho_{sf} \sigma_f \chi_p \chi_\sigma \nabla(T_f \chi_T), \quad (28)$$

$$\rho_{nf} \chi_p \frac{\partial \mathbf{v}_n}{\partial t} = -\frac{\rho_{nf}}{\rho_f} \nabla(p_f \chi_p) - \rho_{sf} \sigma_f \chi_p \chi_\sigma \nabla(T_f \chi_T), \quad (29)$$

where  $\chi_\sigma = 1 + (\chi_p - 1) \left( \frac{3\lambda E_f - qS_f}{2} + \lambda H \right)$ . From eqns. (26, 27, 28, 29) two equations for waves of pressure and temperature follow

$$\begin{aligned} \frac{1}{u_1^2} \frac{\partial^2 p_f}{\partial t^2} &= \nabla^2 p_f + 2 \frac{\nabla \chi_p}{\chi_p} \nabla p_f + \frac{\nabla^2 \chi_p}{\chi_p} p_f, & (30) \\ \frac{1}{u_2^2} \frac{\partial^2 T_f}{\partial t^2} &= \nabla^2 T_f (1 + (\chi_p - 1)M) + \nabla T_f \left( M \nabla \chi_p - (1 - M) \frac{\nabla \chi_p}{\chi_p} \right) + \\ &+ T_f (qS_f - \lambda E_f) \left( \nabla^2 \chi - \frac{(\nabla \chi_p)^2}{\chi_p} \right) + \\ &+ \frac{1}{u_2^2} \frac{N \sigma_f}{\rho_f} \left( \frac{\partial T_f}{\partial \sigma_f} \right)_{\rho_f} \left( \nabla \chi_p \nabla p_f + \frac{(\nabla \chi_p)^2}{\chi_p} p_f \right), & (31) \end{aligned}$$

where  $u_1^2 = (\partial p_f / \partial \rho_f)_{S_f}$ ,  $u_2^2 = \rho_{sf} \sigma_f^2 / \rho_{nf} (\partial T_f / \partial \sigma_f)_{p_f}$  are the squared first and second sound velocities respectively and  $M = (\lambda E_f + qS_f) / 2 + \lambda H$ ,  $N = (3\lambda E_f - qS_f) / 2 + \lambda H$ . On Fig. 2 the profiles for pressure wave and for the temperature wave induced by it are shown. It is seen from eqn. (31) that the coupling between pressure and temperature waves appears even in the absence of  $^4\text{He}$  viscosity and aerogel skeleton inertia, which is undoubtedly the effect of not only fractional dimensionality of nanopore space, but also of the nonextensive nature of thermodynamical quantities for He-II inside nanopores.

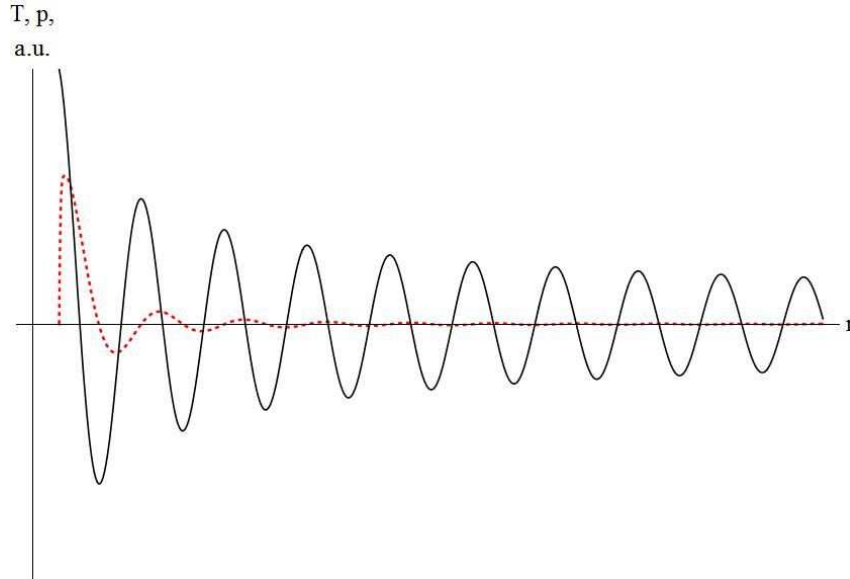


**Figure 2.** Profile for pressure wave (solid line) and the temperature wave induced by it (dashed line).

## 5. Fractional microscopical approach

In contrast to purely phenomenological two-fluid model, as mentioned in Section 2.2, one can start the study of problem from microscopical point of view. In this section the fractional Schrödinger equation will be considered and its application to superfluid at nanoscale will be motivated.

### 5.1. Fractional Schrödinger equation

An alternative point of view on quantum mechanical motion is the so-called Feynman formalism of quantum mechanics, which is focused on the concept of trajectory, and the particle can move

along any possible trajectories. To move a particle from point A to point B one must take into account the contribution of all possible trajectories with the corresponding weight (complex factor). Possible trajectories resemble Brownian trajectory of a free particle and have a fractal dimension of  $\alpha = 2$ .

De Broglie thermal wavelength for the helium atom inside the aerogel at temperatures of about 1 K is about  $10 \text{ \AA}$ , which is in proper relation with the characteristic length scale of the fractal structures formed aerogel. Thus, some quantum-mechanical trajectory of the helium atom will be forbidden due to the influence of the structure of aerogel. Realized trajectory will resemble the motion of a Brownian particle in a porous medium, where the mean square displacement depends on time as  $\langle x^2 \rangle \propto t^{2/\alpha}$ . This phenomenon is called subdiffusion. To describe this type of diffusion an equation with fractional Riesz derivative is used. Probability density function for such case is written in terms of Levy function, which is a generalization of the Gaussian distribution.

Laskin proposed to generalize the Feynman's path integrals to an arbitrary fractal dimension of trajectories  $\alpha$  [38]. From this type of path integrals one can obtain fractional Schrödinger equation which is written as

$$i\hbar \frac{\partial \psi(\mathbf{r}, t)}{\partial t} = D_\alpha (\hbar \nabla)^\alpha \psi(\mathbf{r}, t) + V(\mathbf{r}, t) \psi(\mathbf{r}, t). \quad (32)$$

Here Riesz fractional derivative is introduced as

$$(\hbar \nabla)^\alpha \psi(\mathbf{r}, t) = -\frac{1}{(2\pi\hbar)^3} \int d^3 p e^{i\mathbf{p}\mathbf{r}/\hbar} |\mathbf{p}|^\alpha \varphi(\mathbf{p}, t), \quad (33)$$

$$\varphi(\mathbf{p}, t) = \int d\mathbf{r} e^{-i\mathbf{p}\mathbf{r}/\hbar} \psi(\mathbf{r}, t), \quad (34)$$

and  $D_\alpha$  is the generalized coefficient, the physical dimension of which is  $[D_\alpha] = \text{erg}^{1-\alpha} \cdot \text{cm}^\alpha \cdot \text{sec}^{-\alpha}$ . Thus fractional Hamiltonian can be written in the form

$$\hat{H}_\alpha = D_\alpha (\hbar \nabla)^\alpha + V(\mathbf{r}, t). \quad (35)$$

This type of Hamiltonian has been used to describe the specific heat of noncrystalline solids (glasses) associated with the unusual structure of these materials [39].

### 5.2. Galilean noninvariance of fractional Schrödinger equation

Let us consider transformation of equation (32) when an transition to another inertial frame of reference frame moving with the velocity  $v$  is occurred. Under such transformation the spatial coordinates and time are changed as  $r' = r - vt$ ,  $t' = t$ . Then time and fractional spatial derivative is rewritten as

$$\partial_t f = (\partial_{t'} - v \partial_{r'}) f, \quad (36)$$

$$(\hbar \nabla_r)^\alpha = (\hbar \nabla_{r'})^\alpha. \quad (37)$$

Let us assume that in the resting reference frame  $K$  fractional Schrödinger equation has the form

$$i\hbar \frac{\partial \Psi(\mathbf{r}, t)}{\partial t} = D_\alpha (\hbar \nabla)^\alpha \Psi(\mathbf{r}, t). \quad (38)$$

While changing the frame of reference to the moving one  $K'$ , old wave function is written as [40]

$$\Psi(\mathbf{r}, t) = \varphi(\mathbf{r}', t') e^{i(mv\mathbf{r}'/\hbar + Et'/\hbar)}, \quad (39)$$

where  $\varphi$  denote wave function in new reference frame and  $E = mv^2/2$ . It is easy to show that fractional derivative of product is

$$(\hbar\nabla)^\alpha f(x)g(x) = \frac{1}{(2\pi\hbar)^2} \int dqdp |p+q|^\alpha e^{i(p+q)x/\hbar} \hat{f}(p)\hat{g}(q). \quad (40)$$

Let us substitute eq. (39) in eq. (38) and apply expression for fractional derivative of product (40). With taking into account that Fourier transform of exponential multiplier is proportional to Dirac delta function  $\delta(q - mv)$  one obtains fractional Schrödinger equation in new reference frame in form

$$i\hbar\partial_{t'}\varphi - i\hbar v\nabla_{r'}\varphi + (mv^2 - E)\varphi = \frac{D_\alpha}{2\pi\hbar} \int dp e^{ipr/\hbar} \hat{\varphi}(p) |p + mv|^\alpha. \quad (41)$$

In that case  $E = D_\alpha|mv|^\alpha$ . For Galilean invariance of eqn. (41) one has to keep only time derivative and spatial fractional derivative of order  $\alpha$ . Only value  $v = 0$  keep form of FSE. It leads to

$$r' = r, \quad t' = t, \quad \Psi' = \Psi.$$

Thus, fractional Schrödinger equation is *Galilean noninvariant*, and its form is changed at transition into another inertial frame of reference. As a consequence one needs to choose some special reference frame where, for example, nanoporous media is in a rest as well as to introduce additional potential into two-fluid hydrodynamic model.

## 6. Fractional two-fluid hydrodynamical model

By using Heisenberg representation one can obtain dynamical equations for operators  $\hat{\mathbf{r}}$  and  $\hat{\mathbf{v}} = \frac{d\hat{\mathbf{r}}}{dt}$  by means of general dynamical equation for arbitrary operator  $\hat{O}$

$$\frac{d\hat{O}(t)}{dt} = \frac{\partial\hat{O}(t)}{\partial t} + \frac{i}{\hbar} [\hat{H}_\alpha, \hat{O}]. \quad (42)$$

Then for velocity and acceleration we will obtain next equations

$$\hat{\mathbf{v}} = \alpha D_\alpha |\hat{\mathbf{p}}|^{\alpha-2} \hat{\mathbf{p}}, \quad (43)$$

$$\frac{d\hat{\mathbf{v}}}{dt} = -\frac{i}{\hbar} \alpha D_\alpha \sum_{l=1}^{\infty} \frac{(-i\hbar)^l}{l!} \nabla^l V(\hat{\mathbf{r}}) \frac{(\alpha-1)!}{(\alpha-l-1)!} \hat{\mathbf{p}}^{\alpha-1-l}. \quad (44)$$

Suppose that velocity is more general quantity than momentum [41], one can rewrite (44) in the form

$$\frac{d\hat{\mathbf{v}}}{dt} = -\alpha D_\alpha \frac{(\alpha-1)}{(\alpha D_\alpha)^{(\alpha-2)/(\alpha-1)}} |\hat{\mathbf{v}}|^{\frac{\alpha-2}{\alpha-1}} \nabla V(\hat{\mathbf{r}}), \quad (45)$$

where we left only first spatial derivation from potential  $V$ . From eqn. (32) one can obtain mass conservation law in the form

$$\frac{\partial\rho(\mathbf{r}, t)}{\partial t} + \nabla\mathbf{J}(\mathbf{r}, t) + K(\mathbf{r}, t) = 0, \quad (46)$$

where  $\rho = \Psi^*\Psi$  is density,  $\mathbf{J} = \frac{1}{\alpha} (\Psi^*\hat{\mathbf{v}}\Psi + \Psi\hat{\mathbf{v}}\Psi^*)$  is density flow and

$$K = \frac{i}{\alpha\hbar} (\hat{\mathbf{p}}\Psi\hat{\mathbf{v}}\Psi^* - \hat{\mathbf{p}}\Psi^*\hat{\mathbf{v}}\Psi) \quad (47)$$

is new term, which represent additional sources in fractal space. If we decompose wave function on the basis of plane waves  $\Psi = \sum_{\mathbf{p}} C_{\mathbf{p}} \exp(i\mathbf{p}\mathbf{r}/\hbar)$  then substitution it in the eqn. (47) results in

$$K = \frac{iD_{\alpha}}{\hbar} \sum_{\mathbf{p}_1 \neq \mathbf{p}_2} \mathbf{p}_1 \mathbf{p}_2 C_{p_1}^* C_{p_2} e^{\frac{(\mathbf{p}_2 - \mathbf{p}_1)\mathbf{r}}{\hbar}} (|p_2|^{\alpha-2} - |p_1|^{\alpha-2}).$$

If we assume that density of superfluid helium is almost homogeneous, i.e. we have only set of plane waves with close values of  $\mathbf{p}$  in wave function and helium atoms is strongly delocalized, then one can suppose  $K \approx 0$ . In that case in fractional two-fluid hydrodynamical model one can left continuity equations in the form (2) and (3).

Instead of constant  $D_{\alpha}$  one can introduce new constant with dimension of velocity as  $\alpha D_{\alpha} = v_0^{2-\alpha} m^{1-\alpha}$ . Then dynamical equation (45) for the superfluid component with taking into account thermodynamical relations [15] can be rewritten as

$$\rho_s \frac{d\mathbf{v}_s}{dt} = (\alpha - 1) \left| \frac{\mathbf{v}_s}{v_0} \right|^{\frac{\alpha-2}{\alpha-1}} \left( -\frac{\rho_s}{\rho} \nabla p + \rho_s \sigma \nabla T \right). \quad (48)$$

Also we can suppose the similar form for dynamical equation of density flow and write

$$\frac{d\mathbf{j}}{dt} = -(\alpha - 1) v_0^{\frac{2-\alpha}{\alpha-1}} \left| \frac{\mathbf{j}}{\rho} \right|^{\frac{\alpha-2}{\alpha-1}} \nabla p. \quad (49)$$

Thus equations (2), (3), (48) and (49) form *fractional two-fluid hydrodynamical model* of superfluid helium in nanoporous space. These equations set result in two oscillation equations

$$\frac{\partial^2 p}{\partial t^2} = (\alpha - 1) u_1^2 \nabla \left( \left| \frac{\mathbf{v}}{v_0} \right|^{\frac{\alpha-2}{\alpha-1}} \nabla p \right), \quad (50)$$

$$\begin{aligned} \frac{\partial^2 T}{\partial t^2} &= (\alpha - 1) u_2^2 \nabla \left( \left| \frac{v_s}{v_0} \right|^{\frac{\alpha-2}{\alpha-1}} \nabla T \right) - \\ &-(\alpha - 1) \frac{u_2^2}{\rho \sigma} \nabla \left( \left( \left| \frac{v_s}{v_0} \right|^{\frac{\alpha-2}{\alpha-1}} - \left| \frac{v}{v_0} \right|^{\frac{\alpha-2}{\alpha-1}} \right) \nabla p \right), \end{aligned} \quad (51)$$

where  $u_1$  and  $u_2$  is first and second sound velocity for bulk superfluid helium.

Let us consider approximate solution of equations (50) and (51). By using ‘‘weak fractality’’ approximation  $\alpha - 2 \ll 1$  in low temperature region  $T < 0.5\text{K}$  when  $\rho_n/\rho_s \ll 1$  and  $v_n/v_s \ll 1$  one can rewrite eq. (51) as

$$\frac{\partial^2 T}{\partial t^2} = (\alpha - 1) u_2^2 \left( 1 + \gamma \ln \left| \frac{v_s}{v_0} \right| \right) \nabla^2 T + (\alpha - 2) u_2^2 \frac{\rho_n}{\rho \sigma \rho_s} \left( \frac{v_n}{v_s} - 1 \right) \nabla^2 p, \quad (52)$$

where  $\gamma = (\alpha - 2)/(\alpha - 1) \ll 1$ . We will find solutions in the form

$$p = p_0 + p' e^{i(ukt - kr)}, \quad T = T_0 + T' e^{i(ukt - kr)}$$

and suppose that velocity has dependence  $v = v^0 \exp(i(ukt - kr))$ . As a result one can obtain two type of oscillations: temperature oscillations with sound speed  $u \approx u_2 \left( 1 + (\alpha - 2) \left( 1 + \frac{1}{2} \ln \left| \frac{v_s^0}{v_0} \right| \right) \right)$  and pressure-temperature oscillations with sound speed  $u \approx u_1 \left( 1 + \frac{\alpha-2}{2} \left( 1 + \ln \left| \frac{v^0}{v_0} \right| \right) \right)$ . The latter one has relation between pressure and temperature amplitude  $T' = \beta p'$ , where coupling coefficient has form

$$\beta = ((\alpha - 2) \frac{u_2^2 \rho_n}{\rho \sigma \rho_s} \left( \frac{v_n^0}{v_s^0} - 1 \right)) / (u_2^2 - u_1^2).$$

At low temperatures, when  $u_1^2 \approx \text{const}$ ,  $u_2^2 \approx \text{const}$  and  $\sigma \propto T^n$ , this coupling coefficient should be linear on temperature  $\beta \propto T$ .

## 7. Ab initio simulation of liquid helium-4 in aerogel

We also study the spatial distribution of liquid helium and the energy of its atoms in the restricted space from the microscopic point of view.

There are two independent approaches to the numerical simulation of quantum systems: the quantum Monte Carlo method and the density functional theory. The Monte Carlo method is based on the idea of Feynman path integrals and makes it possible to obtain asymptotically correct solutions. However, this method allows simultaneous simulation of a rather small number of particles. The density functional theory relies on the existence of the one-to-one correspondence between the ground state density of the quantum system and the potential. This makes it possible to reduce the multiparticle problem to the one-particle one in the effective potential. The main drawback of the density functional theory is that the form of this correspondence is not known and it is necessary to search for the approximate form of the effective potential reproducing certain experimental data. However, from the point of view of the computational cost, this method makes it possible to consider problems containing rather large number of quantum particles. In particular, it functioned well in the case of studying the properties of the Bose-Einstein condensate, when one macroscopic wavefunction is sufficient for the description. For this reason, we used one of the methods of the density function theory for superfluid helium on the basis of the Stringari-Dalfovo approximation [42]. To find the ground state, we considered the evolution of the system in imaginary time described by the Schrödinger equation. To exclude the influence of the edge effects, we used periodic boundary conditions in all simulated cells.

We used the molecular dynamics method implemented in the LAMMPS code in order to obtain the model of the porous structure of silica aerogel within the scale of several nanometers [43]. Simulation started with the ideal cell of  $\beta$ -cristobalite, which then was transferred to the amorphous state by cooling from 3000 to 300 K for 500 ps. Then, the gradual stretching and thermalization of the cell at a temperature of 300 K were performed until the characteristic nanopores appeared. This negative pressure rupturing method is described in more detail in [44]. As a result, we obtained a cubic cell with a side of  $47.3 \text{ \AA}$  containing a porous structure of amorphous silicon dioxide with a density of  $0.937 \text{ g/cm}^3$ . The further attempts at stretching of the cell led to the rupture of the structure of the amorphous silicon dioxide and the loss of the connectivity of the structure. For this reason, we decided to keep to this density. The fractal mass dimension of this sample calculated within the scale from 10 to  $25 \text{ \AA}$  [45] was  $D \approx 2.81$ , which is in agreement with the value  $D = 2.85$  for the sample of the same density simulated in [44]. An effective potential of the interaction between the obtained structure and the single helium atom was generated (Fig. 3). Below, this potential will be called the external potential. The interaction between the helium and oxygen atoms was supposed to be pairwise and additive and it was described by the (12-6) Lennard-Jones potential, while the partly hidden silicon atoms were ignored [46]. To be assured that this approach was correct, the ab initio calculation of the potential of the interaction between the single helium atom and the 0.5-nm-thick  $\alpha$ -quartz layer was performed. We used the method of the electron density functional theory implemented in the VASP program [47] (a part of the MedeA software package [48]). The exchange correlation interaction was taken into account using the generalized gradient approximation (GGA-PBE [49]). The calculated potential was approximated by the sum of the pairwise (12-6) Lennard-Jones interactions exclusively between the helium atom and oxygen atoms in the structure. The Lennard-Jones parameters obtained as a result of the approximation ( $\varepsilon = 25.2 \text{ K}$ ,  $\sigma = 2.97 \text{ \AA}$ ) are in good agreement with the analogous parameters calculated in [46] ( $\varepsilon = 28.0 \text{ K}$ ,  $\sigma = 2.95 \text{ \AA}$ ).

Thus, it was demonstrated that it suffices only to take into account the interaction between the helium and oxygen atoms for our problems.

The characteristic potential pits (Fig. 3) concentrated near the concave aerogel surface are well discernible in the calculated profile of the potential energy of the helium atom. This effect is purely geometric and is explained by the increase in the number of the oxygen atoms in the “corners” of the structure [50,51]. The experimental estimate of the binding energy of the  $^3\text{He}$  isotopes with the aerogel surface is in the range from 60 to 250 K [52], which is in good agreement with the values obtained in this work (Fig. 3).

The density functional calculations [42] provide the distribution of the helium density of the simulated aerogel potential. Fig. 4 shows the profiles of the external potential and the helium density along the OX axis (see Fig. 3). The maximum value of the external potential of 1000 K was chosen particularly in order to improve the convergence of calculations. For comparison, we also calculated the distribution of helium in other model potentials: the nonadsorbing aerogel, i.e., aerogel that has a nonnegative potential and only repulses the helium atom, and the adsorbing homogeneous strand (a cylinder with a diameter of 25 Å and the potential well depth of 100 K) parallel to the edge of the cell in its center.

It is of interest to determine the fractional mass dimension  $D$  [45] of helium in the limited geometry space. Let  $B_{\mathbf{X}}(R)$  be the mass of the compound located in the sphere with the radius  $R$  and the center at the point  $\mathbf{X}$ . For the “ideal” fractal with the center at the point  $\mathbf{X}$ , this

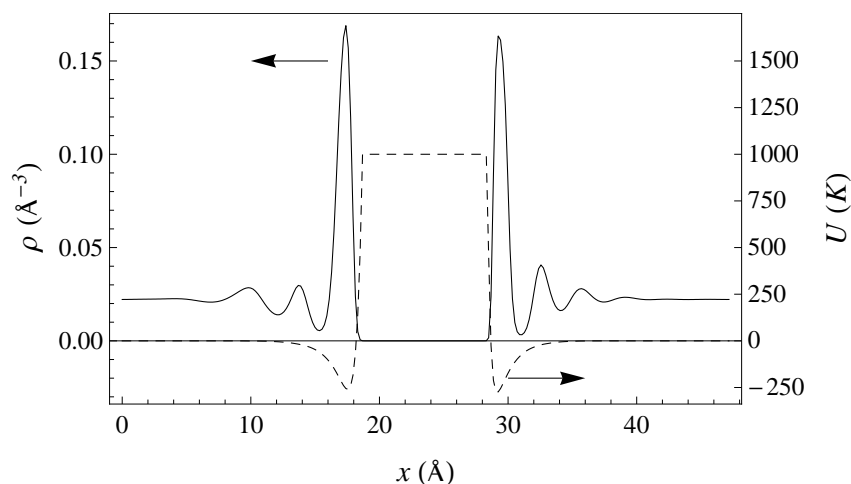


**Figure 4.** Profiles of the external potential of aerogel and the calculated helium density along the  $X$  axis at zero pressure (at the minimum chemical potential).

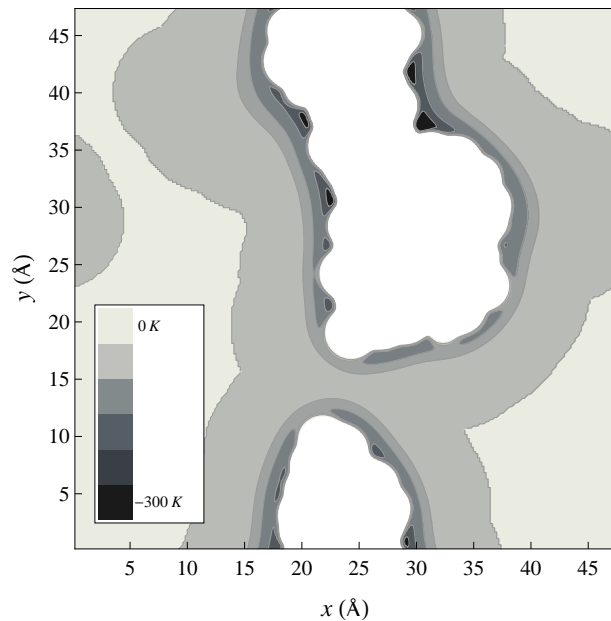


**Figure 3.** Profile of the potential energy of the helium atom in the simulated aerogel cell in the plane  $Z = 0$ . The potential pits in the concave regions are noticeable. Isolines correspond to the potential energies of 0,  $-50$ ,  $-100$ ,  $-200$  and  $-300$  K. The white region corresponds to the aerogel strands where the helium atoms cannot penetrate.

dependence has the form

$$B_{\mathbf{X}}(R) = A \cdot R^D, \quad (53)$$

where  $A$  is a constant. A stochastic fractal (e.g., a strongly disordered material) does not have a certain center. As a consequence, it is necessary to consider the arithmetic averaging of mass function (53) over the different spatial points:  $C(r) = \langle B_{\mathbf{X}}(R) \rangle$ . This function is called the *correlation integral* [45]. Approximating this function by Eq. (53) near zero the origin, one can obtain the correlation dimension of the material. However, this idealization is not applicable to real materials, since the minimum distance is finite and is determined by the size of the constituent particles. In addition, at distances larger than a definite value, the mass dimension  $D$  is 3 because the material within these scales can be considered as uniformly porous. Thus, it is of interest to trace the change in the helium mass dimension in aerogel nanopores  $D(r)$  with distance. For the given  $r$  value, this value was found from the approximation of the correlation integral in the interval  $(r - \delta, r + \delta)$  by Eq. (53), where  $\delta = 3 \text{ \AA}$ . The calculated results of mass dimension for the potential of aerogel, nonadsorbing aerogel, and adsorbing strand are shown in Fig. 5. In addition to the mass dimension of whole helium, we also calculated the mass dimension of only those regions of helium the density of which is below the solidification threshold  $\rho_{\text{solid}} \approx 0.026 \text{ \AA}^{-3}$ . At large scales, the mass dimension should reach the constant level  $D = 3$ . The deviations from this value observed in Fig. 5 can be the consequence of the limitedness of the model, namely, the use of the periodic boundary conditions and the abrupt increase in the helium density near the surface. For comparison, Figs. 5a and 5b show the mass dimension of aerogel calculated analogously. It is seen that the mass dimension within the scales of  $L_F \approx 40 \text{ \AA}$  is  $D < 3$  both for whole helium and for its liquid part in aerogel. The distance  $L_F$  is commensurate with the cell period  $L = 47 \text{ \AA}$  and, therefore, with the upper boundary of the fractality of the considered model of aerogel (Figs. 5a and 5b). It is logical to suppose that helium placed into a porous structure similar to aerogel having the fractal mass dimension within certain scales will also have the fractal mass dimension  $D < 3$  up to these scales.

If the confinement has a simple structure (e.g., parallel strands), helium will have the conventional mass dimension close to 3 even within the scales of the cell period (Fig. 5c).

It is known that the density functional theory demonstrates the instability of the numerical procedures for the calculation of the energy of the system in the case of a strongly inhomogeneous external potential [53]. It was established that the instability in the form of oscillations arises in the term responsible for the potential energy of the system in the external potential. For this reason, for the further calculations without the restriction of generality, the effective potential of aerogel was uniformly scaled to the conditional minimum possible energy of  $-100 \text{ K}$ .

Let us consider the energy of atoms of liquid helium-4 in different external potentials. To demonstrate the nonadditivity of the energy of liquid helium atoms in the limited geometry space, we calculated the total ( $E_{\text{tot}}$ ) and internal ( $E_{\text{self}}$ ) energies of the system divided by the number of particles  $N$  in the considered cell as functions of  $N$  (Fig. 6). These values differ by the external potential energy  $E_{\text{ext}}$ . The kinks observed in the plots for the attractive potentials correspond to the transition from the helium distribution expanded over the whole cell to its localized distribution near the attractive surface. For comparison, the same figures show the analytically calculated dependence of the energy of helium uniformly distributed over the cell in the absence of the external potential on  $N$ . Comparison of Figs. 6a and 6b with an analogous dependence in Fig. 7 from [42] calculated for free helium droplets indicates that the total energy of the system per particle for the unattractive potential ( $U_{\text{ext}} \geq 0$ ) decreases and tends to zero with decreasing number of particles.

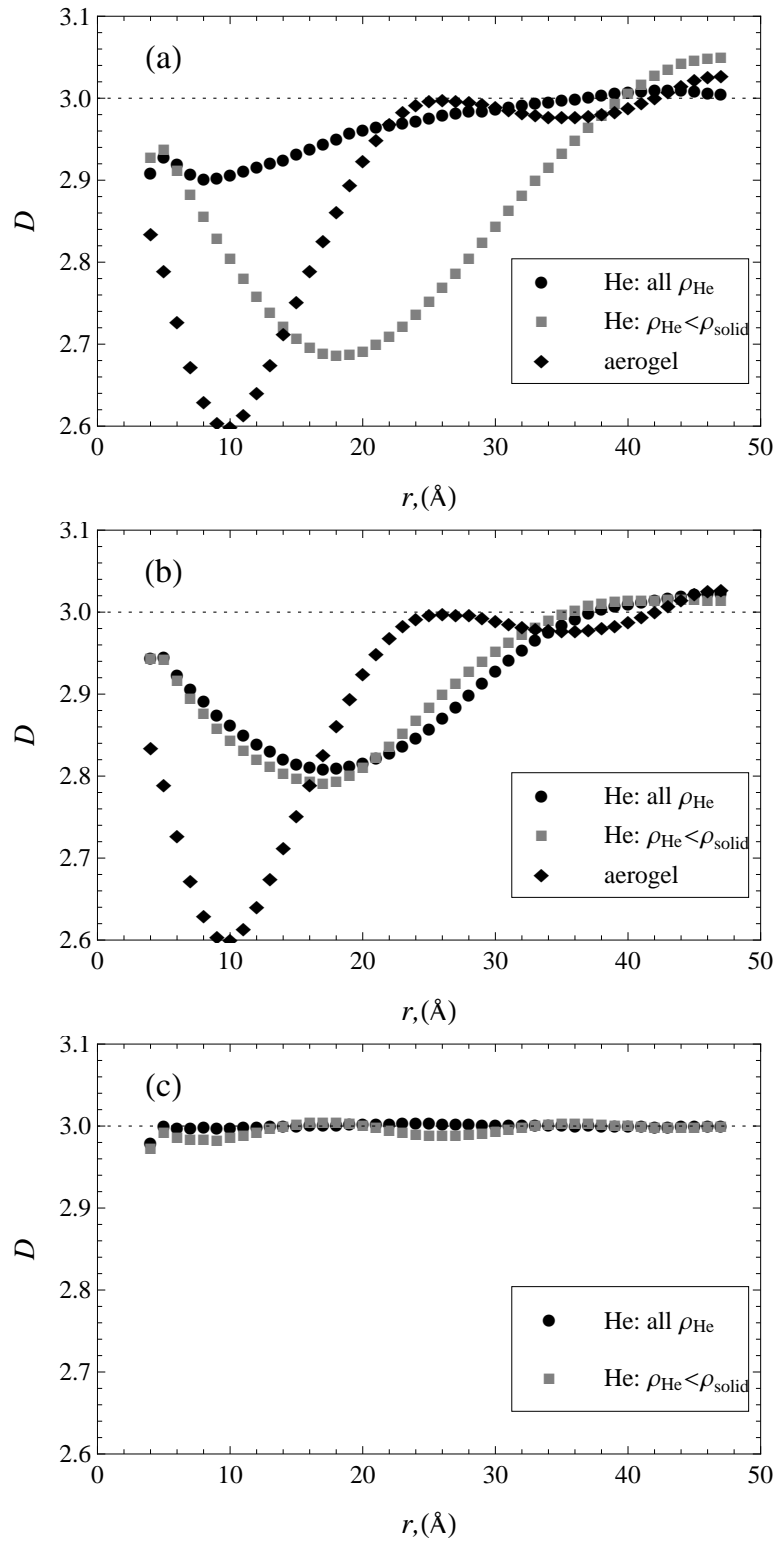


**Figure 5.** Distance dependence of the mass dimension of helium in the space of nanopores in the (a) aerogel and (b) nonadsorbing aerogel and (c) around the adsorbing strand. The calculation is presented for (circles) whole helium and (squares) the liquid part of helium with the density below  $\rho_{\text{solid}} = 0.026 \text{ \AA}^{-3}$ . The mass dimension of aerogel is given by diamonds for comparison.

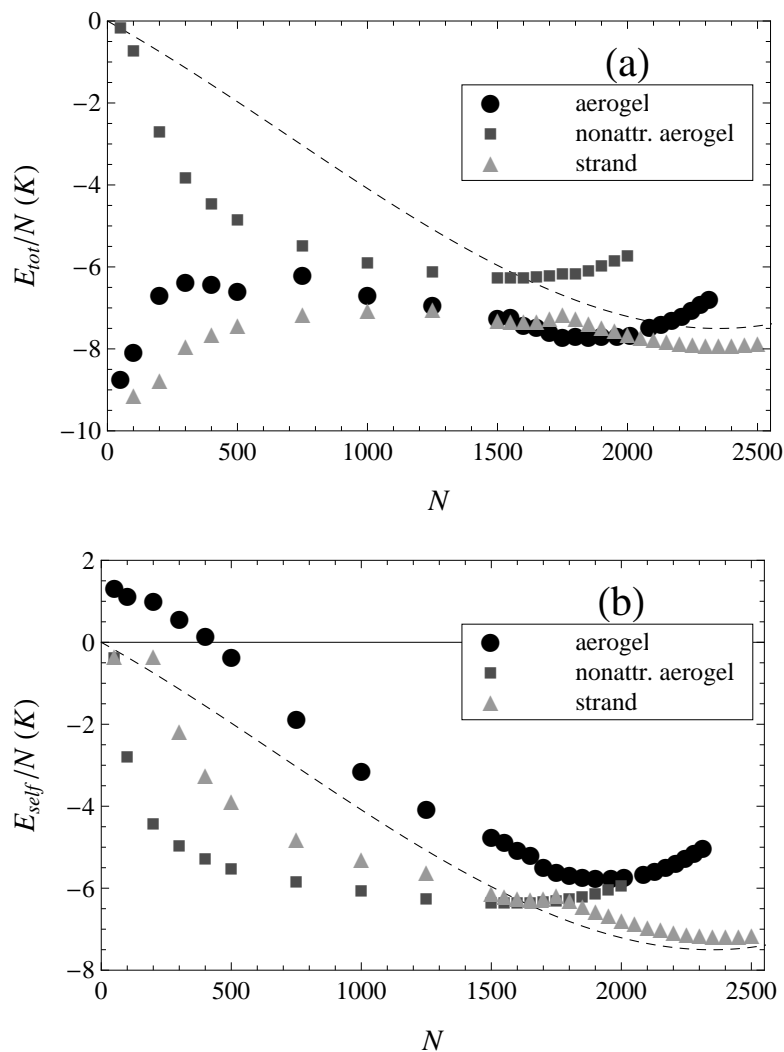


**Figure 6.** Calculated (a) total and (b) internal energies of superfluid helium divided by the number of atoms  $N$  versus  $N$  in the potential of (circles) aerogel, (squares) nonadsorbing aerogel, and (triangles) adsorbing strand. The dashed line is the analytical dependence for the homogeneous free liquid.

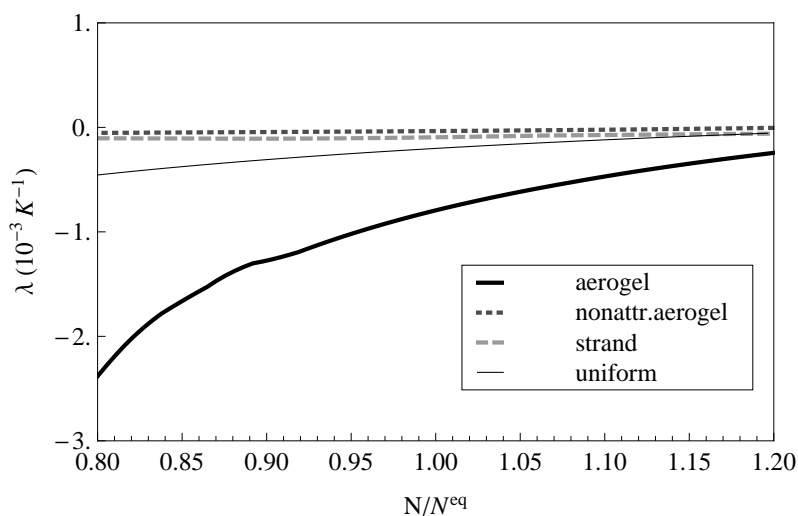


**Figure 7.** Calculated internal energy nonadditivity of superfluid helium versus  $N/N^{eq}$  in the potential of (solid line) aerogel, (dotted line) nonadsorbing aerogel, and (dashed line) adsorbing strand. The thin solid line is the analytical dependence for the homogeneous free liquid.

The local minimum of the function  $E_{\text{tot}}(N)/N$  corresponds to the equilibrium number of helium particles  $N^{\text{eq}}$  at zero pressure. In particular,  $N_{\text{aero}}^{\text{eq}} = 1850$  for aerogel and  $N_{\text{nonattr}}^{\text{eq}} = 1600$  for nonadsorbing aerogel. The equilibrium number of particles for the free homogeneous liquid and the adsorbing strand was  $N_{\text{aero}}^{\text{eq}} = N_{\text{aero}}^{\text{eq}} = 2350$ . This accidental coincidence is explained by the fact that the amount of helium displaced by the strand was equal to the amount of helium adsorbed on its surface.

The specific energy changes with decreasing number of particles. For the case of the non-negative external potential, the specific total energy tends to zero (as is seen for nonadsorbing aerogel and free atoms). For the attractive potential, atoms are first of all adsorbed on the surface, thus decreasing their energy. Taking into account that the attractive potential of aerogel was decreased in these calculations, it is possible to suppose that this effect for the real potential will be expressed more intensively.

The nonextensivity of the internal energy of the system  $E_{\text{self}}$  can be characterized using the parameter  $\lambda$  determined, e.g., from the relation [54]

$$E(N_1 + N_2) = E(N_1) + E(N_2) + \lambda E(N_1)E(N_2). \quad (54)$$

Let us consider a simple division of the system containing  $N$  particles into two equal parts:  $N_1 = N_2 = N/2$ . Fig. 7 shows the dependence of the parameter of the energy nonadditivity on  $N/N^{\text{eq}}$ . It is seen that this parameter tends to zero with increasing number of atoms. This indicates the transition to the thermodynamic limit. The parameter  $\lambda$  for aerogel is the largest in absolute value. Nonadsorbing aerogel has the lowest parameter  $\lambda$ . For comparison, Fig. 7 also shows the analytically calculated dependence for the uniform distribution of helium in the cell. However, it is incorrect to make a comparison with this dependence because helium does not remain homogeneous with decreasing number of particles but forms droplets. It is possible to conclude that the effect of the geometry of the potential on the nonadditivity is not decisive because the parameter  $\lambda$  of the adsorbing strand turns out to be larger than that of nonadsorbing aerogel. The value of the adsorbing potential is determining for the parameter  $\lambda$ .

## 8. Conclusion

It was shown that fractionalized set of hydrodynamical equations with taking into account nonextensivity of He-II inside nanopores leads to coupling between the first and the second sounds that appears even in the absence of viscous friction, which is undoubtedly the effect of fractional dimensionality of nanopore space and nonextensive nature of helium droplets. It was proposed that for the microscopical description of superfluid in nanoporous media with complex fractal structure one can use the fractional Schrödinger equation. But it is necessary to keep in mind that the fractal geometry of nanoporous media leads to the Galilean noninvariance of this equation and as a consequence one needs to choose the special frame of reference where, for example, nanoporous media is in a rest.

One can interpret dynamical equations of fractional quantum operator in Heisenberg representations as a classical dynamical equations in fractal media and generalize them to obtain fractional hydrodynamical set of equations. From this two-fluid fractional hydrodynamical model one can obtain equations of pressure-temperature and pure temperature oscillation. It was shown that the pressure-temperature coupling constant has linear dependence on temperature at low temperature region which provide us with possibility of experimental proof of given model.

By means of density functional theory simulation of superfluid helium in aerogel nanopores it was shown that there are two main effects of the limited geometry affecting the properties

of liquid helium: first, nonextensivity of the energy and, consequently, of other thermodynamic quantities which essentially depends on the value of the adsorbing potential and, second, fractal dimension of liquid helium within the scales of the confinement fractality mainly determined by the geometry. The correlation length of superfluid helium is about  $\xi \approx 3 \text{ \AA}$  at  $T = 0$ , increases with the temperature, and diverges when approaching the  $\lambda$ -point [55]. Thus, the correlation length belongs to the fractality range of aerogel, which considerably affects the phase diagram and the dynamic properties of superfluid helium. Therefore, the inclusion of these two factors is necessary in the phenomenological models of superfluid liquid in the limited space. The fact that the mass dimension of helium depends on the scale under consideration and is not a constant can be important. In addition, since the nonextensivity parameter depends on the attractive potential, it can differ considerably for different regions of the confinement.

## References

1. Naletov V.V, Tagirov M.S, Tayurskii D.A. *Low Temp. Phys.* **28**, 299 (2002)
2. Minnillin A.R, Tayurskii D.A. *JETP Lett.* **72**(12), 616-620 (2000)
3. Tagirov M.S, Yudin A.N., Mamin G.V., et al. *J. Low Temp. Phys.* **148**(5-6), 815-819 (2007)
4. Klochkov A.V., Kuz'min V.V, Safiullin K.R., et al. *JETP Lett.* **88**(12), 823-827 (2008)
5. Wong G., Crowell P., Cho H., et al. *Phys. Rev. Lett.* **65**(19), 2410-2413 (1990)
6. Matsumoto K., Tsuboya H., Yoshino K., et al. *J. Low Temp. Phys.* **148**(5-6), 615-620 (2007)
7. Vasquez C., Paredes R. *Condens. Matter Phys.* **9**(2) 305-317 (2006)
8. Azuah R.T., Glyde H.R., Scherm R., et al. *J. Low Temp. Phys.* **130**(5), 557-567 (2003)
9. Tayurskii D., Lysogorskii Y., Zvezdov D. *J. Phys.: Conf. Ser.* **150**(3), 032110 (2009)
10. Tayurskii D.A., Lysogorskii Y.V. *J. Low Temp. Phys.* **158**(1-2) 237-243 (2009)
11. Bossy J., Pearce J.V., Schober H., et al. *Phys. Rev. Lett.* **101**, 025301-4 (2008)
12. Wada N., Matsushita T., Hieda M., Toda R. *J. Low Temp. Phys.* **157**, 324-351 (2009)
13. Kanamori K., Aizawa M., Nananishi K., Hanada T. *Adv. Mater.* **19**(12), 1589-1593 (2007)
14. Khalatnikov I.M. *An Introduction to the Theory of Superfluidity*, Redwood City: Addison-Wesley, (1988)
15. Tilley D., Tilley J. *Superfluidity and Superconductivity*, 3rd Ed. London: IOP Publishing Ltd, (1990)
16. Coste C. *Eur. Phys. J. B* **253**, 245-253 (1998)
17. Hills R.N., Roberts P.H. *J. Low Temp. Phys.* **30**(5-6), 709-727 (1978)
18. Ginzburg V.L., Pitaevskii L.P. *Sov. Phys. JETP* **7**, 858 (1958)
19. Khalatnikov I.M. *Sov. Phys. JETP* **30**, 268-272 (1970)
20. Hills R.N., Roberts P.H. *Int. J. Eng. Sci.* **15**, 305-316 (1977)
21. Guerst J. *Phys. Rev. B* **22**, 3207 (1980)
22. Ristig M.L., Gernoth K.A. *Found. Phys.* **40**(9-10), 1253-1262 (2009)
23. Mongiovi M.S. *Phys. Rev. B* **48**(9), 6276-6283 (1993)

24. Mongiovi M.S., Peruzza R.A. *Math. Phys.* **54**, 566-583 (2003)
25. Porto J., Parpia J. *Phys. Rev. B* **59**(22), 14583-14592 (1999)
26. Courtens E., Vacher R. *Z. Phys. B: Condens. Matter* **68**, 355-361 (1987)
27. Hasmy A., Anglaret E., Foret M., et al. *Phys. Rev. B* **50**(9), 6006-6016 (1994)
28. McKenna M.J., Slawcki T.M., Maynard J.D. *Physica B* **165**, 581-582 (1990)
29. McKenna M.J., Slawcki T.M., Maynard J.D. *Phys. Rev. Lett.* **66**, 1878 (1991)
30. Biot M.A. *J. Acoust. Soc. Am.* **28**(2), 168 (1956)
31. Feder E. *Fractals*, Springer, (2007)
32. Gell-Mann M., Tsallis C. *Non-extensive Entropy - Interdisciplinary Applications*, Oxford University Press, (2004)
33. Parvan A., Biro T. *Arxiv preprint cond-mat/0607190* (2006)
34. Badescu V. *Adv. Complex Syst.* **11**(01), 43 (2008)
35. Wang Q.A., Nivanen L., Mehaute A.L., et al. *J. Phys. A: Math. Gen.* **35**(33), 7003-7007 (2002)
36. Abe S. *Phys. Rev. E* **63**(6), 061105 (2001)
37. Abe S., Martinez S., Pennini F., et al. *Phys. Lett. A* **281**, 126-130 (2001)
38. Laskin N. *Phys. Rev. E* **66**(5), 56108 (2002)
39. Lenzi E.K., Oliveira B.F., Astrath N.G., et al. *Eur. Phys. J. B* **62**(2), 155-158 (2008)
40. Greenberger D. *Phys. Rev. Lett.* **87**(10), 1-4 (2001)
41. Dong J., Xu M. *J. Math. Phys.* **49**(5), 052105 (2008)
42. Dalfovo F., Lastri A., Pricapenko L., Stringari S. *Phys. Rev. B* **52**, 1193 (1995)
43. Plimpton S. *J. Comput. Phys.* **117**, 1 (1995)
44. Ng T.Y., Yeo J.J., Liu Z.S. *J. Non-Cryst. Solids* **358**, 1350 (2012)
45. Theiler J. *J. Opt. Soc. Am. A* **7**, 1055 (1990)
46. Talu O., Myers A.L. *Colloids Surf. A: Physicochem. Eng. Asp.* **187-188**, 83 (2001)
47. Kresse G., Furthmuller J. *Phys. Rev. B* **54**, 11169 (1996)
48. Materials Design 2012 *Medea Version 2.10* (Angel Fire, NM: Materials Design)
49. Perdew J.P., Burke K., Ernzerhof M. *Phys. Rev. Lett.* **77**, 3865 (1996)
50. Klochkov A.V., Kuzmin V.V., Safiullin K.R., et al. *JETP Lett.* **88**, 823 (2008)
51. Debras C., Tayurskii D., Minisini B., Lysogorskiy Y. *J. Phys.: Conf. Ser.* **324**, 012029 (2011)
52. Alakshin E.M., Gazizulin R.R., Klochkov A.V., et al. *arXiv:1012.2461* (2010)
53. Lehtovaara L., Kiljunen T., Eloranta J. *J. Comput. Phys.* **194**, 78 (2004)
54. Ou C., Li W., Du J., et al. *Physica A* **387**, 5761 (2008)
55. Enss C., Hunklinger S. *Low-Temperature Physics* Springer (2005)

# Exponential temperature dependence of the $\text{Yb}^{3+}$ relaxation in $\text{Y}_{0.98}\text{Yb}_{0.02}\text{Ba}_2\text{Cu}_3\text{O}_x$

A. Maisuradze<sup>1</sup>, A. Shengelaya<sup>2,\*</sup>, E. Pomjakushina<sup>3</sup>, K. Conder<sup>3</sup>, H. Keller<sup>1</sup>, K.A. Müller<sup>1</sup>

<sup>1</sup>Physik-Institut der Universität Zürich, Winterthurerstrasse 190, CH-8057 Zürich, Switzerland

<sup>2</sup>Department of Physics, Tbilisi State University, Chavchavadze av. 3, GE-0128 Tbilisi, Georgia

<sup>3</sup>Laboratory for Developments and Methods, Paul Scherrer Institut, CH-5232 Villigen PSI, Switzerland

\**E-mail: alexander.shengelaya@tsu.ge*

The relaxation of  $\text{Yb}^{3+}$  in  $\text{YBa}_2\text{Cu}_3\text{O}_x$  ( $x = 6.1$  and  $6.4$ ) was studied using Electron Paramagnetic Resonance (EPR). In these samples the  $\text{Yb}^{3+}$  relaxation is dominated by a phonon mechanism. It was shown that the conventional Raman two-phonon process involving acoustic phonons can not describe the temperature dependence of the  $\text{Yb}^{3+}$  relaxation. Instead, the Raman process involving optical phonons or an Orbach-like process via the excited vibronic levels of  $\text{Cu}^{2+}$  ions with energy  $\Omega = 500(50)$  K is responsible for the phononic part of the  $\text{Yb}^{3+}$  relaxation in  $\text{YBa}_2\text{Cu}_3\text{O}_x$ . The present results provide clear experimental evidence that optical phonons or local vibrations are the dominant source of spin-lattice relaxation at sufficiently high temperatures, which cannot be described by the traditional approach using the Debye approximation.

**PACS:** 74.72.-h, 76.30.-v, 76.20.+q

**Keywords:** spin-lattice relaxation, optical phonons, high-temperature superconductivity.

The spin-lattice relaxation rate of paramagnetic ions doped in materials provides important information on fluctuating electric and magnetic fields and has been widely used in solid state physics. The theory of electron spin-lattice relaxation in nonconducting solids was elaborated in classical papers of Heitler and Teller [1], Kronig [2], and Van Vleck [3]. They showed that the mechanism of relaxation consists of modulation of the crystal electric field by the lattice vibrations. The thermal vibrations in these models were considered in the Debye approximation. Whereas the low-frequency end of the phonon spectrum in crystals may be approximated by a simple Debye spectrum, the more dense high-frequency portion associated with optical phonons should be active at high temperatures in multiple phonon spin-lattice relaxation processes. To our knowledge, the first explicit treatment of the optic vibrations in the two-phonon Raman relaxation process was done by Kochelaev for nuclear quadrupole relaxation [4]. He showed that the optical vibrations can be the dominant source of relaxation at room temperatures with almost an exponential temperature dependence due to the narrow range of frequencies for these modes. Experimental studies of nuclear spin-lattice relaxation confirmed this prediction, showing that it is necessary to take into account optical modes in order to explain the temperature dependence of the nuclear quadrupole relaxation rate [5, 6]. Later, also Huang theoretically studied the electron spin-lattice relaxation and found that under certain conditions the optical phonon relaxation process may dominate the conventional acoustic phonon relaxation [7]. However, the importance of the optical phonon contribution in the spin-lattice relaxation was not acknowledged by the Electron Paramagnetic Resonance (EPR) community. In fact there are only a very few experimental publications in EPR, where the optical phonon contribution was

taken into account to explain spin-lattice relaxation data [8,9]. It is remarkable that in the classical textbook of magnetic resonance by Abragam and Bleaney [10] the contribution of optical phonons to spin relaxation is not mentioned. Even in a more recent book concerning EPR there is a statement: “It is only the acoustic modes that are involved in spin-lattice relaxation” [11].

Here we report results of an EPR study of the  $\text{Yb}^{3+}$  relaxation in  $\text{YBa}_2\text{Cu}_3\text{O}_x$  samples with oxygen content  $x = 6.1$  and  $6.4$ . In these samples the  $\text{Yb}^{3+}$  relaxation is dominated by a phonon mechanism. The temperature dependence of this relaxation was determined by measuring the  $\text{Yb}^{3+}$  EPR linewidth in a broad temperature range. The obtained results clearly demonstrate that the traditional Raman mechanism using the Debye approximation cannot describe the phononic contribution to relaxation. Instead, the Raman process involving optical phonons or an Orbach-like process via the excited vibronic levels of  $\text{Cu}^{2+}$  ions with energy  $\Omega = 500(50)$  K is responsible for the phononic part of the  $\text{Yb}^{3+}$  relaxation in  $\text{YBa}_2\text{Cu}_3\text{O}_x$ .

The polycrystalline samples of  $\text{Y}_{1-y}\text{Yb}_y\text{Ba}_2\text{Cu}_3\text{O}_x$  with  $x = 6.1$  and  $6.4$  were prepared by the standard solid state reaction. The as-prepared samples were oxidized in oxygen atmosphere at  $500^\circ\text{C}$ . The required oxygen content in the samples was adjusted by gettering in a closed ampoule with metallic copper ( $850^\circ\text{C}$ , 10 h; cooling  $10^\circ\text{C/h}$ ). The dilute level of the Yb doping ( $y = 0.02$ ) was chosen in order to minimize broadening effects from Yb-Yb interactions and at the same time to obtain a sufficiently strong EPR signal. The EPR measurements were performed with an X-band BRUKER EMX spectrometer equipped with an Oxford Instruments helium flow cryostat. In order to avoid a signal distortion due to skin effects, the samples were ground and the powder was suspended in epoxy. The  $c$ -axes grain-orientation was obtained by placing the samples in a 9 T magnetic field until the epoxy hardened.

The rare-earth site in  $\text{YBa}_2\text{Cu}_3\text{O}_x$  is eight-fold coordinated by oxygens lying in the  $\text{CuO}_2$  bilayers. In this case the eight-fold degeneracy of the ground-state multiplet  $^2F_{7/2}$  of the  $\text{Yb}^{3+}$  ions ( $4f^{13}$ ) is split by the crystal electric field with either a  $\Gamma_7$  or a  $\Gamma_6$  ground state doublet [10]. Generally, this splitting is large enough so that only the lowest lying doublet is appreciably populated. So, EPR signals should be observed only for this doublet. In fact, the observed EPR spectra of  $\text{Yb}^{3+}$  in  $\text{Y}_{0.98}\text{Yb}_{0.02}\text{Ba}_2\text{Cu}_3\text{O}_x$  can be described with an effective spin  $S = 1/2$  and anisotropic  $g$  values [12]. In the sample with oxygen content  $x = 6.4$  the anisotropic  $g$  values  $g_{\parallel} = 3.13(3)$  and  $g_{\perp} = 3.49(3)$  are observed at  $T = 40$  K. The average value  $\bar{g} = 3.37$  is close to  $g = 3.43$  expected for the isolated  $\Gamma_7$  ground doublet [10].

Fig. 1 shows typical EPR spectra for the  $x = 6.4$  sample at different temperatures with the magnetic field applied perpendicular to the  $c$ -axis direction. The EPR lines in the  $g \approx 2$  region are due to  $\text{Cu}^{2+}$  defect centers, which are always present in  $\text{YBa}_2\text{Cu}_3\text{O}_{6+x}$  [13]. The  $\text{Yb}^{3+}$  EPR spectrum at 37 K is rather complex, with a dominant central line and shoulders on each side, which are due to partially resolved hyperfine components from ytterbium isotopes with nonzero nuclear spin. In Fig. 1 one can see that with increasing temperature the  $\text{Yb}^{3+}$  EPR line broadens and the multiple-line structure of the Yb spectra gradually merges into one line which continues to broaden with temperature. This broadening is due to the Yb relaxation and is the subject of the present study.

The anisotropic nature of the  $\text{Yb}^{3+}$  signal, the partially resolved hyperfine structure and the non-ideal grain alignment, make it very difficult to accurately model the complex shape of the Yb EPR spectra and its evolution with temperature. In order to extract the linewidth related to relaxation, we used a similar approach as used in inelastic neutron scattering studies of rare-earth relaxation in cuprates [14]. This method is based on the assumption that the observed line shape consists of two components: a temperature-independent residual function

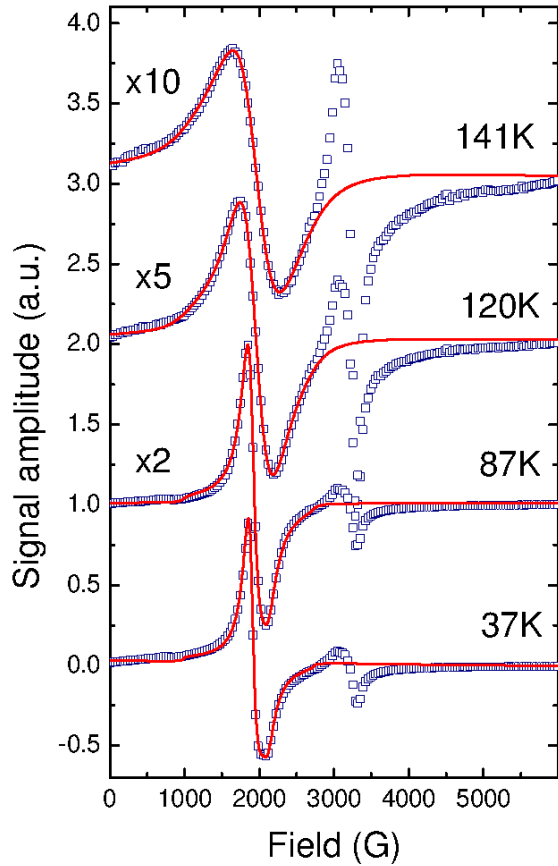


**Figure 1.** EPR spectra in grain oriented  $\text{Y}_{0.98}\text{Yb}_{0.02}\text{Ba}_2\text{Cu}_3\text{O}_{6.4}$  at different temperatures for the magnetic field direction perpendicular to the crystal  $c$ -axis. The solid lines are fits to the data, and include relaxation as described in the text.

illustrated in Fig. 2 for the sample with  $x = 6.4$ , where the relaxation rate is plotted on a logarithmic scale versus inverse temperature. Such an exponential dependence is expected for the Orbach relaxation process via an excited intermediate energy level [15]. In this case  $\Delta$  corresponds to the separation between the ground state doublet and the excited level. According to inelastic neutron scattering experiments the first excited energy level of Yb in  $\text{YBa}_2\text{Cu}_3\text{O}_7$  is about 1000 K above the ground state doublet [16]. Since there is no excited crystal field energy level with  $\Delta \sim 500$  K, the traditional Orbach relaxation mechanism can be excluded.

Another possible relaxation mechanism is the Raman two-phonon process involving acoustic phonons with the following temperature dependence in the case of a Kramers doublet [10]:

$$T_1^{-1}(T) = CT^9 \int_0^{\Theta_D/T} z^8 e^z / (e^z - 1)^2 dz. \quad (1)$$

We found that this expression describes the temperature dependence of the relaxation rate quite well, as shown by the dashed line in Fig. 2. However, the Debye temperature  $\Theta_D = 650(20)$  K obtained from the fit is too large compared to  $\Theta_D = 300$  K reported for low-doped  $\text{YBa}_2\text{Cu}_3\text{O}_x$  [17]. The dotted line in Fig. 2, calculated with  $\Theta_D = 300$  K clearly does not fit the data and shows that a conventional Raman process involving acoustic phonons cannot explain the temperature dependence of the  $\text{Yb}^{3+}$  relaxation rate in  $\text{YBa}_2\text{Cu}_3\text{O}_x$ . It was already mentioned in the introduction that in the vast majority of publications concerning spin relaxation, experimental

due to inhomogeneous broadening and a temperature-dependent function related to relaxational broadening. The exact function used to describe the residual line shape is not important. We used a sum of several Lorentzians to model the inhomogeneous broadening at low temperatures, where relaxational broadening is negligible. The line drawn through the 37 K data in Fig. 1 represents the residual function. Having established the residual function, we kept it fixed at all temperatures and fitted the data at higher-temperature by convolving the residual function with the broadening function of Lorentzian shape. The center, width, and amplitude of the broadening function were the only variable parameters. The resulting fits are shown in Fig. 1.

Our detailed EPR studies have shown that in superconducting  $\text{YBa}_2\text{Cu}_3\text{O}_x$  samples both electronic and phononic processes contribute to the  $\text{Yb}^{3+}$  relaxation [12]. The electronic contribution to relaxation decreases with decreasing  $x$ . Below  $x = 6.4$  the electronic contribution is negligible and the  $\text{Yb}^{3+}$  relaxation is dominated by a phonon mechanism. We observed that the temperature dependence of the relaxation rate follows closely the exponential function  $C \exp(-\Delta/T)$  in both samples ( $x = 6.1$  and 6.4) with  $\Delta \simeq 500(50)$  K. This is demon-

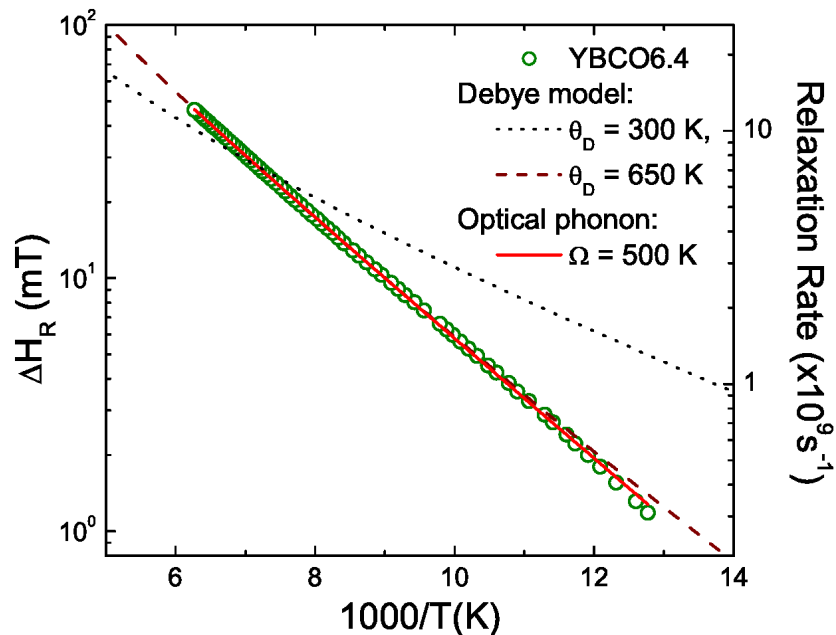


**Figure 2.** Temperature dependence of the relaxation linewidth  $\Delta H_R$  in  $Y_{0.98}Yb_{0.02}Ba_2Cu_3O_{6.4}$  plotted on a logarithmic scale versus inverse temperature. The solid line is a best fit to Eq. (2). The dashed and dotted lines represent the best fits using Eq. (1) with  $\Theta_D = 650$  K and 300 K, respectively.

results are interpreted using the Debye model with a linear dispersion law. The optical modes are taken into account only by extending the acoustical modes beyond the Brillouin zone with the Debye temperature  $\Theta_D$  defined by the total degree of freedom of the lattice. Moreover, using this approach in many publications the authors attempted to extract the Debye temperature from the temperature dependence of the spin-lattice relaxation rate. The dashed line in Fig. 2 shows that in principle it is possible to fit experimental results with such a model, however  $\Theta_D$  extracted from this fit has nothing to do with the real Debye temperature of the material. Therefore, although the Debye model is reasonable to describe the heat capacity properties, our results show that it may be misleading for the spin-lattice relaxation at relatively high temperatures. It is a consequence not only of a completely different dispersion law of optical phonons with a narrow band of frequencies, but also due to very different amplitudes and relative phases of neighboring ions vibrations in comparison with acoustical modes.

For a Raman process with the participation of some local vibrations or optical phonons

$$T_1^{-1}(T) = C \exp(\Omega/T) / [\exp(\Omega/T) - 1]^2, \quad (2)$$

where  $\Omega$  is the optical phonon frequency [4, 7]. The solid line in Fig. 2 represents a best fit to the data using Eq. (2) with  $\Omega \simeq 500(50)$  K. This indicates that the Raman process involving optical phonons describes well the phonon contribution to the  $Yb^{3+}$  spin-lattice relaxation. Optical phonons within this energy range exist in  $YBa_2Cu_3O_x$ : (i) in-plane bond-bending (500-560 K) and (ii) out of plane  $B_{1g}$  (470 K) phonons [18, 19]. Preliminary theoretical calculations taking into account in-plane optical phonons have been performed in order to compare the contribution of acoustical and optical phonons to the  $Yb^{3+}$  spin relaxation in  $YBa_2Cu_3O_x$ . It was found that the optical phonon contribution to relaxation in the temperature range 60-140 K is at least one order of magnitude higher than the contribution from acoustical phonons [20]. Additional theoretical calculations are necessary in order to determine which of the two optical phonon modes (in-plane bond-bending or out of plane  $B_{1g}$ ) mostly contributes to the  $Yb^{3+}$  spin-lattice relaxation.

Finally, it is interesting to note that an exponential temperature dependence of the spin relaxation rate was also observed in an EPR study of crystals containing Jahn-Teller (JT) transition metal ions [21, 22]. In this case relaxation also takes place due to an Orbach-like process via the excited vibronic levels of the JT ion (localized Slonczewski modes) [23]. It would be interesting to search for localized vibronic modes in cuprates using inelastic neutron scattering. Such vibronic modes could lead to the observed exponential temperature dependence of the relaxation rate in YBa<sub>2</sub>Cu<sub>3</sub>O<sub>x</sub> if the Yb<sup>3+</sup> spin relaxation occurs due to coupling to the vibrations of surrounding CuO<sub>6</sub> complexes since Cu<sup>2+</sup> is a strong JT ion.

To summarize, we studied the temperature dependence of the Yb<sup>3+</sup> EPR linewidth in YBa<sub>2</sub>Cu<sub>3</sub>O<sub>x</sub> with oxygen content  $x = 6.1$  and  $6.4$ . It was shown that the Raman process involving optical phonons or an Orbach-like process via the excited vibronic levels of Cu<sup>2+</sup> ions with energy  $\sim 500$  K is responsible for the phononic part of the Yb<sup>3+</sup> relaxation in YBa<sub>2</sub>Cu<sub>3</sub>O<sub>6+x</sub>. Our results demonstrate that optical phonons or local vibrations may provide a dominant contribution to spin-lattice relaxation of paramagnetic ions at sufficiently high temperatures, which cannot be accounted for by the traditional approach using the Debye approximation.

This work was supported by the Swiss National Science Foundation, the SCOPES grant No. IZ74Z0-137322, and the Georgian National Science Foundation grant RNSF/AR/10-16.

## References

1. Heitler W., Teller E. *Proc. Roy. Soc.* **A155**, 629 (1936)
2. Kronig R.deL. *Physica* **6**, 33 (1939)
3. Van Vleck J.H. *Phys. Rev.* **57**, 426 (1940)
4. Kochelaev B.I. *JETP* **10**, 171 (1960)
5. Weber M.J. *Phys. Rev.* **130**, 1 (1963)
6. Hoch M.J.R., Lourens J.A.J., Gordon M.I. *Phys. Rev. B* **13**, 2787 (1976)
7. Huang C.-Y. *Phys. Rev.* **154**, 215 (1967)
8. Kurkin I.N., Chernov K.P. *JETP* **56**, 607 (1982)
9. Ivanshin V. A., Kurkin I.N., Völkel G. *Phys. Stat. Sol. B* **148**, K61 (1988)
10. Abragam A., Bleaney B. *Electron Paramagnetic Resonance of Transition Ions* (Clarendon Press, Oxford, 1970)
11. Pilbrow J.R. *Transition Ion Electron Paramagnetic Resonance* (Clarendon Press, Oxford, 1990)
12. Maisuradze A., Shengelaya A., Kochelaev B.I., Pomjakushina E., Conder K., Keller H., Müller K.A. *Phys. Rev. B* **79**, 054519 (2009)
13. Sichelschmidt J., Elschner B., Loidl A., Kochelaev B.I. *Phys. Rev. B* **51**, 9199 (1995)
14. Boothroyd A.T., Mukherjee A., Murani A.P. *Phys. Rev. Lett.* **77**, 1600 (1996)
15. Dodds S.A., Sanny J., Orbach R. *Phys. Rev. B* **18**, 1016 (1978)

16. Guillaume M., Allenspach P., Mesot J., Staub U., Furrer A., Osborn R., Taylor A.D., Stucki F., Unternährer P. *Solid State Commun.* **81**, 999 (1992)
17. von Molnar S., Torressen A., Kaiser D., Holtzberg F., Penney T. *Phys. Rev. B* **37**, 3762 (1988)
18. Pintschovius L., Reichardt W., Kläser M., Wolf T., Löhneysen H. *Phys. Rev. Lett.* **89**, 037001 (2002)
19. Opel M., Hackl R., Devereaux T.P., Virosztek A., Zawadowski A., Erb A., Walker E., Berger H., Forró L. *Phys. Rev. B* **60**, 9836 (1999)
20. Kutuzov A.S., Kochelaev B.I. (unpublished)
21. Höchli U., Müller K.A. *Phys. Rev. Lett.* **12**, 730 (1964)
22. Höchli U., Müller K.A., Wysling P. *Phys. Letters* **15**, 1 (1965)
23. Müller K.A. in *Magnetic Resonance and Relaxation*, edited by R. Blinc (North-Holland Publishing Company, 1967), pp. 192–208

# Исследование одностенных углеродных зигзагообразных нанотрубок в модели Хаббарда в приближении статических флуктуаций

Г.И. Миронов

Марийский государственный университет, Йошкар-Ола, Россия

*E-mail: mirgi@marsu.ru*

В рамках модели Хаббарда вычислены антикоммутаторные функции Грина и определены энергетические спектры для однослойных углеродных нанотрубок типа зигзаг с учетом конечной кривизны нанотрубок. Полученные спектры элементарных возбуждений для нанотрубок типа зигзаг показали, что «металлические» зигзажные нанотрубки на самом деле являются узкощелевыми полупроводниками. Сравнение с экспериментальными значениями энергетических щелей продемонстрировало совпадение теоретических и экспериментальных значений.

**PACS:** 73.63.Fg, 73.20.Mf, 78.67.Ch, 61.46.Fg, 71.20.Tx, 78.20.Ci

**Keywords:** carbon nanotubes, Hubbard model, electron correlation, energy band, band structure

При конструировании электронных устройств и объединения их в приборы возникает необходимость использовать материалы как с полупроводящими свойствами, так и с более высокой электропроводностью. Углеродные нанотрубки могут стать компонентами будущих наноэлектронных приборов, поскольку они при различных значениях индексов  $(n, m)$  [1], то есть в зависимости от структуры, должны обладать разными электрическими свойствами [2].

Расчеты, выполненные вскоре после открытия углеродных нанотрубок [3-5], показали, что металлическим типом зонной структуры обладают те нанотрубки, для которых разность  $(n - m)$  кратна трем, т.е. практически треть нанотрубок, если предположить, что синтез нанотрубок с разными хиральностями происходит с одинаковыми вероятностями. Остальные нанотрубки, для которых  $(n - m)$  не кратна трем, должны являться полупроводниками.

Потребовалось время, чтобы квантово-химический прогноз [3-5] подтвердился экспериментально [6-9]. Оказалось, что по температурной зависимости сопротивления все нанотрубки можно разделить на две группы. У одних сопротивление незначительно и почти линейно возрастает с понижением температуры, они были идентифицированы как металлы. У другой группы нанотрубок наблюдалась почти линейная зависимость логарифма сопротивления от обратной температуры, что специфично для полупроводников.

Хотя работы [6-9] и показали, что нанотрубки бывают как металлическими, так и полупроводниковыми, исследования не до конца подтвердили предсказанную теорией зависимость характера электропроводности от их геометрии, т.е. от значения индексов  $(n, m)$ , так как полный контроль структуры нанотрубок к тому времени не был достигнут, к тому же из-за применения металлических частиц в качестве катализаторов нанотрубки содержали примеси, влияющие на проводящие свойства.

Это стало возможным с развитием сканирующей туннельной микроскопии и спектроскопии. Для индивидуальных ультрачистых нанотрубок удалось определить и атомную

структуру (хиральность) и электропроводность [10,11]. Анализ экспериментальных данных подтвердил теоретические соображения о зависимости типа проводимости от геометрии нанотрубок. Был сделан вывод, что в согласии с данными квантовой химии нанотрубки, для которых разность  $(n - m)$  кратна трем, являлись металлическими, несмотря на то, что сопротивление с понижением температура не понижалось, хотя для металлических систем сопротивление с понижением температуры должно уменьшаться, а остальные – полупроводниковыми.

Вывод о том, что все нанотрубки  $(n, m)$  с разностью  $(n - m)$ , кратной трем, должны являться металлическими, основан на очень простой теоретической модели, в которой учитывают только топологию химических связей и пренебрегают энергией кулоновского отталкивания электронов с противоположно ориентированными проекциями спинов, оказавшихся на одной орбитали атома. Т.е. пренебрегают тем, что подсистема  $\pi$ -электронов в одностенных нанотрубках является, по сути, сильно коррелированной подсистемой. Пренебрегают также кривизной поверхности нанотрубки, из-за которой атомные  $p_\pi$ -орбитали ориентированы не строго параллельно друг другу. Как показывает более детальный анализ [12, 13] в случае нанотрубок  $(n, 0)$  последнее должно приводить к образованию щели между валентной зоной и зоной проводимости. Для экспериментального обнаружения щелей при температуре 5 К для нанотрубок  $(9, 0)$  в ультравысоком вакууме методами сканирующей туннельной спектроскопии в области уровня Ферми были определены дифференциальные проводимости, значения которых с точностью до постоянного множителя равны плотностям электронных состояний [12]. Измерение вольт-амперной зависимости проводилось для индивидуальной сверхчистой нанотрубки, размещенной на подложке Au(111). Эти данные, действительно, свидетельствуют о существовании у нанотрубок  $(9, 0)$  в области уровня Ферми энергетической щели. Для того, чтобы понять, не подложка ли влияет на проводящие свойства нанотрубок, были проведены измерения на  $\text{Si}_3\text{N}_4$  тонкой подложке, нанесенной на Si [14]. Эксперименты [14] подтвердили наличие узких зон запрещенной энергии для «металлических» нанотрубок. Поэтому нанотрубки типа зигзаг, строго говоря, оказываются узкощелевыми полупроводниками, а не металлами.

Цель нашей работы – исследование зонной структуры одностенных нанотрубок типа зигзаг с учетом модели сильной связи [13], электрон-электронной корреляции в  $\pi$ -электронная подсистема [15-17], конечной кривизны поверхности нанотрубки [12, 13] и объяснение результатов эксперимента [12].

В углеродных нанотрубках углерод находится в  $sp^2$ -гибридизированном состоянии и основной вклад в свойства таких систем вносит  $\pi$ -электронная подсистема. Особенностью  $\pi$ -электронной подсистемы является то, что электроны этой подсистемы оказываются частично как локализованными, так и делокализованными. Из-за перекрытия волновых функций соседних атомов,  $\pi$ -электроны могут перескакивать с узла на соседний узел нанотрубки, вследствие чего на одном узле могут оказаться два  $\pi$ -электрона с разными проекциями спинов. При этом возникает необходимость учета энергии кулоновского отталкивания электронов, оказавшихся на одном узле. Поэтому все чаще физики, занимающиеся нанотрубками, приходят к выводу, что  $\pi$ -электронная подсистема в нанотрубках представляет собой систему с сильными корреляциями. В ряде работ, например [16,17], отмечается, что экспериментальные данные по нанотрубкам нельзя объяснить без привлечения концепции о сильно коррелированных состояниях. Для описания сильно коррелированных систем можно использовать модель Хаббарда [18]. Гамильтониан модели Хаббарда с учетом наличия в нанотрубках двух подрешеток **A** и **C** имеет вид:

$$\hat{H} = \hat{H}_0 + \hat{V}, \quad (1)$$

$$\hat{H}_0 = \sum_{f \in A} \varepsilon \hat{n}_{f\sigma} + \sum_{l \in C} \varepsilon \hat{n}_{l\sigma} + \sum_{f \neq l} B_{fl} \left( \hat{a}_{f\sigma}^\dagger \hat{a}_{l\sigma} + \hat{a}_{l\sigma}^\dagger \hat{a}_{f\sigma} \right), \quad (2)$$

$$\hat{V} = U \sum_{f \in A} \hat{n}_{f\uparrow} \hat{n}_{f\downarrow} + U \sum_{l \in C} \hat{n}_{l\uparrow} \hat{n}_{l\downarrow}, \quad (3)$$

где  $\hat{a}_{j\sigma}^\dagger$ ,  $\hat{a}_{j\sigma}$  – ферми-операторы рождения и уничтожения электронов на узле  $j$  ( $j = f, l$ ) решетки с проекцией спина  $\sigma$ .  $\hat{n}_{j\sigma} = \hat{a}_{j\sigma}^\dagger \hat{a}_{j\sigma}$ ,  $\varepsilon$  – собственная энергия электрона,  $U$  – энергия кулоновского отталкивания электронов с противоположно ориентированными спинами на одной  $p_\pi$ -орбитали,  $B_{fl} = B(f - l)$  – интеграл переноса, описывающий перескоки  $\pi$ -электрона от атома к соседнему атому за счет кинетической энергии и поля наносистемы с учетом кривизны поверхности нанотрубки.

Уравнения движения для операторов рождения электрона в представлении Гейзенберга будут иметь вид ( $j = f, l, i = l, f, \tau = it$ ):

$$\frac{d}{d\tau} \hat{a}_{j\uparrow}^\dagger = \hat{a}_{j\uparrow}^\dagger + \sum_i B_{ji} \hat{a}_{j\uparrow}^\dagger + U \hat{n}_{j\downarrow} \hat{a}_{j\uparrow}^\dagger. \quad (4)$$

Представим оператор числа частиц в (4) в виде:

$$\hat{n}_{j\downarrow}(\tau) = \langle \hat{n}_{j\downarrow} \rangle + \Delta \hat{n}_{j\downarrow}(\tau). \quad (5)$$

Уравнение (4) перепишем в виде:

$$\frac{d}{d\tau} \hat{a}_{f\uparrow}^\dagger = \left( \varepsilon + \left( \frac{n}{2} + S \right) U \right) \hat{a}_{f\uparrow}^\dagger + \sum_{l \in C} B_{lf} \hat{a}_{l\uparrow}^\dagger + U \Delta \hat{n}_{f\downarrow} \hat{a}_{f\uparrow}^\dagger, \quad (6)$$

$$\frac{d}{d\tau} \hat{a}_{l\uparrow}^\dagger = \left( \varepsilon + \left( \frac{n}{2} - S \right) U \right) \hat{a}_{l\uparrow}^\dagger + \sum_{l \in C} B_{lf} \hat{a}_{l\uparrow}^\dagger + U \Delta \hat{n}_{l\downarrow} \hat{a}_{l\uparrow}^\dagger, \quad (7)$$

где мы по аналогии с [19] введены понятия  $n$  – среднего количества  $\pi$ -электронов на одном узле,  $S$  – среднего значения проекции спина  $\pi$ -электрона на узле. В дальнейшем мы ограничимся случаем, когда  $n = 1$  (количество  $\pi$ -электронов совпадает с количеством атомов в нанотрубке). Самосогласованное вычисление среднего значения проекции спина показывает, что в случае конечных температур  $S = 0$ .

Введем для оператора рождения частиц понятие представления «типа представления взаимодействия» [20,21]:

$$\hat{a}_{f\uparrow}^\dagger(\tau) = e^{\hat{H}\tau} \hat{a}_{f\uparrow}^\dagger(0) e^{-\hat{H}\tau} = e^{\hat{H}_0\tau} \left( e^{-\hat{H}_0\tau} e^{\hat{H}\tau} \hat{a}_{f\uparrow}^\dagger(0) e^{-\hat{H}\tau} e^{\hat{H}_0\tau} \right) e^{-\hat{H}_0\tau} = e^{\hat{H}_0\tau} \hat{a}_{f\uparrow}^\dagger e^{-\hat{H}_0\tau}. \quad (8)$$

Для оператора  $\hat{a}_{f\uparrow}^\dagger(\tau)$  в (8), как вытекает из (6), получается следующее уравнение движения:

$$\frac{d}{d\tau} \hat{a}_{f\uparrow}^\dagger = U \Delta \hat{n}_{f\downarrow} \hat{a}_{f\uparrow}^\dagger. \quad (9)$$

Допустим теперь, что физическая величина, соответствующая оператору флуктуации числа частиц  $\Delta \hat{n}_{f\downarrow}$ , является интегралом движения. Это приближение будем, по аналогии с более раннее опубликованными работами [20, 21], называть приближением статических флуктуаций. Приближение  $\Delta \hat{n}_{f\downarrow}(\tau) = \Delta \hat{n}_{f\downarrow}(0)$  упрощает решение уравнения (9), поскольку воспользовавшись операторным равенством  $\hat{n}_{f\downarrow}^2 = \hat{n}_{f\downarrow}$  и записав уравнение движения

для оператора на правой стороне равенства (9), получим замкнутую систему двух дифференциальных уравнений для операторов. Решив получившуюся систему уравнений, будем иметь следующее решение для оператора  $\hat{a}_{f\uparrow}^\dagger(\tau)$ :

$$\begin{aligned} \hat{a}_{f\uparrow}^\dagger(\tau) = & \hat{a}_{f\uparrow}^\dagger(0) \left\{ 1 + \left( \frac{n}{2} + S \right) (e^{U\tau} - 1) \right\} e^{-U(\frac{n}{2}+S)\tau} \\ & + \Delta \hat{n}_{f\downarrow}(0) \hat{a}_{f\uparrow}^\dagger(0) (e^{U\tau} - 1) e^{-U(\frac{n}{2}+S)\tau}. \end{aligned} \quad (10)$$

Аналогичное решение можно получить и для оператора  $\hat{a}_{l\uparrow}^\dagger(\tau)$ . Подставляя получившееся решение (10) в (8) получим:

$$\begin{aligned} \hat{a}_{f\uparrow}^\dagger(\tau) = & e^{\hat{H}_0\tau} \hat{a}_{f\uparrow}^\dagger(0) e^{-\hat{H}_0\tau} \left\{ 1 + \left( \frac{n}{2} + S \right) (e^{U\tau} - 1) \right\} e^{-U(\frac{n}{2}+S)\tau} \\ & + e^{\hat{H}_0\tau} \Delta \hat{n}_{f\downarrow}(0) e^{-\hat{H}_0\tau} e^{\hat{H}_0\tau} \hat{a}_{f\uparrow}^\dagger(0) e^{-\hat{H}_0\tau} (e^{U\tau} - 1) e^{-U(\frac{n}{2}+S)\tau}. \end{aligned} \quad (11)$$

Для другой подрешетки:

$$\begin{aligned} \hat{a}_{l\uparrow}^\dagger(\tau) = & e^{\hat{H}_0\tau} \hat{a}_{l\uparrow}^\dagger(0) e^{-\hat{H}_0\tau} \left\{ 1 + \left( \frac{n}{2} - S \right) (e^{U\tau} - 1) \right\} e^{-U(\frac{n}{2}-S)\tau} \\ & + e^{\hat{H}_0\tau} \Delta \hat{n}_{l\downarrow}(0) e^{-\hat{H}_0\tau} e^{\hat{H}_0\tau} \hat{a}_{l\uparrow}^\dagger(0) e^{-\hat{H}_0\tau} (e^{U\tau} - 1) e^{-U(\frac{n}{2}-S)\tau}. \end{aligned} \quad (12)$$

В (11), (12) введем операторы:

$$\hat{a}_{f\uparrow}^\dagger(\tau) = e^{\hat{H}_0\tau} \hat{a}_{f\uparrow}^\dagger(0) e^{-\hat{H}_0\tau}, \quad \hat{a}_{l\uparrow}^\dagger(\tau) = e^{\hat{H}_0\tau} \hat{a}_{l\uparrow}^\dagger(0) e^{-\hat{H}_0\tau}. \quad (13)$$

Уравнения движения для вновь введенных в (10) операторов рождения электронов в разных подрешетках будут иметь вид:

$$\frac{d}{d\tau} \hat{a}_{f\uparrow}^\dagger = \left( \varepsilon + \left( \frac{n}{2} + S \right) U \right) \hat{a}_{f\uparrow}^\dagger + \sum_{l \in C} B_{lf} \hat{a}_{l\uparrow}^\dagger, \quad (14)$$

$$\frac{d}{d\tau} \hat{a}_{l\uparrow}^\dagger = \left( \varepsilon + \left( \frac{n}{2} - S \right) U \right) \hat{a}_{l\uparrow}^\dagger + \sum_{l \in C} B_{lf} \hat{a}_{f\uparrow}^\dagger. \quad (15)$$

Для решения системы уравнений движения (14), (15) воспользуемся следующими преобразованиями Фурье:

$$\hat{a}_{f\uparrow}^\dagger = \sqrt{\frac{2}{N}} \sum_k \hat{a}_{k\uparrow}^\dagger \exp(-i\mathbf{k}\mathbf{r}_f), \quad \hat{a}_{l\uparrow}^\dagger = \sqrt{\frac{2}{N}} \sum_k \hat{b}_{k\uparrow}^\dagger \exp(-i\mathbf{k}\mathbf{r}_l). \quad (16)$$

Из (14), (15) получим замкнутую систему уравнений движения:

$$\frac{d}{d\tau} \hat{a}_{k\uparrow}^\dagger(\tau) = \left( \varepsilon + \left( \frac{n}{2} + S \right) U \right) \hat{a}_{k\uparrow}^\dagger(\tau) + B_k \hat{b}_{k\uparrow}^\dagger(\tau), \quad (17)$$

$$\frac{d}{d\tau} \hat{b}_{k\uparrow}^\dagger(\tau) = \left( \varepsilon + \left( \frac{n}{2} - S \right) U \right) \hat{b}_{k\uparrow}^\dagger(\tau) + B_k \hat{a}_{k\uparrow}^\dagger(\tau), \quad (18)$$

где  $B_k$  зависит от геометрии нанотрубки и в случае нанотрубок типа зигзаг определяется следующим образом:

$$B_k = \pm B' \sqrt{1 + 4 \cos^2 \left( \frac{\sqrt{3}}{2} k_x a \right) + 4 \cos \left( \frac{3}{2} k_y a \right) \cos \left( \frac{\sqrt{3}}{2} k_x a \right)}. \quad (19)$$

Интеграл перескока  $B'$  с учетом конечной кривизны нанотрубки имеет вид:  $B' = B(1 - W \sin^2 \alpha)$ . Угол  $\alpha$  характеризует отношение расстояния между атомами углерода С-С к радиусу нанотрубки,  $W = 0.08$  – некоторый параметр, определяемый из геометрии нанотрубки типа зигзаг. Смысл перенормировки интеграла переноса  $B$  в том, что из-за конечной кривизны нанотрубки перекрытие волновых функций оказывается меньше по сравнению с графеном, поскольку оси симметрии орбиталей  $\pi$ -электронов соседних атомов углерода оказываются непараллельными друг другу. Для нанотрубки (9,0) угол  $\alpha = 20^\circ$  – окружность на плоскости, проходящей через центры атомов нанотрубки перпендикулярно к оси нанотрубки делится на  $(2\pi/2\alpha)$  одинаковых секторов. Чем больше радиус нанотрубки, тем угол  $\alpha$  по величине меньше, в предельном случае  $\alpha = 0^\circ$  переходим к случаю графена, для которого  $B' = B$ .

Решения для системы операторных уравнений (17), (18) несложно получить, они равны:

$$\hat{a}_{k\uparrow}^\dagger(\tau) = \frac{1}{2}\hat{a}_{k\uparrow}^\dagger(0) \left\{ \left(1 + \frac{SU}{t_k}\right) e^{(\varepsilon + \frac{U}{2} + t_k)\tau} + \left(1 - \frac{SU}{t_k}\right) e^{(\varepsilon + \frac{U}{2}n - t_k)\tau} \right\} + \frac{1}{2}\hat{b}_{k\uparrow}^\dagger(0)\frac{B_k}{t_k} \left\{ e^{(\varepsilon + \frac{U}{2}n + t_k)\tau} - e^{(\varepsilon + \frac{U}{2}n - t_k)\tau} \right\}, \quad (20)$$

$$\hat{b}_{k\uparrow}^\dagger(\tau) = \frac{1}{2}\hat{b}_{k\uparrow}^\dagger(0) \left\{ \left(1 - \frac{SU}{t_k}\right) e^{(\varepsilon + \frac{U}{2} + t_k)\tau} + \left(1 + \frac{SU}{t_k}\right) e^{(\varepsilon + \frac{U}{2}n - t_k)\tau} \right\} + \frac{1}{2}\hat{a}_{k\uparrow}^\dagger(0)\frac{B_k}{t_k} \left\{ e^{(\varepsilon + \frac{U}{2}n + t_k)\tau} - e^{(\varepsilon + \frac{U}{2}n - t_k)\tau} \right\}, \quad (21)$$

где введено обозначение:

$$t_k = \sqrt{S^2U^2 + B_k^2}. \quad (22)$$

Подставив решения для операторов (20), (21) в выражения, получающиеся из (11), (12) после преобразования Фурье (16), воспользовавшись перед этим условиями:  $\Delta n_{f\downarrow}(0) = \Delta n_{\downarrow}$ ,  $\Delta n_{l\downarrow}(0) = \Delta n_{\downarrow}$  – предполагая теперь для простоты дальнейших рассуждений, что операторы флуктуации в начальный момент времени были одинаковыми в пределах подрешеток, можем получить следующие выражения для фурье-образов антикоммутирующих функций Грина:

$$\langle\langle \hat{a}_{k\uparrow}^\dagger | \hat{a}_{k\uparrow} \rangle\rangle_E = \frac{i}{2\pi} \left\{ \frac{\frac{1}{2}(\frac{1}{2} - S) \left(1 - \frac{SU}{t_k}\right)}{E - \varepsilon - U - SU - t_k} + \frac{\frac{1}{2}(\frac{1}{2} + S) \left(1 - \frac{SU}{t_k}\right)}{E - \varepsilon - SU - t_k} + \frac{\frac{1}{2}(\frac{1}{2} - S) \left(1 + \frac{SU}{t_k}\right)}{E - \varepsilon - U - SU + t_k} + \frac{\frac{1}{2}(\frac{1}{2} + S) \left(1 + \frac{SU}{t_k}\right)}{E - \varepsilon - SU + t_k} \right\}, \quad (23)$$

$$\langle\langle \hat{b}_{k\uparrow}^\dagger | \hat{b}_{k\uparrow} \rangle\rangle_E = \frac{i}{2\pi} \left\{ \frac{\frac{1}{2}(\frac{1}{2} + S) \left(1 + \frac{SU}{t_k}\right)}{E - \varepsilon - U + SU - t_k} + \frac{\frac{1}{2}(\frac{1}{2} - S) \left(1 + \frac{SU}{t_k}\right)}{E - \varepsilon + SU - t_k} + \frac{\frac{1}{2}(\frac{1}{2} + S) \left(1 - \frac{SU}{t_k}\right)}{E - \varepsilon - U + SU + t_k} + \frac{\frac{1}{2}(\frac{1}{2} - S) \left(1 - \frac{SU}{t_k}\right)}{E - \varepsilon + SU + t_k} \right\}. \quad (24)$$

Величина  $t_k$  в (23), (24) определяется ранее введенным равенством (22).

Функции Грина (23), (24) характеризуют свойства нанотрубок. Нас в первую очередь интересует энергетический спектр подсистемы  $\pi$ -электронов, который определяется полюсами функций Грина (23), (24).

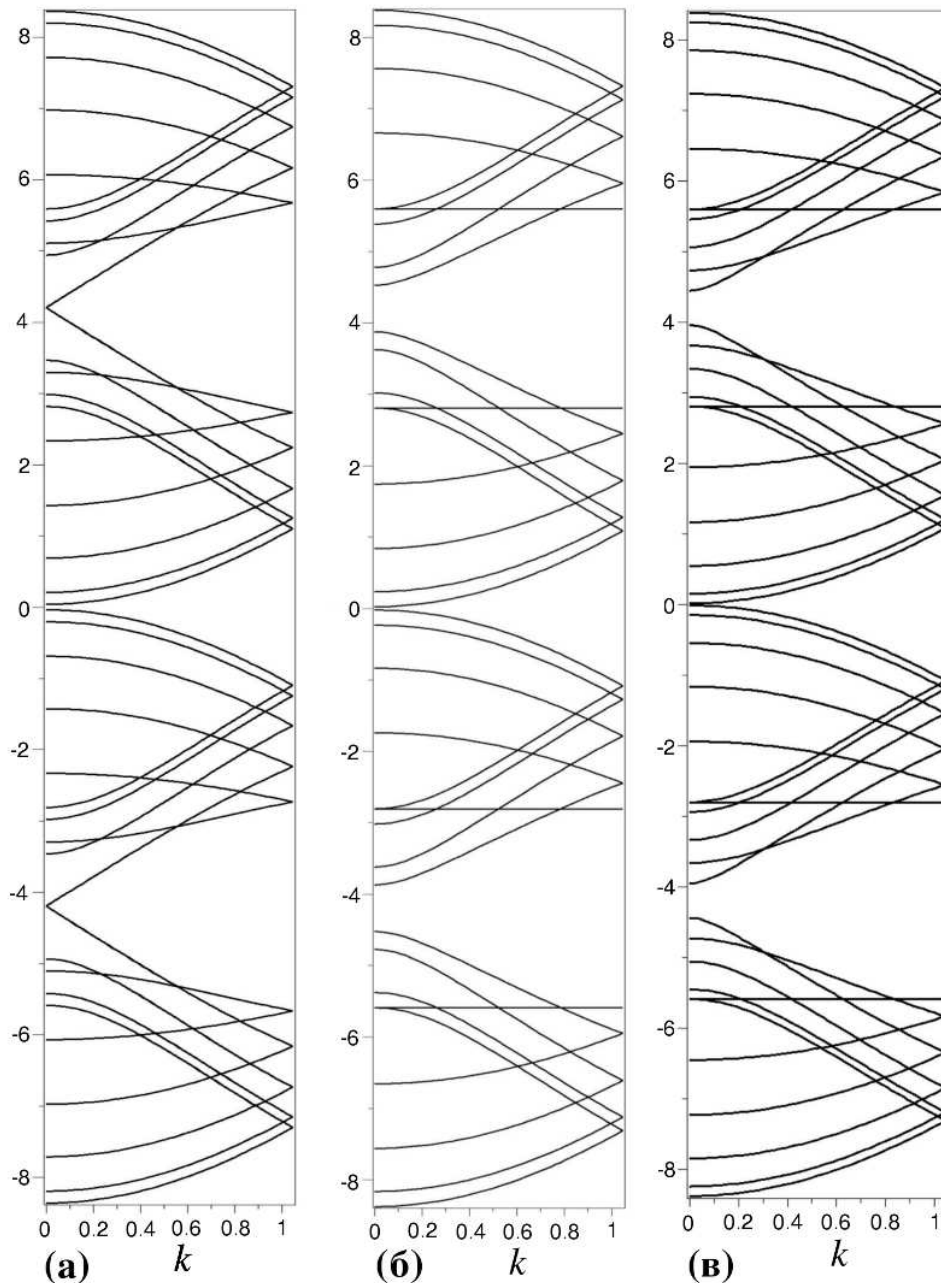


**Рис. 1.** Энергетический спектр для (а) нанотрубки (9,0), (б) нанотрубки (8,0), (в) нанотрубки (10,0) при значениях параметров:  $B = -1 \text{ eV}$ ,  $U = 6 \text{ eV}$ ,  $S = 0$ ,  $n = 1$ ,  $\varepsilon = -U/2$ .

На рис. 1 приведен спектр элементарных возбуждений для зигзажной нанотрубки хиральности (9, 0). На этом же рисунке для сравнения приведены энергетические спектры для нанотрубок типа зигзаг хиральностей (8, 0) и (10, 0). Во всех трех случаях энергетические зоны представлены в виде верхней и нижней хаббардовских подзон. В случае, когда количество  $\pi$ -электронов совпадает с количеством атомов нанотрубки, нижняя хаббардовская подзона полностью заполнена электронами, а верхняя хаббардовская подзона в основном состоянии не заполнена электронами, поэтому энергию Ферми можно отождествить с потолком нижней хаббардовской подзоны. Между валентной зоной (нижней подзоной) и зоной проводимости (верхней хаббардовской подзоной) располагается зона запрещенных энергий конечной ширины. Поэтому все три случая на рис. 1 соответствуют полупроводникам. В случае нанотрубки хиральности (9,0), которая согласно существовавшей ранее в

квантовой химии теории [3-5], должна была иметь металлические свойства, нижняя хаббардовская подзона состоит из 20 ветвей, причем ветви симметричны относительно центра нижней подзоны. Несколько слов о результатах вычислений в работах [3-5]. Полученные в этих работах  $\pi$ -зоны нанотрубок полностью совпадают с нижней хаббардовской подзоной. В этих работах было высказано мнение, что 10 нижних ветвей нижней хаббардовской подзоны образуют «валентную зону», 10 верхних ветвей нижней хаббардовской подзоны – «зону проводимости». Поскольку потолок введенной в этих работах «валентной зоны» и дно «зоны проводимости» касаются в одной точке, то был сделан вывод о том, что нанотрубки (9,0) являются металлами. Энергия, соответствующая касанию «валентной зоны» и «зоны проводимости» была объявлена энергией Ферми. В эксперименте [10] фермиевская энергия при температуре 5 К соответствовала потолку нижней хаббардовской подзоны, поскольку нижняя подзона полностью заполнена электронами. Понятно, что на уровне Ферми была обнаружена энергетическая щель и был сделан вывод о том, что нанотрубка (9,0) является полупроводником. Вид зонной структуры, приведенный нами для (9,0) полностью согласуется с экспериментальными данными. Поэтому можно сказать, что построенная в нашей работе теория позволяет теоретически объяснить полученный в эксперименте [12] вывод о том, что нанотрубка (9,0) является узкощелевым полупроводником.

Несколько иначе обстоит дело в случае нанотрубок (8,0) и (10,0). Согласно упрощенной теории [3-5], эти нанотрубки должны были обладать полупроводниковыми свойствами. Спектры, приведенные для этих нанотрубок в [3-5], соответствуют нижним хаббардовским подзонам на рис. 1(б) и рис. 1(в). В случае нанотрубки (8,0) в работах [3-5] нижние девять ветвей были отождествлены с валентной зоной, а вышележащие девять ветвей этой же нижней хаббардовской подзоны описывались как ветви, принадлежащие зоне проводимости. Между нижними девятью ветвями и верхними девятью ветвями нижней хаббардовской подзоны находится область энергии конечной ширины, которая была отождествлена с запрещенной зоной, и на этом основании был сделан вывод о том, что в отличие от нанотрубки (9,0) нанотрубка хиральностью (8,0) является полупроводником. Аналогичным образом описывались полупроводниковые свойства нанотрубки (10,0). В действительности

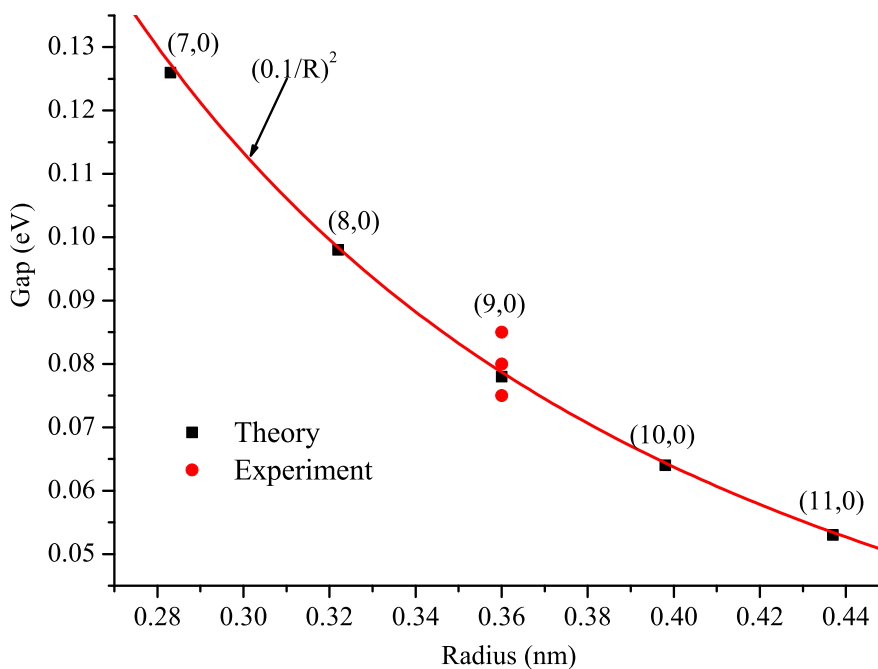


**Рис. 2.** Зависимость ширины щели от радиуса нанотрубки типа зигзаг.

энергия Ферми лежит выше и в области этой энергии во всех трех случаях существует зона запрещенных энергий.

Вернемся теперь к узкой щели между хаббардовскими подзонами для нанотрубки типа зигзаг (9,0). В [12] было получено, что ширина щели для ультрачистой индивидуальной нанотрубки (9,0) находится в пределах  $0.075 \leq \Delta \leq 0.085$  eV. В нашем случае ширина минищели для (9,0) равна 0.078 eV. Таким образом, вычисленная нами ширина запрещенной зоны полностью соответствует экспериментальному значению [12]. Более того, как показано на рис. 2 в согласии с работой [12] зависимость величины минищели для исследуемых нанотрубок оказалась обратно пропорциональной квадрату радиуса нанотрубки.

Таким образом, построенная в нашей работе теория зигзажных одностенных углеродных нанотрубок позволяет объяснить известные экспериментальные факты о том, что зигзажные нанотрубки являются узкощелевыми полупроводниками и предсказать значения минищелей для нанотрубок типа зигзаг, что продемонстрировано на рис. 2.

## Литература

1. Харрис П. *Углеродные нанотрубы и родственные им структуры*. М., Техносфера, 336 с. (2003)
2. Дьячков П.Н. *Электронные свойства и применение нанотрубок*. М., Бином, С. 448 (2011)
3. Saito R., Fujita M., Dresselhaus G., Dresselhaus M.S. *Phys. Rev. B* **46**(2), 1804 (1992)
4. Mintmire J.W., Dunlap D.I., White C.T. *Phys. Rev. Lett.* **68**(5), 631 (1992)
5. Hamada N., Sawada S.-I. *Phys. Rev. Lett.* **68**(10), 1579 (1992)
6. Collins P.G., Zettl A., Bando H., et al. *Science* **278**, 100 (1997)
7. Ebbessen T.W., Lezec H.J., Hiura H., et al. *Nature* **382**, 54 (1996)
8. Kane C.L., Mele E.J., Fisher J.E., et al. *Eur. Phys. Lett.* **41**, 683-688 (1998)
9. Pichler T., Knupfer M., Golden M.S., Fink J. *Phys. Rev. Lett.* **80**(21), 4729 (1998)
10. Wildoer J.W.G., Venema L.C., Rinzler A.G., et al. *Nature* **391**, 59 (1998)
11. Bachtold A., Fuhrer M.S., Plyasunov S., et al. *Phys. Rev. Lett.* **84**(26), 6082-6085 (2000)
12. Charlier J.-C., Blas X., Roche S. *Rev. Mod. Phys.* **79**, 677 (2007)
13. Ouyang M., Huang J.-L., Li C., et al. *Science* **292**, 702 (2001)
14. Deshpande V.V., Chandra B., Caldwell R., et al. *Science* **323**, 106 (2009)
15. Balents L., Fisher M.P.A. *Phys. Rev. B* **55**, R11973 (1997)
16. Wang Z., Psiachos D., Badilla R.F., Mazumdar S. *J. Phys.: Condens. Matter* **21**, 095009 (2009)
17. Bunder J.E., Hill J.M. *Phys. Rev. B* **80**, 153406-1 (2009)
18. Hubbard J. *Proc. Roy. Soc. A* **276**, 238 (1963)
19. Хомский Д.И. *ФММ* **29**, 31 (1970)
20. Mironov G.I. *Phys. Solid State* **48**, 1378 (2006)
21. Mironov G.I. *J. Supercond. Novel Magn.* **20**, 135 (2007)

# How to reduce reproducible measurements to an ideal experiment?

R.R. Nigmatullin\*, R.M. Rakhmatullin, S.I. Osokin

Kazan Federal University, Kremlevskaya 18, 420008 Kazan, Russia

\*E-mail: renigmat@gmail.com

Is it possible to suggest a general theory for consideration of *reproducible* data that are measured in many experiments? One can prove that successive measurements have a *memory* and this important fact allows separate all data on two large classes: *ideal* experiments without memory and experiments with a memory. We introduce the concept of an intermediate model (IM) that helps to describe quantitatively a wide class of reproducible data. Experiments with memory require for their description the Prony's decomposition while experiments without memory are needed for their presentation the Fourier decomposition only. In other words, it means that a measured function extracted from reproducible data can have a *universal description* in the form of the amplitude-frequency response (AFR) that belongs to the generalized Prony's spectrum (GPS). It is shown also how real data distorted by the experimental equipment and how to eliminate these uncontrollable factors in order to reproduce approximately the conditions corresponding to *ideal* experiment. New and elegant solution of elimination of the apparatus (instrument) function is suggested. In an ideal case the decomposition coefficients belong to the Fourier transform and presentation of reproducible data in this form leads to the IM for this case. The suggested general algorithm allows considering many experiments from the unified point of view. The real example based on available electron paramagnetic resonance (EPR) data confirms this general concept. The unified "bridge" between the treated experimental data and a set of competitive hypothesis that pretend for their description is discussed. The results obtained in this paper help to put forward a new paradigm in data/signal processing.

**PACS:** 89.75.-k, 06.30.-k, 02.50.

**Keywords:** Fourier transform, Prony's decomposition, intermediate model, data/signal processing, EPR measurements with/without memory, apparatus function

## List of acronyms:

AFR: amplitude-frequency response.

AF: apparatus (instrumental) function.

IM: intermediate model.

GPS: generalized Prony's spectrum.

LLSM: linear least square method.

QP: quasi-periodic.

REMV: reduced experiment to its mean values.

SRA: sequence of the ranged amplitudes.

EPR: electron paramagnetic resonance.

## 1. Introduction

The section of experimental physics associated with treatment of different data is considered as well-developed. For any newcomer to suggest some new and rather general idea that can touch the basic of this section it seems to be *impossible*. Many books written by prominent

scientists (mathematicians, experimentalists, specialists in statistics of different kind and etc.) [1-10] created a basic stream in this area. This branch of physics and mathematics is very general and many researches that deal with signal/noise processing should understand the basic of this science. The fresh information related to recent achievements in the fractal signal processing is collected in books [11-14]. This information “explosion” creates a certain trend and it definitely increases the limits of applicability of many methods that are developed in this area for analysis of different random sequences and signals. The chaotic and random phenomena are originated from variety of reasons and their specificity dictates different methods for their quantitative description. One of the authors of this paper (RRN) also tried to develop different methods that proved their efficiency in solution of many complex problems [15-20], where the conventional methods do not work properly.

All data can be divided on two large classes: reproducible and unreproducible data, accordingly. In the first case an experimentalist enables to *reproduce* relatively stable conditions of his experiment and can measure the response of the system (object) studied again with some accuracy. For the second type of data (economic-, meteo- geologic-, medical and etc.) the repetition of the same initial conditions becomes impossible and many special methods for analysis of different time series were suggested [6-10]. In the second case the control variable  $x$  is random and the response created by the action of this variable on the object studied is also random and so all responses in the second case cannot be reproducible. But nevertheless in spite of the modern tendency that exists in this area one can formulate the following general question: *Is it possible to develop a general theory (or IM) that allows considering all reproducible data in the frame of the unified and verified concept?* This theory should satisfy to the following requirements:

- R1.** It should give a possibility to express *quantitatively* a set of the measured functions by means of the unified and common set of the fitting parameters.
- R2.** This set of the fitting parameters should form the unified model and many data can be compared in terms of one quantitative “language”. It means that there is a possibility to create general *metrological standard* for consideration of reproducible data from the unified point of view.
- R3.** All calculations that are contained in this general theory should be error *controllable*.
- R4.** It should give a possibility to eliminate the apparatus (instrumental) function and reduce reproducible measurement to an *ideal* experiment.

The further and attentive analysis of the recent results obtained in [21] allows finding a *positive* answer on the general question posed above.

## 2. The basic positions and conclusions of the suggested theory

Let us remind some important points that are necessary for understanding of new theory. Under *ideal* experiment we understand the measured response from the object studied (during the period of time  $T$ ) that is reproduced in each measurement with the *same* accuracy. If  $\text{Pr}(x)$  is chosen as the response (measured) function then from the mathematical point of view it implies that the following relationship is satisfied

$$y_m(x) \cong \text{Pr}(x + m \cdot T_x) = \text{Pr}(x + (m - 1) \cdot T_x), \quad m = 1, 2, \dots, M. \quad (1)$$

Here  $x$  is the external (control) variable,  $T_x$  is a “period” of experiment expressed in terms of the control variable  $x$ . In expression (1) we make a *supposition* that the properties of the

*How to reduce reproducible measurements to an ideal experiment?*

object studied during the period of “time”  $T_x$  is *not* changed. If  $x = t$  coincides with temporal variable then  $T_x = T$  coincides with the conventional definition of a period. The solution of this functional equation is well-known and (in case of discrete distribution of the given data points  $x = x_j$ , ( $j = 1, 2, \dots, N$ )) coincides with the segment of the Fourier series.

$$\text{Pr}(x) = A_0 + \sum_{k=1}^{K \gg 1} \left[ A c_k \cos \left( 2\pi k \frac{x}{T_x} \right) + A s_k \sin \left( 2\pi k \frac{x}{T_x} \right) \right]. \quad (2)$$

We *deliberately* show only the segment of the Fourier series because in reality all data points are always *discrete* and the number of “modes” (coinciding with the coefficients of the Fourier decomposition) is limited. We define here and below by the capital letter  $K$  the *finite* mode. This final mode  $K$  is chosen from the requirement that it is sufficient to fit experimental data with the given (or acceptable) accuracy. As we will see below the value of  $K$  can be calculated from the expression (8) for the relative error located in the given interval [1%-10%]. This interval provides the desired fit of the measured function  $y(x)$  to  $\text{Pr}(x)$  with initially chosen number of modes  $k$  figuring in (2). From these relationships an important conclusion is following. For *ideally* reproducible experiment, which satisfies to condition (1) the F-transform (2) can be used as *intermediate model* (IM) and the number of decomposition coefficients ( $A_0, A c_k, A s_k$ ) equaled  $2K + 1$  can be used as a set of the fitting parameters belonging to the IM. The meaning of these coefficients is well-known and actually this set defines approximately the well-known amplitude-frequency response (AFR) associated with the recorded “signal”  $y(x) \approx \text{Pr}(x)$  coinciding with the measured function. Here we increase only the limits of interpretation of the conventional F-transform with respect to *any* variable  $x$  (including frequency also, if the control variable  $x$  coincides with some current  $\omega$ ) and show that the segment of this transformation can be used for description of an *ideal* experiment. Let us consider more general functional equation

$$F(x + T_x) = aF(x) + b, \quad (3)$$

This functional equation has been considered in the first time in paper [22] by the first author (RRN). The solution of this equation can be written in the following form [22]

$$\begin{aligned} a \neq 1 : F(x) &= \exp(\lambda x/T) \text{Pr}(x) + c_0, \quad \lambda = \ln(a), \quad c_0 = b/(1 - a), \\ a = 1 : F(x) &= \text{Pr}(x) + bx/T_x. \end{aligned} \quad (4)$$

The interpretation of this equation was considered in [22]. From equation (3) the obvious conclusion follows

$$F(x + mT_x) = aF(x + (m - 1)T_x) + b, \quad m = 1, 2, \dots, M. \quad (5)$$

It can be interpreted as repetition of a set of successive measurements corresponding to an *ideal* experiment with memory. Again, a *supposition* about stable properties of the object studied during the period  $T_x$  used for the measurements is conserved (it means that constants  $a$  and  $b$  in (5) do *not* depend on time). This situation, in spite of initial attractiveness *cannot* be performed in reality because a set of uncontrollable factors (as we will see below on real data) can change the set of the fixed slope ( $a$ ) and intercept ( $b$ ). In reality, we might expect that all these constant parameters including the period  $T_x$  will depend on the current number of a measurement  $m$

$$\begin{aligned} y_{m+1}(x) &= a_m y_m + b_m \quad \text{or} \\ F(x + (m + 1)T_x(m)) &= a_m F(x + m \cdot T_x(m)) + b_m, \quad m = 1, 2, \dots, M - 1. \end{aligned} \quad (6)$$

But, nevertheless, the solution (4) is valid in this case also and in the result of the fitting of the function (4) one can express *approximately* the current measurement  $y_m(x)$  in terms of the function (4) that represents itself the chosen IM. From this IM one can obtain a fitting function for description of *reproducible* measurements with the *shortest* memory (6). So, for each measurement from expression (4) one can derive easily the following fitting function

$$\begin{aligned}
 y_m(x) &\cong F_m(x) = B_m + E_m \exp(\lambda_m x / T_x(m)) + \\
 &+ \sum_{k=1}^K [Ac_k(m)yc_k(x, m) + As_k(m)ys_k(x, m)], \\
 yc_k(x, m) &= \exp(\lambda_m x / T_x(m)) \cos(2\pi kx / T_x(m)), \\
 ys_k(x, m) &= \exp(\lambda_m x / T_x(m)) \sin(2\pi kx / T_x(m)).
 \end{aligned} \tag{7}$$

As a matter of fact, there is a period of time  $T$  that determines the *temporal* interval when one cycle of measurement is finished. But experimentalist prefers to work *not* with temporal variable; frequently he works with another variable  $x$  (wavelength, scattering angle, magnetic field and etc.) that is determined by experimental conditions and available equipments used. In this case the connection between the “period”  $T_x$  defined above and real period  $T$  is *not* known. But the desired nonlinear fitting parameter  $T_x$  that enters in (7) can be calculated from the fitting procedure. In order to find the optimal value of this parameter  $T_{\text{opt}}$  that provides the accurate fit we notice that this value should be located approximately in the interval  $[T_{\text{max}}/2, 2T_{\text{max}}]$ , where the value of  $T_{\text{max}}(x)$ , in turn, should be defined as  $T_{\text{max}}(x) = \Delta x \cdot L(x)$ . The value  $\Delta x$  is a step of discretization and  $L(x) = x_{\text{max}} - x_{\text{min}}$  is a length of the interval associated with the current discrete variable  $x$ . This important observation helps us to find the optimal values of  $T_{\text{opt}}$  and  $K$  from the procedure of minimization of the relative error that always exists between the measured function  $y(x)$  and the fitting function (7)

$$\begin{aligned}
 \min[RelErr] &= \min \left[ \frac{\text{stdev} \{y(x) - F(x; T_{\text{opt}}, K)\}}{\text{mean} |y|} \right] \cdot 100\%, \\
 1\% &< \min[RelErr(K)] < 10\%, \\
 T_{\text{opt}} &\in [T_{\text{max}}/2, 2T_{\text{max}}], \quad T_{\text{max}} = (x_j - x_{j-1}) \cdot L(x).
 \end{aligned} \tag{8}$$

The direct calculations show that instead of minimization of the surface  $RelErr(T, K)$  with respect to the unknown variables  $T$  and  $K$  one can minimize the *cross-section* at the fixed value of  $K$ . This initially chosen value of  $K$  should satisfy to the condition that is given by the second row of expression (8). It is obvious that this procedure should be realized for each successive measurement and so we omit the index  $m$  ( $m = 1, 2, \dots, M$ ) in (8) in order *not* to overload this expression with additional parameters. Any experimentalist wants to realize the conditions that are close to an “ideal” experiment with memory expressed by relationship (3). For this aim one can average the set of constants  $a_m$  and  $b_m$  together with the measured functions  $y_m$  in order to replace equation (6) by an *approximate* equation that is close to the *ideal* case (3)

$$\begin{aligned}
 Y(x + \langle T_x \rangle) &\cong \langle a \rangle Y(x) + \langle b \rangle, \\
 Y(x + \langle T_x \rangle) &= \frac{1}{M-2} \sum_{m=2}^M y_m(x), \quad Y(x) = \frac{1}{M-2} \sum_{m=1}^{M-1} y_m(x).
 \end{aligned} \tag{9}$$

The second row in (9) defines the averaged functions that are obtained from the given set of the reproducible measurements. We define this functional equation as the *reduced* experiment to its

*How to reduce reproducible measurements to an ideal experiment?*

mean values (REMV). We should notice here that the constants  $a_m$  and  $b_m$  are calculated from (6) as neighboring slopes and intercepts

$$a_m = \text{slope}(y_{m+1}, y_m), \quad b_m = \text{intercept}(y_{m+1}, y_m),$$

$$m = 1, 2, \dots, M-1, \quad \langle a \rangle = \frac{1}{M-1} \sum_{m=1}^{M-1} a_m, \quad \langle b \rangle = \frac{1}{M-1} \sum_{m=1}^{M-1} b_m, \quad (10)$$

and this set of numbers entering in (9) should be equal  $M-1$ . So, in order to save the calculation resources one can reduce initially the data treatment procedure to consideration of the functional equation (9) for the averaged functions only. The total set of measurements is necessary to justify the functional equation (6). In every experiment the requirement of the shortest memory *cannot* be realized. So, in general case instead of equation (6) showing the realization of the simplest case between the neighboring measurements it is necessary to consider an *ideal* situation when the memory covers  $L$  neighboring measurements. In this case we can write

$$F(x + LT_x) = \sum_{l=0}^{L-1} a_l F(x + lT_x) + b. \quad (11)$$

In reality, as we will see below, one can calculate easily the set of the parameters  $a_l$ ,  $b$  by the LLSM if we suppose that  $L = M$ , where  $M$  coincides with the last measurement. But, up to now, we do *not* know how to calculate the true value of  $L$ . This value is gained by deep physical reasons and true nature of this memory merits a special research. The functional equation (11) describes mathematically a wide class of the QP processes and can be interpreted as follows. The measurement process that takes place during the interval  $[(L-1)T_x, LT_x]$  partly depends on the measurements that have been happened on the previous temporal intervals  $[lT_x, (l+1)T_x]$  with  $l = 0, 1, \dots, L-2$ . The set of the constants  $[a_l]$  ( $l = 0, 1, \dots, L-1$ ) can be *quantitatively* interpreted as the influence of a memory (strong correlations) between the successive measurements. The solution of this generalized functional equation (11) was considered in paper [22] and can be presented in two different forms (A) and (B)

$$(A) \quad \sum_{l=0}^{L-1} a_l \neq 1 : F(x) = \sum_{l=1}^L (\kappa_l)^{x/T_x} \text{Pr}_l(x) + c_0, \quad c_0 = \frac{b}{1 - \sum_{l=0}^{L-1} a_l},$$

$$(B) \quad \sum_{l=0}^{L-1} a_l = 1 : F(x) = \sum_{l=1}^L (\kappa_l)^{x/T_x} \text{Pr}_l(x) + c_1 \frac{x}{T_x}, \quad c_1 = \frac{b}{L - \sum_{l=0}^{L-1} l \cdot a_l}. \quad (12)$$

Here the functions  $\text{Pr}_l(x)$  define a set of periodic functions ( $l = 1, 2, \dots, L$ ) from expression (2), the values  $\kappa_l$  coincide with the roots of the characteristic polynomial

$$P(\kappa) = \kappa^L - \sum_{l=0}^{L-1} a_l \kappa^l = 0. \quad (13)$$

In general, these roots can be positive, negative,  $g$ -fold degenerated (with the value of the degeneracy  $g$ ) and complex-conjugated. We should note also that for the case B in (12) one of the roots  $\kappa_l$  coincides with the unit value ( $\kappa_1 = 1$ ) that leads to the pure periodic solution. As before,

the finite set of the unknown periodic functions  $\text{Pr}_l(x, T_x)$  ( $l = 1, 2, \dots, L$ ) is determined by their decomposition coefficients  $Ac_k^{(l)}$ ,  $As_k^{(l)}$ ,  $l = 1, 2, \dots, L$ ;  $k = 1, 2, \dots, K$ .

$$\text{Pr}_l(x, T_x) = A_0^{(l)} + \sum_{k=1}^{K \gg 1} \left[ Ac_k^{(l)} \cos \left( 2\pi k \frac{x}{T_x} \right) + As_k^{(l)} \sin \left( 2\pi k \frac{x}{T_x} \right) \right] \quad (14)$$

We want to stress here the following fact. The conventional Prony's decomposition [23-25] did *not* have any specific meaning and is considered as an alternative decomposition alongside with other transformations (Fourier, wavelet, Laplace and etc.) used in the signal processing area. But in paper [21] we found an *additional* meaning of this decomposition associated with successive measurements. Solution (12) has general character and other roots from algebraic equation (13) can modify the conventional solution. All possible solutions of the general functional equation (11) for different types of roots were considered in [22]. In the matter of fact, a set of the reproducible measurements having a memory associated with  $L$  neighboring measurements should satisfy to the following functional equation

$$y_m(x) \cong F(x + (L + m)T_x(m)) = \sum_{l=0}^{L-1} a_l^{(m)} F(x + (l + m)T_x(m)) + b_m, \quad (15)$$

$$m = 1, 2, \dots, M.$$

As before, one can realize initially the REMV procedure that close to the *ideal* case (11) with the help of relationships

$$Y(x + L \langle T_x \rangle) = \sum_{l=0}^{L-1} \langle a_l \rangle Y(x + l \langle T_x \rangle) + \langle b \rangle, \quad (16)$$

$$Y(x + l \langle T_x \rangle) = \frac{1}{M-l} \sum_{m=l}^M F(x + (m+l)T_x(m)), \quad l = 1, 2, \dots, L, \quad L < M.$$

The second row in (16) demonstrates a possible averaging procedure that can be applied for calculation of the mean functions. From mathematical point of view the functional equations (16) and (11) are similar to each other but have *different* meaning. The first one (11) is associated with the *ideal* experiment with memory while the second one (16) describes the typical situation of the real experiment when random behavior of the initial measured functions is *reduced* to its *successive* mean values. The averaged coefficients  $\langle a_l \rangle$  and  $\langle b \rangle$  in (16) are found by the linear least square method (LLSM) from the first row of (16). In practice, it is desirable to receive the *minimal* value of  $L$ , because  $L$  increases considerably the number of the fitting parameters that are needed for the final fitting of the measured function. From the mathematical point of view, the reproduction of the general solution of this equation is similar to solution (12) and so it can be omitted. Equation (16) has clear meaning and corresponds to the *linear* presentation of a possible memory that can exist between repeated measurements after averaging procedure. These coefficients reflect also (in some extent) the influence of the experimental uncontrollable factors coming from the measured equipment impact. Earlier, these factors were taken into account only statistically but new concept suggests a direct way for their evaluation. Here we want to demonstrate how to eliminate the apparatus function and reduce the set of the real reproducible measurement to an *ideal* experiment containing the set of periodic functions only. Let us come back to equation (11). From (11) it follows that the functions  $F(x), F(x + T), \dots, F(x + (L - 1)T)$  are linear *independent* and *available* from experimental

*How to reduce reproducible measurements to an ideal experiment?*

measurements in averaged (see expression (16)) or in another sense. So, we have the following system of linear equations

$$\begin{aligned}
 F(x) &= \sum_{l=1}^L EP_l(x) + c_0, \\
 F(x+T) &= \sum_{l=1}^L \kappa_l EP_l(x) + c_0, \\
 F(x+(L-1)T) &= \sum_{l=1}^L \kappa_l^{L-1} EP_l(x) + c_0, \\
 EP_l(x) &= (\kappa_l)^{x/T_x} \text{Pr}_l(x), \quad l = 0, 1, \dots, L-1.
 \end{aligned} \tag{17}$$

From this linear system one can find the unknown functions  $EP_l(x)$  and then restore the unknown periodic functions  $\text{Pr}_l(x)$ . It means that becomes *possible* to realize the reduction of a wide class of reproducible measurements presented initially in the frame of the desired IM and corresponding to the Prony's decomposition to an *ideal* experiment. We note that the  $L$ -th order determinant of system (17) coincides with well-known Vandermonde determinant [26]. It does *not* equal to zero if all roots of equation (13) are different. So, finally we have the *ideal* periodic function that corresponds to reduction of the real set of measurements to an *ideal* (perfect) experiment

$$Pf(x) = \sum_{l=0}^{L-1} \text{Pr}_l(x). \tag{18}$$

To be exact, from our point of view, this function can serve as a “keystone” in the arc of the “bridge” between theory and experiment. In the simplest case (4) we have the obvious relationships

$$\begin{aligned}
 \langle a \rangle \neq 1, \quad \text{Pr}(x) &= (\langle a \rangle)^{-(x/T_x)} \left[ Y(x) - \frac{\langle b \rangle}{1 - \langle a \rangle} \right], \\
 \langle a \rangle = 1, \quad \text{Pr}(x) &= Y(x) - \langle b \rangle \left( \frac{x}{T_x} \right).
 \end{aligned} \tag{19}$$

So, these simple formulas give a solution for the elimination of the apparatus function based on the *verified* suppositions (9) and (16). In the same manner we can consider the case B. The solution for this case is trivial and similar to linear equation (17) with replacement of the left hand side by the functions

$$\Phi(x+lT) = F(x+lT) - c_1 \left( \frac{x}{T} + l \right), \quad l = 0, 1, \dots, L-1. \tag{20}$$

It is instructive also to give formulas for the case  $L = 2$ . These expressions will be used for treatment of the EPR data considered below. After some simple algebraic manipulations one can obtain the following expression corresponding to an *ideal* experiment for this case.

$$\begin{aligned}
 \text{Pr}_{\text{tot}}(x) &= \text{Pr}_1(x) + \text{Pr}_2(x), \\
 \text{Pr}_1(x) &= \left( \frac{Y_1(x) - \kappa_2 Y_0}{\kappa_1 - \kappa_2} \right) \cdot \exp \left( -\frac{x}{T_x} \ln \kappa_1 \right), \\
 \text{Pr}_2(x) &= \left( \frac{\kappa_1 Y_0(x) - Y_1}{\kappa_1 - \kappa_2} \right) \cdot \exp \left( -\frac{x}{T_x} \ln \kappa_2 \right), \\
 Y_0(x) &= F(x) - c_0, \quad Y_1(x) = F(x+T_x) - c_0.
 \end{aligned} \tag{21}$$

Attentive analysis of many data prompts the efficiency of the following *simplified* algorithm.

- S1.** From available set of data one can calculate the mean measurement (with the usage of the conventional expression)

$$\langle y(x) \rangle = \frac{1}{M} \sum_{m=1}^M y_m(x), \quad (22)$$

and the distributions of the corresponding slopes and intercepts that demonstrate “marginal” measurements having a maximal deviations from its mean value (center of the statistical cluster)

$$SL_m = \text{slope}(y_m(x), \langle y(x) \rangle), \quad \text{Int}_m = \text{intercept}(y_m(x), \langle y(x) \rangle). \quad (23)$$

- S2.** From these distributions one can find the measured functions having maximal deviations and form two limits (maximal deviations from both sides with respect to mean function.

$$\langle y(x) \rangle = a_1 y_{up}(x) + a_0 y_{dn}(x) + b \quad (24)$$

Here we realize the case of the reduced memory and “marginal” functions  $y_{up}(x)$ ,  $y_{dn}(x)$  describe the limits of the statistical cluster on two opposite limits, correspondingly. The coefficients  $\{a_{0,1}, b\}$  are found from (24) by the LLSM.

- S3.** The desired roots  $\kappa_{1,2}$  are found from the quadratic equation

$$\kappa^2 - a_1 \kappa - a_0 = 0, \quad (25)$$

and the fit of the function  $y_{dn}(x)$  to the Prony’s decomposition allows finding the optimal value of  $T_x$ .

- S4.** These values ( $\kappa_1$ ,  $\kappa_2$  and  $T_x(\text{opt})$ ), in turn, allow to find the complete periodic function  $\text{Pr}_{\text{tot}}(x)$  from (21) and thereby to realize the desired reduction of the measured data to an *ideal* experiment, when the final function should be expressed in terms of the Fourier decomposition only. In other words, this function obtained from reproducible data measurements can pretend on comparison with competitive hypothesis obtained from the existing theory. If the proper theoretical hypothesis (“best fit” model) is *absent* then  $\text{Pr}_{\text{tot}}(x)$  is decomposed to the finite Fourier series and the AFR of this function can be considered as an IM for this experiment considered.

### 3. EPR experiment

#### 3.1. The elimination of the AF in the presence of a sample

In this paper we consider only one illustrative example. For verification of the basic algorithm we prepare two types of data that are considered in the frame of the unified algorithm described above. The characteristics of the equipment and conditions (parameters) of the EPR equipment used for this simple experiment are the following: The sample used:  $\text{Ce}_{0.8975}\text{Gd}_{0.0025}\text{Y}_{0.1}\text{O}_{2-x}$  (powder with grain size  $5 \pm 2$  nm). Measurements were performed by means of the EPR spectrometer BRUKER ESP 300 [27] with working frequency 9.43 GHz. The spectra were collected at room temperature with the center magnetic field 3.3 kG, sweep width 2 kG, modulation amplitude 2 G, microwave power 10 mW. Twenty scans (each scan contains 1024 measured data points) were realized.

### *How to reduce reproducible measurements to an ideal experiment?*

The resonance (integrated from the measured signal) line for this sample is shown on Fig. 1(a). Three resonance curves corresponding to the mean curves and the limiting measurements are merged practically with each other. The limiting curves being plotted with respect to the mean resonance curve form ideal straight lines that signifies about the high quality of the resonance equipment used. The Figs. 2(a,b) show the distribution of the slopes and intercepts with respect to the mean measurement. This information is useful for the selection of the “marginal” measurements (having the maximal deviations from the mean value to two opposite (up and down) sides) and formation of the approximate relationship (24) for elimination of the AF (apparatus function). Figure 3 demonstrates the test of the relationship (11) for  $L = M$ . The last measurement  $y_{20}$  represents a linear combination of all measurements ( $y_1, y_2, \dots, y_{19}$ ) involved in this measurement process. The accuracy of this fitting is very high and the value of the relative error does not exceed 1%. For this case one can verify easily with the help of the LLSM the link between *all* successive measurements. The distribution of the coefficients  $\{a_m, b\}$ ,  $m = 1, 2, \dots, M - 1$  is shown in Fig. 4. Based on relationships (24) and (25) and the value of period of  $T_x \approx T_{\max}$  that is calculated from expression (8) we can eliminate the influence of the AF and receive the function (21) corresponding to an *ideal* experiment. In the matter of fact, Fig. 5 represents a central result of this paper. The grey resonance curve is free from the influence of the measured device and can be used by theoreticians for comparison with the “best fit” models. If this theory is *absent* then this curve can be decomposed to the Fourier series (2) and the coefficients of this decomposition can be used as the quantitative parameters of the IM. The fit and distribution of the F-coefficients are shown, respectively, in Figs. 6(a,b).

### **3.2. Do high-frequency fluctuations characterizing an empty resonator remember each other?**

The second type of measurements was associated with random fluctuations measured from empty resonator (cell not containing a sample). We analyze 20 successive measurements at room temperature. The main problem can be formulated as follows: in spite of the fact that high frequency fluctuations destroy a memory are there some correlations between measurements that still remember each other? We want to give the justified answer on this question. In Figs. 7(a,b) we demonstrate the obvious fact: the HF fluctuations destroy a memory between measurements. It is seen also in Fig. 7(b) when correlations disappear. The quite opposite situation is observed between integrated curves. The integration destroys the HF fluctuations and restores a possible link between measurements. The Figs. 8(a,b) confirm this observation. The Figs. 9(a,b) show the distributions of the slopes and intercepts calculated with respect to the averaged integrated curve. It is interesting to note that these distributions are concentrated in the vicinity of one (for slopes) and zero (for intercepts) that correspond to an ideal experiment. Figure 10 shows that memory phenomenon between integrated successive curves is conserved. The value of the fitting error is close to 10% and this fit can be considered as acceptable. The distribution of the memory coefficients together with free constant  $b$  is given by Fig. 11. Based on idea of reduction of the memory phenomenon to three significant functions (see equation (24)) one can select “marginal” functions  $yup(x)$  and  $ydn(x)$  describing two opposite limits of the statistical cluster. It helps to calculate the desired ideal curve (24) and use it as the fitting function expression (2). This reduced ideal curve is shown in Fig. 12 (grey line), its fit and the distribution of the decomposition coefficients entering into the F-decomposition are shown in Figs. 13 and 14, accordingly.

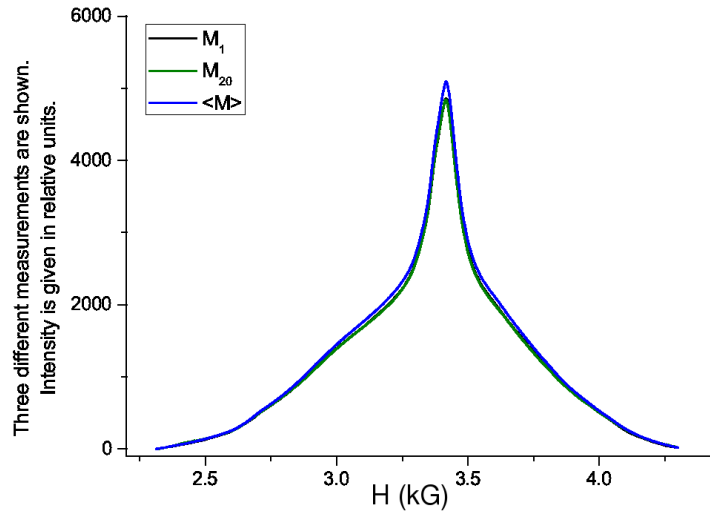


**Figure 1.** Here we demonstrate the EPR resonance line for the chosen sample. All measurements are located inside the limited ones. The mean measurement  $\langle y \rangle$  (blue line) serves as envelope. It signifies about the accuracy of the equipment used. Being plotted with respect to the mean curve their corresponding slopes ( $\text{slope}(y_2, \langle y \rangle) = 1.04648$ ,  $\text{slope}(y_{21}, \langle y \rangle) = 1.05429$ ) are very close to the unit value.

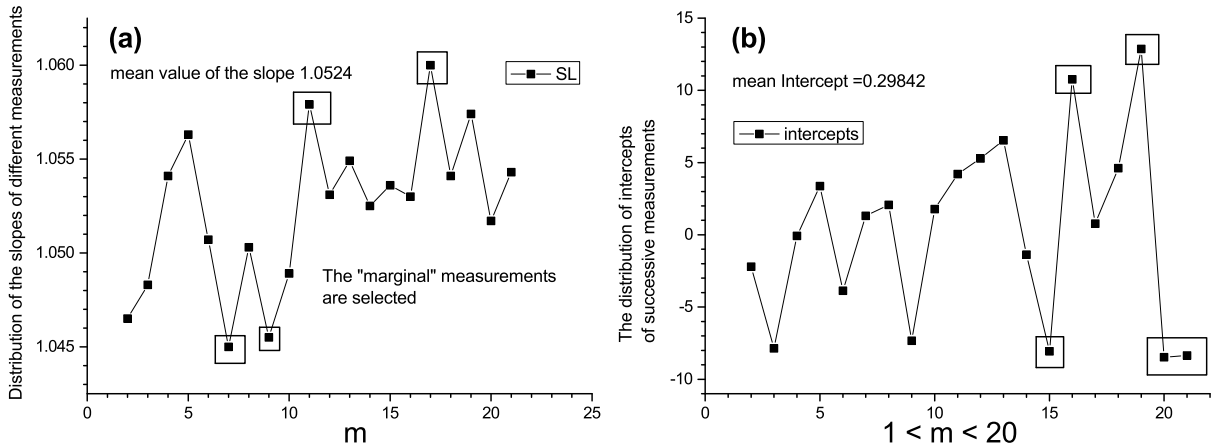


**Figure 2.** (a) The distribution of the slopes with respect to mean measurement  $\langle y \rangle$  corresponding to different measurements is shown here. The measurements having the maximal deviations are marked by squares. They will be used for elimination of the apparatus function with the help of relationship (24). (b) The knowledge about the distribution of intercepts is useful also. The “marginal” measurements (having maximal intercepts) are helpful for elimination the apparatus function with the help of relationship (24).

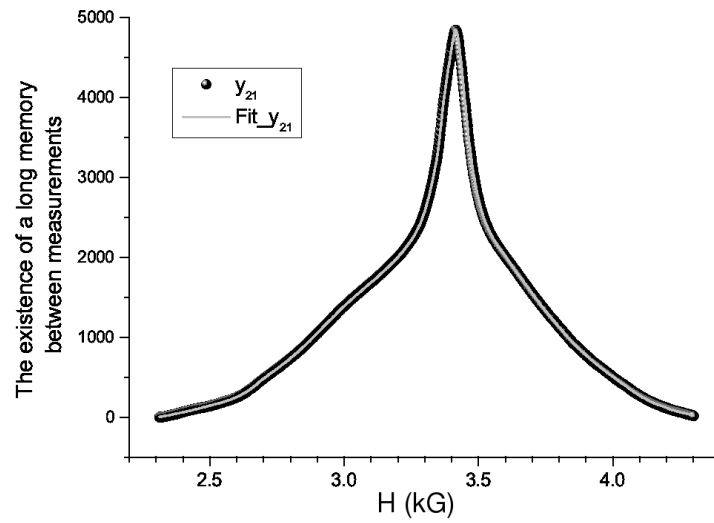


**Figure 3.** Here we demonstrate the long memory phenomenon between the measurements. The last measurement represents (black balls) a linear combination of all previous measurements. The fitting curve is expressed by solid grey line. The distribution of the coefficients is shown on Fig. 4.

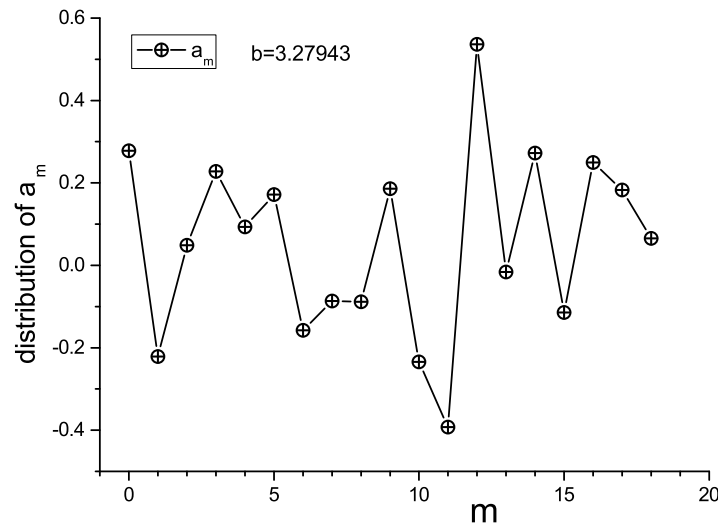


**Figure 4.** Here the distribution of the linear coefficients providing the accurate fit (depicted on the previous figure 3) is shown. The value of the free constant  $b$  is shown inside the frame. It is interesting to note that some measurements give the *negative* contribution. The origin of this phenomenon is not clear but it is tested easily by the LLSM.

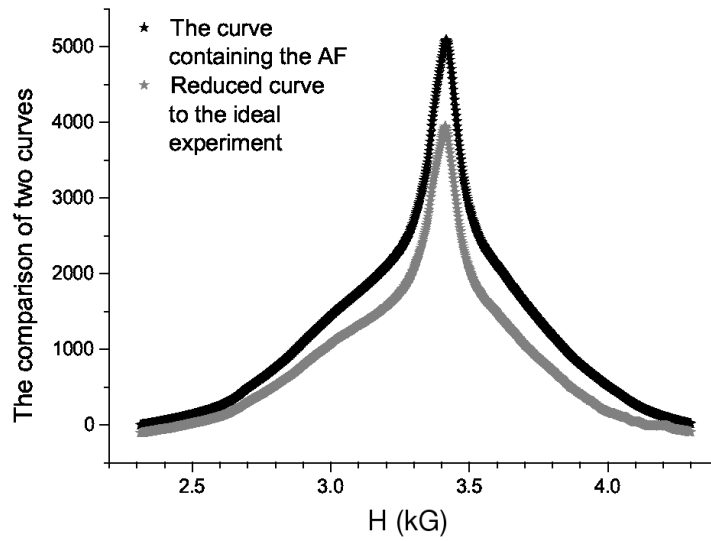


**Figure 5.** This figure represents the central result of the whole research. The grey curve represents the resonance contour that is obtained after elimination of the apparatus (instrumental) function from black curve. Only this curve should be selected for comparison of the existing theory with experiment obtained from this equipment. The standardization of all equipments including the most accurate ones becomes important and actual problem for the whole concept of measurements.

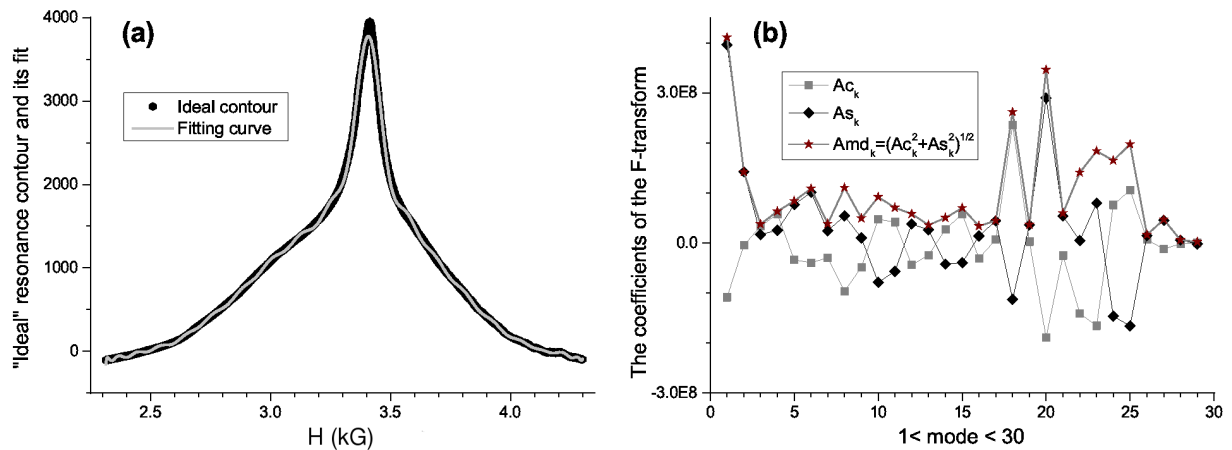


**Figure 6.** (a) The fit of the ideal resonance contour corresponding to an ideal experiment by means of the F-transform. The coefficients of this transformation are found from the fitting procedure. (b) Here we demonstrate the distribution of the decomposition coefficients entering to the F-transform (2). In order to provide the accurate fit of the curve depicted on Fig. 6(a) only 30 modes are necessary. But this relatively large number of the fitting parameters follows from general concept and the “best fit” model is supposed to be *unknown*.

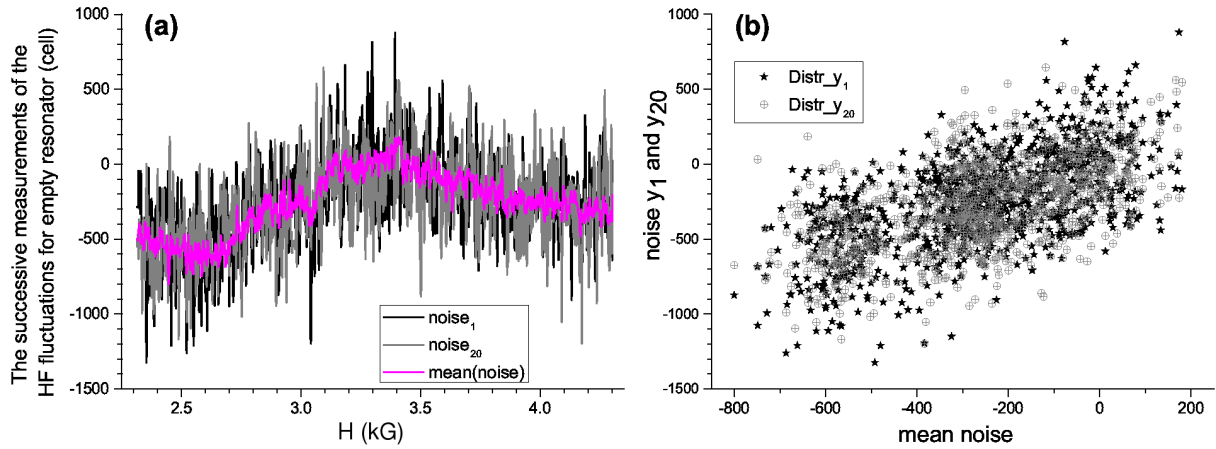


**Figure 7.** (a) A noise recorded from empty resonator (cell). The high-frequency fluctuations destroy a memory between successive measurements. The discrete integration based on summation of rectangles (which is equivalent the taking of the conventional arithmetic mean operation) suppresses the HF fluctuations (magenta line). (b) This plot shows clearly that HF fluctuations destroy a memory between successive measurements.

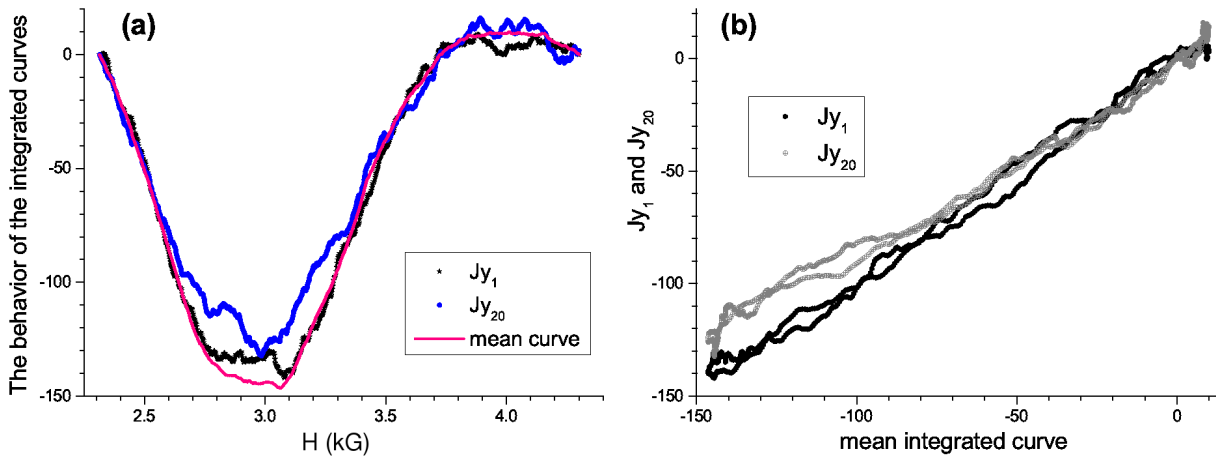


**Figure 8.** (a) The situation is changed after integration. Being integrated with respect to its mean value the HF fluctuations are suppressed and the correlation links are partly restored. The fitting curve is marked by pink solid line. The value of the fitting error is close to 10%. (b) Being plotted with respect to each other these integrated measurements form curves close to the segments of straight lines. So the integration restores the “hidden” memory and these integrated measurements can be treated in the same manner as the previously considered resonance curves.

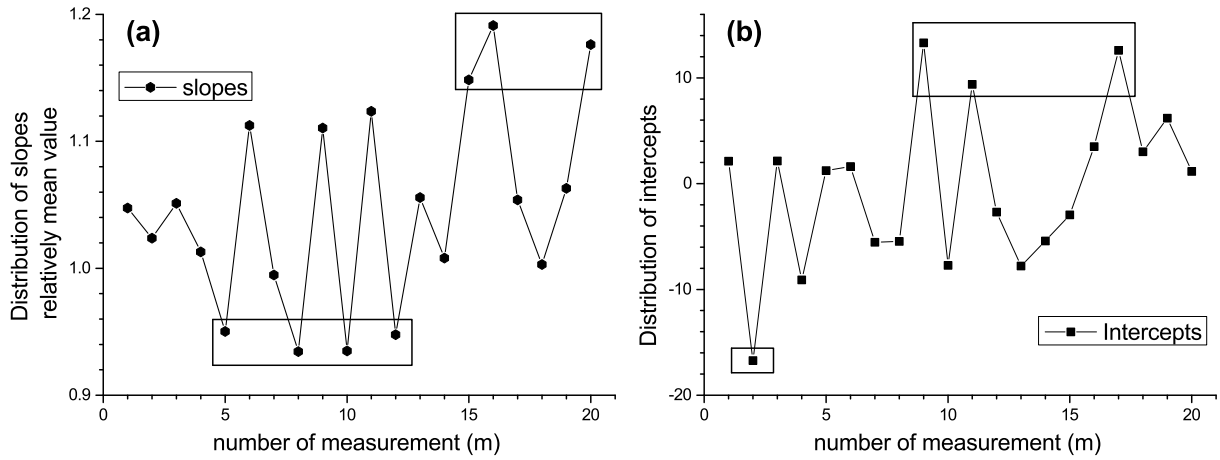


**Figure 9.** (a) As before, we show the distribution of slopes between integrated measurements with respect to the averaged integrated curve. The “marginal” measurements are squared. They are distributed in the vicinity of the slope equaled one that signifies about their proximity to an *ideal* case. (b) We demonstrate here the distribution of intercepts between integrated measurements with respect to the averaged integrated curve. The “marginal” measurements are squared again. They are distributed in the vicinity of zero value that signifies again about their proximity to an ideal case.

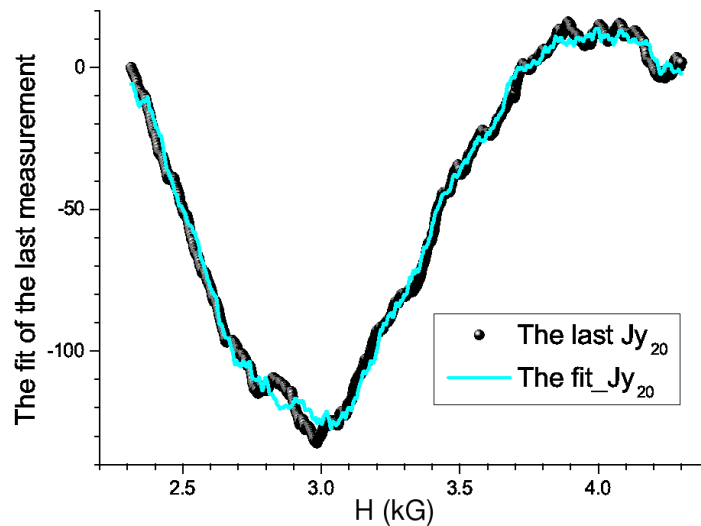


**Figure 10.** Here we show that the memory between integrated measurements is still conserved. The previous measurements ( $Jy_1, Jy_2 \dots, Jy_{19}$ ) demonstrate the satisfactory fit of the last curve  $Jy_{20}$ . The value of the relative error does not exceed 10%.

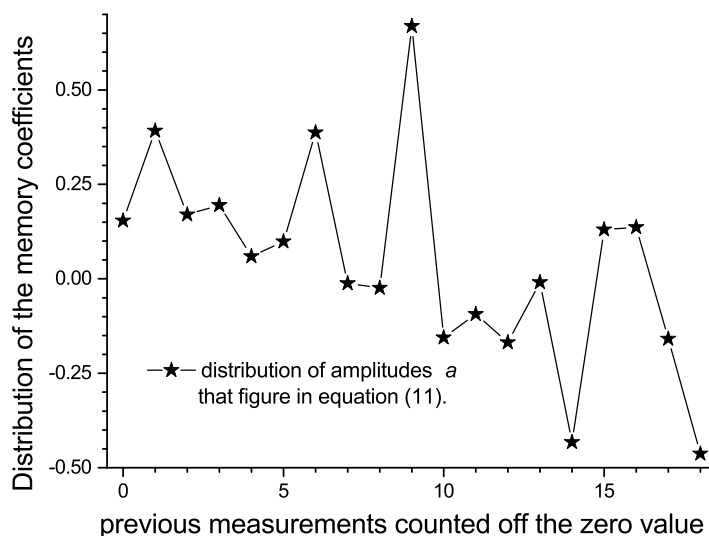


**Figure 11.** Here we demonstrate the distribution of the linear coefficients providing the acceptable fit shown in Fig. 10. The value of the free constant  $b$  is equaled to  $-5.88344$ . It is interesting to repeat again that some measurements give the *negative* contribution. The origin of this phenomenon (existence of memory between correlated sequences) is not clear now but it is tested easily with the help of the LLSM.

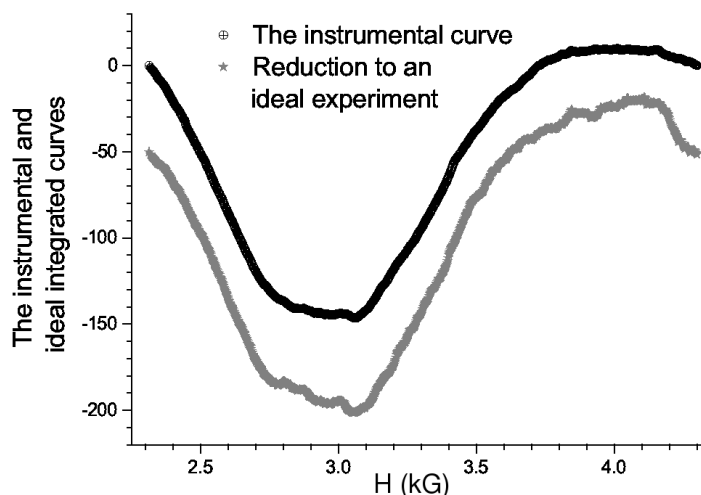


**Figure 12.** The application of expression (21) related to elimination of the AF helps to calculate the curve corresponding to an ideal experiment. The influence of the AF to different types of measurements is different. The grey curve (corresponding to elimination of the instrumental function) can be fitted with the help of expression (2). This plot can be considered also as original and the *central* result of this paper.

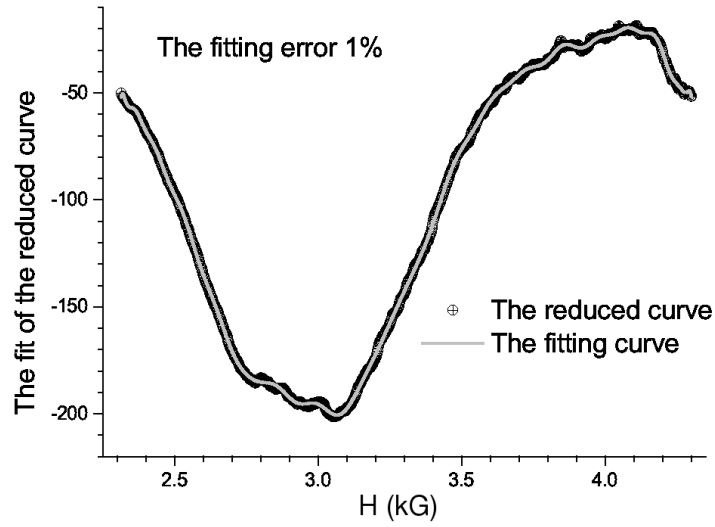


**Figure 13.** The fit of the reduced integrated curve by means of the F-transform. The coefficients of this transformation are found by means the LLSM.

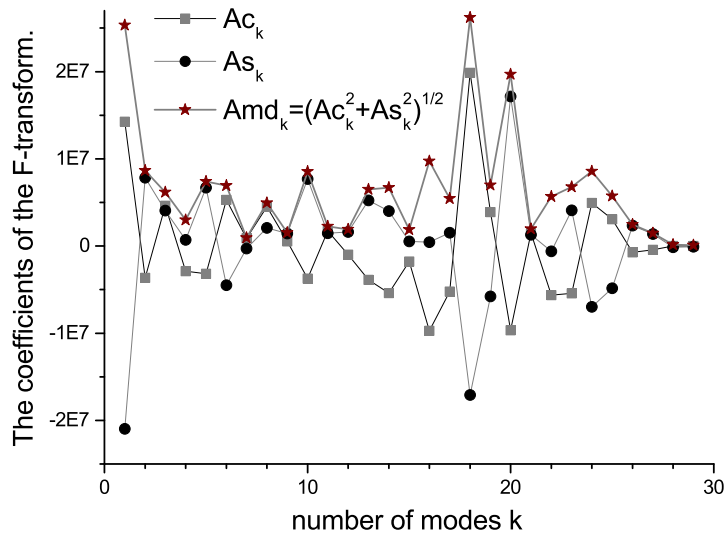


**Figure 14.** Here we demonstrate the distribution of the decomposition coefficients entering to the F-transform (2). In order to provide the accurate fit of the curve depicted in Fig. 13 only 30 modes are necessary. But this relatively large number of the fitting parameters follows from a *general* concept and the “best fit” model for this experiment is supposed to be *unknown*.

#### 4. Results and discussions

In this paper we develop a general theory that allows considering all reproducible data from the unified point of view based on the concept of the IM. This IM has a very general character and allows to express quantitatively a wide set of reproducible data in terms of the Prony's decompositions. We show also *how* to extract the reduced function corresponding to an ideal experiment and this function serves as a keystone between competitive (theoretical) hypotheses with the periodic function obtained from experimental observations. In order to obtain this important result, it is necessary to eliminate the influence of the so-called apparatus (instrumental) function [28–30] that always distorts the reproducible data and present the periodic function in the “pure” form. Only this function can conciliate two opposite points of view and solve the constant debate between theory and experiment. In the last section we should stress the basic supposition that was used in construction of this general theory. We suppose that during the measurement process the properties of the object and equipment are *not* changed essentially in time. If this phenomenon takes place then it is necessary to choose the corresponding range of the control variable  $x$  and optimize the value  $T_x$  in order to suppress this undesirable temporal dependence.

We want to show here that the general solution (12) solves another important problem as *prediction* of behavior of the measured function  $F(x)$  out of the interval of observation of the control variable  $x$ . Imagine that the measured data are fitted properly in the frame of the model (12) and researcher wants to consider this fit out of the interval  $[0, x]$  adding some shift  $\Delta$  to the admissible interval  $x + \Delta$ . *Is it possible to solve this problem in the frame of the general concept or not?* From mathematical point of view, it is necessary to express the function  $F(x \pm \Delta)$  with the help of the function  $F(x)$  reducing new interval of observation to the previous one. The solution expressed in the form of the Prony's decomposition (12) *admits* this separation. The general formula given below contains the *positive* answer for the question posed above.

$$F(x) = \sum_{l=1}^L EP_l(x) + c_0, \quad EP_l(x) = (\kappa_l)^{x/T} \text{Pr}_l(x),$$

$$F(x \pm \Delta) = \sum_{l=1}^L (\kappa_l)^{\pm\Delta/T} (\kappa_l)^{x/T} \text{Pr}(x, \Delta),$$
(26)

where

$$\text{Pr}(x, \Delta) = \sum_{k=1}^K \left[ Ac_k^l(\pm \Delta) \cos\left(2\pi k \frac{x}{T}\right) + As_k^l(\pm \Delta) \sin\left(2\pi k \frac{x}{T}\right) \right],$$

$$\begin{pmatrix} Ac_k^{(l)}(\pm \Delta) \\ As_k^{(l)}(\pm \Delta) \end{pmatrix} = \begin{pmatrix} \cos\left(2\pi k \left(\frac{\Delta}{T}\right)\right) & \pm \sin\left(2\pi k \left(\frac{\Delta}{T}\right)\right) \\ \mp \sin\left(2\pi k \left(\frac{\Delta}{T}\right)\right) & \cos\left(2\pi k \left(\frac{\Delta}{T}\right)\right) \end{pmatrix} \cdot \begin{pmatrix} Ac_k^{(l)} \\ As_k^{(l)} \end{pmatrix}.$$

As one can see from expression (26) the variables  $x$  and  $\Delta$  are *separated* and researcher receive a possibility to consider the shifted function  $F(x + \Delta)$  staying in the *initial* observation interval for control variable  $x$ . The decomposition coefficients  $Ac_k^{(l)}$ ,  $As_k^{(l)}$  of the previous periodic function  $\text{Pr}(x)$  are related with the new ones by means of rotation matrix.

Finishing this final section it is necessary to remind a couple of problems that can merit an interest for the further research:

1. The memory problem that is appeared between neighboring measurements is *not* solved. We proved only that the high-frequency fluctuations destroy a memory but the deep physical

reasons that lead to the functional equation (11) between correlated measurements are not known. In other words, in spite of the fact that long memory during the period of “time”  $T_x$  between measurements exists ( $L = M$ ) the reasons of appearance of a *partial* memory when  $L < M$  are *not* clear. In the paper we show only how to reduce this true memory with the help of the approximate procedure (24). The explanation of this phenomenon will be interesting for many researches working in different branches of natural science.

2. We found the key point that *conciliates* theory and experiment. All competing hypothesis should be presented in the form of the F-transform and compared with the function (18) that is obtained from reproducible measurements. This specific check-point can be sometimes crucial for experimentalists and theoreticians trying to understand the natural phenomenon studied from two opposite sides. But the justified “logic” of the paper prompts that the coincidence of the arguments from both sides should be focused on the expression (18). The illustrative example taken from the conventional EPR experiment leads to the same conclusions. So, one can formulate a problem of creation of the unified metrological concept that should be accepted by many experimentalists in order to supply by reliable data of the theoreticians that want to understand the phenomenon studied from the opposite side.

## Acknowledgments

One of us (RRN) wants to devote this fundamental research to his scientific teacher Dr. Prof. Boris I. Kochelaev to his 80<sup>th</sup> anniversary that will be take place in April of 2014 year. The authors are grateful to D. Zverev for his help in performing of necessary EPR measurements.

## References

1. Tukey J.W. *Exploratory Data Analysis*, Princeton University (1977)
2. Watson G.S. *The Annals of Mathematical Statistics* **42**, 1138 (1971)
3. Johnson N.L., Leone F.C. *Statistics and Experimental Design in Engineering and the Physical Sciences* (2nd edition), John Wiley & Sons (1976)
4. Schenck H.(Jr). *Theories of engineering experimentation* (2nd edition), McGraw-Hill Book Company (1972)
5. Sharaf M.A., Illman D.L., Kowalski B.R. *Chemometrics*, John Wiley & Sons (1988)
6. Aivazyan S.A., Yenyukov I.S., Meshalkin L.D. *Applied Statistics. Study of Relationships*, Reference Edition, Moscow: Finansy i Statistika (1985) [in Russian]
7. Shumway R.H., Stoffer D.S. *Time Series Analysis and Its Applications with Examples*, Springer (2006)
8. Elsner J.B., Tsonis A.A. *Singular Spectrum Analysis. A New Tool in Time Series Analysis*, Springer (1966)
9. Hamilton J.D. *Time Series Analysis*, Princeton University Press (1994)
10. Brockwell P.J., Davis R.A. *Time series: Theory and Methods*, Springer (1991)
11. Hu Sheng, Yang Quan Chen, Tian Shuang Qui *Fractal Processes and Fractional-Order Signal Processing. Techniques and Applications*, Springer (2012)

*How to reduce reproducible measurements to an ideal experiment?*

12. Baleanu D., Guevenc Z.B., Tenreiro Machado J.A. (Editors) *New trends in Nanotechnology and Fractional Calculus Applications*, Springer (2010)
13. Baleanu D., Tenreiro Machado J.A., Luo A.C.J. (Editors) *Fractional Dynamics and Control*, Springer (2012)
14. Luo A.C.J., Tenreiro Machado J.A., Baleanu D. (Editors) *Dynamical Systems and Methods*, Springer (2012)
15. Ciurea M.L., Lazanu S., Stavaracher I., Lepadatu A.M., Iancu V., Mitroi M.R., Nigmatullin R.R., Baleanu C.M. *J. Appl. Phys.* **109**, 013717 (2011)
16. Nigmatullin R.R., Baleanu D., Dinç E., Ustundag Z., Solak A.O., Kargin R.V. *J. Comput. Theor. Nanosci.* **7**, 1 (2010)
17. Nigmatullin R.R., Baleanu Ed.D., Guevenc Z.B., Tenreiro Machado J.A. *New Trends in Nanotechnology and Fractional Calculus Applications*, pp. 43–56, Springer (2010)
18. Nigmatullin R.R. *Commun. Nonlinear Sci. Numer. Simul.* **15**, 637 (2010)
19. Nigmatullin R.R. *Signal Process.* **86**, 2529 (2006)
20. Nigmatullin R.R., Ionescu C., Baleanu D. *Signal, Image and Video Processing*, pp. 1–16, DOI:10.1007/s11760-012-0386-1 (2012)
21. Nigmatullin R.R., Khamzin A.A., Machado J.T. *Phys. Scr.* **89**, 015201 (2014)
22. Nigmatullin R.R. *Phys. Wave Phenom.* **16**, 119 (2008)
23. Osborne M.R., Smyth G.K. *SIAM J. Sci. and Stat. Comput.* **12**, 362 (1991)
24. Kahn M., Mackisack M.S., Osborne M.R., Smyth G.K. *J. Comput. Graph. Stat.* **1**, 329 (1992)
25. Osborne M.R., Smyth G.K. *SIAM J. Sci. Comput.* **16**, 119 (1995)
26. Horn R.A., Johnson Ch.R. *Topics in Matrix Analysis*, Cambridge University Press (1991) [See Section 6.1]
27. The detailed description of this standard instrument can be found in the website: <http://eqdb.nrf.ac.za/equipment/bruker-esp-300-esr-spectrometer>
28. Weisstein E.W. *Instrument Function*. From *MathWorld* – A Wolfram Web Resource, <http://mathworld.wolfram.com/InstrumentFunction.html>
29. O'Connor D.V., Phillips D. *Time-correlated Single Photon Counting*, Academic Press, London (1984)
30. Gorelic V.A., Yakovenko A.V. *Tech. Phys.* **42**, 96 (1997) [*Zh. Tekh. Fiz.* **67**, 110 (1997), in Russian]

# Proximity effect in ferromagnet/superconductor trilayers with triplet correlations in an external magnetic field

Yu.N. Proshin\*, M.V. Avdeev

Kazan Federal University, Kremlevskaya 18, 420008 Kazan, Russia

\**E-mail: yurii.proshin@kpfu.ru*

The properties of the ferromagnet/superconductor (FS) system are theoretically studied in an external magnetic field. We consider the boundary value problem for the Usadel-like equations in the case of so-called “dirty” limit. Basing on the fit of the theory and known experimental data for the real symmetrical CuNi/Nb/CuNi trilayer, we expand numerical predictions on the asymmetrical  $F_1SF_2$  and  $F_1F_2S$  systems. It is shown that the asymmetry essentially influences on the critical properties of the both trilayers. The appearance of peculiar solitary re-entrant superconductivity caused by external magnetic field is predicted for the  $F_1F_2S$  system.

**PACS:** 74.25.Dw, 74.45.+c, 74.50.+r, 74.78.Fk

**Keywords:** proximity effect, spin valve, superconductivity, ferromagnetism, magnetic field

## 1. Introduction

In recent years the study of layered heterostructures consisting of alternating layers ferromagnetic (F) and superconducting (S) metals is attracted keen interest. In such artificial layered systems two competing physical phenomena, superconductivity and magnetism, coexist. It is well known that a ferromagnetism tends to parallel ordering of spins as distinct from a superconductivity which produces antiparallel alignment. Coexistence of these antagonistic phenomena requires specific conditions, that are difficult to satisfy in bulk materials [1]. Fulde and Ferrel [2] contemporaneously with Larkin and Ovchinnikov [3] (FFLO) showed for the ferromagnetic superconductors that the superconducting order parameter may be modulated in real space by an exchange field  $I$  ( $\Delta \sim \exp(i\mathbf{k}_f \mathbf{r})$  where value of wave vector of FFLO pairs  $k_f = v_F/2I$  and  $v_F$  is Fermi velocity). In artificial FS structures where the superconducting and ferromagnetic order parameters are spatially separated this coexistence is possible. Due to the *proximity effect* [4], superconducting correlations can penetrate from the S layer into the F layer. The singlet superconducting correlations decay on very short distance into the ferromagnet layer [5–9]. For strong ferromagnets such as Fe, Ni or Co the decay depth is approximately few nanometers.

On the other hand, the exchange field significantly modifies the superconducting properties of the layered FS systems (so-called magnetic proximity effect [9]). Properties of this systems can be controlled changing the thickness of the S and F layers, and applying the external magnetic field or external voltage, etc. [6–10].

Interplay between of the superconductivity and ferromagnetism leads to many interesting effects [6, 8, 9]. In particular, re-entrant and periodically re-entrant superconductivity was predicted in works [11, 12]. Later the re-entrant superconductivity experimentally was discovered in bilayers V/Fe [13] and Nb/Cu<sub>1-x</sub>Ni<sub>x</sub> [14]. Note, a solitary re-entrant superconductivity was also recently theoretically proposed [15, 16].

Many studies (see for example [17–21]) have been devoted to the FS systems with non-uniform magnetization in the F layers, that leads to the generation of long-range triplet component of the superconducting condensate. This component describes the correlation of electrons

with total spin projection  $S_z = \pm 1$ . The spin-triplet component is not sensitive to the exchange field magnitude, and it leads to that this component penetrates in the F metal on significantly larger distance than the spin-singlet one [17, 22]. This fact for thin-film structures can also lead to strong dependence of the critical temperature  $T_c$  versus the angle  $\phi$  between the directions of the F layers magnetizations [20, 21].

Progress in the fabrication of high-quality FS heterostructures and rich physics of the proximity effect lead to that this field is promising for potential technical applications. Thus the spin valve device based on the three layered FS systems switched by weak external magnetic field was proposed in works [23–25]. The magnetic field can change the mutual orientation of the adjacent F layers magnetizations. As a result the FS system can be switched from the superconducting state to the resistive one. A more detailed implementation of the spin valve is described in the works [26–38] and in reviews [6, 8, 9].

Note, that in the last experimental works [37, 38] a full switch-over from the superconducting state to the resistive one was achieved in an external magnetic field on the three layered FFS systems  $\text{CoO}_x/\text{Fe}(1)/\text{Cu}/\text{Fe}(2)/\text{In}(\text{Pb})$ . The first theory qualitative describing the experimental results on the  $\text{F}_1\text{F}_2\text{S}$  system [37, 38] has been proposed in [21]. However, the approach [21] was based on few approximations: (a) FS interface was assumed completely transparent, that is not realistic for the metals with substantially different band structures, (b) the  $\text{F}_1$  layer thickness was considered infinite and (c) effect of the external magnetic field, at which the experimental measurements [37, 38] were carried out, was not taken into account too.

In this paper we consider a theory of thin-film three layered heterostructures FSF and FFS in the presence of external magnetic field  $\mathbf{H}$  applied parallel to the plane of the contact<sup>†</sup>. Previously an influence of the magnetic field on the properties of the symmetrical FSF system was considered in the works [40–44]. However, the real FS structures are not perfectly symmetrical. Moreover, as will be shown below, the asymmetry in some cases can lead to the higher magnitude of the difference  $\Delta T_c = T_c^{\text{AP}} - T_c^{\text{P}}$  in comparison with the symmetrical case (here  $T^{\text{AP}}$  and  $T^{\text{P}}$  are critical temperatures for the antiparallel and parallel mutual orientation of the magnetizations, respectively). Note, that obtaining a higher magnitude of the difference  $\Delta T_c$  is important for stable operation of the spin valve device. We discuss recent experimental data obtained for FSF trilayer in an external magnetic field by Antropov et al [44]. Using the fitting procedure we extract parameters set for the real FSF system and expand the theoretical description to asymmetrical FSF and FFS trilayers. In the end, based on the fit parameters set, we predict and discuss the peculiar re-entrant superconductivity and *solitary* re-entrant superconductivity induced by external magnetic field for the FFS trilayer.

## 2. Theoretical formulation

In this section we derive the equations for the triplet FS proximity effect near the second order phase transition in the presence the external magnetic field  $\mathbf{H}$ .

### 2.1. Green's functions of the superconducting state

The Gor'kov equations for the anomalous  $\hat{F}^\dagger$  and normal  $\hat{G}$  Green's functions in spin space have the form [45] (here and below we use units in which  $k_B = \mu_B = \hbar = 1$ )

$$\begin{aligned} i\omega\hat{G}(\mathbf{r}_1, \mathbf{r}_2, \omega) - \hat{H}\hat{G}(\mathbf{r}_1, \mathbf{r}_2, \omega) + \Delta(\mathbf{r}_1)\hat{g}\hat{F}^\dagger(\mathbf{r}_1, \mathbf{r}_2, \omega) &= \delta(\mathbf{r}_1 - \mathbf{r}_2), \\ i\omega\hat{F}^\dagger(\mathbf{r}_1, \mathbf{r}_2, \omega) + \hat{H}^*\hat{F}^\dagger(\mathbf{r}_1, \mathbf{r}_2, \omega) - \Delta^*(\mathbf{r}_1)\hat{g}\hat{G}(\mathbf{r}_1, \mathbf{r}_2, \omega) &= 0, \end{aligned} \quad (1)$$

<sup>†</sup>Preliminary short report about possibility of magnetic field influence on the phase diagrams of FS trilayer systems was published in the proceedings of the 19th International Conference on Magnetism (ICM'2012) [39].

where  $\omega = \pi T(2n + 1)$  is the Matsubara frequency with integer  $n$ ;  $\hat{g} = i\hat{\sigma}_2$ ;  $\hat{\sigma}_2$  is the second Pauli matrix;  $\hat{H} = \hat{H}_e + \hat{H}_{\text{ex}}$  and

$$\hat{H}_e = -\frac{1}{2m^*} \left( \nabla - \frac{ie}{c} \mathbf{A} \right)^2 - \mu, \quad \hat{H}_{\text{ex}} = -\mathbf{I} \hat{\boldsymbol{\sigma}}. \quad (2)$$

Here  $\hat{H}_{\text{ex}}$  is the spin exchange interaction, where  $\mathbf{I}$  is the exchange field,  $\hat{\boldsymbol{\sigma}} = (\hat{\sigma}_1, \hat{\sigma}_2, \hat{\sigma}_3)$  are the Pauli matrices,  $\mathbf{A}$  is the magnetic vector potential,  $m^*$  and  $\mu$  are the effective electron mass and the chemical potential, respectively. Self-consistent equation for the s-wave superconducting order parameter  $\Delta(\mathbf{r})$  is defined as follows [45]

$$\Delta^*(\mathbf{r}) = \frac{1}{2} V(\mathbf{r}) T \sum'_{\omega} \text{Tr} \hat{g} \hat{F}^\dagger(\mathbf{r}, \mathbf{r}, \omega), \quad (3)$$

where  $\text{Tr}$  means the trace function, the summation is were performed over repeated spin indices;  $V(\mathbf{r})$  is the electron-electron pairing interaction; the prime on the sum denotes cut-off on the Debye frequency  $\omega_D$ . The solution of the equations (1) can be written near the second order phase transition as

$$\hat{F}^\dagger(\mathbf{r}_1, \mathbf{r}_2, \omega) = \int d^3 \mathbf{s} \hat{f}(\mathbf{r}_1, \mathbf{s}, \omega) \Delta^*(\mathbf{s}) \hat{g} \hat{G}^{(0)}(\mathbf{s}, \mathbf{r}_2, \omega), \quad (4)$$

where Green's functions  $\hat{f}$  and  $\hat{G}^{(0)}$  satisfy the linearized equations

$$i\omega \hat{G}^{(0)}(\mathbf{r}_1, \mathbf{r}_2, \omega) - \hat{H}_e \hat{G}^{(0)}(\mathbf{r}_1, \mathbf{r}_2, \omega) - \hat{H}_{\text{ex}} \hat{G}^{(0)}(\mathbf{r}_1, \mathbf{r}_2, \omega) = \delta(\mathbf{r}_1 - \mathbf{r}_2), \quad (5)$$

$$i\omega \hat{f}(\mathbf{r}_1, \mathbf{r}_2, \omega) + \hat{H}_e^* \hat{f}(\mathbf{r}_1, \mathbf{r}_2, \omega) + \hat{H}_{\text{ex}}^* \hat{f}(\mathbf{r}_1, \mathbf{r}_2, \omega) = \delta(\mathbf{r}_1 - \mathbf{r}_2). \quad (6)$$

Then the complex conjugate of the equation (6) is taken

$$-i\omega \hat{f}^*(\mathbf{r}_1, \mathbf{r}_2, \omega) + \hat{H}_e \hat{f}^*(\mathbf{r}_1, \mathbf{r}_2, \omega) + \hat{H}_{\text{ex}} \hat{f}^*(\mathbf{r}_1, \mathbf{r}_2, \omega) = \delta(\mathbf{r}_1 - \mathbf{r}_2) \quad (7)$$

and the solution is sought in the form

$$\begin{aligned} \hat{f}^*(\mathbf{r}_1, \mathbf{r}_2, \omega) &= -\hat{U}^\dagger \hat{\mathfrak{G}}(\mathbf{r}_1, \mathbf{r}_2, \omega) \hat{U}, \\ \hat{G}^{(0)}(\mathbf{r}_1, \mathbf{r}_2, \omega) &= -\hat{f}^*(\mathbf{r}_1, \mathbf{r}_2, \omega) = \hat{U}^\dagger \hat{\mathfrak{G}}(\mathbf{r}_1, \mathbf{r}_2, \omega) \hat{U}, \end{aligned} \quad (8)$$

where unitary matrix  $\hat{U}$  describes the rotation in spin space, it satisfies  $\hat{U} \hat{H}_{\text{ex}} \hat{U}^\dagger = -I \hat{\sigma}_3$ . Putting substitution (8) into (4) and (7), we immediately obtain

$$\begin{aligned} \hat{F}^\dagger(\mathbf{r}_1, \mathbf{r}_2, \omega) &= -\int d^3 \mathbf{s} (\hat{U}^\dagger \hat{\mathfrak{G}}(\mathbf{r}_1, \mathbf{s}, \omega) \hat{U})^* \Delta^*(\mathbf{s}) \hat{g} \hat{U}^\dagger \hat{\mathfrak{G}}(\mathbf{s}, \mathbf{r}_2, \omega) \hat{U}, \\ i\omega \hat{\mathfrak{G}}(\mathbf{r}_1, \mathbf{r}_2, \omega) - \hat{H}_e \hat{\mathfrak{G}}(\mathbf{r}_1, \mathbf{r}_2, \omega) + I \hat{\sigma}_3 \hat{\mathfrak{G}}(\mathbf{r}_1, \mathbf{r}_2, \omega) &= \delta(\mathbf{r}_1 - \mathbf{r}_2). \end{aligned}$$

Returning to the equation (3) and using the following obvious relations  $\hat{U}^* = \hat{\sigma}_2 \hat{U} \hat{\sigma}_2 = -\hat{g} \hat{U} \hat{g}$  and  $\hat{\mathfrak{G}}^*(\mathbf{r}_1, \mathbf{r}_2, \omega) = \hat{\mathfrak{G}}(\mathbf{r}_2, \mathbf{r}_1, -\omega)$  linearized near  $T_c$ , the equation (3) is reduced to

$$\Delta(\mathbf{r}) = \frac{1}{2} V T \sum'_{\omega} \text{Tr} \int d^3 \mathbf{s} \hat{K}(\mathbf{r}, \mathbf{s}, \omega) \Delta(\mathbf{s}), \quad (9)$$

$$\hat{K}(\mathbf{r}, \mathbf{s}, \omega) = \hat{U}^\dagger \hat{g}^{-1} \hat{\mathfrak{G}}(\mathbf{r}, \mathbf{s}, \omega) \hat{g} \hat{\mathfrak{G}}(\mathbf{r}, \mathbf{s}, -\omega) \hat{U}. \quad (10)$$

The kernel  $\hat{K}$  contains full information about the system, and our central task is to derive the differential equation for the kernel  $\hat{K}$  and the formulation of the corresponding boundary value problem.

## 2.2. The Usadel-like equations and boundary value problem

The next problem is to determine the equation for the kernel (10) convenient for the study of spatially inhomogeneous systems. Heterogeneity in the system may be caused, on the one hand, the presence of external fields, and on the other hand, due to the proximity effect on the FS interfaces. In order to derive differential equation for the kernel  $\hat{K}$  we first consider the homogeneous system. In this case the Fourier transform  $\hat{\mathfrak{G}}(\mathbf{p}, \omega)$  of the Green function  $\hat{\mathfrak{G}}(\mathbf{R}, \omega)$  satisfies

$$i\omega\hat{\mathfrak{G}}(\mathbf{p}, \omega) - (\xi_p - I\hat{\sigma}_z)\hat{\mathfrak{G}}(\mathbf{p}, \omega) = \hat{1}, \quad \xi_p = \frac{p^2}{2m^*} - \mu. \quad (11)$$

The solution of the equation (11) has a simple form

$$\mathfrak{G}_{\alpha\beta}(\mathbf{p}, \omega) = \frac{\delta_{\alpha\beta}}{i\omega - \xi_p + I(\hat{\sigma}_3)_{\alpha\beta}}$$

and hence (in quasiclassical limit, assuming that  $p_F R \gg 1$ )  $\hat{\mathfrak{G}}(R, \omega)$  has the form [45]

$$\mathfrak{G}_{\alpha\beta}(R, \omega) = -\delta_{\alpha\beta} \frac{m^*}{2\pi R} \exp\left(\text{sign}(\omega) ip_F R - \frac{|\omega| - iI(\hat{\sigma}_3)_{\alpha\beta} \text{sign}(\omega)}{v_F} R\right), \quad (12)$$

where  $R = |\mathbf{r}_1 - \mathbf{r}_2|$ ;  $p_F$  and  $v_F$  are the Fermi momentum and Fermi velocity, respectively. Inserting (12) into (10) we obtain explicit form for the kernel  $\hat{K}(R, \omega)$

$$K_{\alpha\beta}(R, \omega) = \delta_{\alpha\beta} \left(\frac{m^*}{2\pi R}\right)^2 \exp\left(-\frac{2|\omega| - i2I(\hat{\sigma}_3)_{\alpha\beta} \text{sign}(\omega)}{v_F} R\right). \quad (13)$$

Note, that in the presence of the spin exchange interaction the kernel is an oscillating function of  $R$  on the characteristic scale of the spin stiffness length  $a_f = v_F/2I$ .

Further the Fourier transform of the kernel  $K_{\alpha\beta}(R, \omega)$  is got

$$\begin{aligned} K_{\alpha\beta}(\mathbf{p}, \omega) &= \int K_{\alpha\beta}(\mathbf{R}, \omega) \exp(-i\mathbf{p}\mathbf{R}) d^3\mathbf{R}, \\ K_{\alpha\beta}(\mathbf{p}, \omega) &= \delta_{\alpha\beta} 2\pi \left(\frac{m}{2\pi}\right)^2 \int_{-1}^1 \frac{dx}{\xi_\omega^{-1} + i(ba_f^{-1} + px)}, \end{aligned} \quad (14)$$

where we introduce the following notation  $b = -(\hat{\sigma}_3)_{\alpha\beta} \text{sign}(\omega)$  and  $\xi_\omega = v_F/2|\omega|$  for convenience. The integral in (14) is equal to

$$J(\eta) = -\frac{i\xi_\omega}{\eta} \ln \left[ \frac{bI|\omega|^{-1} + (\eta - i)}{bI|\omega|^{-1} - (\eta + i)} \right],$$

where  $\eta = p\xi_\omega$  is the dimensionless variable. In fact, the quantity of the parameter  $\eta$  characterizes the spatial scale at which the kernel  $K(R, \omega)$  is varied. We are interested in the case of small  $\eta$ , and we approximate the exact function  $J(\eta)$  by the following expression  $J_{\text{approx}} = A(1 + B\eta^2)^{-1}$  with some complex constants  $A, B$ , and to determine the constants we use the following condition

$$J_{\text{approx}}(0) = J(0), \quad \left. \frac{d^2 J_{\text{approx}}}{d\eta^2} \right|_{\eta=0} = \left. \frac{d^2 J}{d\eta^2} \right|_{\eta=0},$$

it follows that  $A = 2\xi_\omega(1 + ibI/|\omega|)^{-1}$  and  $B = \frac{1}{3}\xi_\omega^2(1 + ibI/|\omega|)^{-2}$ . Accordingly, we can now write the differential equation for the kernel at the form

$$\begin{aligned} \left[ |\omega| - iI(\hat{\sigma}_3)_{\alpha\beta} - \frac{1}{2}D_{\alpha\beta}(\omega, I)\nabla^2 \right] K_{\alpha\beta}(\mathbf{r}, \mathbf{r}', \omega) &= \pi N(0)\delta_{\alpha\beta}\delta(\mathbf{r} - \mathbf{r}'), \\ D_{\alpha\beta}(\omega, I) &= \frac{1}{3} \frac{v_F \xi_\omega}{1 - i(\hat{\sigma}_3)_{\alpha\beta} \xi_\omega / a_f}. \end{aligned} \quad (15)$$

Here  $N(0)$  is density of states at the Fermi level. In the dirty limit, when  $l \ll v_F/2\pi T_c$  ( $l$  is the mean free path length), expression for the  $D_{\alpha\beta}(I, \omega)$  is reduced to (see also review [6])

$$D_{\alpha\beta}(\omega, I) \rightarrow D_{\alpha\beta}(2I\tau_f) = \frac{D}{1 - i2I\tau_f(\hat{\sigma}_3)_{\alpha\beta}}, \quad (16)$$

where  $D$  is diffusion constant and  $\tau_f$  is the elastic scattering time. Note, that the matrix form of the complex diffusion constant (16) is uniquely determined of the microscopic approach given above. This approach consistency is confirmed that the matrix complex diffusion constant enters both in the differential equations (15) and in boundary conditions (see below expressions (22), (23)) in the same manner.

In the presence of magnetic field  $\mathbf{H} = \text{rot}\mathbf{A}$  the differential operator  $\nabla$  is modified to the gauge invariant form  $\nabla - (2\pi i/\Phi_0)\mathbf{A}$  [40, 41], where  $\Phi_0 = \pi c/e$  is the magnetic flux quantum. Next, for convenience, we introduce the pair amplitude function  $\hat{F}(\mathbf{r}, \omega)$  as the integral equation of the kernel  $\hat{K}(\mathbf{r}, \mathbf{s}, \omega)$

$$F_{\alpha\beta}(\mathbf{r}, \omega) = \frac{1}{\pi N(0)} \int K_{\alpha\beta}(\mathbf{r}, \mathbf{s}, \omega) \Delta(\mathbf{s}) d^3\mathbf{s}. \quad (17)$$

Using definition (17) and (15) we obtain the Usadel-like equation [46]

$$\left[ |\omega| - iI(\hat{\sigma}_3)_{\alpha\beta} - \frac{1}{2}D_{\alpha\beta}(2I\tau_f) \left( \nabla - \frac{2\pi i}{\Phi_0} \mathbf{A} \right)^2 \right] F_{\alpha\beta}(\mathbf{r}, \omega) = \delta_{\alpha\beta} \Delta(\mathbf{r}), \quad (18)$$

or in a more general matrix form

$$\begin{aligned} \left( |\omega| + i\hat{H}_{\text{ex}} \right) \hat{F} - \frac{1}{2}D \left( \hat{\mathcal{L}}^2 \hat{F}_1 + \frac{\hat{\sigma}_0 - i2\tau_f \hat{H}_{\text{ex}}}{1 + (2I\tau_f)^2} \hat{\mathcal{L}}^2 \hat{F}_0 \right) &= \hat{\sigma}_0 \Delta(\mathbf{r}), \\ \hat{\mathcal{L}} &= \nabla - (2\pi i/\Phi_0)\mathbf{A}. \end{aligned} \quad (19)$$

Here  $\hat{F}_0$  and  $\hat{F}_1$  are the diagonal and off-diagonal parts of the matrix  $\hat{F}$ , respectively. Note, that under rotation in the spin space  $\hat{F} = \hat{U}^\dagger \hat{\tilde{F}} \hat{U}$  the equation (19) for the  $\hat{\tilde{F}}$  is reduced to (here  $\hat{U} = \exp(\frac{i}{2}\boldsymbol{\phi}(\mathbf{r})\hat{\boldsymbol{\sigma}})$ , and  $\hat{U}\hat{H}_{\text{ex}}(\mathbf{r})\hat{U}^\dagger = -I\hat{\sigma}_3$ )

$$\begin{aligned} (|\omega| - iI\hat{\sigma}_3) \hat{\tilde{F}} - \frac{1}{2}D \left( \hat{\mathcal{D}}^2 \hat{\tilde{F}}_1 + \frac{\hat{\sigma}_0 + i2\tau_f I \hat{\sigma}_3}{1 + (2I\tau_f)^2} \hat{\mathcal{D}}^2 \hat{\tilde{F}}_0 \right) &= \hat{\sigma}_0 \Delta(\mathbf{r}), \\ \hat{\mathcal{D}} = \hat{U} \hat{\mathcal{L}} \hat{U}^\dagger &= \nabla - (2\pi i/\Phi_0)\mathbf{A} - (i/2)\boldsymbol{\Theta}, \end{aligned} \quad (20)$$

where  $\boldsymbol{\Theta} = \nabla(\boldsymbol{\phi}(\mathbf{r})\hat{\boldsymbol{\sigma}})$ . In the limiting case  $2I\tau_f \ll 1$ , the equation (20) is reduced to more simple form

$$\left[ |\omega| - iI\hat{\sigma}_3 - \frac{1}{2}D\hat{\mathcal{D}}^2 \right] \hat{\tilde{F}}(\mathbf{r}, \omega) = \Delta(\mathbf{r}).$$

Combining (17) and (9), the following self-consistent equation on the order parameter can be obtained

$$\Delta(\mathbf{r}) \ln t = \pi T_c \sum_{\omega>0}^{\infty} \text{Tr} \left( \hat{F}(\mathbf{r}, \omega) - \frac{\Delta(\mathbf{r})}{\omega} \right), \quad (21)$$

where  $t = T_c/T_{cs}$  is the reduced critical temperature ( $T_{cs}$  is the superconducting critical temperature for the bulk material without spin exchange interaction).

The equation on the pairing function (19) applied to the layered FS structures should be added by boundary conditions. We are interested in two planar contacts, superconductor-ferromagnet (SF) boundary and ferromagnet-ferromagnet ( $F_1F_2$ ) one. We use the boundary conditions derived by microscopic approach in the work [12]. For the SF interface, where F and S layers occupy the regions  $x < 0$  and  $x > 0$ , respectively, they have the form

$$\begin{aligned} \frac{4}{\sigma_s v_F^s} D_s(\mathbf{n}\hat{\mathcal{L}}) \hat{F}^s \Big|_{x=0} &= \frac{4}{\sigma_f v_F^f} D_f \left[ (\mathbf{n}\hat{\mathcal{L}}) \hat{F}_1^f + \frac{\hat{\sigma}_0 - i2\tau_f \hat{H}_{\text{ex}}}{1 + (2I\tau_f)^2} (\mathbf{n}\hat{\mathcal{L}}) \hat{F}_0^f \right] \Big|_{x=0}, \\ \frac{4}{\sigma_s v_F^s} D_s(\mathbf{n}\hat{\mathcal{L}}) \hat{F}^s \Big|_{x=0} &= \hat{F}^s(0) - \hat{F}^f(0), \end{aligned} \quad (22)$$

and for the  $F_1F_2$  interface

$$\begin{aligned} &\frac{4}{\sigma_{f1} v_F^{f1}} D_{f1} \left[ (\mathbf{n}\hat{\mathcal{L}}) \hat{F}_1^{f1} + \frac{\hat{\sigma}_0 - i2\tau_{f1} \hat{H}_{\text{ex}}^{f1}}{1 + (2I\tau_{f1})^2} (\mathbf{n}\hat{\mathcal{L}}) \hat{F}_0^{f1} \right] \Big|_{x=0} \\ &= \frac{4}{\sigma_{f2} v_F^{f2}} D_{f2} \left[ (\mathbf{n}\hat{\mathcal{L}}) \hat{F}_1^{f2} + \frac{\hat{\sigma}_0 - i2\tau_{f2} \hat{H}_{\text{ex}}^{f2}}{1 + (2I\tau_{f2})^2} (\mathbf{n}\hat{\mathcal{L}}) \hat{F}_0^{f2} \right] \Big|_{x=0}, \\ &\frac{4}{\sigma_{f1} v_F^{f1}} D_{f1} \left[ (\mathbf{n}\hat{\mathcal{L}}) \hat{F}_1^{f1} + \frac{\hat{\sigma}_0 - i2\tau_{f1} \hat{H}_{\text{ex}}^{f1}}{1 + (2I\tau_{f1})^2} (\mathbf{n}\hat{\mathcal{L}}) \hat{F}_0^{f1} \right] \Big|_{x=0} = \hat{F}^{f2}(0) - \hat{F}^{f1}(0). \end{aligned} \quad (23)$$

Here  $\mathbf{n}$  is the unit normal vector to the SF ( $F_1F_2$ ) interface; the indices  $s$ ,  $f1$ , and  $f2$  denote S,  $F_1$ , and  $F_2$  layers;  $\sigma_s$  and  $\sigma_f$  are the transparencies from the S and F side, respectively [6]. Note, that the boundary conditions at the interface (22), (23) take into account the fulfillment of the condition of detailed balance

$$\sigma_s v_F^s N_s = \sigma_f v_F^f N_f, \quad \sigma_{f1} v_F^{f1} N_{f1} = \sigma_{f2} v_F^{f2} N_{f2}, \quad (24)$$

where  $N_{s,f}$  is the density of states on the Fermi surface for the S and F layers, respectively. The boundary conditions at the outer surfaces have the form

$$(\mathbf{n}\hat{\mathcal{L}}) \hat{F}^{s,f} = 0. \quad (25)$$

The set of the equations (19), (21) and the appropriate boundary conditions (22), (23), (25) are sufficient to calculate critical temperature  $T_c$  of the SF layered structures.

### 3. The FS trilayers

#### 3.1. The $F_1SF_2$ trilayer

We choose the coordinate system so that the left  $F_1$  layer is located in region  $-d_{f1} - d_s/2 < x < -d_s/2$ , S layer is  $-d_s/2 < x < d_s/2$  and right  $F_2$  layer is  $d_s/2 < x < d_s/2 + d_{f2}$ . The magnetization vector of the  $F_1$  layer may be rotated  $\mathbf{M}_1(0, M_1 \sin \phi, M_1 \cos \phi)$ , while the magnetization of the  $F_2$  layer is fixed  $\mathbf{M}_2(0, 0, M_2)$ . Hence unitary matrix  $\hat{U}$  (see (20)) has the form

$$\hat{U} = \begin{pmatrix} \cos \frac{\phi}{2} & i \sin \frac{\phi}{2} \\ i \sin \frac{\phi}{2} & \cos \frac{\phi}{2} \end{pmatrix}.$$

The magnetic field  $\mathbf{H}$  is applied parallel to the plane FS interface  $\mathbf{H}(0, 0, -H)$ . In figure 1 the geometry of the problem is shown. Note that the diagonal matrix elements  $F_{11} = F_{22}^* = F_s$  include the singlet component of the pair amplitude and the triplet component, with zero projection of the total spin on the quantization axis ( $S_z = 0$ ), while the off-diagonal components  $F_{12} = -F_{21}^* = F_t$  correspond to the triplet component with  $S_z = \pm 1$ .

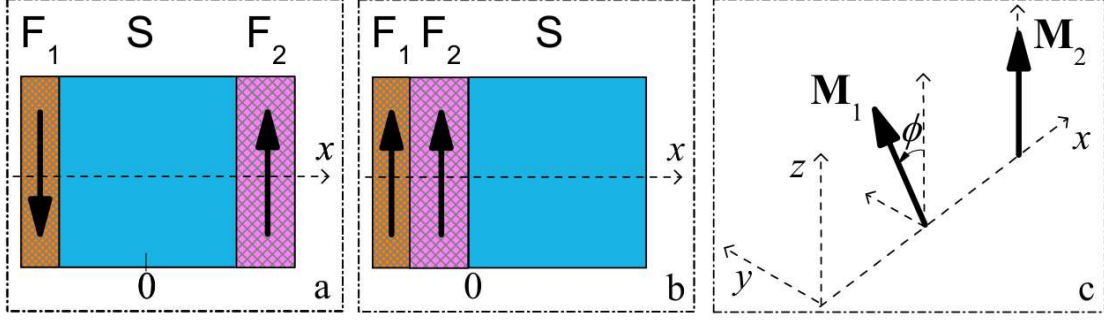


**Figure 1.** Geometry of the problem.

(a) F<sub>1</sub>SF<sub>2</sub> trilayer with antiparallel (AP) mutual orientation of F layers magnetizations ( $\phi = 180^\circ$ );

(b) F<sub>1</sub>F<sub>2</sub>S trilayer with parallel (P) mutual orientation of F layers magnetizations ( $\phi = 0^\circ$ );

(c) Schematic illustration of the magnetization vectors ( $\mathbf{M}_1$  and  $\mathbf{M}_2$ ) orientation with arbitrary angle  $\phi$ .

Using the approximation  $\Delta_f = 0$ , solutions for the pair amplitude can be written as: for the S layer

$$F_s^s(x, \omega) = \frac{\Delta_s}{\omega + \frac{1}{2}D_s Q_s^2 h^2} + \Delta_s A_s \cosh(k_s x) + \Delta_s B_s \sinh(k_s x), \quad (26)$$

$$F_t^s(x, \omega) = A_t \cosh(k_s x) + B_t \sinh(k_s x),$$

for F<sub>1</sub> layer ( $\hat{F} = \hat{U}^\dagger \hat{F} \hat{U}$ )

$$\tilde{F}_s^{f1}(x, \omega) = C_{s1} \cosh(k_{h1}(x + d_{f1} + d_s/2)), \quad (27)$$

$$\tilde{F}_t^{f1}(x, \omega) = C_{t1} \cosh(k_{f1}(x + d_{f1} + d_s/2))$$

and for the F<sub>2</sub> layer

$$F_s^{f2}(x, \omega) = C_{s2} \cosh(k_{h2}(x - d_{f2} - d_s/2)), \quad (28)$$

$$F_t^{f2}(x, \omega) = C_{t2} \cosh(k_{f2}(x - d_{f2} - d_s/2)).$$

Here wave numbers are defined as follows

$$k_s^2 = \frac{2\omega}{D_s} + Q_s^2 h^2, \quad k_{f1,2}^2 = \frac{2\omega}{D_{f1,2}} + Q_{f1,2}^2 h^2, \quad (29)$$

$$k_{h1,2}^2 = \frac{2(\omega - iI_{1,2})(1 - i2I\tau_{f1,2})}{D_{f1,2}} + Q_{f1,2}^2 h^2,$$

$$Q_\alpha^2 = \left( \frac{2\pi H_c}{\Phi_0} \right)^2 \langle x^2 \rangle_\alpha, \quad \alpha = (f_1, s, f_2),$$

where  $h = H/H_c$  is reduced magnetic field ( $H_c$  is critical parallel field of the isolated S layer); angle brackets denote averaging over the thickness  $d_{s,(f)}$  of the S(F) layers, respectively. For simplification we also use approximation  $\Delta(x) \approx \langle \Delta(x) \rangle = \Delta_s$ . For qualitative examination this approximation is justified for thin-film systems under consideration (see below Section 4). Used approximation is much better than popular single-mode approximation [6, 8]. Note, that our approximation  $\Delta(x) \approx \text{const}$  in numerical realization is simpler and faster than exact solution [20, 21], at the same time the deflection in results for these approaches is very small for parameters under consideration.

The self-consistent equation (21) is reduced to

$$\ln t = 2\pi T_c \sum_{\omega > 0}^{\infty} \left( \frac{1}{\omega + \frac{1}{2}D_s Q_s^2 h^2} + \text{Re} A_s(\omega) \frac{\sinh(k_s d_s/2)}{k_s d_s/2} - \frac{1}{\omega} \right). \quad (30)$$

### 3.2. The $F_1F_2S$ trilayer

We choose the coordinate system so that the S layer occupies the region  $0 < x < d_s$ ,  $F_1$  and  $F_2$  layers occupy the regions  $-d_{f1} - d_{f2} < x < -d_{f2}$  and  $-d_{f2} < x < 0$ , respectively.

In a similar manner we write the solutions for the pair amplitude: for the S layer

$$F_s^s(x, \omega) = \frac{\Delta_s}{\omega + \frac{1}{2}D_s Q_s^2 h^2} + \Delta_s C_s^s \cosh(k_s(x - d_s)),$$

$$F_t^s(x, \omega) = C_t^s \cosh(k_s(x - d_s)),$$

for the  $F_2$  layer

$$F_s^{f2}(x, \omega) = A_s^{f2} \cosh(k_{h2}x) + B_s^{f2} \sinh(k_{h2}x),$$

$$F_t^{f2}(x, \omega) = A_t^{f2} \cosh(k_{f2}x) + B_t^{f2} \sinh(k_{f2}x)$$

and for the  $F_1$  layer ( $\hat{F} = \hat{U}^\dagger \hat{F} \hat{U}$ )

$$\tilde{F}_s^{f1}(x, \omega) = C_s^{f1} \cosh(k_{h1}(x + d_{f1} + d_{f2})),$$

$$\tilde{F}_t^{f1}(x, \omega) = C_t^{f1} \cosh(k_{f1}(x + d_{f1} + d_{f2})).$$

The self-consistent equation on the reduced critical temperature  $t$  is written as

$$\ln t = 2\pi T_c \sum_{\omega > 0}^{\infty} \left( \frac{1}{\omega + \frac{1}{2}D_s Q_s^2 h^2} + \text{Re } C_s^s(\omega) \frac{\sinh(k_s d_s)}{k_s d_s} - \frac{1}{\omega} \right). \quad (31)$$

## 4. Results and discussions

The discussion of our numerical results complies with following logical chain. At first we discuss recent experimental data obtained for symmetrical FSF trilayer in an external magnetic field by Antropov et al [44]. Then we use a fitting procedure to find parameters of our theoretical model for the CuNi/Nb/CuNi trilayer. Using these parameters of real systems we expand our theoretical description to asymmetrical  $F_1SF_2$  system in external magnetic field. To discuss possible spin-switch applications we calculate very important parameter,  $\Delta T_c = T^{\text{AP}} - T^{\text{P}}$ . We show that the  $\Delta T_c$  is higher for asymmetrical case. Moreover we generalize this approach on the asymmetrical FFS system, obtain qualitative agreement with recent experiment on the  $\text{Fe}_1/\text{Fe}_2/\text{Pb}$  trilayer [47] and predict peculiar re-entrant superconductivity and solitary re-entrant superconductivity induced by external magnetic field.

### 4.1. The CuNi/Nb/CuNi trilayer behaviour in magnetic field

Firstly we discuss the FSF system. Antropov et al [44] used the alloy  $\text{Cu}_{41}\text{Ni}_{59}$  as soft ferromagnets and the niobium as superconductor. The critical parameters of this system were measured in the external magnetic field. Two important dependencies were got in this work [44]: (1) temperature dependence of perpendicular and parallel critical magnetic fields  $H_{c2}$  for symmetrical FSF samples with  $d_{f1} = d_{f2} = d_{\text{CuNi}}/2$  and with the Nb layer thickness  $d_{\text{Nb}} = 15.5$  nm were obtained for various thicknesses of the ferromagnetic layers; (2) superconducting transition temperature  $T_c$  were got in relation to the total thickness of ferromagnetic layers  $d_{\text{CuNi}}$  for different values of both perpendicular ( $H_{\perp}$ ) and parallel ( $H_{\parallel}$ ) magnetic field. To explain own experimental data they were used method of fundamental solution [20] of the Usadel equations [46]. All theoretical curves within their fit procedure are very close to experimental points.

Our approach differs from theoretical method used in work [44]: the matrix complex diffusion constant (16) arises and simplified approximations (see section 3.1 and discussion below)

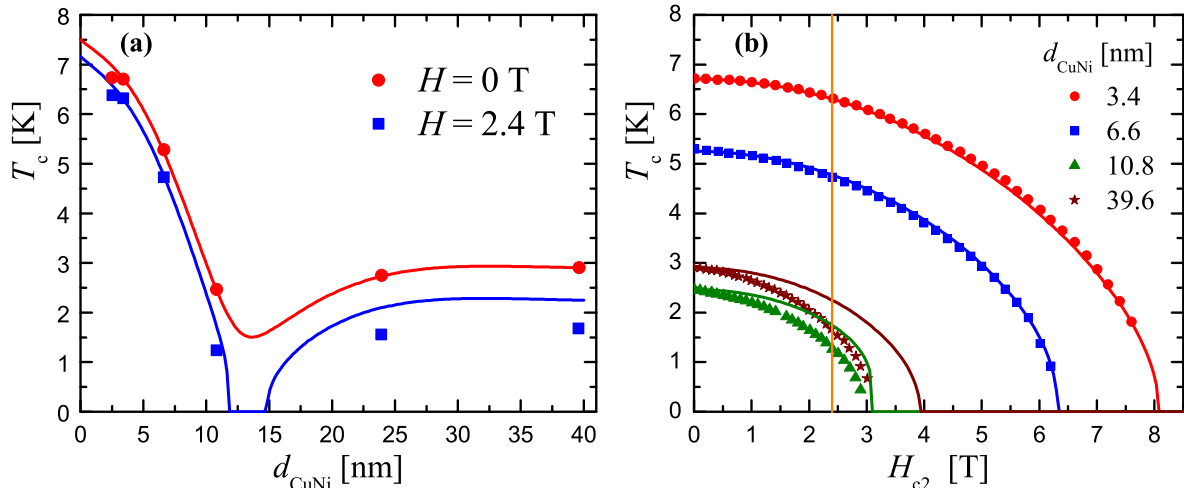


**Figure 2.** Fitting the theory to known experimental data of the  $\text{Cu}_{41}\text{Ni}_{59}/\text{Nb}/\text{Cu}_{41}\text{Ni}_{59}$  trilayer for parallel magnetic field orientation [44]. (a) Critical temperature versus the total thickness of ferromagnetic layers. Experimental data points are denoted by symbols. (b) Temperature dependence of parallel critical magnetic field with fixed Nb layer thickness  $d_{\text{Nb}} = 15.5$  nm and with varied total thickness of the F layers  $d_{f1} = d_{f2} = d_{\text{CuNi}}/2$ . Experimental data are shown by symbols. Solid lines represent results of the fitting our theory.

are made. Moreover possible triplet correlations and differences in physical and geometrical properties of F layers can be taken into account.

Below we try to describe the experimental data for parallel orientation of magnetic field [44] according to approach of section 3.1 (see figure 2). Our fitting procedure is also distinct from one used in the cited work. In figure 2a the dependence of the critical temperature vs total thickness of both CuNi layers is shown for  $H = 0$  T and  $H = 2.4$  T. We start with the  $T_c(d_{\text{CuNi}})$  curve fitting on the experimental points at zero magnetic field (red solid circles in figure 2a). The mutual orientation of magnetizations was not discussed in the work [44], and for definiteness we suppose that the F layers magnetizations are parallel (P). This fitting step provided us the set of theory parameters without magnetic field. In order to find the last parameter, critical magnetic field  $H_c(0)$  for isolated S layer, we use the set deduced above and fit the experimental points on figure 2b at thicknesses  $d_{\text{CuNi}} = 3.4$  nm. The set of fit parameters are given by

$$\begin{aligned} a_f &= 18.62 \text{ nm}, & l_f &= 2.79 \text{ nm}, & l_s &= 5.97 \text{ nm}, \\ I &= 231.9 \text{ K}, & T_{c0} &= 7.5 \text{ K}, & H_{c2}(0) &= 9.35 \text{ T}, \\ \sigma_s &= 3.77, & n_{sf} &= 4.49, \end{aligned} \quad (32)$$

where  $I$  is exchange field in ferromagnet,  $a_f = v_F/2I$  is spin stiffness length,  $l_{s(f)}$  is free path length in S(F) layer respectively,  $\sigma_{s(f)}$  is transparency from the S(F) side and  $n_{sf} = v_F^s N_s / v_F^f N_f = \sigma_f / \sigma_s$  (see relation (24)). At last, to use all dimensional parameters we substitute  $\xi_{s0}(\text{Nb}) = 38$  nm [48]. All the other theoretical dependencies in present paper are obtained with this single set of parameters (32).

We have got a good agreement of our theoretical curves with corresponding experimental points as in original work [44] in which the exact numerical approach (method of the fundamental solution) was applied. This is a positive argument for our approach which is simpler and essentially faster in numerical analysis.

Obtained parameters (32) have reasonably good values. The important theory parameter is  $2I\tau_f = l_f/a_f$  which characterizes simultaneously both magnetic properties of ferromagnet and

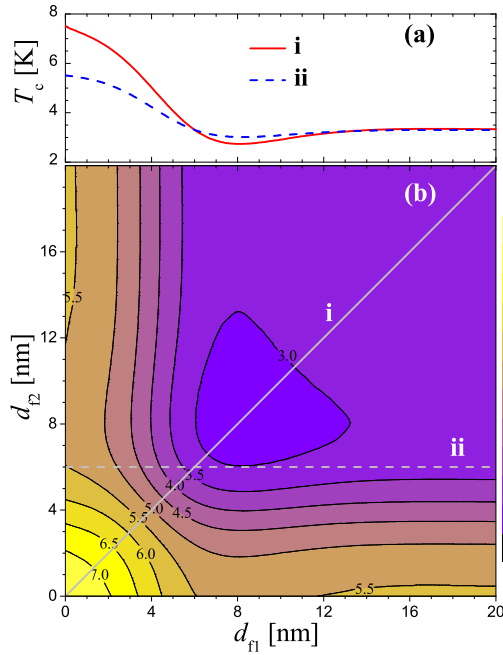


**Figure 3.** The influence of an asymmetry on the  $T_c^{\text{AP}}$  for CuNi/Nb/CuNi trilayer without magnetic field. (a) The curves  $T_c(d_f)$  for symmetric case (i) and for fixed  $d_{f2} = 6$  nm (ii); (b) The  $T_c(d_{f1}, d_{f2})$  map. The slices (i) and (ii) correspond to lines in (a).

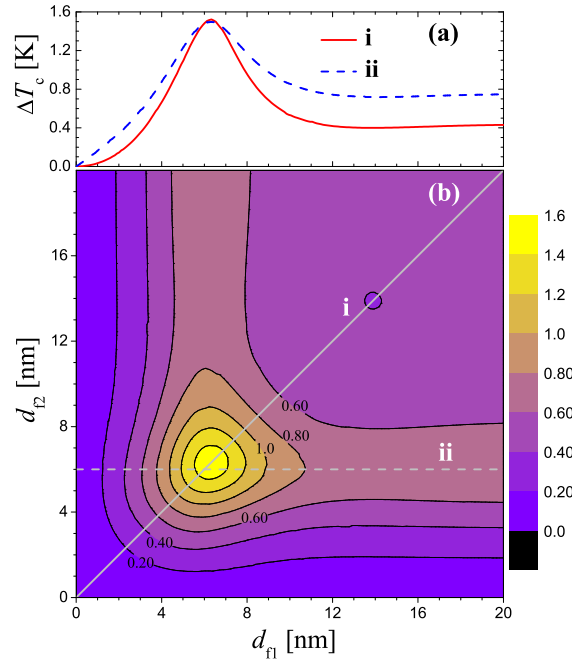


**Figure 4.** The influence of an asymmetry on the  $\Delta T_c$  for CuNi/Nb/CuNi trilayer without magnetic field. (a) The curves  $\Delta T_c(d_f)$  for symmetric case (i) and for fixed  $d_{f2} = 6$  nm (ii); (b) The  $\Delta T_c(d_{f1}, d_{f2})$  map. The slices (i) and (ii) correspond to lines in (a).

the metal purity. Obtained values  $2I\tau_f = 0.15 < 1$  and  $l_s = 5.97$  nm  $< \xi_s = \sqrt{l_s \xi_{s0}/3} = 8.7$  nm satisfy the usability condition of the Usadel equations [6, 8]. In other hand, value  $I$  indicates that Cu<sub>41</sub>Ni<sub>59</sub> alloy is soft magnet and it is in accordance with known Curie temperature for bulk sample of this alloy,  $T_{\text{Curie}} \simeq 180$  K [49] and  $T_{\text{Curie}} \simeq 219$  K [50].

Note that our theoretical calculations (see figure 2a) as previous theoretical results [44] display the re-entrant superconductivity appearance at magnetic field increasing (it was predicted in our works [43, 51]). However the experimental data [44] (see also symbols in figure 2a,b) do not prove the re-entrant superconductivity existence in parallel magnetic field conclusively. Experimental points in a possible nonsuperconducting region (near  $d_{\text{CuNi}} \simeq 12.5$  nm) are still lacking. Our main goal is theoretical analysis of behaviour of asymmetrical FS systems ( $F_1SF_2$  and  $F_1F_2S$  trilayers) in magnetic field. So, we described above the experimental data [44] only for an extraction of parameters of real FS layered system.

In figure 3b the  $T_c(d_{f1}, d_{f2})$  map is shown for the AP mutual orientation of the F layers magnetizations without external magnetic field. The diagonal solid line *i* in figure 3b corresponds to the symmetrical case of FSF trilayer with the equal thicknesses  $d_{f1} = d_{f2}$ , and asymmetrical case for fixed  $d_{f2} = 6$  nm is shown by the dashed line *ii*. Both  $T_c(d_{f1})$  slices are presented in figure 3a. The red solid line *i* for the AP state can be compared with the red solid line for the P state in figure 2a (recall that in figure 2a  $d_{f1} = d_{f2} = d_{\text{CuNi}}/2$ ). Note that the AP line goes higher than the P one [24, 25, 52, 53]. It is clearly seen in next figure 4 where the dependencies  $\Delta T_c(d_{f1}, d_{f2}) = T_c^{\text{AP}} - T_c^{\text{P}}$  are shown.

The value  $\Delta T_c$  is very important one for spin switch applications. The greater values of  $\Delta T_c$  lead to more stable work of spin switch. We see in figure 4a that blue dashed curve *ii* corresponding to asymmetrical case runs above the red solid line *i* for symmetrical one for all

thicknesses practically. The slice *ii* corresponds to maximal  $\Delta T_c$  difference at this parameter set. On plateau this difference for asymmetrical case is almost two times larger than  $\Delta T_c$  for symmetrical one.

#### 4.2. The $F_1F_2S$ trilayer behaviour in magnetic field

In this part of paper we discuss the numerical results for the  $F_1F_2S$  system obtained in our theoretical model (see section 3.2) with the parameters set found above. We suppose also that magnetizations  $\mathbf{M}_1$  and  $\mathbf{M}_2$  can be rotated by external magnetic field relative to each other (see figure 1c). It corresponds to the setup of recent experimental works [38, 54] (see also the references therein).

So, we investigate the influence of triplet correlations appearance, external magnetic field, and geometry parameters on critical temperature  $T_c$  and difference  $\Delta T_c$ .

It is very interesting to compare the phase diagrams for the  $F_1SF_2$  and  $F_1F_2S$  systems made of the same materials and with equivalent parameters sets. So, the figure 5 presents the  $\Delta T_c(d_{f1}, d_{f2})$  map and  $\Delta T_c(d_f)$  curves for the  $F_1F_2S$  trilayer which are similar to ones for the  $F_1SF_2$  system in figure 4. We continue to use dimensional parameters  $T_c$ ,  $H_c$ ,  $d_f$ ,  $d_s$  in order to keep an uniformity of presented results, though the theoreticians usually prefer to work with dimensionless values. The FFS system is an asymmetrical system in principle, and it is reflected in the  $\Delta T_c(d_{f1}, d_{f2})$  map in figure 5b. Here is a large region with negative  $\Delta T_c$  in distinction to the FSF setup (figure 4b). Firstly a such possibility of  $\Delta T_c < 0$  was theoretically proposed by Fominov et al [21]. In our map the slices *i* and *ii* denoted by white solid and dashed lines, respectively, cross this region with negative  $\Delta T_c$ . Note, that our slice *ii* – blue dashed line – in figure 5a corresponds qualitatively to the experimental dependence  $\Delta T_c(d_{f2})$  in Fig. 2 [47], and shape of our dot dashed line *iii* suits to qualitative description of the experimental points  $\Delta T_c(d_{f1})$  in Fig. 3 [47]. It should be mentioned that the huge difference in the  $\Delta T_c$  magnitude between the theory and experiment can be partially explained by that their FFS system [47] has contained very strong rigid ferromagnet (Fe) while the  $\text{Cu}_{41}\text{Ni}_{59}$  alloy is a soft magnetic, and there is large Cu spacers (4 nm) between adjacent Fe layers in their FFS design [47].

Note, that the maximal value  $\Delta T_c$ , which has observed in the FSF and FFS experiments [26–32, 36–38, 47, 54–58] at present moment, does not exceed 0.1 K. Unfortunately, the existing theoretical approaches of the FS proximity effect predict the greater quantity of this value [6, 8, 20, 21, 24, 25, 33, 52].

Nevertheless, it is clearly seen that the maximal  $\Delta T_c$  difference for the FFS setup is some three times larger than for the FSF one at the same conditions. So, we suppose that FS trilayer systems in the FFS design are more

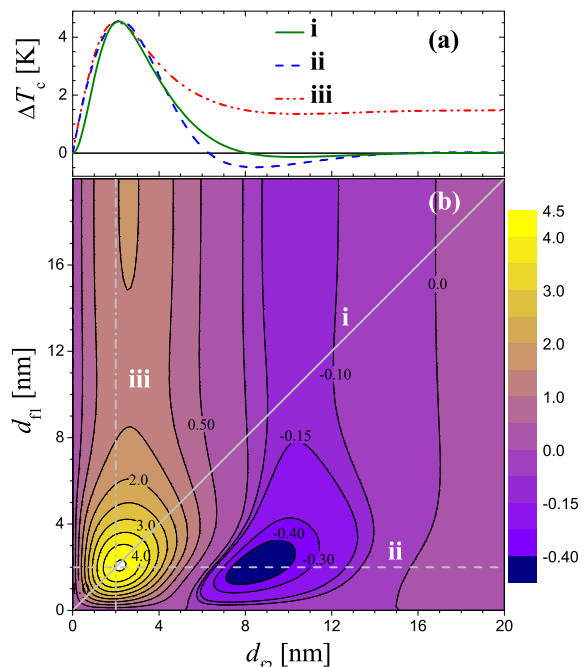


**Figure 5.** The influence of an asymmetry on the  $\Delta T_c$  difference for  $F_1F_2S$  trilayer without magnetic field. (a) The curves  $\Delta T_c(d_f)$  for symmetric case (*i*), for fixed  $d_{f1} = 2$  nm (*ii*), for fixed  $d_{21} = 2$  nm (*iii*); (b) The  $\Delta T_c(d_{f1}, d_{f2})$  map. The slices (*i*), (*ii*) and (*iii*) correspond to lines in (a).

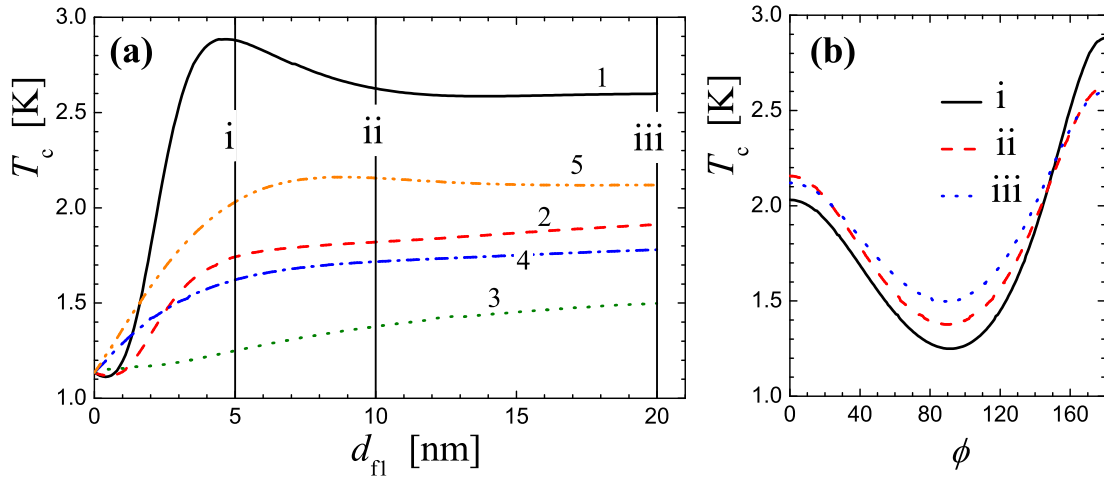


**Figure 6.** The influence of the triplet correlations on the critical temperature  $T_c$  for  $F_1F_2S$  system without magnetic field. (a)  $T_c(d_{f1})$  dependence at various angle  $\phi$ : (1) 180°, (2) 135°, (3) 90°, (4) 45°, (5) 0°; (b) The angular dependencies  $T_c(\phi)$  at three various  $F_1$  layer thicknesses  $d_{f1}$ : (i) 5 nm, (ii) 10 nm and (iii) 20 nm, which correspond slices in (a).

perspective to observe the spin switch effect. It agrees with recent experimental works (see for example [37, 47, 54] and references therein).

Above we considered only collinear mutual orientation of the magnetisations cases (P and AP state). As mentioned in section 1 the triplet component of the pair amplitude with total spin projections  $S_z = \pm 1$  appears in the general case of arbitrary value of the angle  $\phi$  between the magnetisations (see figure 1c). The influence of the triplet correlations on the critical temperature  $T_c$  is shown in figure 6. The figure 6a shows the  $T_c(d_{f1})$  dependence at various angle  $\phi$ . The  $F_2$  layer thicknesses is fixed,  $d_{f2} = 6$  nm.

First, we note a fast initial increase of the functions  $T_c(d_{f1})$ . This is due to the fact that the point  $d_{f2} = 6$  nm corresponds to the minimum of the  $T_c(d_{f2})$  function for the  $F_2S$  bilayer (see slice at  $d_{f1} = 0$  in figure 7b). Therefore, the increasing the  $F_1$  layer thickness leads to the  $T_c$  increase. This effect is the most pronounced at the AP case (curve 1 in figure 6a) due to partial compensation of the exchange interactions of the adjacent ferromagnets. With further increase of the  $F_1$  layer thickness the pair amplitude decays rapidly and, as a consequence, the  $T_c(d_{f1})$  dependence reaches a plateau.

As it was pointed out in Introduction, the  $T_c(d_{f1})$  curves at  $\phi \neq 0, \pi$  reach a plateau at large thicknesses ( $d_{f1} > 20$  nm) due to the presence of the long-range triplet component of the pair amplitude with  $S_z = \pm 1$  [18].

The angular dependencies  $T_c(\phi)$  at three various the  $F_1$  layer thicknesses marked in figure 6a by vertical thin solid lines (i, ii, iii) are displayed in figure 6b. The curves  $T_c(\phi)$  have a minimum at  $\phi \simeq 90^\circ$ . This is in a good agreement with the results obtained in the work [21]. Analogous angular dependencies  $T_c(\phi)$  for the FFS trilayers were observed in the experiments [38, 54].

As mentioned above the external magnetic field can lead to a qualitative change in the phase diagrams of the FS system. So, the re-entrant superconductivity appearance at magnetic field increasing in the FS bilayers and FSF trilayers was firstly predicted in our theoretical works [43, 51], and it was experimentally observed in the work [44]. In this regard, the influence of an external magnetic field on the phases diagrams of the FFS trilayers is an interesting point. In figure 7(a) the  $T_c(d_{f1})$  curves for the antiparallel mutual orientation of the magnetizations are plotted at the four different values of magnetic field  $H$ . The thickness  $d_{f2} = 6$  nm is fixed.

The curve 1 corresponding  $H = 0$  in figure 7(a) is the same line as curve 1 in figure 6(a). For clear visualisation the  $T_c(d_{f1}, d_{f2})$  map at  $H = 0$  is displayed in figure 7b. As in the FSF case the magnetic field variation leads to qualitative change of the  $T_c(d_{f1})$  dependence. Note, that in this FFS case a superconductivity appears only starting at some finite thickness of the  $F_1$  layer. This can be called as “peculiar re-entrant” superconductivity. The curve  $T_c(d_{f1})$  has a maximum and then it reaches a plateau. New feature can be predicted with the magnetic field increase. Thus the *solitary* re-entrant superconductivity is shown in figure 7(a) at  $H = 4.1$  T (see curve 4). It should be emphasized that there are important conditions for occurrence of the reentrant and solitary re-entrant superconductivity in external magnetic field: a) the  $F_2$  layer thickness should correspond to the minimum of function  $T_c(d_{f1} = 0, d_{f2})$  (or to the minimum of  $T_c(d_{f2})$  for bilayer  $F_2S$ ); b) the FFS system must be in the AP state.

## 5. Conclusions

In this work we consider the asymmetrical  $F_1SF_2$  and  $F_1F_2S$  trilayers. Our theoretical approach taking into account of the asymmetry and triplet superconducting correlations is valid in the external magnetic field presence as in real experimental setup for the FS spin valve explorations. The numerical results and figures are based on the new parameters which are obtained from comparison of our theory and recent experiment [44], which is described adequately by our theoretical model. It is shown that asymmetry and external magnetic field can essentially influence on the critical properties of considered systems. In particular, we have shown that both asymmetrical trilayers may be more effective in experimental realization of spin switch regime. We can also conclude that the asymmetrical  $F_1F_2S$  trilayer is more perspective candidate for possible spin valve applications. The solitary re-entrant superconductivity induced by external magnetic field is predicted for the last layered system.

## Acknowledgments

This work would be not appeared without a long-standing cooperation with Prof. Tsarevskii S.L. and Prof. Khusainov M.G. The paper is dedicated to their blessed memory.

The work is partially supported by the Ministry of Education and Science of Russian Federation and by Russian Fund for Basic Research (grant 13-02-01202).

The both authors are thankful to professor Boris I. Kochelaev for support, which he renders over many years, and wish to B.I.K. a health, a happiness and a lot of years for productive and successful life. Yu.P. is personally grateful to B.I.K. for choice, which he made thirty-seven years ago. Yu.P. is indebted to his dear Mentor for very kind and friendly relation, and he believes that their friendship will be continued for a long time.

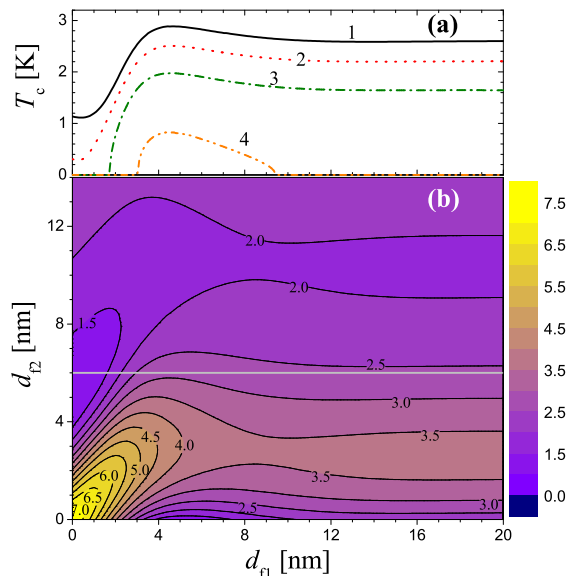


**Figure 7.** Magnetic field influence on the phase diagrams of the  $F_1F_2S$  system. (a) The dependence  $T_c(d_{f1})$  for the AP state for some values of the external magnetic field: (1)  $H = 0$ , (2)  $H = 2$  T, (3)  $H = 3$  T, (4)  $H = 4.1$  T; the  $F_2$  layer thickness is fixed  $d_{f2} = 6$  nm; (b) The  $T_c(d_{f1}, d_{f2})$  map at  $H = 0$ . The horizontal solid line corresponds to slice 1 in (a).

## References

1. Ginzburg V. L., *JETP* **4**, 153 (1957).
2. Fulde P., Ferrell R., *Phys. Rev.* **135**, A550 (1964).
3. Larkin A., Ovchinnikov Y., *Zh. Eksp. Teor. Fiz.* **47**, 1136 (1964).
4. de Gennes P. G., *Rev. Mod. Phys.* **36**, 225 (1964).
5. Demler E. A., Arnold G. B., Beasley M. R., *Phys. Rev. B* **55**, 15174 (1997).
6. Izyumov Y. A., Proshin Y. N., Khusainov M. G., *Physics-Uspeski* **45**, 109 (2002).
7. Golubov A. A., Kupriyanov M. Y., Il'ichev E., *Rev. Mod. Phys.* **76**, 411 (2004).
8. Buzdin A., *Rev. Mod. Phys.* **77**, 935 (2005).
9. Efetov K. B., Garifullin I. A., Volkov A. F., Westerholt K., “*Magnetic Heterostructures*” (Springer Berlin / Heidelberg, 2008) Chap. Proximity Effects in Ferromagnet/Superconductor Heterostructures, pp. 251–290.
10. Ryazanov V. V., Oboznov V. A., Prokofiev A. S., Bolginov V. V., Feofanov A. K., *J. Low Temp. Phys.* **136**, 385 (2004).
11. Khusainov M., Proshin Y., *Phys. Rev. B* **56**, R14283 (1997).
12. Proshin Y. N., Khusainov M. G., *Zh. Eksp. Teor. Fiz.* **113**, 1708 (1998).
13. Garifullin I. A., Tikhonov D. A., Garif'yanov N. N., Lazar L., Goryunov Y. V., Khlebnikov S. Y., Tagirov L. R., Westerholt K., Zabel H., *Phys. Rev. B* **66**, 020505 (2002).
14. Zdravkov V., Sidorenko A., Obermeier G., Gsell S., Schreck M., Müller C., Horn S., Tidecks R., Tagirov L. R., *Phys. Rev. Lett.* **97**, 057004 (2006).
15. Khusainov M., Khusainov M., Ivanov N., Proshin Y., *JETP Lett.* **90**, 359 (2009).
16. Proshin Y., Khusainov M., Khusainov M., *Physica C* **470**, 874 (2010).
17. Bergeret F. S., Volkov A. F., Efetov K. B., *Phys. Rev. Lett.* **86**, 4096 (2001).
18. Bergeret F. S., Volkov A. F., Efetov K. B., *Rev. Mod. Phys.* **77**, 1321 (2005).
19. Volkov A. F., Bergeret F. S., Efetov K. B., *Phys. Rev. Lett.* **90**, 117006 (2003).
20. Fominov Y. V., Golubov A. A., Kupriyanov M. Y., *JETP Lett.* **77**, 510 (2003).
21. Fominov Y. V., Golubov A. A., Karminskaya T. Y., Kupriyanov M. Y., Deminov R. G., Tagirov L. R., *JETP Lett.* **91**, 308 (2010).
22. Champel T., Eschrig M., *Phys. Rev. B* **72**, 054523 (2005).
23. Oh S., Youm D., Beasley M., *Appl. Phys. Lett.* **71**, 2376 (1997).
24. Tagirov L. R., *Phys. Rev. Lett.* **83**, 2058 (1999).
25. Buzdin A. I., Vedyayev A. V., Ryzhanova N. V., *Europhys. Lett.* **48**, 686 (1999).
26. Gu J. Y., You C.-Y., Jiang J. S., Pearson J., Bazaliy Y. B., Bader S. D., *Phys. Rev. Lett.* **89**, 267001 (2002).
27. Potenza A., Marrows C. H., *Phys. Rev. B* **71**, 180503 (2005).
28. Westerholt K., Sprungmann D., Zabel H., Brucas R., Hjörvarsson B., Tikhonov D. A., Garifullin I. A., *Phys. Rev. Lett.* **95**, 097003 (2005).
29. Moraru I. C., Pratt W. P., Birge N. O., *Phys. Rev. Lett.* **96**, 037004 (2006).
30. Rusanov A. Y., Habraken S., Aarts J., *Phys. Rev. B* **73**, 060505 (2006).
31. Steiner R., Ziemann P., *Phys. Rev. B* **74**, 094504 (2006).

32. Moraru I. C., Pratt W. P., Birge N. O., *Phys. Rev. B* **74**, 220507 (2006).
33. Proshin Y. N., Zimin A., Fazleev N. G., Khusainov M. G., *Phys. Rev. B* **73**, 184514 (2006).
34. Singh A., Sürgers C., Löhneysen H. V., *Phys. Rev. B* **75**, 024513 (2007).
35. Kim D. H., Hwang T., *Physica C* **455**, 58 (2007).
36. Nowak G., Zabel H., Westerholt K., Garifullin I., Marcellini M., Liebig A., Hjörvarsson B., *Phys. Rev. B* **78**, 134520 (2008).
37. Leksin P. V., Garif'yanov N. N., Garifullin I. A., Schumann J., Vinzelberg H., Kataev V., Klingeler R., Schmidt O. G., Büchner B., *Appl. Phys. Lett.* **97**, 102505 (2010).
38. Leksin P. V., Garif'yanov N. N., Garifullin I. A., Fominov Y. V., Schumann J., Krupskaya Y., Kataev V., Schmidt O. G., Büchner B., *Phys. Rev. Lett.* **109**, 057005 (2012).
39. Avdeev M. V., Tsarevskii S. L., Proshin Y. N., *J. Korean Phys. Soc.* **63**, 466 (2013).
40. Radović Z., Dobrosavljević-Grujić L., Buzdin A. I., Clem J. R., *Phys. Rev. B* **38**, 2388 (1988).
41. Krunavakarn B., Yoksan S., *Physica C* **440**, 25 (2006).
42. Avdeev M., Khusainov M., Proshin Y., Tsarevskii S., *Solid State Phenom.* **152**, 462 (2009).
43. Avdeev M., Khusainov M., Proshin Y., Tsarevskii S., *Supercond. Sci. Technol.* **23**, 105005 (2010).
44. Antropov E., Kalenkov M. S., Kehrle J., Zdravkov V. I., Morari R., Socrovisciuc A., Lenk D., Horn S., Tagirov L. R., Zaikin A. D., Sidorenko A. S., Hahn H., Tidecks R., *Supercond. Sci. Technol.* **26**, 085003 (2013).
45. Abrikosov A. A., Gorkov L. P., *JETP* **12**, 1243 (1961).
46. Usadel K. D., *Phys. Rev. Lett.* **25**, 507 (1970).
47. Leksin P. V., Kamashev A. A., Garif'yanov N. N., Garifullin I. A., Fominov Y. V., Schumann J., Hess C., Kataev V., Büchner B., *JETP Lett.* **97**, 478 (2013).
48. Kittel C., *Introduction to Solid State Physics*, 6th ed. (John Wiley & Sons, Inc., New York, 1986).
49. Ahern S., Martin M., Sucksmith W., *Proceedings of the Royal Society of London. Series A. Mathematical and Physical Sciences* **248**, 145 (1958).
50. Shunk F. A., Hansen M., Anderko K., *Constitution of Binary Alloys*, 2 (McGraw-Hill, 1969).
51. Avdeev M. V., Proshin Y. N., Khusainov M. G., Tsarevskii S. L., *Phys. Met. Metall.* **111**, 537 (2011).
52. Proshin Y. N., Izyumov Y. A., Khusainov M. G., *Phys. Rev. B* **64**, 064522 (2001).
53. Fominov Y. V., Chtchelkatchev N. M., Golubov A. A., *Phys. Rev. B* **66**, 014507 (2002).
54. Zdravkov V. I., Kehrle J., Obermeier G., Lenk D., Krug von Nidda H.-A., Müller C., Kupriyanov M. Y., Sidorenko A. S., Horn S., Tidecks R., Tagirov L. R., *Phys. Rev. B* **87**, 144507 (2013).
55. Leksin P. V., Garif'yanov N. N., Garifullin I. A., Schumann J., Kataev V., Schmidt O. G., Büchner B., *Phys. Rev. B* **85**, 024502 (2012).
56. Leksin P. V., Garif'yanov N. N., Garifullin I. A., Schumann J., Kataev V., Schmidt O. G., Büchner B., *Phys. Rev. Lett.* **106**, 067005 (2011).
57. Zhu J., Krivorotov I. N., Halterman K., Valls O. T., *Phys. Rev. Lett.* **105**, 207002 (2010).
58. Cadden-Zimansky P., Bazaliy Y. B., Litvak L. M., Jiang J. S., Pearson J., Gu J. Y., You C.-Y., Beasley M. R., Bader S. D., *Phys. Rev. B* **77**, 184501 (2008).

# Local magnetic field distribution of the vortex lattice near surface of superconducting plate

E.P. Sharin

North-Eastern Federal University, Belinskogo 58, 670016 Yakutsk, Russia

*E-mail:* ep.sharin@s-vfu.ru

Within the framework of the London model the distribution of local magnetic field near the surface of plate of anisotropic type-II superconductor is found when the external magnetic field is perpendicular to the axis of symmetry of the crystal. There is obtained the distribution of the local magnetic field depending on the distance to the surface of the superconducting plate. It is shown that the lineshape of distribution of local magnetic field near the surface changes considerably as compared with the distribution in the depth of massive superconductor. This change should be taken into account when interpreting experimental data on the observation of the local magnetic field in the near-surface region of massive superconductor and in thin superconducting films (thickness is less than the depth of penetration of the magnetic field in the superconductor).

**PACS:** 76.30.-v, 68.65.-k

**Keywords:** high-temperature superconductor, magnetic field distribution, lineshape of nuclear magnetic resonance

## 1. Introduction

The methods of nuclear magnetic resonance (NMR) is now widely used to study the properties of type-II superconductors including high-temperature ones. NMR experiments have played a big role in understanding of the dynamics of vortices in high-temperature superconductors. For a reliable interpretation of lineshape along with the uniform width determined by the nonhomogeneous dynamics of interaction of the spin system of nuclei with the conduction electrons and between them, it is necessary to take into account the inhomogeneity of the local magnetic field in the superconductor, i.e. the inhomogeneous NMR line width [1]. In the study of the vortex lattice by the NMR method the distribution of magnetic field is usually used which is formed in the thickness of the massive superconductor, assuming that the inhomogeneity of the local field is the same both in the depth of the superconductor and on its surface. However, it is known [2–4] that the local magnetic field considerably changes as it approaches the surface of the superconductor. However, the spatial distribution of the magnetic field in the superconductor near its surface significantly differs from the distribution of the local field in the depth of the superconductor. In the present paper this problem is solved on the basis of the generalized London equations with the use of appropriate boundary conditions. There has been found the dependence of distribution of magnetic field in the unit cell of the vortex lattice on the distance to the surface of superconducting plate when the external magnetic field is perpendicularly directed to the axis of symmetry of the crystal. Numerical calculations showed that for intermediate values of magnetic field  $H_{c1} < H < H_{c2}$  the distribution of fields of vortex lattice significantly changes near the surface and turns into a uniform field over the surface at the distances of the order of the averaged penetration depth of the magnetic field. There have been obtained map of magnetic field distribution, the lineshape of nuclear magnetic resonance depending on the distance to the surface of the anisotropic superconductor.

## 2. Basic equations

We will consider a superconducting plate of thickness  $d$  placed in a magnetic field and occupying the space  $-d/2 < z < d/2$ . The density of free energy of an anisotropic superconductor [1–3]:

$$8\pi F = \int (\mathbf{h}_s^2(\mathbf{r}) + \lambda^2 m_{\alpha\beta} \text{curl}_\alpha \mathbf{h}_s(\mathbf{r}) \text{curl}_\beta \mathbf{h}_s(\mathbf{r})) dv, \quad (1)$$

where  $\mathbf{h}_s(\mathbf{r})$  is the local magnetic field in the superconductor,  $dv$  is a volume element;  $m_{\alpha\beta} = M_{\alpha\beta}/M_{av}$  is a given phenomenological tensor;  $M_{av} = (M_1 M_2 M_3)^{1/3}$  and  $M_{av}$  are the principal values of the “mass tensor”  $M_{\alpha\beta}$ . The principal values of mass tensor  $m_{\alpha\beta}$  are related by the relation  $m_1 m_2 m_3 = 1$ . For the majority of high-temperature superconductors it is possible to put  $m_1 = m_2 < m_3$  and then it is only needed to know the mass ratio  $\Gamma = m_3/m_1$ . The anisotropic parameter  $\Gamma$  can be determined experimentally [1, 5], for example, from the ratio of two critical fields directed in one case along the plane  $ab$ , and the other along the crystal axis  $c$ . In the system of coordinates  $(X, Y, Z)$  related to the basic crystal axes where the  $Z$  axis is perpendicular to the layers the tensor  $m_{\alpha\beta}$  is diagonal [1]. Varying the formula for the free energy of the anisotropic superconductor (1) with respect to  $\mathbf{h}_s(\mathbf{r})$ , we will get the following equations for the magnetic field:

$$h_{s,\alpha} - \lambda^2 m_{kl} \varepsilon_{\alpha l \delta} \varepsilon_{k \gamma \beta} h_{s\beta;\delta\gamma} = \Phi_0 \nu_\alpha \sum_\nu \delta(\mathbf{r} - \mathbf{r}_\nu). \quad (2)$$

Here the notation is introduced, for example,  $h_{s\beta;\delta\gamma} = \partial^2 h_{s\beta} / \partial \delta \partial \gamma$ , where  $\alpha, \beta, \gamma, \delta = x, y, z$ ; further,  $\Phi_0$  is the magnetic flux quantum, so that the magnetic induction  $B = \Phi_0/S$ ,  $S$  is the area of the unit cell of the vortex lattice,  $\varepsilon_{\alpha l \delta}$  is the antisymmetric tensor,  $\nu$  is the unit vector along the direction of vortices. In the last equation the term in the right-hand side takes into account the singularities in the vortices.

In the region  $z < d/2$  and  $z > d/2$  the distribution of the magnetic field is defined by the Maxwell equations in vacuum:

$$\begin{aligned} \text{curl } \mathbf{h}_v(\mathbf{r}) &= 0, \\ \text{div } \mathbf{h}_v(\mathbf{r}) &= 0, \end{aligned} \quad (3)$$

where  $\mathbf{h}_v(\mathbf{r})$  is the magnetic field in the vacuum.

The equations (1) and (2) on the boundary between two media are supplemented with the following boundary conditions:

$$\begin{aligned} h_{sn}(x, y, \pm d/2) &= h_{vn}(x, y, \pm d/2), \\ (\text{curl } \mathbf{h}_v(\mathbf{r}))_z|_{z=0} &= 0, \end{aligned} \quad (4)$$

Here  $h_{sn}(\mathbf{r})$  and  $h_{vn}(\mathbf{r})$  are the normal components of the field in the superconductor and in the vacuum, respectively. From the physical point of view the first condition means that the normal components of the field on the boundary of the media change continuously, and the second condition takes into account that fact that the component of the current normal to the surface is absent.

The field  $\mathbf{h}(\mathbf{r})$  has the periodicity of the vortex lattice in the plane  $(x, y)$ , so that we can expand it in a Fourier series:

$$\begin{aligned} \mathbf{h}(\boldsymbol{\rho}, z) &= \sum_{\mathbf{G}} \mathbf{f}(\mathbf{G}, z) e^{i\mathbf{G}\boldsymbol{\rho}}, \\ \mathbf{f}(\mathbf{G}, z) &= \frac{B}{\Phi_0} \int \mathbf{h}(\boldsymbol{\rho}, z) e^{-i\mathbf{G}\boldsymbol{\rho}} d\boldsymbol{\rho}, \end{aligned} \quad (5)$$

where  $\mathbf{h}(\boldsymbol{\rho}, z)$  is the Fourier transform of magnetic field,  $\mathbf{G}$  is the reciprocal lattice vector,  $\boldsymbol{\rho}$  is the position vector. The solutions for the Fourier components of the field satisfying the boundary conditions (4) when  $\mathbf{G} \neq 0$  have the form:

in the superconductor ( $-d/2 \leq z \leq d/2$ )

$$\begin{aligned} f_{sx}(G, z) &= -i \frac{BG_x(1 + \lambda^2 m_1 G_x^2)}{q_3 D_2} \sinh\left(\frac{q_3 d}{2}\right) \sinh(q_1 z), \\ f_{sy}(G, z) &= -i \frac{BG_y}{q_3 D_2} \left\{ \sinh\left(\frac{q_1 d}{2}\right) \sinh(q_3 z) + \lambda^2 m_1 G_x^2 \sinh\left(\frac{q_3 d}{2}\right) \sinh(q_1 z) \right\}, \\ f_{sz}(G, z) &= \frac{B}{\lambda^2 m_3 q_3^2} - \frac{B}{q_3 D_2} \left\{ G_y^2 \sinh\left(\frac{q_1 d}{2}\right) \cosh(q_3 z) \right. \\ &\quad \left. + \lambda^2 m_1 q_1 q_3 G_x^2 \sinh\left(\frac{q_3 d}{2}\right) \cosh(q_1 z) \right\}, \end{aligned} \quad (6)$$

in the vacuum ( $|z| > d/2$ )

$$\begin{aligned} f_{vx}(G, z) &= \pm i \frac{BG_x(1 + \lambda^2 m_1 G_x^2)}{q_3 D_2} \sinh\left(\frac{q_1 d}{2}\right) \sinh\left(\frac{q_3 d}{2}\right) e^{G(\frac{d}{2} \pm z)}, \\ f_{vy}(G, z) &= \pm i \frac{BG_y(1 + \lambda^2 m_1 G_x^2)}{q_3 D_2} \sinh\left(\frac{q_1 d}{2}\right) \sinh\left(\frac{q_3 d}{2}\right) e^{G(\frac{d}{2} \pm z)}, \\ f_{vz}(G, z) &= \pm i \frac{BG(1 + \lambda^2 m_1 G_x^2)}{q_3 D_2} \sinh\left(\frac{q_1 d}{2}\right) \sinh\left(\frac{q_3 d}{2}\right) e^{G(\frac{d}{2} \pm z)}, \end{aligned} \quad (7)$$

where

$$\begin{aligned} q_1 &= \frac{1}{\lambda^2 m_1} + G^2, \quad q_3 = \frac{1}{\lambda^2 m_1} - \frac{m_1}{m_3} G_x^2 + G_y^2, \quad G = \sqrt{G_x^2 + G_y^2}, \\ D_2 &= \lambda^2 m_3 \left\{ G_y^2 \sinh\left(\frac{q_1 d}{2}\right) \cosh(q_3 z) + q_3 G(1 + m_1 G_x^2) \sinh\left(\frac{q_1 d}{2}\right) \right. \\ &\quad \left. + \lambda^2 m_1 q_1 q_3 G_x^2 \cosh\left(\frac{q_1 d}{2}\right) \right\} \sinh\left(\frac{q_3 d}{2}\right), \end{aligned}$$

the upper sign corresponds to the case when  $z > d/2$  and the lower sign corresponds to the case when  $z < -d/2$ .

### 3. Distribution of magnetic field

Since it is difficult to analytically perform the inverse Fourier transform of the obtained solutions, then we will do it numerically. The pattern of distribution of the magnetic field in the real space is obtained by means of the standard procedure of fast fourier transform (FFT) for two-dimensional periodic functions. Following the papers [1–3], we introduce a nonorthogonal system of reference  $\eta, \zeta$ :

$$\eta = x - y \cos \phi, \quad \zeta = y / \sin \phi. \quad (8)$$

In this system of reference  $\mathbf{h}(\eta + nb_1, \zeta + mb_2) = \mathbf{h}(\eta, \zeta)$ , where  $m, n$  are integer numbers. Then, instead of (5) we have:

$$\begin{aligned} \mathbf{h}(\eta, \zeta, z) &= \sum_{n,m} \mathbf{f}(p, q, z) e^{i(p\eta + q\zeta)}, \\ \mathbf{f}(p, q, z) &= B \int d\eta d\zeta \mathbf{h}(\eta, \zeta, z) e^{-i(p\eta + q\zeta)}, \end{aligned} \quad (9)$$

where  $p = \frac{2\pi n}{|\mathbf{b}_1|}$ ,  $q = \frac{2\pi m}{|\mathbf{b}_2|}$ ,  $\mathbf{b}_1$  and  $\mathbf{b}_2$  are basis vectors of unit cell of the vortex lattice.

It is convenient to introduce the dimensionless quantities  $\mathbf{h} = \mathbf{h}\lambda^2/\Phi_0$ ,  $\mathbf{B} = \mathbf{B}\lambda^2/\Phi_0$ ,  $\rho = \rho/\lambda$ ,  $\mathbf{G} = \mathbf{G}\lambda$  i.e. the length is measured in the units of length of the penetration depth of the magnetic field, and the field is measured in the units of  $\Phi_0/\lambda^2$ . To present results we will use numerical estimates for the anisotropic parameter  $\Gamma$  and the field  $B$  given in the papers [1, 6]. We will choose the mass ratio  $\Gamma = m_3/m_1 = 25$ , which reflects the anisotropy of the high-temperature superconductor  $\text{YBa}_2\text{Cu}_3\text{O}_{7-\delta}$  with  $T_c = 90$  K. We will take the magnetic field  $h = 2$ , which is much higher than  $H_{c1}$  in the interval interesting for us  $0 < \theta < \pi/2$ .

In the Fig. 1 the map of distribution of longitudinal component of magnetic field  $h_z$  in the unit cell of the vortex lattice is presented in the case when the external magnetic  $\mathbf{B}$  is perpendicularly directed relative to the axis of symmetry of the crystal on the surface of superconducting plate ( $z = d/2$ ). The distance to the surface is given in the units of the averaged depth of penetration of the magnetic field,  $\lambda$ ; the magnetic field is in the units of  $\Phi_0/\lambda^2$ . It should be noted that the distribution of the fields of the vortex lattice significantly changes near the surface of the superconductor and turns into the uniform one over the surface at distances of the order of the averaged depth of penetration of the magnetic field  $\lambda$ .

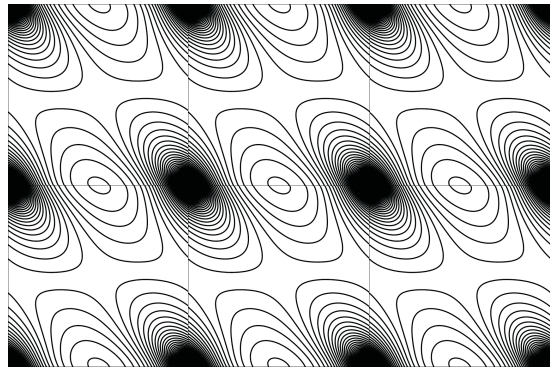


**Figure 1.** The map of the distribution of the longitudinal component of the magnetic field  $h_z$  on the surface of superconducting plate ( $z = d/2$ ) in the unit cell of the vortex lattice when  $\mathbf{B} \perp \mathbf{c}$ .

#### 4. Lineshape of magnetic resonance

The inhomogeneous distribution of the magnetic field  $|\mathbf{h}|$  in the unit cell of the vortex lattice, obviously, makes a contribution to the broadening of the magnetic resonance line in the superconductor [4, 7, 8]. In the case when it is the only source of broadening the form of the magnetic resonance line, in particular NMR accurately reproduces the distribution function of the local fields in the vortex lattice [4, 8]. In order to get a more detailed picture of the distribution of the fields as a function of distance to the surface of the superconductor, we will calculate the lineshape of the magnetic resonance for the layer at a distance  $z$  (in the units of  $\lambda$ ) above the surface of the superconducting plate. Meanwhile the accuracy of calculation is determined by the number of points into which the unit cell of the vortex lattice is divided in which the local magnetic field  $\mathbf{h}(\mathbf{r})$  is calculated (in our case  $1024 \times 1024$  points were used). The form of the resonance line is determined by direct count of the relative number of points in the plane  $(x, y)$  for which the value of the field lies in  $h$  and  $h + \delta h$ , while the wings of the magnetic resonance line correspond to the maximum of the magnetic field located at the center of the vortex and the minimum in the valley of relief of the field distribution, and the peak of the NMR line corresponds to the saddle points which are on lines, connecting tops. The results of such calculation are shown in Fig. 2. In this figure the values of the field  $h$  are plotted on the axis of abscissa, from  $h_{\min}$  in the middle of the superconducting plate ( $z = 0$ ) to  $B$ , i.e., part of curves for  $h > B$  is not shown (in this region they fall monotonically to zero). The values of the minimum field  $h_{\min} = 1.9778$ . As expected, the magnetic resonance line narrows and its peak shifts to the value of the external field as we move from the depth of the superconductor to the surface and beyond it.

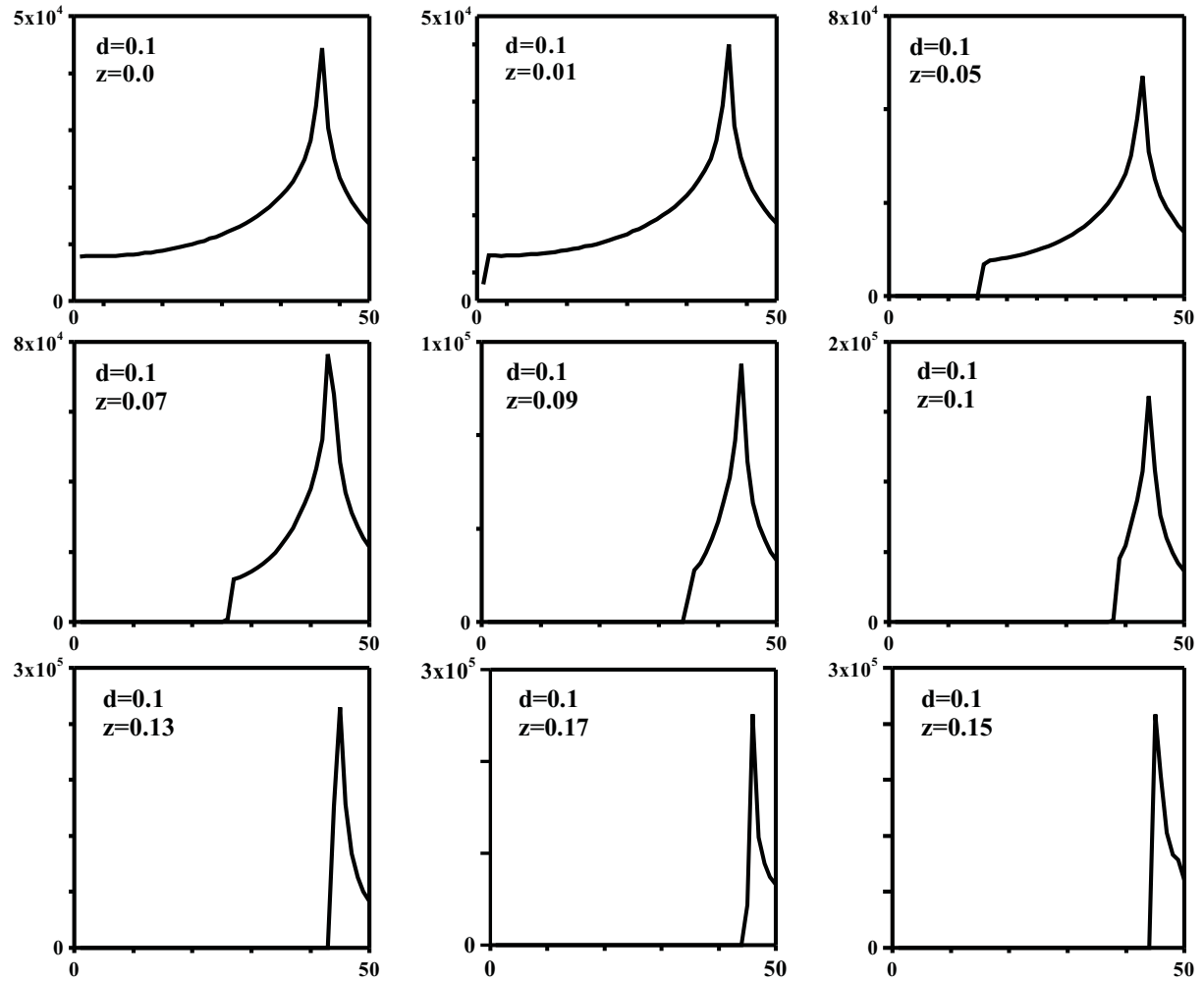


**Figure 2.** The line form of magnetic resonance at  $B = 2.0$  depending on the distance to the surface of thin superconducting plate with the thickness  $d = 0.1$ . The values of the field  $50(h - h_{\min})/(B - h_{\min})$  are plotted on the abscissa axes, the intensity in relative units is plotted on the ordinate axes.

## 5. Conclusions

The performed calculations showed that the distribution of the local magnetic field of the vortex lattice near the surface of the superconductor still has the features of the vortex lattice, but is very different from the field in the thickness of the superconductor and becomes uniform over the surface at distances from it of the order of the averaged penetration depth of the magnetic field. A characteristic feature of the local field near the surface is the presence of transverse field components, which are different from zero for any orientation of the external magnetic field relative to the crystal axes, while in the thickness of the superconductor they appear only in oblique orientations of the field. It should be noted that in the study of the vortex lattice by NMR methods with the help of a probe on the surface of the superconductor, there appears an additional broadening of the resonance line, if the thickness of the probe is not negligible as compared with the magnetic field penetration depth  $\lambda$ . This is due to the fact that the position of the peak of the NMR line depends on the distance to the surface of the superconductor, and the resulting line shape is determined by the superposition of the resonance lines shown in Fig. 2. The stated shows that any determination of magnetic parameters of superconductor associated with the measurements of the local field near its surface should be based on the appropriate analysis of the near-surface distribution of the fields of the vortex lattice.

## References

1. Thiemman S. L., Radovic Z., Kogan V. G., *Phys. Rev.* **39**, 11406 (1989).
2. Kochelaev B. I., Sharin E. P., *Superconductivity: Physics, Chemistry, Technics* **5**, 1982 (1992) [in Russian].
3. Kochelaev B. I., Sharin E. P., *Superconductivity: Physics, Chemistry, Technics* **5**, 1931 (1992) [in Russian].
4. Pozek M., Habermeier H. U., Maier A., Mehring M., *Physica C* **269**, 61 (1996).
5. Kogan V. G., Simonov A. Y., Ledvij M., *Phys. Rev. B* **48**, 392 (1993).
6. Farrell D. E., Williams C. M., Bannal N. P., Kogan V. G., *Phys. Rev. Lett.* **61**, 2805 (1988).
7. Brandt E. H., *Phys. Rev. B* **37**, 2349 (1988).
8. Maclaughlin D. E., *Solid State Phys.* **31**, 1 (1976).

# Influence of electron correlations on magnetic properties in transition metals in view of degeneration

V.E. Shilov, E.V. Shilova\*

Mari State University, 424001 Yoshkar-Ola, Russia

\*E-mail: crabflo@mail.ru

A transition from high-spin state to low-spin state is considered. The self-energy is calculated in one-loop approximation. The three-orbital periodic Anderson-Hubbard model is used to obtain an initial segment of an optical branch in view of degeneration. The possibility of experimental verification of the received result by a method of non-elastic dispersion of slow neutrons is discussed.

**PACS:** 75.40.Gb

**Keywords:** high-spin state, low-spin state, state hybridization, section of dispersion, one-loop approximation

## 1. Introduction

In transition metals compounds with narrow bands the electron-electron correlations features are caused by orbital degeneration. The main difference between the degenerate states and non-degenerate states consists in possibility of existence of two electrons with parallel spins on the same site of a crystal lattice. This possibility is the result of degeneration in orbital quantum number. The degeneration in orbital quantum number can be removed by crystal field only in part.

## 2. Model Hamiltonian

The present work is devoted to research of slow neutrons dispersion in the frameworks of the generalized Anderson-Hubbard model with degeneration. Basically, the compounds containing transition metals have a cubic symmetry. These compounds can be most consistently described by Hubbard model [1], which takes into account such important features as Anderson *s-d* hybridization [1], transmitting movement on a lattice and the Hund exchange interaction. We investigate system, described by the following Hamiltonian  $\tilde{H}$

$$\tilde{H} = H_1 + H_2 + H_3 + H_4 + H_5 + H_6, \quad (1)$$

where

$$\begin{aligned} H_1 &= \sum_{i,\sigma,m=a,b,c} \frac{I_m}{2} n_{i\sigma}^m n_{i\bar{\sigma}}^m, & H_2 &= \frac{U}{2} \sum_{\substack{i,\sigma,\sigma' \\ m,n=a,b \\ m \neq n}} n_{i\sigma}^m n_{i\sigma'}^n, & H_3 &= J \sum_i S_i^a S_i^b, \\ H_4 &= \sum_{\substack{i,\sigma,m \\ m=a,b,c}} (E^m + \sigma H) d_{i\sigma m}^\dagger d_{i\sigma m}, & H_5 &= \frac{V_0}{2} \sum_{i,\sigma} [(a_{i\sigma}^\dagger + b_{i\sigma}^\dagger) c_{i\sigma} + \text{h.c.}], \\ H_6 &= \sum_{\substack{i,j,\sigma \\ m=a,b,c}} t_{ij}^{mm} d_{i\sigma m}^\dagger d_{j\sigma m} + \sum_{i,j,\sigma} t_{ij}^{ab} (a_{i\sigma}^\dagger b_{j,\sigma} + \text{h.c.}) \end{aligned} \quad (2)$$

and  $I_m = I_a = I_b = I_1$ ,  $I_c = I_2$  are Hubbard repulsions between electrons on orbitals  $a, b, c$  transforming on representation  $t_{2g}$ ,  $n_{i\sigma}^m$  is the particles number operator on orbitals  $m = a, b, c$ ;  $J$  is integral of exchange interaction on orbitals  $t_{2g}$ ;  $S_i$  is the operator of a spin on corresponding orbital;  $E^m$  is atomic energy of orbitals;  $d_{j\sigma m}, d_{j\sigma m}^\dagger$  is field operators corresponding to free and localized electrons at site  $j$  with spin projection  $\sigma$  on orbitals  $a, b, c \in t_{2g}$ ;  $H$  is the applied magnetic field;  $t_{ij}^{ab}$  is the energy of tunneling on corresponding orbitals from site  $i$  to site  $j$ ;  $E^m = E^a = E^b = E - \mu$ ,  $E^c = \varepsilon - \mu$  are the energies of orbitals, counted from Fermi level  $\mu$ ,  $V_0$  is energy of electron hybridization of electrons on orbitals  $a$  and  $b$  with electrons on orbital such as  $c$  (hybridization of Anderson),  $U$  is the Coulomb inter-orbital interaction.

### 3. Energy Spectrum

Further, we shall consider a case of almost half filled  $t_{2g}$ -symmetrical states, which are sub bands when the electronic states undergo transitions between two- and three-particle states.

According to the Hund rule, the lowest three-particle state has spin  $S = 3/2$  and quadruple degeneration of a spin projection. As a typical example ferromagnetic iron Fe can be viewed, where electron states are between configurations  $3d^24sp^6$  and  $3d^34sp^5$  [2]. This fact specifies the important role of the Anderson interaction. After diagonalization of one-site term of Hamiltonian (1) corresponding to non-overlapped atomic states the one-particle operators are represented as a linear combination of transitions between  $N$  and  $N + 1$  states.

Below we shall consider transitions:  $|\sigma\sigma\sigma\rangle \rightarrow |L^\sigma\rangle$ . The symmetrized wave functions and energy levels corresponding to this transitions are as follows

$$\begin{aligned} |L^\sigma\rangle &= \gamma a_\sigma^\dagger b_\sigma^\dagger |0\rangle + \delta (a_\sigma^\dagger + b_\sigma^\dagger) c_\sigma^\dagger |0\rangle, & E(L^\sigma) &= \varepsilon_4 + 2\bar{\sigma}H + \frac{1}{2}\sqrt{\varepsilon_2^2 + 2V_0^2}, \\ |\sigma\sigma\sigma\rangle &= a_\sigma^\dagger b_\sigma^\dagger c_\sigma^\dagger |0\rangle, & E(\sigma\sigma\sigma) &= \varepsilon_3 - \sigma H, \end{aligned}$$

where

$$\begin{aligned} \varepsilon_2 &= I_1 - I_2 + E^a - E^c + J/2, & \varepsilon_3 &= U - J/2 + 2E^a + E^c, \\ \varepsilon_4 &= \frac{1}{2}(U - J/2 + 3E^a + E^c), & \varepsilon_5 &= U - J/2 + E^a - E^c, \\ \gamma &= \frac{V_0}{\sqrt{2(d-c)^2 + V_0^2}}, & \delta &= \frac{d-c}{\sqrt{2(d-c)^2 + V_0^2}}, & d-c &= \frac{1}{2}\sqrt{\varepsilon_5^2 + V_0^2} - \frac{\varepsilon_5}{2}. \end{aligned}$$

One-particle operators are expressed in terms of Hubbard operators  $X_q^p$  by a standard way [3, 4]:

$$\begin{aligned} a_\sigma^\dagger &= \alpha\sigma \left( X_{2aT_{bc}^{\bar{\sigma}\bar{\sigma}}} + \frac{1}{\sqrt{3}}X_{2aT_{bc}^{T\sigma}} + \sqrt{\frac{2}{3}}X_{2aT_{bc}^{T\bar{\sigma}}} \right) + \delta \left( X_{\sigma\sigma\sigma}^{L\sigma} + \frac{1}{\sqrt{3}}X_{T_{\bar{\sigma}}}^{L\bar{\sigma}} + \sqrt{\frac{2}{3}}X_{T_{\sigma}}^{L\sigma\bar{\sigma}} \right), \\ b_\sigma^\dagger &= \alpha\sigma \left( X_{2aT_{ac}^{\bar{\sigma}\bar{\sigma}}} + \frac{1}{\sqrt{3}}X_{2aT_{ac}^{T\sigma}} + \sqrt{\frac{2}{3}}X_{2aT_{ac}^{T\bar{\sigma}}} \right) + \delta \left( X_{\sigma\sigma\sigma}^{L\sigma} + \frac{1}{\sqrt{3}}X_{T_{\bar{\sigma}}}^{L\bar{\sigma}} + \sqrt{\frac{2}{3}}X_{T_{\sigma}}^{L\sigma\bar{\sigma}} \right), \\ c_\sigma^\dagger &= \beta\sigma \left( X_{2aT_{ac}^{\bar{\sigma}\bar{\sigma}}} + \frac{1}{\sqrt{3}}X_{2aT_{ac}^{T\sigma}} + \sqrt{\frac{2}{3}}X_{2aT_{ac}^{T\bar{\sigma}}} \right) + \gamma \left( X_{\sigma\sigma\sigma}^{L\sigma} + \frac{1}{\sqrt{3}}X_{T_{\bar{\sigma}}}^{L\bar{\sigma}} + \sqrt{\frac{2}{3}}X_{T_{\sigma}}^{L\sigma\bar{\sigma}} \right), \\ \alpha &= \frac{b-a}{\sqrt{2(b-a)^2 + V_0^2}}, & \beta &= \frac{V_0}{\sqrt{2(b-a)^2 + V_0^2}}, & b-a &= \frac{1}{2} \left( \sqrt{(\varepsilon_2 + U)^2 + V_0^2} - \varepsilon_2 \right). \end{aligned}$$

Let's calculate a spectrum of spin waves in one-loop approximation [3]:

$$\omega(\mathbf{q}) = \lambda\alpha (+ + +, L^\sigma) - \Sigma^{+++,-++(1)}(\mathbf{q}) - \Sigma^{+++,-++(2)}(\mathbf{q}),$$

where

$$\begin{aligned}\Sigma^{+++,-++(1)} &= \sum_p \Theta(\xi(\mathbf{p})) [t(\mathbf{q} - \mathbf{p}) - t(\mathbf{p})] \delta, \\ \Sigma^{+++,-++(2)} &= \sum_p \Theta(\xi(\mathbf{p})) [t(\mathbf{p}) - t(\mathbf{q} - \mathbf{p})] \delta^2, \\ \xi(\mathbf{p}) &= \lambda \boldsymbol{\alpha} (+ + +, L^\sigma) + f_\alpha t(\mathbf{p}) - \mu, \quad i\omega_n \rightarrow \omega \pm i\delta.\end{aligned}$$

For group of transition metals (Fe, Ni, Co...) where the bond between localized and delocalized electrons is particularly strong (according to various experiments [5–7]), the Anderson interaction ( $s$ - $d$ -hybridization) plays an important role. As a result, one-site magnetic moment takes non-integer values (for iron its value equals  $2.2 \mu_B$ , and  $d$ -electrons get kinetic energy. In this connection it is necessary to mention the R. Zaitsev's work [3], where the role of strong interaction in the same cell and an opportunity of the quantitative description of ferromagnetism Ni and  $\alpha$ -Fe was investigated. In another work [8] the role of a periodic part of the Anderson interaction was investigated, moreover the authors received singular contribution near the Fermi level which results in resonant peak in density of states.

#### 4. Neutron Dispersion

From the viewpoint of comparison of localized description and band description of the electron in the compounds containing transition metals, the experiments investigating dispersion of thermal neutrons are most interesting. The method of dispersion of thermal neutrons allows to measure directly the law of a dispersion in a wide interval of transferred energy  $\hbar\omega$  ( $10 \text{ meV} \leq \omega \leq 10^3 \text{ meV}$ ) and momentum  $q$  ( $0.1 \text{ \AA}^{-1} \leq q \leq 10 \text{ \AA}^{-1}$ ) Ferromagnetic metals have pronounced peaks of non-elastic dispersion of neutrons on spin waves. The account of additional interactions in Hamiltonian (1) (the Hund exchange interaction and the Coulomb intersite interaction which are neglected in works [3, 8]) allows to come nearer to a real situation in pure transition metals. Investigation of a magnetic excitation spectrum in optical and acoustic ranges is important from the viewpoint of comparison of localized (an acoustic part of a spectrum) and band (optical) models of magnetism. A large number of models reflects a large number of magnetic behavior of real magnetics.

We have considered the case when the system undergoes transitions between two- and three-hole high-spin states and we shall estimate a section of non-elastic dispersion of neutrons in one-loop approximation.

The spin waves spectrum was determined in case of transitions from the three-particle level to the two-particle level on  $a$ -type orbitals, based on Dyson's equation

$$-\omega + \lambda \boldsymbol{\alpha} (+ + +, L^\sigma) - \text{Re}\Sigma_{L^\sigma}^{+++}(\mathbf{k}, \omega) = 0,$$

where  $\lambda$  is eigenvalues vector,  $\boldsymbol{\alpha} (+ + +, L^\sigma)$  is root vector of twice degenerated Hubbard models,  $\Sigma_{L^\sigma}^{+++}(\mathbf{k}, \omega)$  is self-energy part for the transitions from the three-particle level to the two-particle level on  $a$ -type orbitals. The second derivative of section of neutron dispersion on spin wave is:

$$\frac{d^2\sigma}{d\Omega d\omega} \propto \delta(\omega - \omega_{L^\sigma}^{+++}) = \delta(E_{p'} - E_p \pm \hbar\omega_S(\mathbf{q})),$$

where

$$\hbar\omega_S(\mathbf{q}) = \lambda \boldsymbol{\alpha} (+ + +, L^\sigma) - \frac{q^2}{2m^*} \frac{(1 - c^*)}{\sqrt{2}} \left( 1 + \frac{V_0}{2(d - c)^2} \right)^{-1/2},$$

$J$  is the Hund exchange interaction,  $m^*$  is the effective mass determined by energy of tunneling,  $c^*$  is concentration of electrons in partially underfilled band. These parameters are determined by transitions on  $a$ -type orbitals.

## 5. Summary

Problems of strong electronic correlations are discussed several tens of years. In review of Izyumov and Kurmaev [9] the importance of strong electronic correlations is shown for the large class of materials. In the hematite  $\text{Fe}_2\text{O}_3$  the electronic correlation  $d^5$  ions of iron can be realized in low spin state as well as in high spin state [2]. To explain this case it is necessary to use the calculation methods which include the correlation effects. Weak distortion of octahedron field results in splitting of  $t_{2g}$  state on  $a_{1g} + e_g^\pi$  and  $e_g^\sigma$ . We take into account these features of a spectrum for a case when  $e_g^\sigma$  is represented by two equivalent Hubbard orbitals and  $a_{1g}$  is a narrow band. In works [2, 3] it is shown, that in pure metals (Fe, Co, Mn) the electron system undergoes transitions between low-spin state and high-spin state. In the present work the calculation of a spectrum spin excitation is carried out, and dependence of section of slow neutrons dispersion on transitions from three-particle state to the two-particle states is obtained.

We performed the calculation of scattering cross-section taking into account dispersion of Coulomb interactions, exchange interactions and hybridization in the periodic Anderson model. As a result we obtain, that the optical mode depends on parameter of the Anderson's hybridization and hole concentration in the narrow band, and the Hund exchange energy in case of transitions to  $a$ -type orbitals. The dependence of optical gap on original (i.e. one-site) structure of energy spectrum is obtained. Detailed comparison of these results with experimental data for a number of metals (Fe, Ni, Mn, etc.), manganites and superconducting materials is needed and it will be done in following works.

## References

1. Hubbard J. *Proc. Roy. Soc. A.* **276**, 238 (1963)
2. Kozhevnikov A.V., Lukoyanov A.V., Anisimov V.I., Korotin M.A. *JETP* **105**, 1035 (2007)
3. Zaitsev R.O. *JETP* **43**, 574 (1976)
4. Vedyayev A.V., Ivanov V.A., Shilov V.E. *Theor. Math. Phys.* **64**, 756 (1985)
5. Kuzemsky A.L. *Physics of Elementary Particles and Atomic Nuclei* **12**, 366 (1981) [in Russian]
6. Kuzemsky A.L. *Int. J. Mod. Phys. B* **16**, 803 (2002)
7. Ododo J.C., Anyakoha M.W. *J. Phys. F: Met. Phys.* **13**, 2335 (1983)
8. Izyumov Y.A., Alexeev D.S. *Phys. Met. Metall.* **99**, 123 (2005)
9. Izyumov Y.A., Kurmaev E.Z. *Physics-Uspokhi* **51**, 23 (2008)

# Probing the metal-to-insulator transition in $\text{LaCu}_3\text{Ru}_x\text{Ti}_{4-x}\text{O}_{12}$ by Gd-ESR

B. Schmidt<sup>1</sup>, H.-A. Krug von Nidda<sup>1,\*</sup>, S. Riegg<sup>1</sup>, S.G. Ebbinghaus<sup>2</sup>, A. Reller<sup>3</sup>, A. Loidl<sup>1</sup>

<sup>1</sup>Experimental Physics V, Center for Electronic Correlations and Magnetism, University of Augsburg, D-86159 Augsburg, Germany

<sup>2</sup>Solid State Chemistry, Martin-Luther University Halle-Wittenberg, D-06099 Halle, Germany

<sup>3</sup>Resource Strategy, University of Augsburg, D-86159 Augsburg, Germany

\**E-mail: kvn@physik.uni-augsburg.de*

$\text{LaCu}_3\text{Ru}_x\text{Ti}_{4-x}\text{O}_{12}$  undergoes a metal-to-insulator transition (MIT) from a heavy-fermion metal ( $x = 4$ ) with moderately enhanced electronic masses to an antiferromagnetic insulator ( $x = 0$ ) with colossal dielectric constants. So far, the exact value  $x_c$  of the MIT could not be obtained from electrical resistivity or specific-heat data, which are governed by local-moment scattering and Schottky anomalies, respectively. To investigate the MIT by electron spin resonance (ESR) technique, polycrystalline samples of the solid-solution series  $\text{La}_{1-y}\text{Gd}_y\text{Cu}_3\text{Ru}_x\text{Ti}_{4-x}\text{O}_{12}$  were synthesized for the substitution range  $1 \leq x \leq 4$  and  $0.05 \leq y \leq 0.15$ , where  $\text{Gd}^{3+}$  ( $^8S_{7/2}$  ground state) serves as ESR probe. For  $x = 4$  the  $\text{Gd}^{3+}$  ESR linewidth exhibits an enhanced Korringa relaxation at low temperatures ( $T < 50$  K) as typically expected for heavy-fermion metals. This metallic contribution gradually diminishes on decreasing Ru content  $x$  and vanishes for  $x = 2.25$  localizing the MIT close to the onset of spin-glass behavior arising for  $x \leq 2$ .

**PACS:** 71.27.+a, 71.30.+h, 76.30.-v

**Keywords:** heavy fermions, metal-to-insulator transition, electron spin resonance

## 1. Introduction

Originally heavy-fermion behavior was observed in intermetallic compounds containing elements with partially filled  $4f$  or  $5f$  shells, like Ce, Yb or U. Prominent examples are, e.g.,  $\text{CeAl}_3$ ,  $\text{CeCu}_2\text{Si}_2$ ,  $\text{YbRh}_2\text{Si}_2$ , and  $\text{UPt}_3$  [1–4]. Due to the Kondo effect, below a certain characteristic temperature  $T^*$  of the order of 10 K the local  $f$  moments become screened by the conduction electrons. In turn, these materials exhibit metallic properties with strongly enhanced effective masses  $m^*/m_e \approx 1000$  with respect to the free electron mass  $m_e$  resulting in a correspondingly strong enhancement of the Sommerfeld coefficient of the specific heat as well as of the Pauli susceptibility. Later on, also several  $d$ -electron derived heavy-fermion compounds have been discovered in the large manifold of transition-metal oxides, like the magnetically frustrated spinel  $\text{LiV}_2\text{O}_4$  or the perovskite  $\text{Gd}_{1-x}\text{Sr}_x\text{TiO}_3$  at the metal-to-insulator transition (MIT) close to  $x = 0.2$  [5, 6]. In these compounds not only the Kondo effect but also electronic correlations due to frustration or due to the Mott-Hubbard MIT have been suggested to be responsible for the mass enhancement. A brief review can be found in Ref. [7].

In this review, typical heavy-fermion effects on the magnetic resonance properties are illustrated: With respect to usual metals, a strongly enhanced linear increase of the electron spin resonance (ESR) linewidth of appropriate probe spins as well as of the nuclear magnetic resonance (NMR) spin-lattice relaxation rate is observed on increasing temperature  $T$  for  $T < T^*$ . To higher temperatures an intermediate regime governed by spin fluctuations finally transforms into the usual linear Korringa relaxation with moderate slope. While NMR is measured on

appropriate nuclei like Cu, Al, Si, or Pt, the ESR signal of the Kondo ion itself is usually not detectable, because the linewidth is of the order of the characteristic temperature and, hence, by far larger than the conventional ESR frequencies of 9 or 35 GHz. An exception are systems with strong ferromagnetic correlations like  $\text{YbRh}_2\text{Si}_2$  or  $\text{CeRuPO}$  [8, 9]. Thus, usually small amounts of an appropriate ESR probe have to be doped into the compound of interest. In  $4f$  or  $5f$  derived compounds this is often  $\text{Gd}^{3+}$  with electron configuration  $4f^7$ , i.e., a half-filled  $4f$  shell and stable spin-only  $S = 7/2$  state [10]. Due to vanishing orbital momentum the direct spin-lattice relaxation is negligible and the relaxation via the conduction electrons becomes dominant. The power of  $\text{Gd}^{3+}$ -ESR to help elucidating the heavy-fermion state in canonical correlated electron systems has been demonstrated, e.g., in Refs. [11–13].

Here we focus on perovskite-related  $\text{LaCu}_3\text{Ru}_4\text{O}_{12}$  [14], which exhibits very similar electronic properties like isostructural  $\text{CaCu}_3\text{Ru}_4\text{O}_{12}$ , in spite of different electronic filling due to trivalent La instead of divalent Ca [15]. With a Sommerfeld coefficient  $\gamma = 85 \text{ mJ mol}^{-1} \text{ K}^{-2}$  per formula unit derived from the specific heat,  $\text{CaCu}_3\text{Ru}_4\text{O}_{12}$  is a moderately mass enhanced Fermi liquid showing intermediate valence properties above 2 K, but reveals non-Fermi-liquid behavior for lower temperatures [16–18]. For  $\text{LaCu}_3\text{Ru}_4\text{O}_{12}$  on the other hand, low-temperature specific-heat measurements revealed a Sommerfeld coefficient of  $139 \text{ mJ mol}^{-1} \text{ K}^{-2}$  per formula unit, indicating a comparable moderate heavy-fermion behavior [15]. In  $\text{LaCu}_3\text{Ru}_x\text{Ti}_{4-x}\text{O}_{12}$  the substitution of Ru by non-magnetic  $\text{Ti}^{4+}$  ( $3d^0$ ) reduces the mass enhancement as documented from heat-capacity data and a metal-to-insulator transition (MIT) was expected when roughly half of the ruthenium ions is replaced by titanium [15]. However, the exact concentration  $x_c$  of the MIT is masked due to a breakdown of the Fermi-liquid behavior in the resistivity for  $x < 3$  and Schottky-like anomalies in the specific heat. For  $x \leq 2$  a spin-glass phase shows up at low temperatures, which finally transforms into an antiferromagnetically ordered ground state for  $x < 0.5$ . The question, whether the onset of the spin-glass phase correlates with the MIT, could not be answered on the basis of resistivity and specific-heat measurements so far.

Therefore, electron-spin resonance (ESR) experiments were carried out to investigate in detail the local magnetic properties of the copper and ruthenium ions. Unfortunately, the spin-moment of Ru relaxes by far too fast to yield a well measurable ESR signal. Furthermore, the copper-spin moment also becomes covered by this effect and Cu-ESR is only observable for  $x = 0$  [19]. Thus, we doped small amounts of  $\text{Gd}^{3+}$  as ESR probe on the La site. This enabled us to access locally the electronic properties of  $\text{LaCu}_3\text{Ru}_4\text{O}_{12}$  and the MIT induced by Ti substitution.

## 2. Experimental details

Polycrystalline samples of  $\text{La}_{1-y}\text{Gd}_y\text{Cu}_3\text{Ru}_x\text{Ti}_{4-x}\text{O}_{12}$  were synthesized for  $1 \leq x \leq 4$  by solid-state reaction from the binary oxides  $\text{La}_2\text{O}_3$  (Chempur, 99.9%),  $\text{Gd}_2\text{O}_3$  (Aldrich, 99.9%),  $\text{RuO}_2$  (Chempur, 99.9%),  $\text{TiO}_2$  (Aldrich, 99.9%), and  $\text{CuO}$  (HelmAG, 99.5%) mixed in appropriate molar amounts. Before synthesis,  $\text{La}_2\text{O}_3$ ,  $\text{Gd}_2\text{O}_3$ , and  $\text{RuO}_2$  were dried for 6 hours at  $900^\circ\text{C}$  in a box furnace. The starting compounds were powdered in an agate mortar with isopropanol. After drying the mixture was pelletized and calcined for 48 hours at  $1040^\circ\text{C}$  in a muffle furnace. Excess  $\text{CuO}$  was added as a flux and removed after the reaction using diluted hydrochloric acid according to Ref. [20]. X-ray diffraction (performed in a *Seifert* TT 3003 diffractometer using  $\text{Cu } K_{\alpha 1, \alpha 2}$  radiation) proves the proper perovskite derived cubic structure  $A'A''_3B_4\text{O}_{12}$ , space group  $Im\bar{3}$  (No. 204), of the samples as exemplarily illustrated in Fig. 1 for the sample with  $x = 3.5$  and  $y = 0.05$ . In this structure La and Cu occupy the sites  $A'$  and  $A''$ , respectively,

whereas Ru and Ti statistically share the  $B$  site [21]. The corresponding Rietfeld refinement has been performed with the program *FullProf Suite* [22].

The concentration dependence of the lattice parameters for all samples under consideration is depicted in Fig. 2. The main frame proves that 5% of gadolinium do not change the cubic lattice parameter  $a$  significantly: The cell parameter  $a$  increases approximately linearly with ruthenium concentration  $x$ , while the changes due to the gadolinium doping remain within experimental uncertainties ( $\pm 3$  mÅ). This is further evident from the inset, which illustrates that only for  $y = 0.15$  a small reduction of the lattice parameter of the order of 0.05% can be recognized.

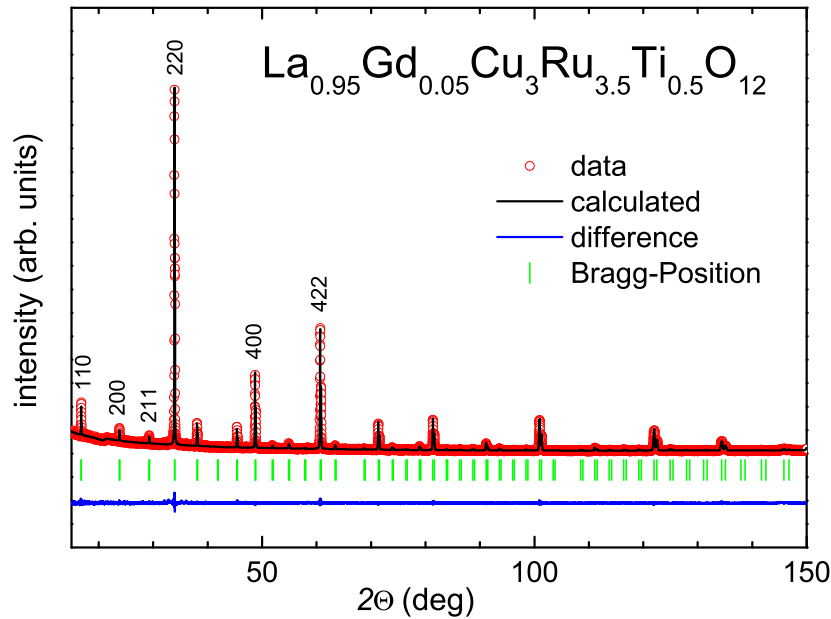


**Figure 1.** Exemplary x-ray diffraction pattern of  $\text{La}_{0.95}\text{Gd}_{0.05}\text{Cu}_3\text{Ru}_{3.5}\text{Ti}_{0.5}\text{O}_{12}$  and result of Rietfeld refinement.

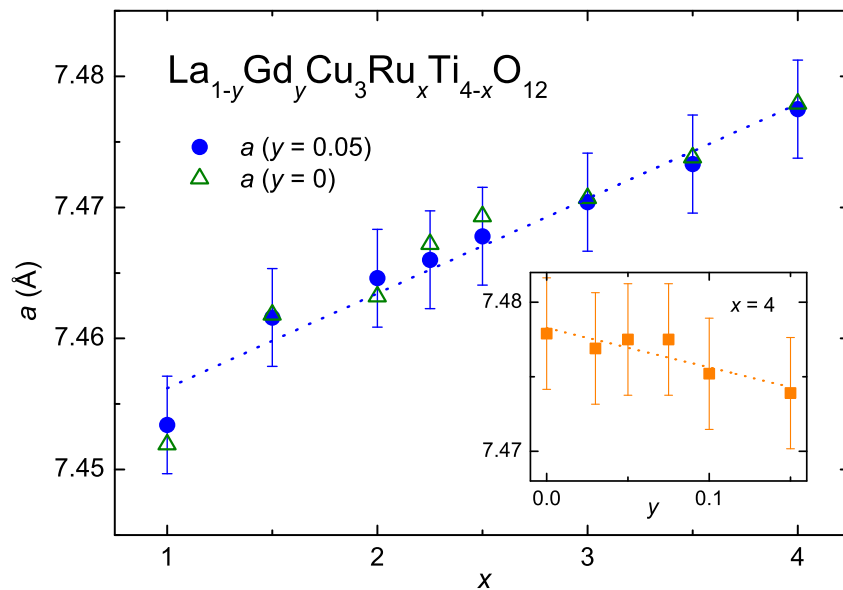


**Figure 2.** Dependence of the cubic lattice parameter  $a$  in  $\text{La}_{1-y}\text{Gd}_y\text{Cu}_3\text{Ru}_x\text{Ti}_{4-x}\text{O}_{12}$  on the Ru concentration  $x$  in the regime  $1 \leq x \leq 4$  for  $y = 0$  and  $y = 0.05$ . Inset: Dependence of  $a$  on the Gd concentration  $y$  for  $x = 4$ .

The magnetic susceptibility was investigated using a commercial SQUID magnetometer (*Quantum Design* MPMS5) for temperatures  $2 \leq T \leq 400$  K. It turned out that the temperature dependence of the susceptibilities could be well described by the sum of independent contributions of undoped  $\text{LaCu}_3\text{Ru}_x\text{Ti}_{4-x}\text{O}_{12}$  and of the Gd spins. This indicates that the influence of the Gd spins on the basic properties of the undoped compounds is of minor importance. Thus, Gd is well suited to probe the electronic properties of  $\text{LaCu}_3\text{Ru}_x\text{Ti}_{4-x}\text{O}_{12}$  without disturbing them.

The ESR experiments have been performed at X-band frequency ( $\nu \approx 9.4$  GHz) in a *Bruker* ELEXSYS E500 continuous-wave spectrometer. For cooling an *Oxford Instruments* ESR 900 continuous He-gas flow cryostat was used providing temperatures  $4.2 \leq T \leq 300$  K. Because of the applied Lock-In technique with field modulation, the ESR spectra record the field derivative  $dP_{\text{abs}}/dH$  of the microwave power absorbed by the sample due to induced magnetic dipolar transitions between the Zeeman levels of the probe spins as a function of the static external magnetic field  $H$ .

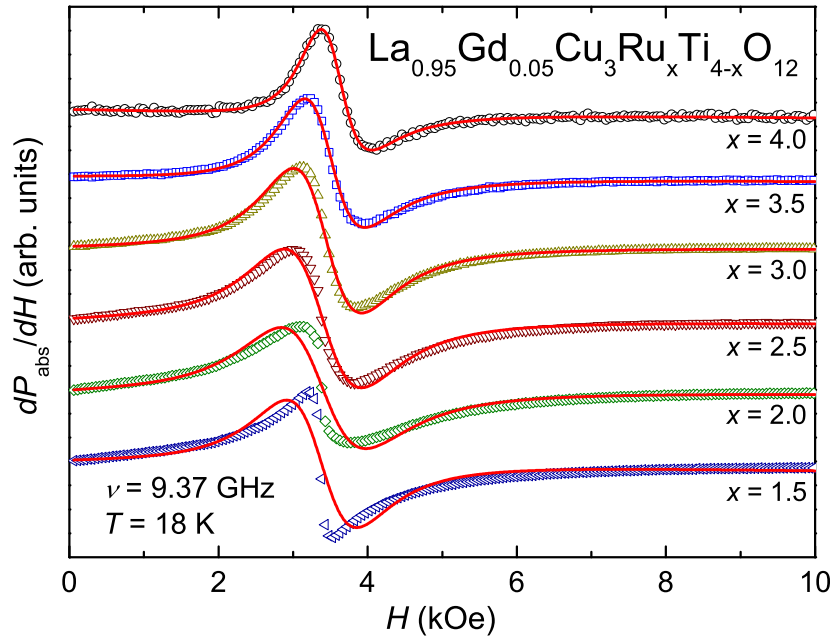
### 3. Results

Fig. 3 depicts characteristic  $\text{Gd}^{3+}$ -ESR spectra taken in  $\text{La}_{0.95}\text{Gd}_{0.05}\text{Cu}_3\text{Ru}_x\text{Ti}_{4-x}\text{O}_{12}$ . The spectrum of  $x = 4$  is characteristic for the metallic regime. The asymmetric single exchange-narrowed line is well described in terms of a Dyson-type shape, i.e. an asymmetric Lorentz line which contains a certain contribution  $0 \leq \alpha \leq 1$  of dispersion besides the usual absorption because of the skin effect arising from the conductivity [23, 24]. Moreover, due to the large linewidth  $\Delta H$  observed at elevated temperatures, the counter resonance at negative resonance field  $-H_{\text{res}}$  had to be taken into account when fitting the ESR spectra [25]. In comparison to  $x = 4$  with  $\alpha = 0.78$  the spectrum becomes nearly symmetric ( $\alpha \rightarrow 0$ ) on decreasing  $x$ , resulting from decreasing conductivity on approaching the metal-to-insulator transition. At the same time deviations from the ideal Lorentz shape become significant for  $x \leq 2$  and the fit is poor for  $x = 1.5$ . This indicates the breakdown of the exchange narrowing in the insulating regime, i.e. because of the lack of conduction electrons. Thus, already from the ESR line shape we are able to localize the MIT close to  $x = 2$ .

Before going into details of the MIT, we describe the influence of the Gd concentration  $y$  on the ESR properties of  $\text{La}_{1-y}\text{Gd}_y\text{Cu}_3\text{Ru}_4\text{O}_{12}$ . Fig. 4 shows the temperature dependence of the resonance linewidth  $\Delta H$  for different Gd concentrations  $0.05 \leq y \leq 0.15$ . For all samples we recognize a steep linear increase of the linewidth with temperature with a slope of about 24 Oe/K up to about 50 K. For higher temperatures  $\Delta H(T)$  exhibits a negative curvature. The data for  $y > 0.075$  exhibit a significantly increasing residual linewidth  $\Delta H_0$  indicating the influence of disorder or non-zero contribution of the Gd-Gd interactions. It has to be noted, however, that the  $g$  value of  $\text{La}_{1-y}\text{Gd}_y\text{Cu}_3\text{Ru}_4\text{O}_{12}$  is practically independent on the Gd concentration at  $g = 1.89$ .

Nevertheless, to be sure that the Gd-Gd interaction does not influence the results, we performed all ESR investigations of the Ti:Ru substitutional series using a Gd concentration  $y = 0.05$ . Fig. 5 shows the temperature dependence of linewidth (main frame) and  $g$  value (inset) for  $2 \leq x \leq 4$ . For lower Ru contents the evaluation with a single exchange-narrowed line is not reasonable any more. With decreasing Ru content one recognizes a significant increase of the residual linewidth. All data sets intersect each other close to 35 K and exhibit qualitatively a similar temperature dependence with a clearly linear increase below 50 K followed by a weaker linear increase at elevated temperatures. Only the absolute slope systematically

decreases with decreasing  $x$  on approaching  $x = 2$ . The  $g$  values are only weakly temperature dependent and gradually increase with decreasing  $x$  from  $g(x = 4) \approx 1.89(1)$  approaching  $g(x = 2) \approx 1.99(1)$ .



**Figure 3.** Typical ESR signals for  $\text{La}_{0.95}\text{Gd}_{0.05}\text{Cu}_3\text{Ru}_x\text{Ti}_{4-x}\text{O}_{12}$  with different Ru content  $x$ . The red solid lines indicate the fits by a Dyson-type shape as described in the text. Deviations show up for  $x \leq 2$  indicating the insulating regime where the exchange-narrowing process by conduction electrons drops out.

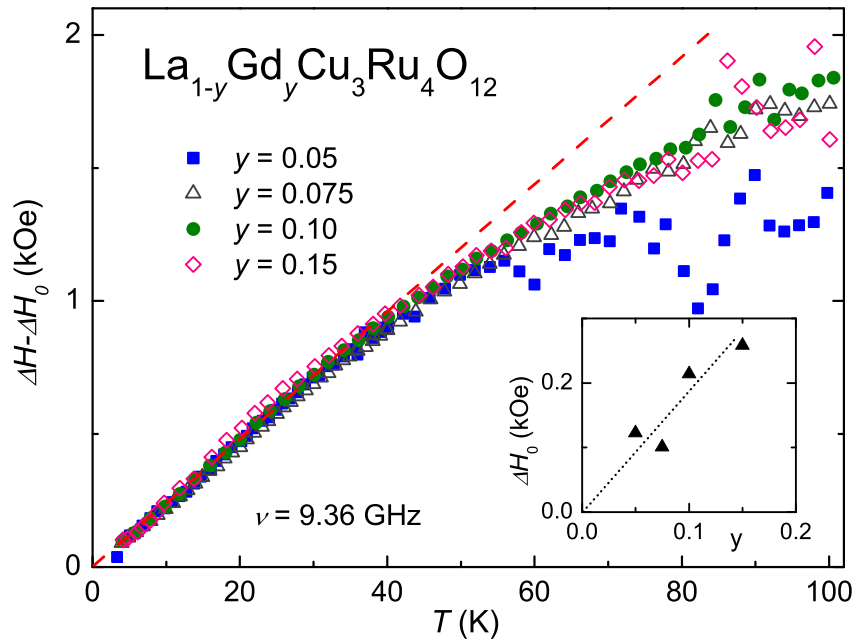


**Figure 4.** Temperature dependence of the resonance linewidth  $\Delta H$  after subtraction of the residual linewidth  $\Delta H_0$  for  $\text{La}_{1-y}\text{Gd}_y\text{Cu}_3\text{Ru}_4\text{O}_{12}$  with different Gd concentration  $0.05 \leq y \leq 0.15$ . The dashed line indicates the linear Korringa regime at low temperatures due to enhanced effective electronic masses. Inset: Dependence of the residual linewidth on  $y$ .

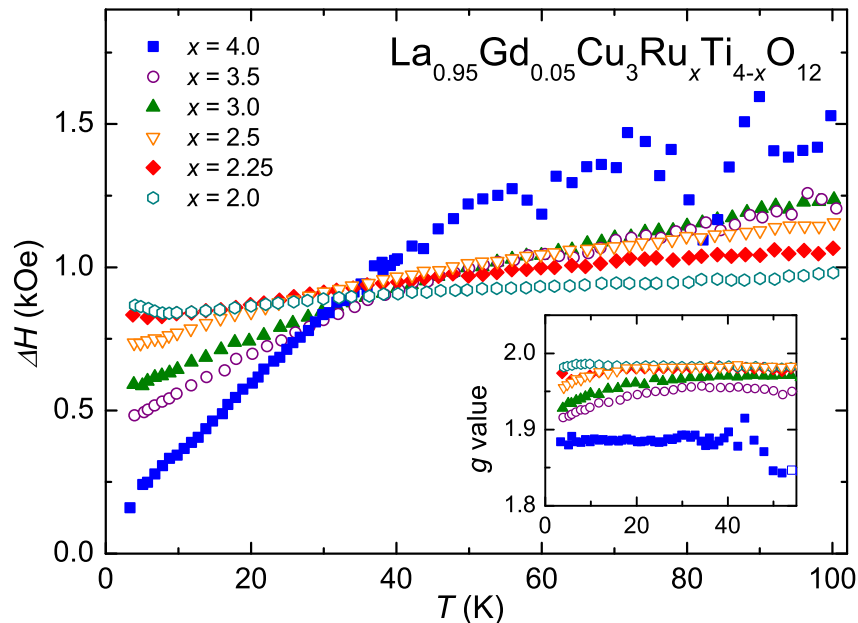


**Figure 5.** Temperature dependence of the resonance linewidth  $\Delta H$  for  $\text{La}_{0.95}\text{Gd}_{0.05}\text{Cu}_3\text{Ru}_x\text{Ti}_{4-x}\text{O}_{12}$  for  $2 \leq x \leq 4$ . Inset: Temperature dependence of the corresponding  $g$  values.

#### 4. Discussion

The observed properties of the resonance linewidth in  $\text{La}_{1-y}\text{Gd}_y\text{Cu}_3\text{Ru}_4\text{O}_{12}$  are characteristic for heavy-fermion compounds. NMR measurements on  $^{101}\text{Ru}$  and  $^{63}\text{Cu}$  in the related compound  $\text{CaCu}_3\text{Ru}_4\text{O}_{12}$  have shown that at low temperatures the effective electronic masses are strongly enhanced on the Ru site, but turn out to become even reduced at the Cu site [18]. Thus, compared to the canonical  $4f$ -electron based heavy-fermion compounds like  $\text{CeCu}_2\text{Si}_2$  or  $\text{CeAl}_3$ , ruthenium plays the role of the  $4f$ -Kondo ion, which is screened by the conduction electrons. Hence, following Ref. [26] the ESR linewidth consists of two contributions, i.e. one due to the direct exchange of the Gd spin with the conduction electrons and the second due to the indirect Ruderman-Kittel-Kasuya-Yosida (RKKY) exchange with the fluctuating Ru spins transferred by the conduction electrons. This can be expressed by:

$$\Delta H - \Delta H_0 = \Delta H_{\text{ce}} + \Delta H_{\text{Ru}} = b_{\text{K}}T + A_{\text{RKKY}}T\tau\chi_{\text{Ru}} \quad (1)$$

where  $\Delta H_0$  contains all temperature independent contributions due to disorder or impurities. The first term is the usual Korringa relaxation linear in temperature  $T$  with the slope  $b_{\text{K}} \propto \langle J^2(q) \rangle N^2(E_{\text{F}})$  determined by the electronic density of states  $N(E_{\text{F}})$  at the Fermi energy  $E_{\text{F}}$  and the exchange integral  $J$  averaged over all possible momentum transfers  $q$ . The second term depends on the fluctuation time  $\tau$  of the Ru spins and on their static susceptibility  $\chi_{\text{Ru}}$ . The prefactor  $A_{\text{RKKY}}$  averages over the squared RKKY exchange integrals. In canonical heavy-fermion compounds for temperatures far below the characteristic temperature  $T^*$ , the spin fluctuation time is approximately temperature independent  $\tau(T) \propto 1/T^*$  and the susceptibility is Pauli-like but strongly enhanced with respect to usual metals. This results in an enhanced Korringa-like linear increase of the linewidth for  $T \ll T^*$ . For elevated temperatures  $T \gtrsim T^*$  the fluctuations become faster  $\tau(T) \propto T^{-1/2}$  following Ref. [27]. The susceptibility decreases with a Curie-Weiss law  $\propto (T - \Theta)^{-1}$ . Thus, the heavy-fermion contribution becomes gradually suppressed, providing the bare Korringa relaxation via the conduction electrons at high temperatures.

In Gd doped  $\text{LaCu}_3\text{Ru}_4\text{O}_{12}$  a characteristic temperature of about  $T^* \approx 50$  K separates the linear Korringa-like low-temperature regime with an enhanced slope of  $b_L \approx 24$  Oe/K from the high-temperature regime with an asymptotic Korringa slope of  $b_H \approx 7$  Oe/K. This enhancement by a factor of about 3 is significantly weaker than the factor of 40 obtained from  $^{101}\text{Ru}$ -NMR in  $\text{CaCu}_3\text{Ru}_4\text{O}_{12}$ . This can be explained by the fact that the ESR probe feels the enhancement only via the RKKY interaction which decreases  $\propto 1/R^6$  with the distance  $R$  of the ESR probe from the Ru ions, while NMR measures in that case directly at the Ru ions where the heavy fermion masses are formed [12].

Similar to the linewidth we can consider the  $g$  value to contain contributions from the Pauli susceptibility of the conduction electrons  $\Delta g_{ce} \propto J(0)N(E_F)$  as well as from the local moments of the Ru ions  $\Delta g_{\text{Ru}} \propto \chi_{\text{Ru}}$  mapping the local susceptibility analogously to the Knight shift in NMR. Indeed, Gd doped  $\text{LaCu}_3\text{Ru}_4\text{O}_{12}$  exhibits a significant negative  $g$  shift  $\Delta g = g - g_{\text{ins}} \approx -0.1$  from its insulator value  $g_{\text{ins}} = 1.993$  [28]. Compared to usual metals this seems to be surprising, because the uniform magnetic polarization of the conduction electrons in the external field usually gives rise to an additional internal magnetic field supporting the external field and, therefore, to a positive  $g$  shift. However, the exchange geometry including  $d$  electrons sometimes can reverse the sign as reported earlier in Gd-doped Laves phases [10] and also recently in iron pnictides [29]. The quite large absolute value of the  $g$  shift corroborates the heavy-fermion properties of  $\text{LaCu}_3\text{Ru}_4\text{O}_{12}$ .

On substitution of ruthenium by titanium the characteristic heavy-fermion type contribution to the linewidth remains discernible but becomes gradually suppressed down to  $x = 2$ . Although the characteristic temperature derived from the kink at  $T^* \approx 50$  K is not changed, the absolute value of this relaxation contribution strongly decreases on decreasing Ru content  $x$  while only the temperature independent residual linewidth increases. At the same time the  $g$  value progressively approaches the insulator value. This behavior strongly reminds of the situation in the canonical heavy-fermion compound  $\text{Y}_{1-x}\text{Ce}_x\text{Al}_2$ , where the magnetic  $\text{Ce}^{3+}$  (electronic configuration  $4f^1$ ) Kondo ion is gradually replaced by non magnetic  $\text{Y}^{3+}$  ions. In that compound Gd-ESR was applied to characterize the transformation from the concentrated Kondo lattice to diluted Kondo ions [26]. Indeed, those experiments revealed the local character of the Kondo effect even in the concentrated heavy-fermion lattice, because the linewidth can be understood just as the sum of independent contributions of  $\text{Ce}^{3+}$  spin fluctuations and conduction electrons, where the strength of the former is just proportional to the concentration  $x$  of the cerium ions with only slightly varying characteristic temperature  $T^* \approx 10$  K.

The main difference between  $\text{Y}_{1-x}\text{Ce}_x\text{Al}_2$  and  $\text{LaCu}_3\text{Ru}_x\text{Ti}_{4-x}\text{O}_{12}$  is the fact that the former compound is a metal in the whole concentration range, while the latter undergoes a metal-to-insulator transition, which from electrical resistivity measurements could only roughly be localized in the range  $2 \leq x \leq 3$  [21]. This means that on decreasing Ru content, not only the contribution due to Ru spin fluctuations but also the direct Korringa relaxation is switched off as the MIT takes place. Therefore, to identify the MIT, Fig. 6 depicts the dependence of both the low-temperature slope  $b_L$  and the high-temperature slope  $b_H$  on the Ru content  $x$ , characterizing the contributions of Ru spin fluctuations as well as the direct Korringa relaxation, respectively. As expected, the relaxation due to Ru spin fluctuations monotonously decreases on decreasing Ru content  $x$ , while the direct Korringa contribution decreases only slightly until it drops to  $b_H < 1$  Oe/K at  $x = 2.25$ .

Thus, the MIT in  $\text{LaCu}_3\text{Ru}_x\text{Ti}_{4-x}\text{O}_{12}$  is characterized just by fading of the metallic relaxation contributions without any critical divergence. This is in contrast to the behavior observed

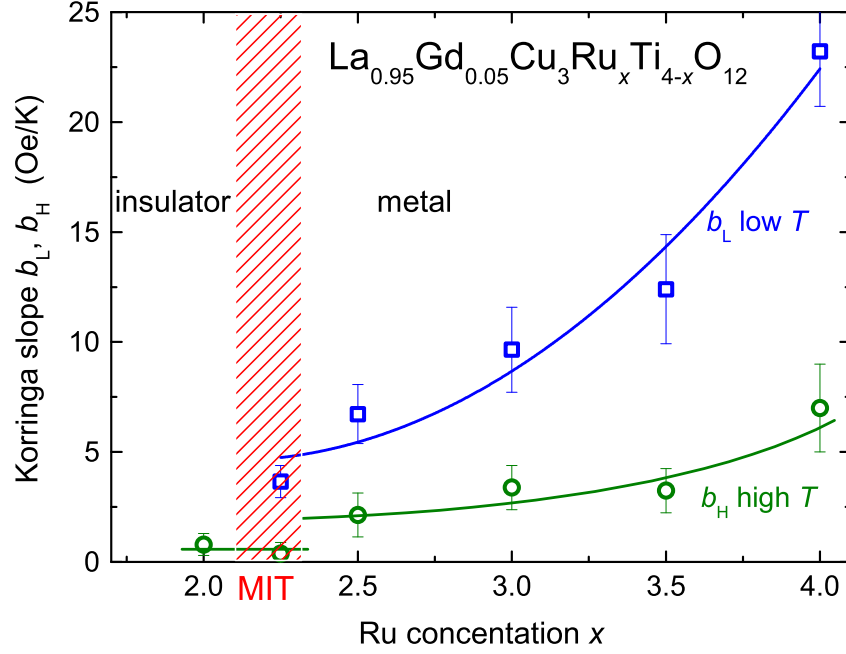


**Figure 6.** Korringa slope  $b_L$  and  $b_H$  determined from the temperature dependence of the ESR linewidth below and above 50 K, respectively, as a function of the Ru content  $x$  for  $\text{La}_{0.95}\text{Gd}_{0.05}\text{Cu}_3\text{Ru}_x\text{Ti}_{4-x}\text{O}_{12}$ .

for example in  $\text{Gd}_{1-x}\text{SrTiO}_3$  [6]. where the heavy-fermion type relaxation contribution diverges on approaching the MIT from the metallic regime due to diverging effective electronic masses as also documented by specific-heat measurements on the related compounds  $\text{La}_{1-x}\text{Sr}_x\text{TiO}_3$  and  $\text{Y}_{1-x}\text{Ca}_x\text{TiO}_3$  [30, 31]. The basic difference is that in those compounds the substitution does not replace the Ti ions themselves but only changes the electronic filling on the Ti sites between  $3d^0$  ( $x = 1$ ,  $\text{Ti}^{4+}$ ) and  $3d^1$  ( $x = 0$ ,  $\text{Ti}^{3+}$ ). The  $3d$  electrons can move on the Ti lattice and the correlations increase with increasing number of  $3d$  electrons, giving rise to enhancing effective masses and finally to the formation of the Mott insulator.

In contrast, in  $\text{LaCu}_3\text{Ru}_x\text{Ti}_{4-x}\text{O}_{12}$ , the magnetic  $\text{Ru}^{4+}$  ions (electronic configuration  $4d^4$  determined from XANES) [21], at which the heavy-fermion formation takes place, are substituted by nonmagnetic  $\text{Ti}^{4+}$  ions with empty  $3d$  shells. Therefore, Ti substitution breaks the lattice periodicity of the heavy-fermion system and strongly disturbs the  $4d$  band structure. This in turn inhibits the conductivity, while the electronic filling remains unaffected by the substitution. Note also that regarding previous NMR measurements in  $\text{CaCu}_3\text{Ru}_4\text{O}_{12}$ , electronic mass enhancement is not expected at the copper site. Thus, as soon as approximately 50% of the Ru ions are replaced by Ti ions, practically all Cu- $3d$  electrons are randomly localized at the Cu ions giving rise to the insulating state and spin-glass phase at low temperatures.

## 5. Conclusion

The present investigations clearly show that electron spin resonance as a local probe is able to access electronic properties in a solid, which are otherwise difficult or even impossible to obtain by means of bulk methods like electrical resistivity or specific-heat measurements. In  $\text{LaCu}_3\text{Ru}_x\text{Ti}_{4-x}\text{O}_{12}$  the conductivity is strongly affected by local moment scattering leading to an increasing resistivity with decreasing temperature for  $x \leq 3$  in the metallic regime. At the same time the specific heat is governed by the corresponding Schottky anomalies. Therefore, only the spin relaxation of the ESR probe Gd allowed determining the evolution of the electronic ground state, which changes from a heavy-fermion metal at  $x > 2.25$  into a semiconductor or

insulator with spin-glass ground state for lower Ru content  $x \leq 2$ . Thus, the Ru concentration of the metal-to-insulator transition can be approximately localized at  $x_c \approx 2.25$

## Acknowledgments

We thank Dana Vieweg for x-ray and SQUID measurements and Zakir Seidov for experimental support. We gratefully acknowledge the financial support granted by the Bavarian graduate school (Resource strategy concepts for sustainable energy systems) of the Institute of Materials Resource Management (MRM) of the University of Augsburg and by the Deutsche Forschungsgemeinschaft (DFG) within the collaborative research unit TRR 80 (Augsburg, Munich, Stuttgart).

## References

1. Andres K., Graebner J. E., Ott H. R., *Phys. Rev. Lett.* **35**, 1779 (1975).
2. Steglich F., Aarts J., Bredl C. D., Lieke W., Meschede D., Franz W., Schäfer H., *Phys. Rev. Lett.* **43**, 1892 (1979).
3. Trovarelli O., Geibel C., Mederle S., Langhammer C., Grosche F. M., Gegenwart P., Lang M., Sparn G., Steglich F., *Phys. Rev. Lett.* **85**, 626 (2000).
4. Stewart G. R., *Rev. Mod. Phys.* **56**, 755 (1984).
5. Kondo S., Johnston D. C., Swenson C. A., Borsa F., Mahajan A. V., Miller L. L., Gu T., Goldman A. I., Maple M. B., Gajewski D. A., Freeman E. J., Dille N. R., Merrin J., Kojima K., Luke G. M., Uemura Y. J., Chmaissem O., Jorgensen J. D., *Phys. Rev. Lett.* **78**, 3729 (1997).
6. Heinrich M., Krug von Nidda H.-A., Fritsch V., Loidl A., *Phys. Rev. B* **63**, 193103 (2001).
7. Krug von Nidda H.-A., Bulla R., Büttgen N., Heinrich M., Loidl A., *Eur. Phys. J. B* **34**, 399 (2003).
8. Sichelschmidt J., Ivanshin V. A., Ferstl J., Geibel C., Steglich F., *Phys. Rev. Lett.* **91**, 156401 (2003).
9. Förster T., Sichelschmidt J., Krellner C., Geibel C., Steglich F., *J. Phys.: Condens. Matter* **22**, 435603 (2010).
10. Elschner B., Loidl A., in Gschneidner K. A. Jr., Eyring L. (eds.), *Handbook on the Physics and Chemistry of Rare Earths, Vol. 24*, p. 221 (Elsevier Science B. V., Amsterdam, 1997).
11. Schlott M., Elschner B., Herrmann M., Assmus W., *Z. Phys. B* **72** 385 (1988).
12. Krug von Nidda H.-A., Schütz A., Heil M., Elschner B., Loidl A., *Phys. Rev. B* **57**, 14344 (1998).
13. Mair S., Krug von Nidda H.-A., Lohmann M., Loidl A., *Phys. Rev. B* **60** 16409 (1999).
14. Ramirez A. P., Lawes G., Li D., Subramanian M. A., *Solid State Commun.* **131**, 251 (2004).
15. Büttgen N., Krug von Nidda H.-A., Kraetschmer W., Günther A., Widmann S., Riegg S., Krimmel A., Loidl A., *J. Low Temp. Phys.* **161**, 148 (2010).

16. Kobayashi W., Terasaki I., Takeya J.-I., Tsukada I., Ando Y., *J. Phys. Soc. Jpn.* **73**, 2373 (2004).
17. Krimmel A., Günther A., Kraetschmer W., Dekinger H., Büttgen N., Loidl A., Ebbinghaus S. G., Scheidt E.-W., Scherer W., *Phys. Rev. B* **78**, 165126 (2008).
18. Krimmel A., Günther A., Krätschmer W., Dekinger H., Büttgen N., Eyert V., Loidl A., Sheptyakov D. V., Scheidt E.-W., Scherer W., *Phys. Rev. B* **80**, 121101 (2009).
19. Dittl A., Krohns S., Sebald J., Schrettle F., Hemmida M., Krug von Nidda H.-A., Riegg S., Reller A., Ebbinghaus S. G., Loidl A., *Eur. Phys. J. B* **79**, 391 (2011).
20. Ebbinghaus S. G., Weidenkaff A., Cava R. J., *J. Solid State Chem.* **167**, 126 (2002).
21. Ebbinghaus S. G., Riegg S., Götzfried T., Reller A., *Eur. Phys. J. Special Topics* **180**, 91 (2010).
22. Rodriguez-Carvajal J., *Physica B* **192**, 55 (1993).
23. Feher G., Kip A. F., *Phys. Rev.* **98**, 337 (1955).
24. Dyson F. J., *Phys. Rev.* **98**, 349 (1955).
25. Joshi J. P., Bhat S. V., *J. Magn. Reson.* **168**, 284 (2004).
26. Coldea M., Schaeffer H., Weissenberger V., Elschner B., *Z. Phys. B* **68**, 25 (1987).
27. Cox D. L., Bickers N. E., Wilkins J. W., *J. Appl. Phys.* **57**, 3166 (1985).
28. Abragam A., Bleaney B., *Electron Paramagnetic Resonance of Transition Ions* (Clarendon, Oxford, 1970).
29. Dengler E., Deisenhofer J., Krug von Nidda H.-A., Khim S., Kim J. S., Kim K. H., Casper F., Felser C., Loidl A., *Phys. Rev. B* **81**, 024406 (2010).
30. Tokura Y., Taguchi Y., Okada Y., Fujishima Y., Arima T., Kumagai K., Iye Y., *Phys. Rev. Lett.* **70**, 2126 (1993).
31. Taguchi Y., Tokura Y., Arima T., Inaba F., *Phys. Rev. B* **48**, 511 (1993).

## Список научных работ Б.И. Кочелаева

### List of publications by B.I. Kochelaev

1. Б.И. Кочелаев. К теории спин-решеточной релаксации ядерных спинов в ионных кристаллах. ЖЭТФ, **37**, 242 (1959).
2. Б.И. Кочелаев. Продольная релаксация ядерных спинов при сверхнизких температурах в парамагнитном кристалле. ЖЭТФ, **38**, 999 (1960).
3. Б.И. Кочелаев. К теории спин-решеточной релаксации парамагнитных ионов в комплексах. ФТТ, **2**, 1423 (1960).
4. Б.И. Кочелаев. Влияние дефектов кристалла на спин-решеточную релаксацию. ДАН, **131**, 105 (1960).
5. Б.И. Кочелаев. К теории спин-решеточной релаксации ядерных спинов, окруженных октаэдрическим комплексом. Оптика и спектроскопия, **9**, 257 (1960).
6. Б.И. Кочелаев. Спин-решеточная релаксация парамагнитных ионов в комплексах  $\text{XY}_6$ . В сб. Парамагнитный резонанс. Доклады на совещании по парамагнитному резонансу, Изд-во Казанского университета, с. 74-78 (1960).
7. Б.И. Кочелаев. Некоторые вопросы теории спин-решеточного взаимодействия в ионных кристаллах. Диссертация на соискание ученой степени кандидата физ.-мат. наук. Харьковский государственный университет, (1960).
8. Б.И. Кочелаев. Релаксационное поглощение звука в парамагнетике. ЖЭТФ, **41**, 423 (1961).
9. С.А. Альтшулер, Б.И. Кочелаев, А.М. Леушин. Парамагнитное поглощение звука (обзор). УФН, **75**, 459 (1961).
10. Б.И. Кочелаев. Резонансное вращение плоскости поляризации звука в парамагнетике. ФТТ, **4**, 1559 (1962).
11. Л.К. Аминов, Б.И. Кочелаев. Влияние спин-фононного взаимодействия на спектр парамагнитного резонанса. ФТТ, **4**, 1604 (1962).
12. Л.К. Аминов, Б.И. Кочелаев. О спин-решеточном взаимодействии в кристаллах, содержащих выделенные парамагнитные комплексы. ФТТ, **4**, 3273 (1962).
13. Л.К. Аминов, Б.И. Кочелаев. Спин-спиновые взаимодействия через поле фононов в парамагнитных кристаллах. ЖЭТФ, **42**, 1303 (1962).
14. Н.Г. Колоскова, Б.И. Кочелаев, У.Х. Копвиллем. Нерезонансное поглощение ультразвука спин-системой. Физич. проблемы спектроск. Изд-во АН СССР, **11**, 91 (1963).
15. Б.И. Кочелаев. Антиферромагнетизм, обусловленный спин-фононным взаимодействием. ЖЭТФ, **44**, 235 (1963).
16. Б.И. Кочелаев. К теории некоторых явлений в парамагнетике, обусловленных спин-фононным взаимодействием. Сб. "Парамагнитный резонанс", Изд-во Казанского университета, с. 78 (1964).

17. В.И. Кочелаев. Spin coupling by the conduction electrons. *J. Phys. Chem. Solids*, **25**, 1483 (1964).
18. Б.И. Кочелаев. Спин-спиновые взаимодействия через электроны проводимости в полупроводниках. *ФТТ*, **7**, 2859 (1965).
19. С.А. Альтшулер, Б.И. Кочелаев. Сдвиг компонент тонкой структуры релеевской линии рассеяния света в парамагнетике. *ЖЭТФ*, **49**, 862 (1965).
20. Б.И. Кочелаев. Сверхтонкая структура релеевской линии рассеяния света в парамагнетике. *ДАН*, **166**, 833 (1966).
21. М.И. Каганов, Б.И. Кочелаев, В.Г. Песчанский. XII Всесоюзное совещание по физике низких температур. *УФН*, **89**, 719 (1966).
22. Б.И. Кочелаев. Спектр парамагнитного резонанса с учетом электронно-колебательного взаимодействия в случае сильной связи. *ФТТ*, **9**, 2180 (1967).
23. Н.Г. Колоскова, Б.И. Кочелаев. Спектр парамагнитного резонанса с учетом электронно-колебательного взаимодействия в случае слабой связи. *ФТТ*, **9**, 2948 (1967).
24. Б.И. Кочелаев, Ш.Ш. Башкиров, Э.К. Садыков. О спин-фононном взаимодействии ядер парамагнитных ионов. *ФТТ*, **9**, 3238 (1967).
25. Б.И. Кочелаев. Теория динамических эффектов в парамагнитных кристаллах. Диссертация на соискание ученой степени доктора физико-математических наук. Казанский государственный университет, (1967).
26. М.Н. Алиев, Б.И. Кочелаев. Спин-решеточные колебания в парамагнетике. *Изв. ВУЗов, Физика*, **2**, 7 (1968).
27. Н.Г. Колоскова, Б.И. Кочелаев. Теория спинового эха в локальных полях. Сб. "Парамагнитный резонанс", в. 4, с. 29. Изд-во Казанского университета, (1968).
28. S.A. Al'tshuler, V.I. Kochelaev. Some peculiarities of Rayleigh light scattering in paramagnetic crystals. In book "Polarisation, Matiere et Rayonnement" volume jubilaire en l'honneur d'A.Kastler, Presses Universitaires de France, Paris, 1969, pp 17-25.
29. Б.И. Кочелаев, Ш.Ш. Башкиров, Э.К. Садыков. К теории акустического резонанса на ядрах парамагнитных ионов группы железа. *Изв. ВУЗов, Физика*, **4**, 92 (1969).
30. M.N. Aliev, V.I. Kochelaev. The statistical theory of nuclear magnetic resonance line shape in crystals with paramagnetic impurities. *Phys. Status Solidi B*, **35**, K71 (1969).
31. Н.М. Аминов, Б.И. Кочелаев. Квазилокальные колебания решетки, индуцированные электронными переходами. *ФТТ*, **11**, 2906 (1969).
32. С.А. Альтшулер, Б.И. Кочелаев. Методы исследования спин-фононного взаимодействия в парамагнетиках. *Изв. АН СССР, сер. физ.*, **35**, 883 (1971).
33. С.А. Альтшулер, Р.М. Валишев, Б.И. Кочелаев, А.Х. Хасанов. Обнаружение лавины фононов с помощью мандельштам-бриллюэновского рассеяния света в условиях импульсного насыщения ЭПР. *Письма в ЖЭТФ*, **13**, 535 (1971).

34. В.И. Kochelaev. Bose-Einstein Condensation of Magnons. Proc. XVI Congress AMPERE, Bucharest, 1971, p. 131.
35. Б.И. Кочелаев. Распространение флуктуаций намагниченности в твердом парамагнетике. Сб. "Парамагнитный резонанс 1944–1969", с. 229. Наука, Москва, (1971).
36. Б.И. Кочелаев. Исследования фононной системы по мандельштам-бриллюэновскому рассеянию света в условиях насыщения парамагнитного резонанса. ЖЭТФ, **62**, 630 (1972).
37. Н.М. Аминов, Б.И. Кочелаев. О возможности возникновения "фотонной лавины" при насыщении крыла линии ЭПР. Письма в ЖЭТФ, **15**, 224 (1972).
38. Б.И. Кочелаев, Р.Р. Нигматуллин. К теории насыщения ЭПР при низких температурах. ФТТ, **14**, 3413 (1972).
39. Н.Е. Алексеевский, И.А. Гарифуллин, Б.И. Кочелаев, Э.Г. Харахашьян. ЭПР на локализованных магнитных моментах в сверхпроводнике. Письма в ЖЭТФ, **18**, 323 (1973).
40. Р.Г. Деминов, Б.И. Кочелаев. Стационарное вынужденное мандельштам-бриллюэновское рассеяние света в парамагнетике в условиях акустического парамагнитного резонанса. ЖЭТФ, **66**, 907 (1974).
41. Р.Г. Деминов, Б.И. Кочелаев. Фотонная лавина в молекулярных кристаллах. ФТТ, **16**, 3703 (1974).
42. Р.М. Валишев, Б.И. Кочелаев, А.Х. Хасанов. Усиление электромагнитных колебаний, обусловленное неравновесностью диполь-дипольного резервуара парамагнетика. ФТТ, **16**, 3724 (1974).
43. Н.Е. Алексеевский, И.А. Гарифуллин, Б.И. Кочелаев, Э.Г. Хаарахашьян. Об упорядочении магнитных примесей в сверхпроводниках. Письма в ЖЭТФ, **24**, 540 (1976).
44. Ю.Е. Котельников, Б.И. Кочелаев. Дипольная плазма в молекулярных кристаллах. ФТТ, **18**, 3578 (1976).
45. С.А. Альтшулер, Р.М. Валишев, Р.Г. Деминов, Б.И. Кочелаев, А.Х. Хасанов. Мандельштам-бриллюэновское рассеяние света на горячих фонах в парамагнетиках. Акустический журнал, **22**, 764 (1976).
46. Н.М. Галеева, Б.И. Кочелаев. Упругое взаимодействие магнитных центров в примесном парамагнетике. ФТТ, **19**, 1354 (1977).
47. В.И. Kochelaev, Yu.E. Kotelnikov. On the Bose-Einstein condensation of excitons. Phys. Status Solidi B, **81**, 747 (1977).
48. Н.Е. Алексеевский, И.А. Гарифуллин, Б.И. Кочелаев, Э.Г. Харахашьян. Электронный парамагнитный резонанс на локализованных магнитных состояниях в сверхпроводящей системе La-Eg. ЖЭТФ, **72**, 1523 (1977).
49. Б.И. Кочелаев, Р.Х. Сабиров, Г.Г. Халиуллин. Ширина линии магнитного резонанса в разбавленном парамагнетике. ФТТ, **19**, 152 (1977).

50. А.А. Косов, Б.И. Кочелаев. Электронный парамагнитный резонанс на локализованных магнитных моментах в бесщелевых сверхпроводниках. *ЖЭТФ*, **74**, 14 (1978).
51. Е.С. Гринберг, Р.Г. Деминов, Б.И. Кочелаев. Теория фоновой лавины, вызванной неравновесностью дипольного резервуара. *ФТТ*, **20**, 363 (1978).
52. С.А. Альтшулер, А.В. Дуглав, Б.И. Кочелаев, А.Х. Хасанов. Усиление нерезонансного поглощения ультразвука в парамагнетике, обусловленное неравновесным состоянием диполь-дипольного резервуара. *Proc. XX Congress AMPERE, Tallin, 1978*, p. 238.
53. Ю.Е. Котельников, Б.И. Кочелаев. Рассеяние света на колебаниях дипольной плазмы. *ФТТ*, **20**, 2036 (1978).
54. Б.И. Кочелаев, А.А. Косов. Динамика локализованных магнитных моментов в бесщелевых сверхпроводниках. В сб. "Парамагнитный резонанс", в.14, с.3. Изд-во Казанского университета, (1978).
55. Б.И. Кочелаев, А.Х. Хасанов. Лавина фононов, индуцированная неравновесностью дипольного резервуара. В кн. "Проблемы магнитного резонанса", М., Наука, 1978, с. 111.
56. В.И. Kochelaev, N.G. Koloskova, A.A. Kosov. Exchange narrowing of the EPR line in superconductors. *Proc. XX Congress AMPERE, Tallinn, 1978*, p. 209.
57. Ф.Л. Аухадеев, В.А. Гревцев, Б.И. Кочелаев, Б.З. Малкин, М.А. Теплов. Исследование магнитоакустических колебаний в парамагнетике  $\text{LiErF}_4$ . В материалах X Всесоюзной конференции "Акустическая спектроскопия, квантовая акустика, акустоэлектроника", Изд-во ФАН, 1978, с. 27.
58. Б.И. Кочелаев, Л.Р. Тагиров, М.Г. Хусаинов. Пространственная дисперсия спиновой восприимчивости электронов проводимости в сверхпроводнике. *ЖЭТФ*, **76**, 578 (1979).
59. Н.М. Галеева, Б.И. Кочелаев, Н.Ф. Фаткуллин. К теории спин-решеточной релаксации, вызванной локализованными поворотами кристаллической решетки. *ФТТ*, **22**, 2333 (1980).
60. А.В. Дуглав, Н.Г. Колоскова, Б.И. Кочелаев, А.Х. Хасанов. Резонансное парамагнитное поглощение звука в условиях диполь-дипольных взаимодействий. *ЖЭТФ*, **79**, 2367 (1980).
61. T.S. Altshuler, I.A. Garifullin, V.I. Kochelaev, E.G. Kharakhashyan, G.G. Khaliullin. Korringa Relaxation Rate of Exchange-Coupled Localised Moments in Metals. *Phys. Status Solidi B*, **98**, K85 (1980).
62. Б.И. Кочелаев, М.Г. Хусаинов. Форма линии ЭПР в сверхпроводнике второго рода. *ЖЭТФ*, **80**, 1480 (1981).
63. Е.С. Гринберг, А.В. Дуглав, Н.Г. Колоскова, Б.И. Кочелаев. О насыщении диполь-дипольного резервуара нерезонансным ультразвуком. *ЖЭТФ*, **80**, 2356 (1981).
64. Е.С. Гринберг, Б.И. Кочелаев, Г.Г. Халиуллин. Обменное сужение линии магнитного резонанса в разбавленных сверхпроводниках. *ФТТ*, **23**, 397 (1981).

65. Б.И. Кочелаев, М.Г. Хусаинов. Форма линии парамагнитного резонанса в бесщелевых сверхпроводниках II рода. ФТТ, **23**, 1237 (1981).
66. Е.С. Гринберг, А.В. Дуглав, Н.Г. Колоскова, Б.И. Кочелаев. Прямое поглощение низкочастотного ультразвука диполь-дипольным резервуаром и эффекты насыщения. Материалы XI Всесоюзной конференции по акустоэлектронике и квантовой акустике, Изд-во "Дониш", Душанбе, 1981, с. 284.
67. Е.Г. Гринберг, А.В. Дуглав, Б.И. Кочелаев. Поглощение энергии электромагнитного и звукового полей низкой частоты некрамерсовыми ионами  $\text{Ho}^{3+}$  в монокристалле. ЖЭТФ, **82**, 888 (1982).
68. Б.И. Кочелаев, В.Ф. Фролов. О возможности наблюдения акустического спинового резонанса электронов проводимости в металлах. Письма в ЖЭТФ, **35**, 214 (1982).
69. С.А. Альтшулер, Б.И. Кочелаев, Ю.Г. Назаров, А.Х. Хасанов. Исследование ЭПР, спиновой и фононной кинетики в ионных парамагнитных кристаллах при помощи мандельштам-бриллюэновского и комбинированного рассеяния света. Изв. АН СССР, сер. физ. **46**, 418 (1982).
70. Н.Е. Алексеевский, И.А. Гарифуллин, Б.И. Кочелаев, Г.Г. Халиуллин, Э.Г. Харахашьян. Электронный парамагнитный резонанс в сверхпроводящем соединении  $\text{LaGdIn}$ . ЖЭТФ, **82**, 1979 (1982).
71. Б.И. Кочелаев, Ю.Г. Назаров, А.Х. Хасанов. Сверхрассеяние света на спиновой системе парамагнитных ионов. Письма в ЖЭТФ, **33**, 475 (1983).
72. А.А. Антипин, Б.И. Кочелаев, В.И. Шленкин. Электронная спин-решеточная и фазовая релаксация в фосфатных стеклах, активированных иттербием. Письма в ЖЭТФ, **39**, 155 (1984).
73. Б.И. Кочелаев, В.Ф. Фролов. Об акустическом спиновом резонансе в металлах с парамагнитными примесями. ФТТ, **26**, 1228 (1984).
74. Б.И. Кочелаев, Б.М. Хасанов. Возможности наблюдения акустического парамагнитного резонанса в жидких кристаллах. ФТТ, **26**, 3046 (1984).
75. G.G. Khaliullin, B.I. Kochelaev. Spin-Wave Excitations of Paramagnetic Impurities in Superconductors. Phys. Lett., **106A**, 318 (1984).
76. B.I. Kochelaev. Magnetic resonance and relaxation at very low temperatures. S.A. Al'tshuler memorial lecture. In: XXIIInd Congress AMPERE on magnetic resonance and related phenomena proceedings, eds. K.A. Müller, R. Kind, J. Roos, University Zürich, Switzerland, 1984, p. 2-7.
77. А.А. Антипин, Б.И. Кочелаев, С.Б. Орлинский, Д.А. Фупман, В.И. Шленкин. Проявление двухуровневых систем в электронной фазовой релаксации в фосфатных стеклах при низких температурах. ЖЭТФ, **88**, 1001 (1985).
78. B.I. Kochelaev, L.R. Tagirov. Exchange-Field Narrowing Process for the Inhomogeneously Broadened EPR in Superconductors. Solid State Commun., **53**, 961 (1985).

79. Б.И. Кочелаев, Д.А. Фушман. Поглощение звука в стеклах, обусловленное взаимодействием двухуровневых систем. ФТТ, **27**, 2779 (1985).
80. Б.И. Кочелаев, Л.Р. Тагиров. Сужение линии ЭПР обменным полем в сверхпроводнике. ЖЭТФ, **89**, 1358 (1985).
81. Б.И. Кочелаев, Ю.Н. Прошин. Влияние стохастического магнитного пробоя на парамагнитный резонанс электронов проводимости в чистых металлах (Zn, Mg). ФТТ, **27**, 265 (1985).
82. Б.И. Кочелаев, Ю.Г. Назаров, А.Х. Хасанов, Д.В. Чистяков. Спин-комбинационное сверхрассеяние света в условиях нагрева резонансных фононов. Изв. АН СССР, сер. физ., **50**, 213 (1986).
83. М.В. Еремин, А.Ю. Завидонов, Б.И. Кочелаев. Взаимодействие примесных кристаллических центров в анизотропных упругих средах. ЖЭТФ, **90**, 537 (1986).
84. Б.И. Кочелаев, Л.Р. Тагиров. Сужение неоднородно и дипольно уширенных линий ЭПР обменным полем в сверхпроводнике. Радиоспектроскопия, Пермь, с. 69, (1987).
85. Н.Е. Алексеевский, И.А. Гарифуллин, Н.Н. Гарифьянов, Б.И. Кочелаев, А.В. Митин, В.И. Нижанковский, Л.Р. Тагиров, Е.П. Хлыбов. ЭПР в системе Y-Gd-Ba-Cu-O. Письма в ЖЭТФ, **46**, 292 (1987).
86. М.В. Еремин, Б.И. Кочелаев, А.Ю. Завидонов. Взаимодействие ионов Се через поле фононов в этилсульфатах. ФТТ, **29**, 2490 (1987).
87. S.A. Altshuler, A.Kh. Khasanov, B.I. Kochelaev. Studies of spin systems by means of light scattering in paramagnetic crystals. In "Spectroscopy of solids contains Rare Earth Ions", ed. A.A. Kaplyanskii and R.M. Macfarlane, ch. 10, p. 607. North-Holland, Amsterdam, (1987).
88. Н.Е. Алексеевский, И.А. Гарифуллин, Н.Н. Гарифьянов, Б.И. Кочелаев, В.Н. Нижанковский, А.В. Митин, Л.Р. Тагиров, Е.П. Хлыбов. ЭПР на локализованных моментах в сверхпроводящих металлооксидах. ЖЭТФ, **94**, 276 (1988).
89. Н.Е. Алексеевский, И.А. Гарифуллин, Н.Н. Гарифьянов, Б.И. Кочелаев, В.Н. Нижанковский, А.В. Митин, Л.Р. Тагиров, Е.П. Хлыбов. Электронные свойства системы YBaCuO. Письма в ЖЭТФ, **48**, 36 (1988).
90. Н.Е. Алексеевский, И.А. Гарифуллин, Н.Н. Гарифьянов, Б.И. Кочелаев, В.Н. Нижанковский, А.В. Митин, Л.Р. Тагиров. Парамагнитные центры Cu в образцах YBaCuO с различной степенью орторомбичности. ФТТ, **30**, 1568 (1988).
91. Б.И. Кочелаев, О.В. Недопёкин. Спиновое комбинационное рассеяние света на парамагнитных ионах. ФТТ, **30**, 2476 (1988).
92. Б.И. Кочелаев, Д.А. Таюрский. Спиновая кинетика в парамагнетиках при низких температурах. ФТТ, **30**, 3075 (1988).
93. B.I. Kochelaev, N.I. Alekseevskii, I.A. Garifullin, N.N. Garifyanov, A.V. Mitin, V.I. Nizhankovskii, L.R. Tagirov, G.G. Khaliullin, E.P. Khlybov. EPR of paramagnetic centers in high

- temperature superconductors. Proc. 24<sup>th</sup> AMPERE Congress on Magnetic resonance and related phenomena, 1989, pp. 429-446.
94. А.В. Митин, В.Н. Нижанковский, И.А. Гарифуллин, Н.Н. Гарифьянов, Б.И. Кочелаев, Г.Г. Халиуллин, Л.Р. Тагиров. EPR study of polycrystal line superconductors with YBaCuO structure. *J. Low Temp. Phys.*, **77**, 87 (1989).
  95. Б.И. Кочелаев, А.Е. Соловьев. Учет продольных флуктуаций в резонансном рассеянии фононов с двухуровневыми системами. *ФТТ*, **32**, 743 (1990).
  96. В.И. Kochelaev, L.R. Tagirov. Modification of exchange interaction of localized moments via conduction electrons in superconductors and its manifestations. In "Resonances", a volume in honor of N. Bloembergen, ed. by V.D. Levenson *et al.*, World Scientific, p. 39 (1990).
  97. В.И. Kochelaev, L.R. Tagirov, I.A. Garifullin, N.N. Garifyanov, G.G. Khaliullin, N.E. Alekseevskii, A.V. Mitin, V.I. Nizhankovskii, E.P. Khlybov. Single-crystal EPR study of high- $T_c$  superconductor YBa<sub>2</sub>Cu<sub>3</sub>O<sub>7- $\delta$</sub> . *Experimentelle Technik der Physik*, **38**, 359 (1990).
  98. Б.И. Кочелаев, Д.А. Таюрский. О спектре элементарных возбуждений в парамагнитных кристаллах с простой кубической решеткой. "Магнитный Резонанс-91", Материалы симпозиума, посвященного 80-летию С.А. Альшулера, Казань, 1991, с. 39.
  99. Б.И. Кочелаев, Е.П. Шарин. Пространственное распределение магнитного поля вне тонкой анизотропной сверхпроводящей пластины. *СФХТ*, **5**, 1931 (1992).
  100. Б.И. Кочелаев, Е.П. Шарин. Распределение локального магнитного поля вихревой решетки вблизи поверхности анизотропного сверхпроводника. *СФХТ*, **5**, 1982 (1992).
  101. В.И. Kochelaev, L. Kan, B. Elschner, S. Elschner. Spin dynamics in La<sub>2</sub>Sr<sub>2x</sub>CuO<sub>4</sub> doped with Mn as revealed by an EPR study. *Phys. Rev. B*, **49**, 13106 (1994).
  102. В.И. Kochelaev. Spin Temperature and Non-Equilibrium Phonons. in "NMR and More", a volume in honor of ANATOLE ABRAGAM, ed. by M. Goldman and M. Porneuf, Les Editions de Physique Les Ulis, p. 277, (1994).
  103. В.И. Kochelaev. Discovery of Electron Spin Resonance. In "Encyclopedia of Nuclear Magnetic Resonance", vol. 1, ed. by John Wiley & Sons, Ltd., (1995).
  104. В.И. Kochelaev, J. Sichelschmidt, B. Elschner, and A. Loidl. EPR study of the dynamic spin susceptibility in heavily doped YBa<sub>2</sub>Cu<sub>3</sub>O<sub>6+d</sub>. *Phys. Rev. B*, **51**, 9199 (1995).
  105. В.И. Kochelaev, Yu.V. Yablokov. The Beginning of Paramagnetic Resonance. World Scientific, Singapore, Hong Kong, 176 pp, (1995).
  106. Р.Г. Деминов, Б.И. Кочелаев, Л.Р. Тагиров. Явление магнитного узкого горла в La<sub>2-x</sub>Sr<sub>x</sub>CuO<sub>4+d</sub> и его использование для изучения спиновой динамики CuO<sub>2</sub> - плоскостей. *ФТТ*, **38**, 2293 (1996).
  107. Б.И. Кочелаев, Ю.Н. Прошин, С.Л. Царевский. Форма линии магнитного резонанса в сверхпроводниках второго рода с учетом скин-эффекта. *ФТТ*, **38**, 3220 (1996).

108. S.I. Belov, B.I. Kochelaev. Spin waves in Heisenberg two-dimensional antiferromagnets  $S = 1/2$  with skyrmions. *Solid State Commun.*, **103**, 249 (1997).
109. J. Sichelschmidt, B. Elschner, B. Lemor, B. Kochelaev, and A. Loidl. Intrinsic EPR in  $\text{LaSrCuO}_4$ : Manifestation of Three-Spin Polarons. *Phys. Rev. Lett.*, **79**, 4274 (1997).
110. С.И. Белов, Б.И. Кочелаев. Элементарные спиновые возбуждения в гейзенберговском антиферромагнетике  $S = 1/2$  со скирмионами. *ФТТ*, **39**, 574 (1997).
111. S.I. Belov, B.I. Kochelaev. Nuclear spin relaxation in two-dimensional Heisenberg antiferromagnet  $S = 1/2$  with skyrmions. *Solid State Commun.*, **106**, 207 (1998).
112. B.I. Kochelaev. Spin-Phonon Interaction and the EPR Linewidth in  $\text{La}_2\text{CuO}_4$  and Related Cuprates. *J. Supercond.* **12**, 53 (1999).
113. B. Elschner, B. Kochelaev, J. Sichelschmidt and A. Loidl. Intrinsic Electron Paramagnetic Resonance in  $\text{La}_{2x}\text{Sr}_x\text{CuO}_4$ : Manifestation of three Spin Polarons. *J. Supercond.* **12**, 57 (1999).
114. B.I. Kochelaev, A. Shengelaya, Guo-meng Zhao, H. Keller, K.A. Müller. EPR in  $\text{La}_{1-x}\text{Ca}_x\text{MnO}_3$ : Relaxation and bottleneck. *Phys. Rev. B*, **61**, 5888 (2000).
115. С.И. Белов, Б.И. Кочелаев. Ширина линии электронного парамагнитного резонанса в двумерном гейзенберговском антиферромагнетике  $S = 1/2$  со скирмионами. *ФТТ*, **42**, 499 (2000).
116. A. Shengelaya, H. Keller, K.A. Müller, B.I. Kochelaev, K. Conder. Tilting mode relaxation and oxygen isotope effect in  $\text{La}_{2x}\text{Sr}_x\text{CuO}_4$  studied by electron paramagnetic resonance. *J. Supercond. Novel Magn.*, **13**, 955 (2000).
117. S.I. Belov, B.I. Kochelaev. Skyrmions in 2D quantum Heisenberg antiferromagnet: static magnetic susceptibility. In: "Stripes and related phenomena", Kluwer Academic/ Plenum Publisher, New York, p. 349-354 (2000).
118. A. Shengelaya, H. Keller, K.A. Müller, B.I. Kochelaev, K. Conder. Tilting mode relaxation in the electron paramagnetic resonance of oxygen-isotope-substituted  $\text{La}_{2x}\text{Sr}_x\text{CuO}_4:\text{Mn}^{2+}$ . *Phys. Rev. B*, **63**, 144513 (2001).
119. Ch. Kegler, N. Büttigen, H.-A. Krug von Nidda, A. Krimmel, L. Svistov, B.I. Kochelaev, A. Loidl, A. Prokofiev, and W. Assmus. Magnetic resonance on  $\text{LiCuVO}_4$ . *Eur. Phys. J. B*, **22**, 321-326 (2001).
120. M. Heinrich, H.-A. Krug von Nidda, A. Krimmel, A. Loidl, R.M. Eremina, A.D. Ineev, B.I. Kochelaev, A.V. Prokofiev, W. Assmus. Structural and magnetic properties of  $\text{CuSb}_2\text{O}_6$  probed by ESR. *Phys. Rev. B*, **67**, 224418 (2003).
121. B.I. Kochelaev, A.M. Safina, A. Shengelaya, H. Keller, K.A. Müller, K. Conder. Three-Spin-Polarons and Their Elastic Interactions in Cuprates. *Mod. Phys. Lett. B*, **17**, 415 (2003).
122. B.I. Kochelaev, E.V. Shilova, J. Deisenhofer, H.-A. Krug von Nidda, A. Loidl, A.A. Mukhin, A.M. Balbashov. Phase Transitions and Spin Relaxation in  $\text{La}_{0.95}\text{Sr}_{0.05}\text{MnO}_3$ . *Mod. Phys. Lett. B*, **17**, 459 (2003).

123. S. Belov, B.I. Kochelaev. Magnetic Properties and Spin Kinetics of Two-Dimensional Heisenberg Antiferromagnets. *Mod. Phys. Lett. B*, **17**, 487 (2003).
124. J. Deisenhofer, B. I. Kochelaev, E. Shilova, A.M. Balbashov, A. Loidl, and H.-A. Krug von Nidda. Orbital order parameter in  $\text{La}_{0.95}\text{Sr}_{0.05}\text{MnO}_3$  probed by electron spin resonance. *Phys. Rev. B*, **68**, 214427 (2003).
125. Б.И. Кочелаев, А.М. Сафина. Режим электронного узкого горла для парамагнитных примесей в металлах в случае анизотропного обменного взаимодействия. *ФТТ*, **46**, 224 (2004).
126. A. Shengelaya, M. Bruun, B.I. Kochelaev, A. Safina, K. Conder, K.A. Müller. Metallic phase in lightly doped  $\text{La}_{2-x}\text{Sr}_x\text{CuO}_4$  observed by electron paramagnetic resonance. *Phys. Rev. Lett.* **93**, 017001 (2004).
127. A.D. Ineev, B.I. Kochelaev. Creation and stability of skyrmion state in two-dimensional magnets with doping. *Magn. Reson. Solids*, **7**, 1-6 (2005).
128. С.И. Белов, А.Д. Инеев, Б.И. Кочелаев. Эволюция магнитных свойств родительских соединений высокотемпературных сверхпроводников при допировании. Ученые записки Казанского государственного университета, сер. физ.-мат. науки, **147**, кн. 2, с. 30-41 (2005).
129. B.I. Kochelaev, G.B. Teitelbaum. Nanoscale Properties of Superconducting Cuprates Probed by the Electron Paramagnetic Resonance. In "Superconductivity in Complex Systems" Eds. K.A. Muller, A. Bussman-Holder. Springer-Verlag. Berlin Heidelberg, P. 203-266 (2005).
130. Б.И. Кочелаев, С.И. Белов, А.Д. Инеев. Исследование магнитных свойств и спиновой кинетики слабодопированных купратов на основе скирмионного подхода. Письма в ЖЭТФ, **81**(8), 478-480 (2005).
131. B.I. Kochelaev. 85th Birthday of Nicolas Bloembergen. *EPR news letter*, **15**(1), 13 (2005).
132. А.В. Аганов, М.В. Еремин, Б.И. Кочелаев, Б.З. Малкин, Э.К. Садыков, В.Д. Скирда, М.С. Тагиров. Резонансные свойства конденсированных сред. "История науки в Казанском университете 1980-2003 гг.", изд-во Казанского университета, с. 62-70 (2005).
133. S.I. Belov, A.D. Ineev, B.I. Kochelaev. Evolution of magnetic properties and spin kinetics of cuprates with hole doping. *J. Supercond. Novel Magn.*, **19**, 19 (2006).
134. B.I. Kochelaev. 20 Years after the Discovery of Cuprate Superconductors. *EPR news letter*, **16**(2-3), 14-15 (2006).
135. B.I. Kochelaev, F. Waldner. Skyrmions in Lightly Doped Cuprates? In "High  $T_c$  Superconductors and Related Transition Metal Oxides". Special Contributions in Honor of K. Alex Muller on Occasion of his 80th Birthday. Eds: Bussmann-Holder A., Keller H. Springer-Verlag Berlin Heidelberg, 191-199 (2007).
136. А.В. Аганов, Б.И. Кочелаев, И.И. Силкин, М.Х. Салахов, М.С. Тагиров, "Первооткрыватель (о Е.К. Завойском)", журнал "Казань", **9**, 10-14 (2007).

137. Б.И. Кочелаев. "На переднем крае науки. Открытие электронного парамагнитного резонанса и нобелевские премии", журнал "Казань", **9**, 48-49 (2007).
138. А.В. Аганов, Б.И. Кочелаев, М.Х. Салахов, И.И. Силкин, М.С. Тагиров, "Е.К. Завойский-основоположник магнитной радиоспектроскопии", Новости ЯМР в письмах. Юбилейный выпуск. 1745-1764 (2007).
139. A. Shengelaya, B.I. Kochelaev, K. Conder, H. Keller. Electronic Phase Separation and Unusual Isotope Effects in  $\text{La}_{2-x}\text{Sr}_x\text{CuO}_4$  Observed by Electron Paramagnetic Resonance. In "High  $T_c$  Superconductors and Related Transition Metal Oxides". Special Contributions in Honor of K. Alex Muller on Occasion of his 80th Birthday. Eds: Bussmann-Holder A., Keller H. Springer-Verlag Berlin Heidelberg, 287-302 (2007).
140. A.S. Kutuzov, A.M. Skvortsova, S.I. Belov, J. Sichelschmidt, J. Wykhoff, I. Eremin, C. Krellner, C. Geibel, B.I. Kochelaev. Magnetic susceptibility of  $\text{YbRh}_2\text{Si}_2$  and  $\text{YbIr}_2\text{Si}_2$  on the basis of a localized 4f electron approach. J. Phys.: Condens. Matter., **20**, 455208 (2008).
141. B.I. Kochelaev, S.I. Belov, A.M. Skvortsova, A.S. Kutuzov, J. Sichelschmidt, J. Wykhoff, C. Geibel, F. Steglich Why could electron spin resonance be observed in a heavy fermion Kondo lattice? Eur. Phys. J. B, **72**, 485 (2009).
142. A. Maisuradze, A. Shengelaya, B.I. Kochelaev, E. Pomjakushina, K. Conder, H. Keller, K.A. Muller. Probing the  $\text{Yb}^{3+}$  spin relaxation in  $\text{Y}_{0.98}\text{Yb}_{0.02}\text{Ba}_2\text{Cu}_3\text{O}_x$  by electron paramagnetic resonance. Phys. Rev. B, **79**, 054519 (2009).
143. Б.И. Кочелаев. Квантовая теория (конспект лекций, часть 1). Издательство Казанского университета, 2009, 100 стр.
144. J. Sichelschmidt, T. Kambe, I. Fazlishanov, D. Zakharov, H.-A. Krug von Nidda, J. Wykhoff, A. Skvortsova, S. Belov, A. Kutuzov, B.I. Kochelaev, V. Pashchenko, M. Lang, C. Krellner, C. Geibel, F. Steglich. Low temperature properties of the electron spin resonance in  $\text{YbRh}_2\text{Si}_2$ . Phys. Status Solidi B, **247**, 747-750 (2010).
145. B. Kochelaev, S. Belov, A. Skvortsova, A. Kutuzov, J. Sichelschmidt, J. Wykhoff, C. Geibel, F. Steglich. Kondo effect can help to see Electron Spin Resonance. Europhysicsnews, **41**, 11 (2010).
146. Б.И. Кочелаев. Квантовая теория (конспект лекций, часть 2). Издательство Казанского университета, 2010, 119 стр.
147. S.I. Belov, A.S. Kutuzov, B.I. Kochelaev. Spin relaxation in Kondo lattices. J. Phys.: Conf. Ser., **324**, 012017 (2011).
148. B.I. Kochelaev. Semen A. Altshuler: scientist, mentor, teacher. J. Phys.: Conf. Ser., **324**, 011002 (2011).
149. С.И. Белов, Б.И. Кочелаев, А.М. Скворцова, А.С. Кутузов. Природа электронного парамагнитного резонанса в кондо-решетке с тяжелыми фермионами. Ученые записки Казанского университета, сер. физ.-мат. науки. **153**(1), 38-47 (2011).

150. S.I. Belov, A.S. Kutuzov, B.I. Kochelaev, J. Sichelschmidt. Kondo lattice with heavy fermions: peculiarities of spin kinetics. *J. Phys.: Condens. Matter.*, **24**, 365601 (2012).
151. A.A. Vishina, A. Maisuradze, A. Shengelaya, B.I. Kochelaev, H. Keller. Inhomogeneous broadening of the EPR signal of the Yb ions in domain walls of lightly doped antiferromagnetic cuprates, *Magn. Reson. Solids*, **14**, 12102 (2012).
152. Л.Р. Тагиров, Б.И. Кочелаев, Р.Г. Деминов, Н.Х. Усеинов. Приложения двухвременных термодинамических функций Грина в физике твердого тела (конспект лекций на английском языке). Казанский федеральный университет, 2012, 101 с.
153. Б.И. Кочелаев. Квантовая теория (конспект лекций). Издательство Казанского университета, 2013, 222 стр.

*Список сокращений названий журналов*

ДАН	Доклады АН СССР
ЖЭТФ	Журнал экспериментальной и теоретической физики
Изв. АН СССР	Известия АН СССР
Изв. ВУЗов	Известия ВУЗов
Письма в ЖЭТФ	Письма в Журнал экспериментальной и теоретической физики
СФХТ	Сверхпроводимость: Физика, Химия, Технология
УФН	Успехи физических наук
ФТТ	Физика твердого тела
Eur. Phys. J.	European Physical Journal
J. Low Temp. Phys.	Journal of Low Temperature Physics
J. Phys. Chem. Solids	Journal of Physics and Chemistry of Solids
J. Supercond.	Journal of Superconductivity
J. Supercond. Novel Magn.	Journal of Superconductivity and Novel Magnetism
Magn. Reson. Solids	Magnetic Resonance in Solids, Electronic Journal
Mod. Phys. Lett.	Modern Physics Letters
Phys. Lett.	Physics Letters
Phys. Rev.	Physical Review
Phys. Rev. Lett.	Physical Review Letters
Phys. Status Solidi	Physica Status Solidi
Solid State Commun.	Solid State Communications

## Ученики Б.И. Кочелаева

### Pupils of B.I. Kochelaev

			к.ф.-м.н. Ph.D.	д.ф.-м.н. Doct.Sci.
1.	Алиев М.Н.	Aliyev M.N.	1969	1989
2.	Царевский С.Л.	Tsarevskii S.L.	1971	1994
3.	Аминов Н.М.	Aminov N.M.	1972	
4.	Нигматуллин Р.Р.	Nigmatullin R.R.	1974	1993
5.	Демин Р.Г.	Deminov R.G.	1976	
6.	Сабилов Р.Х.	Sabirov R.Kh.	1977	
7.	Котельников Ю.Е.	Kotel'nikov Yu.E.	1978	
8.	Косов А.А.	Kosov A.A.	1979	1992
9.	Галеева Н.М.	Galeeva N.M.	1980	
10.	Гринберг Е.С.	Grinberg E.S.	1981	
11.	Тагиров Л.Р.	Tagirov L.R.	1981	1996
12.	Хусаинов М.Г.	Khusainov M.G.	1981	1997
13.	Фазлеев Н.Г.	Fazleev N.G.	1981	
14.	Фролов В.Ф.	Frolov V.F.	1984	
15.	Назаров Ю.Г.	Nazarov Yu.G.	1984	
16.	Фушман Д.А.	Fushman D.A.	1985	
17.	Трутнев К.Ф.	Trutnev K.F.	1987	
18.	Хасанов Б.М.	Khasanov B.M.	1987	
19.	Прошин Ю.Н.	Proshin Yu.N.	1988	1995
20.	Тайурский Д.А.	Tayurskii D.A.	1989	2001
21.	Миронов Г.И.	Mironov G.I.	1989	2008
22.	Соловьев А.Е.	Solovyev A.E.	1990	
23.	Чистяков Д.В.	Chistyakov D.V.	1991	
24.	Усеинов Н.Х.	Useinov N.Kh.	1992	
25.	Недопекин О.В.	Nedopekin O.V.	1992	
26.	Шарин Е.П.	Sharin E.P.	1993	
27.	Белов С.И.	Belov S.I.	1997	
28.	Еремин И.М.	Eremin I.M.	1999	
29.	Сафина А.М.	Safina A.M.	2004	
30.	Шилова Е.В.	Shilova E.V.	2004	
31.	Инеев А.Д.	Ineev A.D.	2005	
32.	Кутузов А.С.	Kutuzov A.S.	2009	
33.	Вишина А.А.	Vishina A.A.	2012	
34.	Андроненко С.И.	Andronenko S.I.		2013

АКТУАЛЬНЫЕ ПРОБЛЕМЫ  
ФИЗИКИ КОНДЕНСИРОВАННЫХ СРЕД

Том 2

Подписано в печать 12.11.2014.

Бумага офсетная. Печать цифровая.

Формат 60x84 1/16. Гарнитура «SFRM 1095, CMR 10».

Усл. печ. л. 11,85. Тираж 120 экз. Заказ 43/8

Отпечатано с готового оригинал-макета  
в типографии Издательства Казанского университета

420008, г. Казань, ул. Профессора Нужина, 1/37

тел. (843) 233-73-59, 233-73-28